HIGH-RESOLUTION MAPS OF FRII DRAGNS

A thesis submitted to the University of Manchester
for the degree of Doctor of Philosophy
in the Faculty of Science and Engineering

2021

Katie Lyn Hesterly

Department of Physics and Astronomy in the School of Natural Sciences

Contents

List of Tables

List of Figures

The University of Manchester

ABSTRACT OF THESIS submitted by **Katie Lyn Hesterly**
for the Degree of Doctor of Philosophy and entitled
High-Resolution Maps of FRII DRAGNs September 2019.

Supermassive black holes at the centre of galaxies are strongly linked to relativistic plasma outflows seen in nearly 10% of all active galaxies. These outflows may be responsible for producing the most energetic particles in the universe, and are known to influence the formation and evolution of structure in the universe. While it is clear that jets are transporting matter and energy to great distances, the mechanism for doing so is poorly understood. A longstanding problem in jet physics is the appearance of two flavours of jets. Entrainment appears to play a role in sources with a higher surface brightness closer to the central region. For edge-brightened sources like Cygnus A, what mechanism allows them to sustain a well-collimated relativistic jet out to many kiloparsecs? Previous studies of kiloparsec-scale jets were limited by sensitivity, bandwidth, and resolution. Modern interferometers offer a chance to observe jets across many frequencies with excellent sensitivity and resolution.

The work presented in this thesis is part of the e-MERLIN Extragalactic Jets Legacy Project which seeks to probe sub-arcsecond structures at 1.5 and 5 GHz. The project aims to shine new light on key areas such as: (1) What are the transverse structures in the jet like?; (2) Is there any evidence for a spine-sheath along the jet?; and (3) Can we link acceleration to areas of brightening? Presented here are high resolution and sensitivity radio maps of two powerful FRII quasars − 3C 334 and 3C 263, and one powerful FRII radio galaxy − Cygnus A, with observations from the combined e-MERLIN and JVLA arrays.

The 1.5 GHz radio map of 3C 334 is the highest-resolution map to date. The improved maps reveal new knots along the jet and hotspots previously unresolved in the next best resolution maps. Within the counterjet "head" feature, we identify a centrally placed secondary hotspot. While this was identified in previous maps, the feature did not qualify as a hotspot at lower resolutions. Details of the radio structure and an analysis of the apparent jet opening angle is discussed.

A spectral index map created at 1.5 and 5 GHz (matched to a common resolution) is provided. Evidence in support of jet precession is outlined based on the alignment of many distinct features within the quasar's lobes.

The e-MERLIN+JVLA 1.5 GHz map of 3C 263 has revealed a strikingly straight, narrow, and mostly unresolved jet. A previously unresolved knot close to the core is identified. The high-resolution maps reveal a narrow deflecting jet entering the east hotspot. At VLA resolution the feature was considered a part of the jet due to the orientation and placement but was significantly less resolved. The hotspots in the west lobe are resolved into complex smaller features.

The e-MERLIN maps of Cygnus A provided a unique resolution to its hotspots and jet at 1.5 and 5 GHz. In both observations the transient observed by the JVLA was detected at a position of α =19:59:28.328, δ = +40°44′01.″913 at 1.5 GHz, and α = 19:59:28.3227, δ = +40°44′01.″9280 at 5 GHz. The SED indicates the flux at each frequency ($S_{1.5} = 5.2 \pm 2.2$ mJy and $S_5 = 4.05 \pm 0.5$ mJy) is consistent with the estimated flux ($\sim 3 - 4$ mJy). At 5 GHz a structure extending $\sim$0.″10 from the centre of the core and perpendicular to the direction of the jet is imaged. This may be support for the higher frequency JVLA detection of a torus, but sidelobes around the core reduce our confidence in the detection .

Declaration

No portion of the work referred to in this thesis has been submitted in support of an application for another degree or qualification of this or any other university or other institute of learning.

Copyright

Acknowledgements

There are many people who should be acknowledged and thanked for their encouragement and support over the past four years. First of all, I would like to thank my supervisor at Manchester, Paddy Leahy, for giving me the opportunity to be a part of the e-MERLIN Extragalactic Jets Legacy Project. I am grateful for Paddy's advice, guidance, and invaluable support. I would also like to thank Robert Laing for his assistance with the work in this thesis. Without Paddy and Robert this thesis would not have been possible.

To my family, this thesis would not have been possible without you. There isn't enough space in this thesis to describe the sacrifices my family made to get me to this point. I am forever grateful for having such an amazing family that never once discouraged me from doing astrophysics and did everything they could to help me succeed. I could not have done anything without all of them.

To my friends - Tim, Chance, Fernando, Jen, Emma, Hongming, and everyone else, I am grateful for the emotional and mental support they offered, especially at the end. Whether they provided me with an ample supply of snacks and food, helped me dig myself out of a Python coding disaster, or simply offered me a distraction from research when it was needed, it was greatly appreciated.

I am grateful for the University of Manchester and e-MERLIN support: Ant Holloway, Javier Moldon, and Rob Beswick. Thank you for assistance with calibration and computing.

I want to thank all of the facilities and databases that contributed to my research. e-MERLIN is a National Facility operated by the University of Manchester at Jodrell Bank Observatory on behalf of STFC. The National Radio Astronomy Observatory is a facility of the National Science Foundation operated under cooperative agreement by Associated Universities, Inc. This research has made use of the NASA/IPAC Extragalactic Database (NED), which is provided

by the Jet Propulsion Laboratory, California Institute of Technology, under contract with the National Aeronautics and Space Administration. This research has made use of NASA's Astrophysics Data System.

List of Abbreviations

AGN	Active galactic nuclei
AIPS	Astronomical Image Processing System
AVC	Automatic voltage correction (AVC)
BAL QSO	Broad absorption line quasi-stellar objects
BL Lac	BL Lacertae object
BLR	Broad line region
CASA	Common Astronomy Software Applications
CMB	Cosmic microwave background
CS1	Confusing source 1
CS2	Confusing source 2
Cyg A	Cygnus A
DRAGN	Double radio source associated with a galactic nucleus
DSA	Diffusive shock acceleration
e-MERLIN	enhanced Multi Element Remotely Linked Interferometer Network
FITS	Flexible Image Transport System
FRI	Fanaroff-Riley I
FRII	Fanaroff-Riley II
FSRQ	Flat spectrum radio quasar
FWHM	Full width at half maximum
HST	Hubble Space Telescope
JVLA	The Jansky Very Large Array (after 2010 upgrades)
MS	Measurement set
NELG	Narrow-emission line galaxy
NLRG	Narrow line radio galaxy
NRAO	National Radio Astronomy Observatory
RFI	Radio frequency interference
QSO	Quasi-stellar objects
SED	Spectral energy distribution
SERPent	Scripted E-merlin Rfi-mitigation PipelinE for iNTerferometry
SMBH	Supermassive black hole
SSRQ	Steep spectrum radio quasar
SPW	Spectral window
VLBI	Very Long Baseline Interferometry
VLA	The Very Large Array (before 2010 upgrades)

Conventions

Throughout this thesis, I adopt the most recent cosmology parameters for a flat universe presented by Planck Collaboration (2018): $H_0 = (67.4 \pm 0.5)$ km s^{-1} Mpc^{-1}, $\Omega_m = 0.315 \pm 0.007$, and $\Omega_\Lambda = 0.6889 \pm 0.0056$. The cosmological calculator created by Wright (2006) determined the pixel scale and angular size distance for all of the quasars and radio galaxies. The unit of flux density is defined as 1 Jy$= 10^{-26}$ W m^{-2} Hz^{-1}. J2000 coordinates are used unless otherwise stated. The convention for the spectral index used for this thesis is $S \propto \nu^{\alpha}$.

Chapter 1

Introduction

More than 100 billion galaxies have been discovered in the universe. The majority of these are "normal" galaxies - the observed radiation output is equal to the combined output of all of the stars in the galaxy. A minority of galaxies ($10\% - 15\%$) appear to have a similar morphology to normal galaxies but the output of emission, especially around the nuclear region, is greater than that which can be accounted for by the stellar population (Ho et al., 1997). These galaxies are active galaxies. Although the name suggests that the entire galaxy is active, it is only the very central region that is active. These galaxies can produce up to nearly a thousand times more power than a normal galaxy. The extremely bright active nuclear regions are referred to as active galactic nuclei (AGN). AGN have been observed to have a combination of some features including radio jets, strong and weak emission lines, and variability. A broad range of emission may be found in AGN from radio waves to γ-rays. Differences and causes for the unique AGN properties will be discussed later in this chapter.

AGN remain some of the most powerful and mysterious objects in the universe in part due to the diverse and numerous features present, or in some cases not present. Extragalactic radio jets, the main focus of this thesis, are produced by a small population of AGN. Jets may be supplying the surrounding environment with energy that can influence the evolution of structure within the Universe (Blandford et al., 2018). Despite being some of the brightest objects in the sky due to the tremendous luminosity produced, past attempts to image the AGN have proved to be challenging. With Very Long Baseline Interferometry (VLBI) the powerhouse and mechanisms that are responsible for producing the observed emission are being probed. Combining VLBI with smaller arrays provides the

necessary spatial scales to establish high resolution without losing the shorter *uv* coverage. Details regarding the theory of interferometry and calibration strategies are discussed in Chapter 2.

1.1 Motivation

There are still many unanswered questions regarding the two flavours of jet producing AGN: Fanaroff-Riley I (FRI) and Fanaroff-Riley II (FRII). Longstanding questions include:

- Is the matter content of the material along jets and lobes composed of electron-positron plasma or electron-proton plasma (Sikora and Madejski, 2000; Romero et al., 2017)? If protons are a large component of the material are they accelerated to relativistic speeds? Are there differences in composition between FRIs and FRIIs (Croston et al., 2018)? Does entrainment alter the composition of jets between parsec- and kiloparsec-scales (Hughes and Miller, 1991)?

- How are the particles accelerated along the jet in FRII sources? Does the power to accelerate and collimate the jets come from the rotational energy of the black hole or from the power released in the accretion flow (Blandford and Znajek, 1977; Blandford and Payne, 1982; Romero et al., 2017)? Does acceleration take place in or near the knots as a result of shocks?

- Why do FRI jets suddenly brighten a few kpc from the nucleus (Laing and Bridle, 2008)? What are the jet velocities and powers close to the brightening points (Laing and Bridle, 2008)? What are the entrainment rates in low-luminosity sources?

- Do jets have relativistic spines? If there is a spine-sheath, in what ways do spine-sheaths influence the interstellar medium (Walg et al., 2013)? How do these environments influence the jets?

- What is the strength of the magnetic field in relativistic sources? Do the magnetic fields help jets in FRII sources maintain collimation out to kiloparsec scales? What do spectral gradients reveal about the magnetic field structure along the jet (Clausen-Brown et al., 2011)?

Historically interferometers were unable to provide decent *uv* or bandwidth coverage. Modern upgrades to interferometers have improved on these limitations along with improvements to the sensitivity. Today telescopes can see details never before observed.

This thesis aims to use the intermediate baseline length radio interferometer e-MERLIN (enhanced Multi Element Remotely Linked Interferometer Network) with the more compact Jansky Very Large Array (JVLA) to gain new insight into high-power radio jets and hotspots. Work done is part of the e-MERLIN Extragalactic Jets Legacy Project which seeks to utilise advances in the e-MERLIN hardware with the sub-arcsecond resolution. It is the hope of the project that new information obtained from high-resolution radio maps may contribute to the overall understanding of differences between the two flavours of AGN jets (see §1.2.3).

1.2 Active Galactic Nuclei

1.2.1 Radio-loud Versus Radio-quiet

Only a small population of active galaxies are strong radio emitters. At least 90% of AGN have a radio luminosity below 10^{23} WHz^{-1} at 1.4 GHz (e.g., Condon et al., 1982; Peterson, 1997a; Kukula et al., 1998). Over the years many papers have described various definitions to distinguish between radio-loud or radio-quiet AGN (e.g., Kellermann et al., 1989; Sikora et al., 2007). For simplicity, this thesis adopts the definition described by Kellermann et al. (1989). The radio luminosity at 5 GHz (F_{5GHz}) and the optical luminosity in the B filter (F_B) define the radio loudness parameter R as:

$$R = \frac{F_{5GHz}}{F_B}. \tag{1.1}$$

When $R \geq 10$ the source is considered radio-loud. Only $\sim 10\%$ of all AGN are radio-loud.

Spectral energy distributions (SEDs) of radio-loud and radio-quiet AGN appear similar when compared from optical to X-ray wavelengths. In the radio and γ-ray parts of the spectrum the SEDs deviate. In Fig. 1.1 an SED of a radio-loud source is compared to an SED of a radio-quiet source (Elvis et al., 1994). At radio frequencies the diverging SEDs reveal a luminosity difference of approximately 10^3 (Urry and Padovani, 1995). Radio emission in radio-loud AGN is produced

by synchrotron emission from a relativistic jet (see §1.6). In many radio-quiet AGN, radio emission is attributed to coronal activity, star formation, accretion of material and ejection of plasma, and the interaction of radiation with the surrounding medium (Panessa et al., 2019). However, some Seyfert galaxies, which are radio-quiet, have been observed with synchrotron jets as well (e.g., Dibai et al., 1983; Roy et al., 1998). Other features in the AGN SED include:

1. mm-break: A sharp drop in power in the sub-millimeter band to radio. Synchrotron self-absorption is most likely the cause of this drop (Elvis et al., 1994).

2. IR continuum−optical: Blackbody emission from hot dust surrounding the black hole and thermal bremsstrahlung produced by the narrow-line region clouds (Contini et al., 2004).

3. Inflection: Point where the energy output of the AGN is at a minimum. This point coincides with the peak of the host galaxy's starlight contribution (Wilkes, 1999).

4. UV bump: Also known as the big blue bump (BBB). The BBB is often attributed to thermal emission produced by the accretion disk (Elvis et al., 1994).

5. Gap: Absorption of emission by gas and dust within the Milky Way (Savage et al., 1993).

6. XUV excess: The rise in the SED toward the EUV from both sides indicates that the same physical mechanism that produces the BBB may be responsible (Elvis et al., 1994). Better signal to noise (S/N) has increased the number of soft excess detections.

7. Hard X-ray component: Produced by the hot corona (Haardt and Maraschi, 1991).

Differences between radio-loud and radio-quiet AGN extend beyond SED deviations in the radio spectrum. Host galaxy type has been shown to be one of these differences. Radio-loud galaxies are associated with elliptical galaxies that have undergone recent merger activity. Radio-quiet AGN have been shown to be hosted by spiral and elliptical galaxies. Additionally, space density for radio-loud galaxies is $\sim$ 10 times lower than that of radio-quiet galaxies (Wilson and

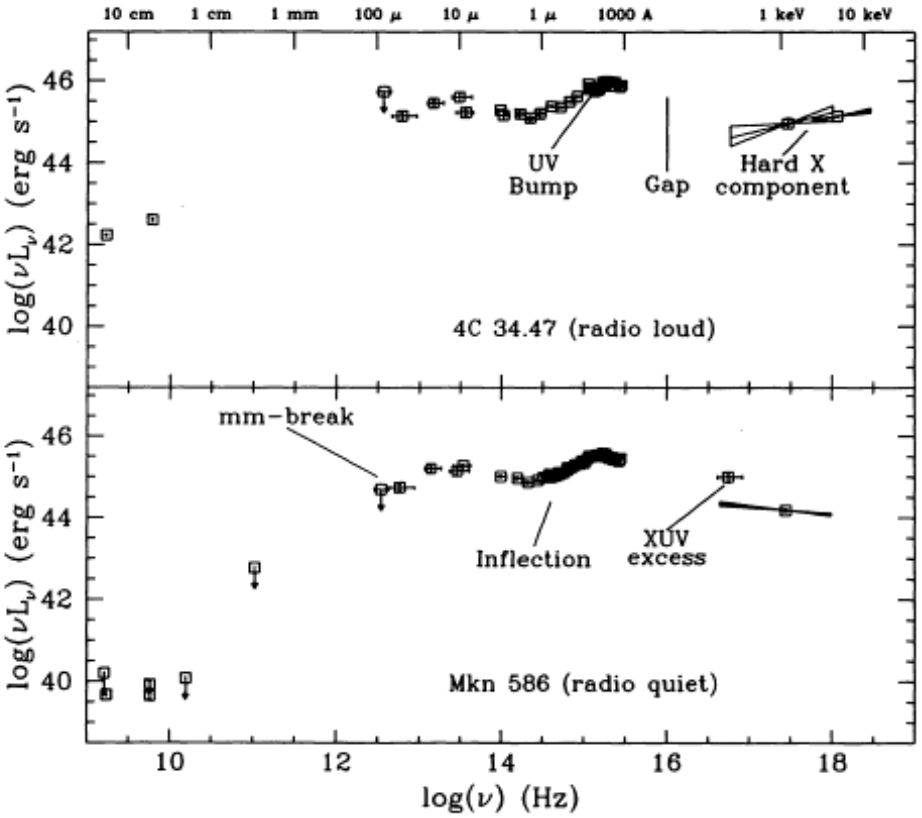

Figure 1.1: A comparison of SEDs between a radio-loud galaxy (4C 34.47, top) and a radio-quiet quasar (MrK 586, bottom). A similar trend is followed between 10 μm and soft X-rays but variations are present outside of this wavelength. The part of the SED labeled "gap" is an effect caused by absorption at these wavelengths by gas and dust within the Milky Way (Savage et al., 1993). Image is reproduced from Elvis et al. (1994).

Colbert, 1995). A complete list of AGN divided by type and radio luminosity is provided in Table 1.1. Additional sub-classes of AGN are discussed in the following sections.

Table 1.1: AGN are divided into different groups based on the emission lines observed and whether the source is radio-loud or radio-quiet.

	Type 0	**Type 1**	**Type 2**
Radio-loud	Blazars FSRQ	Broad Line Radio Galaxies Radio-loud Quasar	NLRG
Radio-quiet	BAL QSO	Seyfert 1 Radio-quiet QSO	Seyfert 2 NELG

1.2.2 Emission Lines

Electrons in an atom that are struck by an incoming photon can absorb some of the photon's energy. The newly gained energy allows the electron to move from its ground state to a higher energy level. To return to the ground state the electron must lose the extra energy. The electron releases the energy as a photon with a frequency ν that is determined by the difference in energy E between the two levels and Planck's constant h:

$$E_2 - E_1 = h\nu. \tag{1.2}$$

The electron can move through many energy levels before returning to its ground state, analogous to a ladder. As the electron travels down the "ladder", a photon is released with a frequency corresponding to the difference between the previous energy level and the new energy level. A large population of electrons at different energy levels will result in emission spread over many frequencies.

Most AGN are characterised by the presence of two types of strong emission lines: (i) those dominated by narrow emission lines (type 2) and (ii) those revealing both narrow and broad emission lines (type 1) (e.g., Sauty et al., 2002; Netzer, 1987; Antonucci, 1993; Urry and Padovani, 1995; Sulentic et al., 2000). The remaining small percentage of AGN have unusual or no emission lines. BL Lacertae objects (BL Lac) are an example of AGN where no emission lines are present. Spectral observations have revealed a featureless, non-thermal continuum instead (Sauty et al., 2002). A list of AGN objects separated by type is presented along with the radio-loud division in Table 1.1. The sub-types of AGN will be discussed later in the chapter.

Broad emission lines are largely influenced by the location of the gas and dust in the accretion disk. In regions close to the inner edge of the disk, speeds are capable of reaching $\sim 0.8c$ (e.g., Boettcher et al., 2012; Risaliti et al., 2013). Gas and dust orbiting near the outer edge are traveling at much slower speeds. From the relationship between the differences in orbital speeds $\Delta\, v$, the speed of light c, and the wavelength of the emitted line λ,

$$\frac{\Delta\lambda}{\lambda} \approx \frac{\Delta v}{c}, \tag{1.3}$$

it is apparent that the wavelength observed is spread across multiple wavelengths $\Delta\,\lambda$ to produce a Doppler broadened emission line (Boettcher et al., 2012). Theories regarding possible explanations for the presence of broad emission lines in some AGN and not in other AGN is discussed further in this chapter.

1.2.3 Radio Galaxies

The first detection of a jet associated with a galaxy came from photographic observations of Messier 87 (M87), also named NGC 4486 (Curtis, 1918). Nearly 30 years after the discovery of M87's optical jet, astronomers searching for locations of radio sources determined that M87 aligned with the Virgo A radio source (Bolton et al., 1949). Observations at 5 GHz revealed three components of the structure: a northern component that coincides with a structure extending from the nucleus and aligns with the optical jet, a southern component that extends from the nucleus, and an unresolved central component that is positioned at the optical nucleus (Graham, 1970).

Hey, Parsons, and Phillips (1946) began a radio frequency study of the northern sky using modified anti-aircraft antennas. This led to the discovery of a strong radio source with the rapid, irregular fluctuations shown in Fig. 1.2 (Hey et al., 1946). This region, now known as Cygnus A (3C 405), was thought to be a small collection of sources varying over a short period of time. More observations revealed that Cygnus A was stable and only appeared to vary as a result of ionised gas in the ionosphere causing the waves to refract (Ryle and Hewish, 1950). A few years later Baade & Minkowski (1954) used optical observations and spectroscopy to identify a giant elliptical galaxy merging with another elliptical galaxy where radio emission was previously observed. Although the original interpretation was that there are two galaxies colliding, the "gap" between colliding galaxies turned

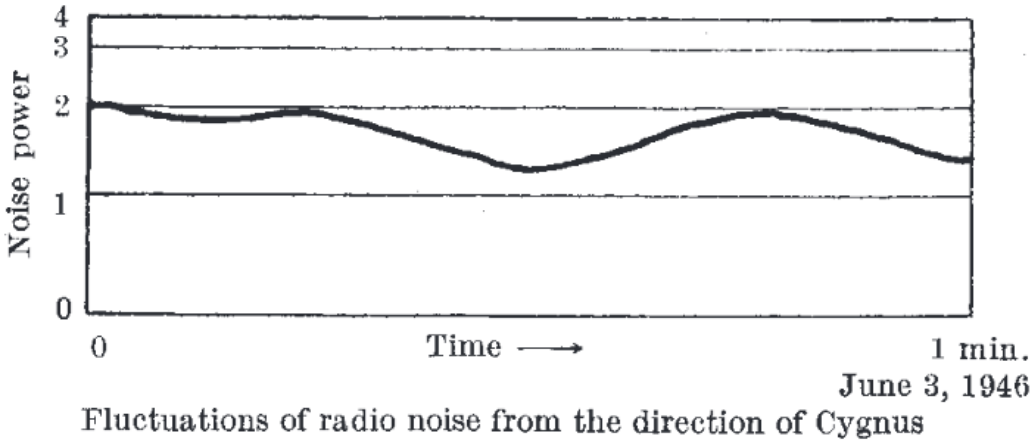

Figure 1.2: Cygnus A radio noise fluctuations reproduced from (Hey et al., 1946).

out to be the dust lane of an elliptical galaxy. Around the same time, Jennison and Das Gupta (1953) connected a two element interferometer at Jodrell Bank Observatory to improve resolution of Cygnus A. By doing so they were able to demonstrate that the structure of Cygnus A consisted of two large lobes of radio emission each stretching 51 arcseconds in length and separated by a total distance of 1.28 arcminutes (Jennison and Das Gupta, 1953). The radio lobes were shown to be positioned well beyond the optical galaxy. Despite the close proximity, this led the pair to conclude that the colliding galaxies seen in the visible spectrum and the radio emission seen in the lobes were not correlated (Jennison and Das Gupta, 1953). It wasn't until additional 1.6 GHz observations were done using the Mark II & Mark III baseline at Jodrell Bank that a weak component was discovered midway between two radio lobes (Peckham, 1973). The weak component was found to be strongly associated with the optical galaxy as it was positioned within a few arcseconds of its host (Peckham, 1973). The alignment of galaxies with radio emission in Cygnus A, M87, and many additional sources (e.g., Bolton et al., 1949) led to the acceptance that high latitude sources are indeed radio galaxies.

With improvements in telescope resolution, features in radio galaxies began to take shape. Four components of a radio galaxy may be detected: a core, lobes, jets, and hotspots. In some cases all four features are detected.

Lobes

Large extended emission, found on projected scales as small as several arcseconds up to scales as large as a few arcminutes, are classified as 'lobes'. Following the definition in Leahy (1993), a lobe can be summarised with the following: (1) A lobe is large structure that has well-defined boundary; (2) The intensity approaches zero towards the edge of the lobe; (3) The lobe has an intrinsic polarization up to 40%. Lobes are made of plasma that is believed to be transported from a region close to the AGN by the jets. This material may be polarized and can have a steep spectra ($\alpha < -0.7$) that steepens further from the hotspot (e.g., Alexander and Leahy, 1987; Hardcastle, 2015).

Hotspots

Hotspots are the compact (typically < 1 kpc but can be larger) regions of bright emission associated with the end of the jet (e.g., Blandford and Rees, 1974; Laing, 1982; Muxlow and Garrington, 1991). According to Bridle et al. (1994a), a hotspot must satisfy the conditions provided in the following summary.

(a) Hotspots must have a surface brightness > 4 times the surrounding lobe and jet emission.

(b) Each must be brighter than all of the other features in the lobe.

(c) A hotspot must be located in a position that is further than the end of the jet (if detected).

(d) The deconvolved FWHM of a hotspot should be less than $< 5\%$ of the largest diameter of the source.

Hotspots are not universally alike and can be classified by how diffuse the features appear. It should be noted that this classification is not always reliable as it can be resolution-dependent. Laing (1989) describes two types of hotspots that are summarised in the following:

Primary: The bright, compact features located where the jet terminates.

(a) Generally primary hotspots are located on the sides of the extended lobes, positioned slightly further back from the leading edge. Some examples of hotspots can be found at the far ends of the lobes, such as in 3C 204 (Laing, 1989), although this is less common.

(b) It is rare to observe more than one substructure that is bright and compact.

(c) Some primary components have been shown to contribute $< 2\%$ of the total flux density of the source (e.g., 3C 427.1) (Laing, 1989). Faint primary hotspots are best detected by arrays with high sensitivity.

Secondary: The fainter, more diffuse hotspots surrounding the primary hotspots.

(a) Double hotspots refers to the identification of two discrete hotspot components - a primary and secondary.

(b) Flaring hotspots describes a primary and secondary hotspot within the same structure. In this scenario a primary hotspot expands and curves away from the compact region.

The term 'hotspot complex' is used if more than one hotspot components are identified and are separated at the peak by 10% of the largest angular size of the radio source (Leahy et al., 1997). Hotspot complexes are bright regions in the diffuse lobe but separation between the large structure and the substructure is not well-defined. Hotspots are associated with more powerful jets that terminate with a shock. A typical hotspot has a spectral index between $-1.0 < \alpha < -0.5$ (Muxlow and Garrington, 1991).

Jets

Jets are narrow structures that appear to connect emission from the cores to the lobes. This thesis follows the definition of a jet given by (Bridle, 1986). Jets are (a) features that are aligned with the nucleus, (b) at least four times longer than the width, and (c) identifiable as a distinct feature from the surrounding environment either spatially or by contrast in brightness (Bridle, 1986). Jets may contain 'pockets' of brighter emission which are defined as knots (Bridle et al., 1994a). The typical spectral index of a jet ranges between $-1.0 \leq \alpha \leq -0.5$ in strong flavour jets (Hardcastle, 2015). In jets that dissipate at smaller scales the spectral index is close to $\alpha \sim -0.6$ (Hardcastle, 2015). The opening angle can vary between different jets. Typically strong jets have opening angles $< 5^\circ$ where as weak jets have larger opening angles ($5^\circ - 30^\circ$) (Bridle, 1984, 1982). Jets are often described as "outflows" from the nucleus despite there being no direct evidence that jets are outflows. It is only indirectly that we find evidence

that jets are a flow of energy and matter (e.g., Schilizzi, 1988; Hughes and Miller, 1991).

Core

A core is a compact, unresolved feature at resolutions $\geq 0\farcs1$ (Bridle et al., 1994a; Muxlow and Garrington, 1991) of intense radio emission located near the centre of the radio structure. In a typical AGN radio source with an optically identified host galaxy, the core and galaxy are coincident. Bridle et al. (1994a) prefer that the core be labeled as a 'central feature.' Their argument is that the core is highly resolution-dependent and the term incorrectly assumes that the feature is the central engine instead of the jet's opaque base (Konigl, 1981; Bridle et al., 1994a). In this thesis the central feature will be referred to as a core to remain consistent with most literature.

Most cores have a radio spectrum that is flat or inverted ($-0.3 \leq \alpha \leq 0.3$ between 100 MHz $\leq \nu \leq$ 10 GHz) over many frequencies (e.g., Phinney, 1985; Marscher, 1977). A flat spectrum is believed to be the result of synchrotron self-absorption of the jet base (Kellermann and Pauliny-Toth, 1981). It is widely accepted that electrons spiraling in a magnetic field at relativistic speeds produce the radio emission. This process is called synchrotron radiation and is discussed in §1.6. Not all of the emitted synchrotron radiation reaches the observer. As the radiation propagates away from the source it may scatter off another electron. The process is called synchrotron self-absorption. If a photon is scattered many times before exiting the source, most of the flux is hidden from the observer. Only a thin layer close to the surface is visible. The superposition of many distinct self-absorbed synchrotron components, each with a peak at a different frequency (Cotton et al., 1980), leads to a flat spectrum (Phinney, 1985).

The Fanaroff-Riley Dichotomy

Radio galaxies are associated with giant elliptical galaxies with a non-thermal continuum spectrum that is strong in radio frequencies. Because morphological differences were observed extending from a few kiloparsec to a few megaparsec, a study by Fanaroff & Riley (1974) suggested a division based on the surface brightness of the lobe. The two flavours suggested were the edge-darkened Fanaroff-Riley Class I (FRI) and the edge-brightened Fanaroff-Riley Class II (FRII) (Fanaroff and Riley, 1974).

A source is classified as an FRI when the distance between the two brightest regions of emission located on opposite sides of the AGN is less than one half the total extent of the radio emission (Fanaroff and Riley, 1974). FRI sources are brighter in regions closer to the galaxy and decrease in brightness and become decollimated and more plume-like as distance increases (Fanaroff and Riley, 1974). This is described as edge-darkened. At radio frequencies the structure is complex near the galaxy and shows evidence of flows away from the galaxy (Fanaroff and Riley, 1974). Observations of FRI sources typically reveal a jet and a counterjet with diffuse emission extending well beyond the jet structure. Emission is dominated by that which is produced by the jet and core (Smith, 2012). The FRI class radio galaxies can be described as being either bridged or plumed by visually inspecting the morphology. A bridged FRI reveals a lobe of radio emission centred between the nucleus, or core if observed, and the end of a jet (Leahy and Perley, 1991). The oldest plasma is located in the bridge (Muxlow and Garrington, 1991). An example of 3C 296, a bridged FRI, is provided in Fig. 1.3a (Leahy and Perley, 1991). Plumed FRI sources show a narrow jet expanding in width and decreasing in brightness from the end of a bright jet. The boundary of a plumed source is poorly defined and is resolution-dependent (Muxlow and Garrington, 1991). A radio frequency image of 3C 31 is provided in Fig. 1.3b. It is not uncommon for FRI sources to have large bends in the jet that may change direction multiple times along its path.

FRII sources are described as edge-brightened. That is the emission tends to end in hotspots that are further from the central galaxy than FRI sources. Fanaroff & Riley (1974) defined sources with the two brightest regions of emission separated by a distance that is more than half of the extent of the structure as class FRII. Lobes with at least one hotspot are visible on both sides of the central core. While FRII sources have been observed with a jet and a counterjet, many do not reveal a counterjet. The jets that are observed are typically well-collimated. An image of Cygnus A is provided in Fig. 1.4a to show a source with a two-sided jet; A map of 3C 175 is given as an example of a source with a one-sided jet in Fig. 1.4b.

In addition to the gross morphological division identified by Fanaroff and Riley (1974) there are observable differences that suggest more fundamental processes may contribute to structural type. Separation by morphology revealed a clear division, although not sharply defined, in luminosity between FRI and FRII

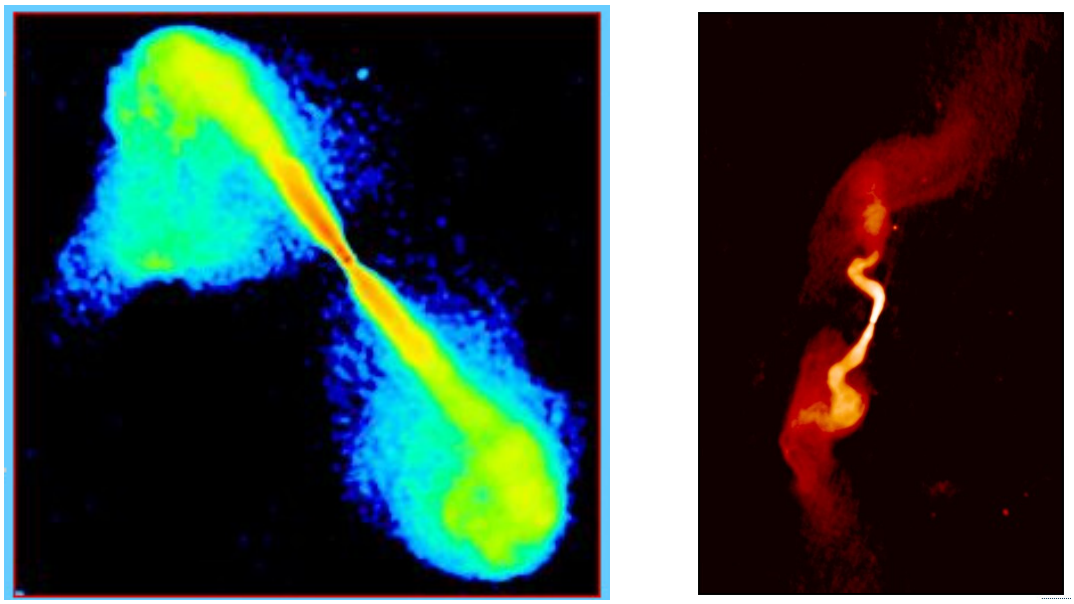

(a) (b)

Figure 1.3: (a) Intensity map of bridged FRI 3C 296 reproduced from (Leahy and Perley, 1991) (b) Plumed FRI 3C 31 is reproduced from (Laing et al., 2001).

sources. FRI sources typically have powers below 10^{25} WHz^{-1} at 1.4 GHz while FRII sources are often more powerful with power above 10^{25} WHz^{-1} (Fanaroff and Riley, 1974). Estimates of jet speeds vary from near c in FRII to near $0.03c$ in FRI (Smith, 2012). Although both types are hosted by elliptical galaxies, galaxies hosting FRIIs are bluer and are more likely to be found in galaxies that have undergone merging (Heckman et al., 1986; Smith and Heckman, 1989). Environments have also been shown to vary between radio galaxies found nearby and those with large redshifts. Local FRI ($z< 0.5$) have been observed in dense environments such as galaxy clusters or large groups, whereas FRII type galaxies are often associated with a field galaxy (Hill and Lilly, 1991; Saripalli, 2012). This trend does not extend to large redshift observations. Both FRI and FRII galaxies located at large redshifts are found in rich cluster environments (Hill and Lilly, 1991; Saripalli, 2012).

1.2.4 Seyfert Galaxies

Although not known at the time, Seyfert galaxies were the first group of active galactic nuclei to be discovered. Spiral galaxies were thought to be either gaseous objects similar to nebulae or a collection of distant unresolved stars (Shields,

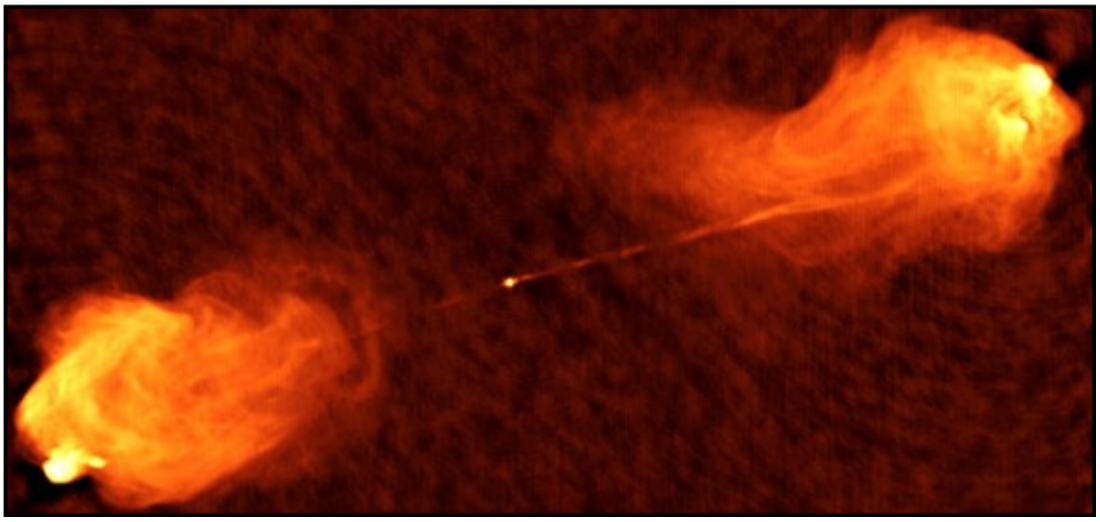

(a)

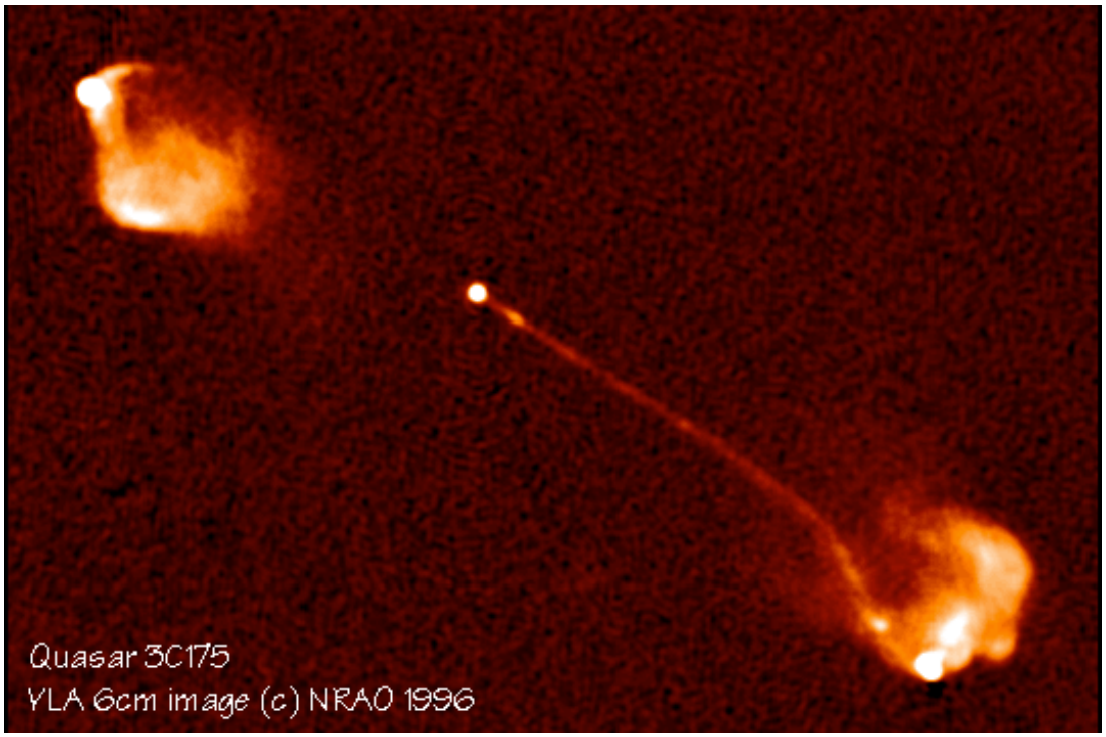

(b)

Figure 1.4: (a) Cygnus A is an example of an FRII galaxy with a jet and a counter jet. Image is reproduced from Carilli et al. (1988). (b) 3C 175 is a one-sided FRII galaxy. Image is reproduced from Bridle et. al. (1994a).

1999). An early study by Fath (1909) looked at the spectra of various spiral "nebulae" and concluded that most revealed a continuous spectrum with dark absorption lines, spectra that is expected for stellar objects. However, in the case of NGC 1068, bright emission lines found in gaseous nebulae along with dark absorption lines were observed (Fath, 1909). Additional work confirmed the presence of emission and absorption lines and revealed a disk-like structure to the emission lines (Slipher, 1917). A study by Carl Seyfert (1943) revealed that these lines were broader than ordinary stellar sources and belonged to galaxies with much brighter nuclear regions.

Seyfert galaxies, as the peculiar spiral galaxies are now known, are estimated to make up no more than 2% of the spiral galaxy population (Halliday, 1969). A Seyfert galaxy is structurally similar to normal spiral galaxies but differs in nuclear brightness. While the majority of nuclear emission observed in galaxies is associated with the many billions of stars that comprise them, that may not be the case for Seyfert galaxies. Observations reveal a nuclear region much brighter and more compact than other spiral galaxies but less luminous than quasars, another type of AGN that is discussed in the following section (Davidson and Netzer, 1979). They stand out among other spirals in that Seyfert galaxies are highly variable, with brightness changing in timescales of several hours in some cases, and reveal emission line spectra (Peterson et al., 1984, 1998). The quick change in luminosity suggests some Seyferts may have nuclear regions as small as 0.025 pc (Anderson, 1974). Differences in spectra contribute to two categories of Seyfert galaxies that follow a naming convention described based on the presence of certain emission lines. Spectra of Seyfert 1 galaxies, unsurprisingly consistent with type 1 AGN, show narrow emission lines with widths that extend several hundred kms^{-1} and broad emission lines observed to have widths up to 10^4 kms^{-1} (Rodriguez-Pascual et al., 1997). Seyfert 2 show only narrow emission lines in the observed spectra.

1.2.5 Quasars

Improvements to Cambridge's radio telescopes in the late 1950's led to the revision of a catalog of radio sources (Bennett, 1962; Edge et al., 1959). The newly refined 3C catalog provided astronomers a list of known radio sources and their corresponding coordinates. From this a search began for optical counterparts to the radio detections. Observations of 3C 273 at visible wavelengths revealed that

the radio source appeared to align with a blue star-like object with a wispy jet protruding from it (Hazard et al., 1963). An optical image of 3C 273 from the Hubble Space Telescope is shown in Fig. 1.5. Around this time the powerful radio source 3C 48 was also discovered. Optically, 3C 48 looked like a star but it's spectrum did not look like one (Matthews and Sandage, 1963). Subsequent studies produced accurate positions of bright galaxies to show that the nucleus of the largest member of a small galaxy group has the same redshift ($z = 0.16$) as 3C 273. The AGN radio emitting sources were given the name "quasar", short for quasi-stellar radio source.

The number of known quasars has grown from a handful at first to over a million in recent times thanks to the Sloan Digital Sky Survey. Due to large sky surveys the definition of a quasar has improved. Initial detection of quasars revealed strong radio emissions. This led to an incorrect assumption that all quasars are radio-loud. It is now known that most quasars are radio-quiet and we rely on optical emissions to discover them. For quasars the nuclear emission outshines the host galaxy's light by up to 1000 times (Robson, 1996). As a result, stellar absorption lines may not be detected and if they are, they are very weak. Quasars resemble point sources in optical detections with ground-based telescopes. This can be problematic for detection when located in a vast sky full of other point sources. Thankfully, several unique properties allow astronomers to separate quasars from other galaxies and faint stars. The quasar's emission lines are broad and highly redshifted. Redshifts can range from $\sim z = 0.1$ to $z = 7.1$. The emission lines of quasars resemble those of Seyfert galaxies. Quasars, however, occupy a more luminous ($M_B < -23$) region than Seyfert 1 galaxies (Kauffmann and Haehnelt, 2002). This makes them the most luminous of the AGN subclasses.

For reasons that are described in §1.3, radio galaxies and radio-loud quasars are believed to be the same type of object but viewed at different angles to the line of sight (Barthel, 1989a). This means many of the same features described in §1.2.3 for radio galaxies - jets, hotspots, lobes, core, and the Fanaroff-Riley classification (Fanaroff and Riley, 1974) - can be identified in or applied to quasars as well. For this reason the term 'DRAGN' (double radio source associated with a galactic nucleus) (Leahy, 1993) will be used when describing features or properties shared by both radio galaxies and quasars. DRAGNs are identified by the presence of a jet, lobe, or hotspot complex in the radio spectrum (Leahy, 1993).

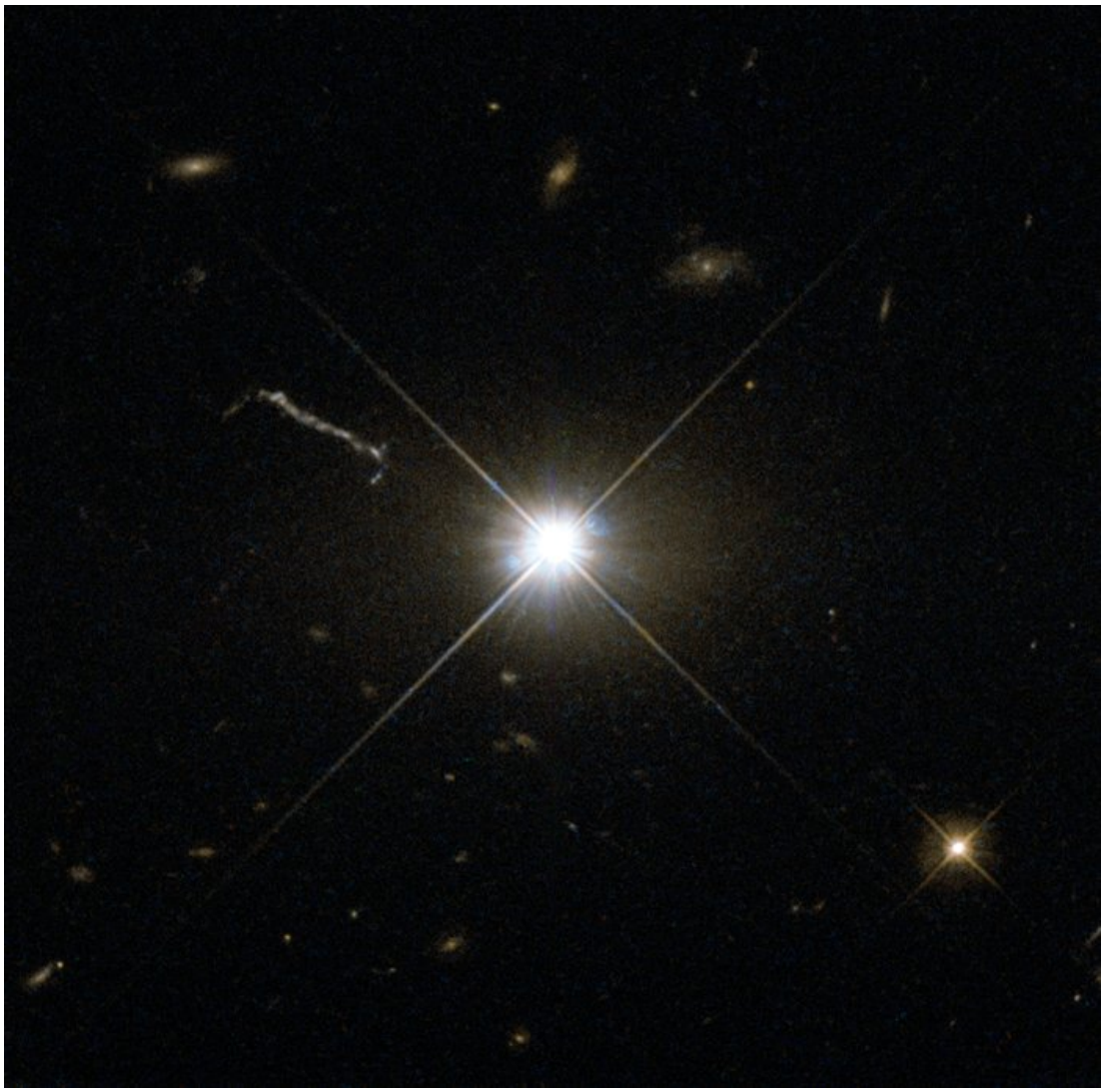

Figure 1.5: Image captured by the Hubble Space Telescope (HST) of 3C 273 reveals the star-like appearance of quasars in the optical. Shown in the image are neighboring galaxies, mostly in the same cluster, and a jet pointed toward the "star". Image is reproduced courtesy of NASA.

1.2.6 Blazars

The German astronomer Cuno Hoffmeister unknowingly identified the first blazar as a short-period variable star while studying over 300 other variable stars (Hoffmeister, 1929). Decades later the object in question, named BL Lacertae, or BL Lac for short, was observed to have highly irregular variability which was unusual for stars. Further studies found the "star" to be a strong radio wave emitter with a high redshift (Shen, 1970). Since then many objects have been identified with similar characteristics. Blazars are believed to be objects similar to quasars for reasons that will be discussed later in this chapter. Blazars can be classified as different sub-types depending on the presence of any of the following properties: (a) unusual, weak, or absent emission or absorption lines near the core, (b) a high degree of polarization, (c) high redshift, and (d) high variability from the radio spectrum through the optical spectrum (Stein et al., 1976; Massaro et al., 2012).

1.3 Orientation Dependent Unified Model

The identification of many different classes of AGN made understanding the objects that host and the processes that create the peculiar differences difficult to explain. The creation of the unified model of AGN used a single object to explain many of the observed properties. Many of the differences are linked to the angle at which the object is viewed at and the conditions of the environment the emission is created in (e.g., Antonucci, 1993; Urry and Padovani, 1995; Sauty et al., 2002). The unified model provided in Fig. 1.6 shows the components of the active region with proposed viewing angle positions for different classes of AGN (Beckmann and Shrader, 2012). The top half of the image shows how the viewing angle affects certain types of radio-loud AGN. The bottom half shows the effect of viewing angle on a few types of radio-quiet AGN. Missing from Fig. 1.6 are radio-quiet quasars. Radio-quiet quasars would be found on the bottom right side of the diagram.

At the heart of most galaxies is a supermassive black hole (SMBH) (e.g., Lynden-Bell, 1969; Blandford and Znajek, 1977). The unified model suggests that an AGN galaxy is accreting matter onto this black hole from a magnetised accretion disk. Close to the black hole and accretion disk are moving clouds of dense gas that become photoionised from radiation produced by the disk (Robson, 1996). It is in this region that the broad emission lines originate. Some of the

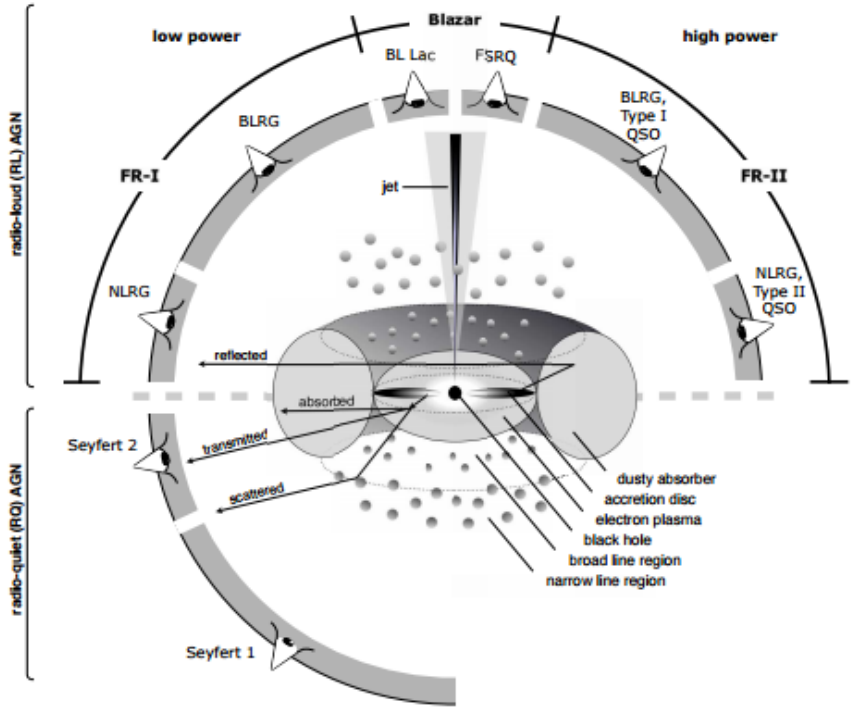

Figure 1.6: Unified scheme to describe AGN types based on viewing angles. The image is divided into a top half that shows how the viewing angle can explain some radio-loud AGN and a bottom half that describes how the viewing angle explains some radio-quiet AGN. When viewing AGN close to the polar axis relativistic beaming of the radio jets map swamp emission lines, making them weak. When viewing AGN at high angles to the polar axis the torus obscures the dense region of ionised gas that is responsible for the broad emission lines. Figure is reproduced from Beckmann and Schrader (2012).

radiation produced by the disk is able to bypass the dense clouds only to ionise low density gas that occupies the area above and below the accretion disk at kpc-scales. This low density ionised gas produces the narrow emission lines that are observed. Encircling the accretion disk is a torus of dust and gas that obscures the accretion disk and broad line region when viewed edge-on. In AGN that radiate more powerfully a radio jet may be produced.

In a classic study by Barthel (1989a), orientation along the line of site to the AGN structure in Fig. 1.6 could explain some of the differences between AGN objects. In objects close to the plane of the sky, 90° from the polar axis, a classic radio galaxy (symmetric double lobes, a jet, and counterjet) is seen (Barthel, 1989a; Robson, 1996). Neither jet is beamed toward the observer, thus

not greatly affected by Doppler boosting or deboosting (see §1.5.4). Objects oriented at angles greater than $40° - 50°$ from the polar axis are beamed toward the observer (Barthel, 1989a,b). Relativistic effects lead to asymmetrical lobes and jets that are seen in FRII quasars. Barthel (1989a) unified FRII quasars and FRII radio galaxies for the first time. They were no longer considered separate objects but rather a byproduct of the orientation angle.

The unified model also provides a simple explanation for the presence of certain emission lines. For viewing angles above $\sim 60°$ from the polar axis the absence of broad lines in type 2 galaxies can be attributed to obscuration of the broad line region by the dusty torus. At larger angles the torus suppresses the non-thermal continuum and broad emission lines. These type 2 AGN would include Seyfert 2, NLRG (shown in Table 1.1) and narrow line QSO. Viewing angles below $\sim 60°$ may account for type 1 AGN as both the broad and narrow emission line regions are visible. The torus is no longer obscuring the dense cloud of ionised gas near the accretion disk. These AGN are labeled on Fig. 1.6 as BLRG and Seyfert 1 and also include type 1 QSOs. For radio-loud AGN, observations within a few degrees of the polar axis of the system may account for type 0 AGN such as blazars. In this observing window relativistic beaming may be boosting the radio waves, and swamping the emission lines to be weak or not detected at all (Wiita, 2006). The unified model is designed to explain the presence of certain emission lines but cannot explain differences between radio-loud and radio-quiet galaxies or the differences between FRI and FRII flavours of radio galaxies and quasars.

1.4 Energy Production

From the unified theory for AGN discussed in §1.3, the most likely candidate for powering the high rate of emission is a supermassive black hole. More specifically, it is powered by infalling material accreting at a high rate onto the supermassive black hole. To understand how a black hole may be responsible first consider a supermassive black hole with a mass M. The maximum luminosity that a source with a mass M can radiate is referred to as the Eddington luminosity $L_{\rm Edd}$. The Eddington luminosity is derived in numerous textbooks including Rybicki and Lightman (1979). The definition of the Eddington luminosity:

$$L_{\rm Edd} = \frac{4\pi GMmc}{\sigma_e}, \tag{1.4}$$

where σ_e is the Thomson scattering cross section for a photon interacting with an electron, m is the mass of the electron-proton pair, c is the speed of light, and G is the gravitational constant (Peterson, 1997b). Mass m includes electron and proton masses due to coupling of the two particles. Radiation pressure drives the electrons away but the resulting radially directed electric field drags the protons along with the electrons.

The Eddington luminosity can be used to estimate the lowest mass possible for an energy source. Powerful quasars and FRII sources can have luminosities around 10^{46} ergs s^{-1}. Using this value for L_{Edd} in Eqn. 1.4 gives a lower limit of $M \approx 10^8$ M$_\odot$. The size of the AGN core can be approximated from the variability time scales. Using the shortest observed times, a few hours, as an example, the distance across the core must be small enough for the light to travel in this short time. Thus, the core of an AGN with a luminosity of 10^{46} ergs s^{-1} is smaller than 10 AU (1.49×10^{12} m).

Equation 1.4 provided a lower limit to the mass of the AGN core. Alternatively, we can use the size estimates of the core to estimate the mass of the powering body. The gravitational potential V between a body with a mass m separated from a larger body with a mass M at some distance r, is given by

$$V = \frac{GMm}{r}. \tag{1.5}$$

The escape velocity v_e of a smaller object with a mass m gives the kinetic energy, $1/2mv_e^2$. To escape the gravitational force between the two objects, the smaller object must have a kinetic energy equal to or greater than the gravitational potential,

$$\frac{1}{2}mv_e^2 = \frac{GMm}{r}, \tag{1.6}$$

where

$$v_e = \sqrt{\frac{2GM}{r}}. \tag{1.7}$$

For black holes, the escape velocity is $v_e = c$. The Schwarzschild radius r_s represents the radius at which the escape velocity and the speed of light are equal. From Eqn. 1.6 the mass of a body is expressed as

$$M = \frac{r_s c^2}{2G}. \tag{1.8}$$

A radius of 10 AU also gives a black hole mass on the order of 10^8 M$_\odot$.

The luminosity of the emitted radiation is expressed as

$$L = \epsilon \dot{M} c^2, \tag{1.9}$$

where $\dot{M}$ is the mass accretion rate and ϵ is the fraction of the rest mass energy that is radiated away. If the emitted radiation exceeds $L_{\rm Edd}$ the radiation pressure will induce winds and blow away much of the potential fuel, thus limiting the accretion rate. The Eddington accretion rate is then

$$\dot{M} = \frac{L}{\epsilon c^2}. \tag{1.10}$$

Assuming an efficiency ϵ of 0.1 and a luminosity of 10^{46} ergs s^{-1} (10^{39} J s^{-1}) results in an accretion rate on the order of 10^{23} kg s^{-1}. This is equivalent to approximately a few solar masses a year.

1.5 The Jets in DRAGNs

It is evident that outflows occur in a wide range of astrophysical objects − including objects such as comets, proto-planetary nebulae, and young stellar objects (YSOs) (e.g., Lai et al., 2017; Trammell and Goodrich, 2002; Seale and Looney, 2008). Although some properties may be shared between the different astrophysical jets, it is only the extragalactic jets that will be discussed in this thesis. The term "jet" in this thesis refers to jets in DRAGNs unless otherwise stated.

The jets in DRAGNs are powerful, well-collimated outflows that transport energy and matter away from the nucleus. Jets are thought to be a product of a combination of processes including the accretion of matter, magnetic mechanisms, and the rotation of a supermassive black hole (e.g., Blandford and Rees, 1974; Pudritz et al., 2007). In the past optical detections of jets were difficult, making visible jets rare. Modern instruments and improved spectral resolution make probing jets at optical wavelengths easier, increasing the number of known visible jets. In many cases it is still the radio radiation produced by material flowing along the jets that reveals a structure. Observations of jets have revealed a vast assortment of morphologies, such as those described in §1.2.3. Interestingly, jets may appear one-sided, two-sided without lobes, or twin-lobed. Explanations for the appearance of one-sided jets is discussed in §1.5.4. With VLBI, jets are observed at distances of less than a parsec (pc) up to mega parsecs (Mpc)

(Blandford et al., 2018). Multi-frequency observations reveal jets from low energy radio waves through powerful gamma rays.

1.5.1 Launching

The best model for jet launching comes from the work of Blandford and Znajek (1977). According to the unified theory, at the centre of an AGN is a rotating SMBH surrounded by an accretion disk of magnetised plasma (Antonucci, 1993).

Gas spiraling into the black hole will drag the frozen magnetic field lines. The charge distributions provide a force-free environment where the magnetic field lines can corotate with the black hole. The current loops passing near the black hole's horizon are influenced by forces from the magnetic field. The rotational energy of the supermassive black hole is efficiently extracted by the magnetic field through the process known as magnetic braking. The black hole's loss of angular momentum is captured by the magnetic field and used to launch particles from the polar axis (Blandford and Znajek, 1977). The motion of the particle along the field lines is analogous to a bead on a wire. The "bead" (ionised plasma) is centrifugally accelerated along the magnetic field lines, unable to cross them. The ejected plasma is forced to remain collimated. Jets are known to form at distances of $\leq 100\ R_G$ (Blandford and Znajek, 1977).

1.5.2 Acceleration and Dynamics

It is widely accepted that FRI and FRII DRAGNs are the results of continuous outflows via a jet and its interaction with the surrounding environment (e.g., Blandford and Rees, 1974; Williams and Gull, 1984). Both FRI and FRII jets are likely launched at relativistic speeds and maintain these speeds at least through pc-scales (e.g., Laing, 1993, 1994; Bicknell, 1994; Pearson, 1996). The maximum speed of sound c_s for a relativistically moving plasma is $c/\sqrt{3}$ (Blandford and Rees, 1974; Hardcastle, 2015). Both FRI and FRII jets are initially relativistic and supersonic but differences between the two flavours becomes more apparent at kiloparsec-scales ($\sim 1 - 10$ kpc) (Hardcastle, 2008). At kiloparsec-scales FRI jets are thought to decelerate to sub-sonic or trans-sonic speeds as a result of entrainment of external mass at the jet boundary or from stellar winds within the jet (e.g., Bicknell, 1995; Laing, 1993, 1994, 1996; Laing and Bridle, 2002; Bowman et al., 1996). FRII jets, however, are thought to be powerful enough to

propogate through the environment of the host galaxy without decelerating (e.g., Williams, 1991; Blandford and Rees, 1974).

Particle acceleration can be linked to collisionless shocks in FRII jets (e.g., Cawthorne, 1991; Kirk, 1997). Plasma flowing at relativistic speeds provides a suitable environment to develop different types of shocks that can re-energise, accelerate, and re-collimate the plasma to kiloparsec or even megaparsec distances (Cawthorne, 1991). First-order Fermi acceleration (also called diffusive shock acceleration, or DSA) is a leading explanation for particle acceleration to GeV-TeV energies in DRAGNs (Blandford and Eichler, 1987; Böttcher et al., 2015). DSA occurs when a fast moving particle from upstream encounters a shock wave. The magnetic field around the shock can reflect the charged particle many times downstream and upstream, increasing its velocity each time. Eventually the particle can be accelerated enough to move past the shock. Additionally, relativistic jets of DRAGNs show evidence of a fast, inner spine surrounded by a slower, outer sheath (e.g., Giroletti et al., 2004; Meliani and Keppens, 2007; Mizuno et al., 2007). Difference between the low-density spine and the denser sheath are affected by Kelvin-Helmholtz instabilities that produce velocity shears. Relativistic speeds mixed with localised instabilities create the perfect shock forming environments that give rise to DSA.

1.5.3 Particle Content

The particle content of radio jets and lobes remains a long-standing problem. The physical processes that produce and sustain the jets are tied to the composition (e.g., Gomez et al., 1993, 1994; Sol et al., 1989). It is assumed that relativistic electrons are responsible for the synchrotron emission produced. The structure of the jet provides some clues about the additional components of the jet. The presence of a well-collimated structure composed of electrons requires an oppositely charged particle, such as a proton or positron, to remain electrically neutral. If relativistic electrons are responsible for the synchrotron emission, non-relativistic (thermal) protons could be a major component of the plasma (Leahy, 1991). Observations and theoretical simulations have conflicting evidence stating either an electron-proton (normal plasma) or electron-positron (pair plasma) can be acceptable elements of the jet under different conditions.

Multi-wavelength and polarization studies of jets provided the first evidence in support of an electron-positron pair composition. Crucial to these arguments

are polarization studies surrounding Faraday conversion. When linearly polarized light passes through a medium with a magnetic field parallel to its path, the plane of the polarized light will rotate in an effect called Faraday rotation. In cases where linearly polarized emission enters a magnetised medium and becomes circularly polarized, the effect is called Faraday conversion. Detection of Faraday conversion in 3C 279 and in three other sources can be explained if the components of the jet are electron-positron pairs (Wardle et al., 1998). Wardle et al. (1998) argue that the energy distributions needed to extend to low energies and to allow observations of circular polarization can only be attributed to pair plasma. Both Faraday rotation and conversion are effects produced by the lowest energy electrons. Their claim is based on the strong fractional linear polarization observed on parsec scales and absence of Faraday rotation. Electrons and positrons gyrating in opposite directions can limit the amount of Faraday rotation in the jet (Wardle et al., 1998). This along with detection of Faraday conversion, which requires the energy distributions of radiating particles (γ_{min}) to be much less than $\gamma_{min} \ll 100$, suggests that jets are comprised of electron-positron pairs. These results were disputed by Ruszkowski and Begelman (2002) who used 100% normal plasma in a turbulent magnetic field to produce the same effect in models. A study by Celotti and Fabian (1993) argued that electron-proton jets should be the most common due to annihilation of electron-positron pairs in the inner regions of the outflow. Observations of M87 reveal a luminosity consistent with electron-positron plasma (Reynolds et al., 1996).

It could, however, be the case that jets are a mixture of electron-proton and electron-positron pairs. A study by Sikora and Madejski (2000) found that jets made entirely of electron-positron pairs overpredict soft X-rays and jets made of entirely electron-proton pairs cannot explain the detection of stronger nonthermal X-ray radiation. Sol et al. (1989) suggest the composition varies between the inner jet and outer jet. Their model predicts electron-positron pairs from the innermost part of the accretion disk, and electron-proton pair plasma from the mildy relativistic wind. A mixture of particle composition such as this reduces the amount of electron-positron pairs needing to reach relativistic speeds (Sol et al., 1989). It also provides a simple explanation for differences between highly relativistic speeds at parsec-scales with mildly relativistic speeds at large kiloparsec distances (Sol et al., 1989).

1.5.4 Relativistic Beaming and Superluminal Motion

Superluminal Motion and Distances

Hubble's law is an important tool for studying the distances to astrophyscical objects like AGN. The Hubble distance-redshift equation is expressed as

$$v = H_0 r, \tag{1.11}$$

where v is the recessional speed of the source, H_0 is the Hubble constant, and r is the proper distance which changes with time. Excluding the cosmological expansion of the universe, the velocity in Eqn. 1.11 is related to redshift z by

$$v = cz. \tag{1.12}$$

If we account for the expansion of space, the proper distance becomes the comoving distance $r_{\rm eff}$ if r is multiplied to a factor $(1 + z)$. Hubble's law then can be used to express the comoving distance using the effective redshift $Z_{\rm eff} = z/(1+z)$ (Leahy and Perley, 1991),

$$r_{\rm eff} = \frac{cZ_{\rm eff}}{H_0}. \tag{1.13}$$

Assuming the cosmology defined at the beginning of this thesis, the projected linear size of a source D can be determined from

$$D = \frac{r_{\rm eff}\Theta}{(1+z)}, \tag{1.14}$$

where Θ is the angular size of the source on the plane of the sky (Leahy and Perley, 1991).

The idea that a jet is composed of fast moving plasma was not inherently obvious at first. This was in part due to the challenge in tracking the motion of knots or smaller structures in large-scale jets. Typically the large size of the jet masks the displacements of these features which are on milli-arcsecond scales. Observations with VLBI probed regions at parsec-scales to peer into the inner region of the jet. Blobs of emission at parsec-scales were traced over years to reveal a gradual increase in separation from the core (Wehrle et al., 2001). In Fig. 1.7a a blob is shown moving away away from the fixed core of a source. Over time the blob appears to move away and a new blob takes its place. In Fig. 1.7b the appearance of a new blob is shown over a six year time period.

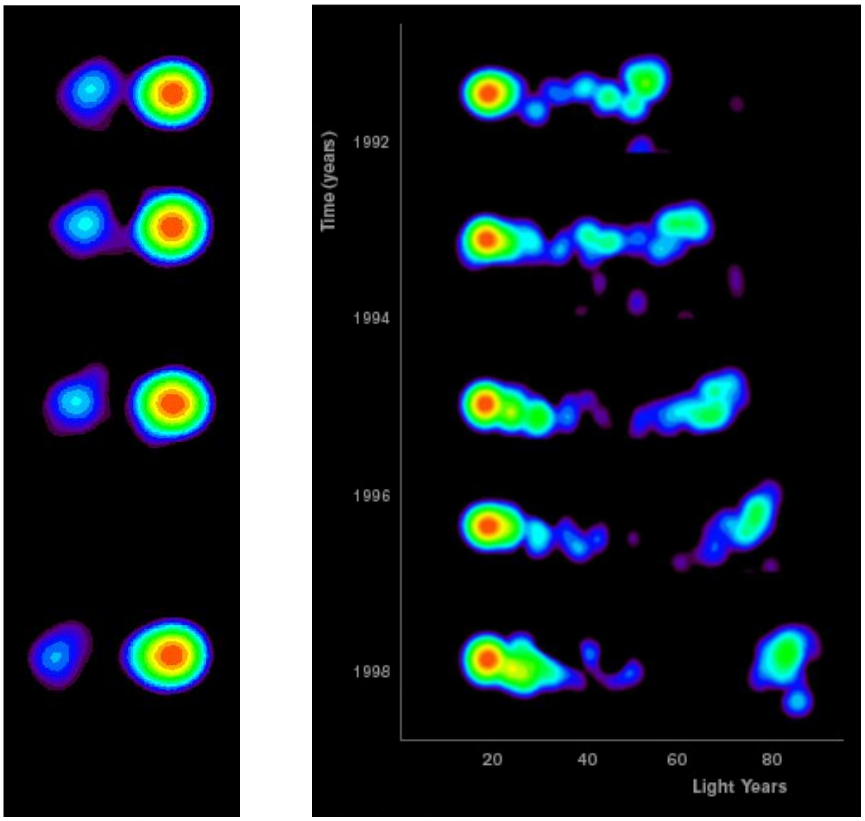

(a) (b)

Figure 1.7: (a) Superluminal motion detected in the blazar 0827+243. Image is reproduced from Piner et al. (2004). (b) Superluminal motion and appearance of new emission blobs in the quasar 3C 279. Image is reproduced from Wehrle et al. (2001).

To move distances observable by us in a few short years requires the blobs to move at speeds greater than the speed of light c, or at least appear to move at a speed exceeding c (e.g., Piner et al., 2004; Wehrle et al., 2001). The apparent superluminal transverse motion occurs when two conditions are met: (i) the material in the jet is flowing relativistically, and (ii) the jet is beamed at a small angle to the line of sight (Robson, 1996). Superluminal motion can be explained using the geometry of the motion of a blob with respect to the line of sight, as shown in Fig. 1.8. A blob of emission is shown at point B traveling along a path in the direction of C at an angle inclined to the observer at point A. At point B the blob emits radiation at time t, which reaches the observer at point A at time Δt. The observed time Δt_{obs} at point A for the blob to move from point B to a position along the BC path is given by:

$$\Delta t_{obs} = \frac{c\Delta t - v\Delta t \cos(\Phi)}{c}. \tag{1.15}$$

From Eqn. 1.15, the blob moves at an apparent speed β_{app} of (Cawthorne, 1991)

$$\beta_{app} = \frac{\beta c \sin\Phi}{(1 - \beta\cos\Phi)}. \tag{1.16}$$

When the angle approaches $\Phi = \sin^{-1}(\frac{1}{\gamma})$, where γ is the Lorentz factor, $\frac{1}{\sqrt{1-\beta^2}}$, maximum speed is reached (Smith, 2012). Detection of superluminal motion at parsec-scales is evidence in support of an outflow from a central source.

Equation 1.15 was derived under the assumption that the source is at a low redshift. For DRAGNs and many other AGN hosts at high redshift z, it is necessary to include the affects of the expansion of the universe. Accounting for high redshift with the factor $(1 + z)$, Δt_{obs} can be written as

$$\Delta t_{obs} = \Delta t(1 - \beta\cos\Phi)(1 + z). \tag{1.17}$$

Time in front of the approaching relativistic jet is being compressed. As a result the blob appears to move a greater distance in a shorter period of time, even reaching speeds that appear to exceed the speed of light.

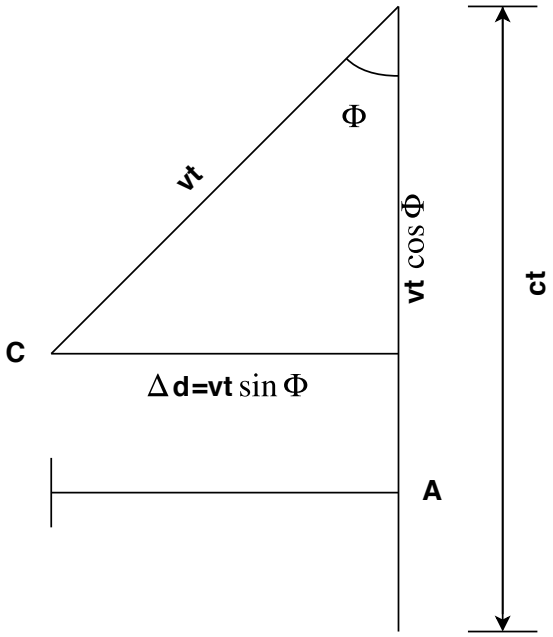

Figure 1.8: Projection of a blob at point B moving towards point C at an angle inclined towards the observer at point A. The apparent velocity, β_{app}, is given by $\frac{\Delta d}{\Delta t_{obs}}$.

Relativistic Boosting and Deboosting

Rees (1966) was the first to predict the influence of relativistic speeds from AGN sources on their observable properties. In his paper he suggested the flux can change on rapid timescales due to relativistic time dilation and is responsible for the appearance of boosted energy in emission (Rees, 1966). Radio observations of quasars 3C 279 and 3C 273 were confirmation that superluminal motion was possible (Whitney et al., 1971; Cohen et al., 1971). As the blob moves along its path at relativistic speeds towards the observer, the emitted emission, S_{em}, is boosted to the observed flux, S_{obs}, values as described by the equation:

$$S_{obs} = S_{em}[\gamma(1 - \beta \cos \Phi)]^{3-\alpha}. \tag{1.18}$$

Jets pointed away from the observer are deboosted in energy by the same effect; a lower energy output could explain the one-sidedness observed in relativistic jets (Krolik, 1999; Smith, 2012).

1.6 Synchrotron Radiation

Unless otherwise stated, the work presented here follows Rybicki and Lightman (1979).

Radio emission produced from astrophysical sources is linked to the non-thermal radiative process called synchrotron radiation. Relativistic electrons moving through a jet will encounter a magnetic field (**B**); the electrons will travel in a helical motion around the **B** field lines. The acceleration of the particles creates perturbations in field lines to produce radiation. Considering the relativistic motion of a particle with a charge q in a magnetic field and an electric field **E**, the Lorentz force describes the motion of a particle as

$$\frac{dp}{dt} = q\mathbf{E} + \frac{q}{c}(\mathbf{v} \times \mathbf{B}), \tag{1.19}$$

where $p = \gamma mv$ (Rybicki and Lightman, 1979). The work done on a particle with a mass m is

$$\frac{d}{dt}(\gamma mc^2) = q\mathbf{v} \cdot (\mathbf{E} + \frac{\mathbf{v}}{c} \times \mathbf{B}) = 0. \tag{1.20}$$

For electrons spiraling around a magnetic field, $\mathbf{E} = 0$. Equation. 1.19 is written as

$$\frac{d\mathbf{v}}{dt} = \frac{q}{\gamma mc}\mathbf{v} \times \mathbf{B}. \tag{1.21}$$

Splitting velocity into the parallel $\mathrm{v}_{\parallel}$ and perpendicular $\mathrm{v}_{\perp}$ components shows how the motion changes along the path:

$$\frac{d\mathbf{v}_{\parallel}}{dt} = \frac{q}{\gamma mc}\mathbf{v}_{\parallel} \times \mathbf{B} = 0, \tag{1.22}$$

$$\frac{dv_{\perp}}{dt} = \frac{q}{\gamma mc}\mathbf{v}_{\perp} \times \mathbf{B}. \tag{1.23}$$

The equation of motion for $v_{\perp}$ reveals constant acceleration around a circle with an angular frequency ω_B defined as

$$\omega_B = \frac{qB}{\gamma mc}. \tag{1.24}$$

The electromagnetic radiation emitted by the helical motion of an electron in a magnetic field is harmonics of the frequency given by Eqn. 1.24. This frequency is dependent upon the strength of the the magnetic field and is often emitted in

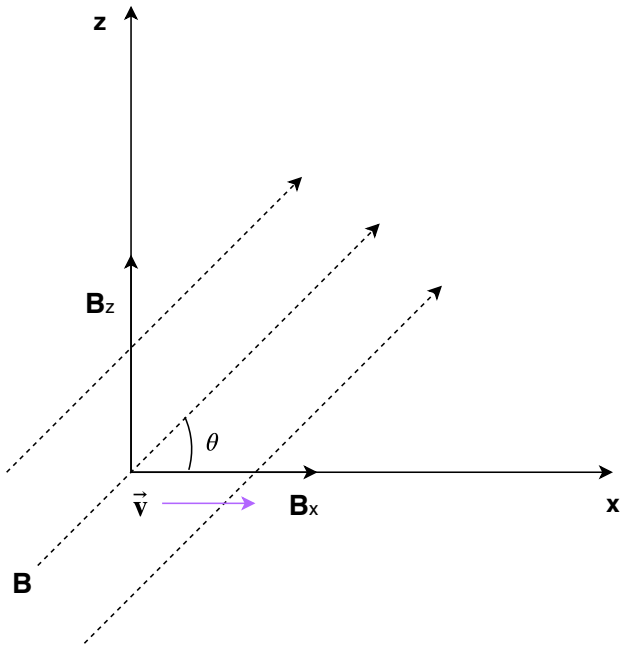

Figure 1.9: The reference frame for an electron moving through a magnetic field at relativistic speeds. Coordinate frame is reproduced from Longair (2011).

radio frequencies.

The instantaneous rest frame of the electron, shown in Fig. 1.9, can be used to derive the rate of energy loss in synchrotron radiation. The force $\mathbf{F}'$ on the electron is

$$\mathbf{F}' = q(\mathbf{E}' + \mathbf{v}' \times \mathbf{B}'). \tag{1.25}$$

At rest the instantaneous velocity is $\mathbf{v}' = 0$, leaving only $\mathbf{F}' = q\mathbf{E}'$. The electric field is then broken into the components along each axis to give

$$\begin{aligned} E'_x &= E_x = 0, \\ E'_y &= \gamma(E_y - vB_z) = -v\gamma B_z = -v\gamma B \sin\theta, \\ E'_z &= \gamma(E_z + vB_y) = 0. \end{aligned} \tag{1.26}$$

Solving for the acceleration using Eqn. 1.26 yields

$$\frac{dv'}{dt} = -\frac{q\gamma v B_z \sin\theta}{m}. \tag{1.27}$$

The power radiated by the electron in the rest frame is given by the Larmor

formula

$$-\left(\frac{dE}{dt}\right)' = \frac{q^2a^2}{6\pi\epsilon_0 c^3}, \tag{1.28}$$

where $a=\frac{dv'}{dt}$ that is defined in Eqn. 1.27 (Longair, 2011). Since this is a Lorentz invariant, substituting Eqn. 1.27 into Eqn. 1.28 also gives

$$-\left(\frac{dE}{dt}\right) = \frac{q^4\gamma^2v^2B^2\sin^2\theta}{6\pi\epsilon_0 c^3m^2}. \tag{1.29}$$

Equation 1.29 can be further rewritten with $c^2 = (\mu_0\epsilon_0)^{-1}$ and the Thomson cross section $\sigma_T = \frac{q^4}{6\pi m^2\epsilon_0^2c^4}$ as

$$\begin{aligned} -\left(\frac{dE}{dt}\right) &= 2\left(\frac{e^4}{6\pi\epsilon_0^2c^4m^2}\frac{v^2cB^2\gamma^2\sin^2\theta}{2c\mu_0}\right), \\ -\left(\frac{dE}{dt}\right) &= 2\left(\frac{v}{c}\right)^2\frac{\sigma_T cB^2\gamma^2\sin^2\theta}{2\mu_0}. \end{aligned} \tag{1.30}$$

For ultra-relativistic speeds, where $v \to c$, using the form of the Lorentz factor $\gamma = \frac{E}{mc^2}$ allows Eqn. 1.30 to approximated to

$$-\frac{dE}{dt} \propto B^2E^2. \tag{1.31}$$

Synchrotron losses increase at a rate of γ^2; high-energy electrons cool at a greater rate than low-energy electrons. This important result helps determine the age of an electron population from synchrotron emission.

Relativistic aberration of a light source θ_o is

$$\cos\theta_o = \frac{\cos\theta_s - \frac{v}{c}}{1 - \frac{v}{c}\cos\theta_s}, \tag{1.32}$$

where v is the speed of the electron and θ_s is the angle to the line of sight. Responsible for the relativistic beaming discussed in §1.5.4, another consequence of this effect is that the emission from the electron will be tilted towards the direction of motion. Figure 1.10 is used to show the cones of emission produced by the relativistically moving electron. Considering the case where the pitch angle is $\theta' = 90°$ in the frame of the electron, the aberration formula in the laboratory frame is

$$\sin\theta = \frac{\sin\theta'}{\gamma(1 + \frac{v}{c}\cos\theta')} = \frac{\sin(90°)}{\gamma(1 + \frac{v}{c}\cos(90°))} = \frac{1}{\gamma}. \tag{1.33}$$

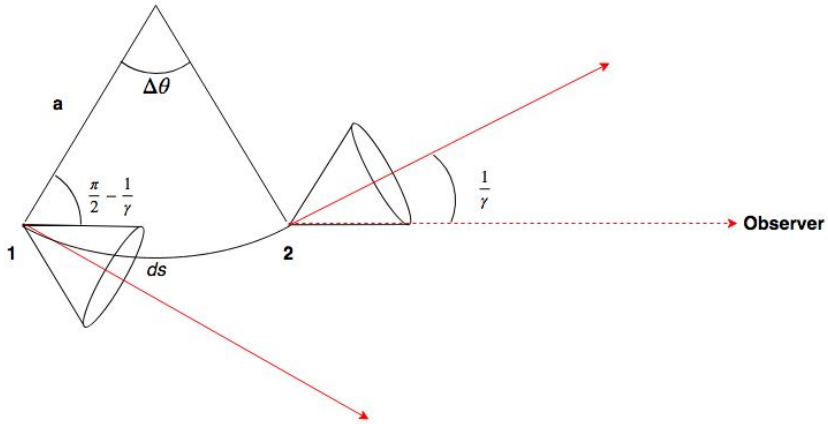

Figure 1.10: Emission cones from an accelerated electron in a magnetic field. Diagram is reproduced from Rybicki (1979).

Using the small angle approximation simplifies the angular width θ from $\sin\theta = \frac{1}{\gamma}$ to $\theta \sim \frac{1}{\gamma}$ (Longair, 2011).

The observer detects pulses at point 1 and point 2. The distance between pulses at these points Δs is given by

$$\Delta s = a\Delta\theta, = \frac{2a}{\gamma} \tag{1.34}$$

where a is the radius of curvature and $\Delta\theta = \frac{2}{\gamma}$ from Fig. 1.10. Returning to Eqn. 1.21 and using $dv = \Delta v = v\Delta\theta$ and $\Delta s = v\Delta t$ instead yields

$$\frac{\Delta\theta}{\Delta s} = \frac{1}{a} = \frac{qB\sin\alpha}{\gamma mcv} = \frac{\omega_B \sin\alpha}{v}, \tag{1.35}$$

with α being defined as the pitch angle. From the relationship derived in Eqn. 1.34 and with Eqn. 1.35, Δs can be approximated to

$$\Delta s \approx \frac{2v}{\gamma\omega_B \sin\alpha}. \tag{1.36}$$

The travel time between points 1 and 2 is $\Delta t = t_2 - t_1$ can be determined from $\Delta s = v\Delta t$. The difference in arrival time, $\Delta T = T_2 - T_1$, is affected by the delay

times for light propagation. Solving for Δt using Eqn. 1.36 gives

$$\Delta t \approx \frac{2}{\gamma \omega_B \sin \alpha}. \tag{1.37}$$

Converting to the coordinate system of the observer and taking into consideration the Doppler effect gives

$$\Delta T = \frac{2}{\gamma \omega_B \sin \alpha}\left(1 - \frac{v}{c}\right). \tag{1.38}$$

In the case of synchrotron emission produced in AGN jets $\gamma \gg 1$, hence

$$1 - \frac{v}{c} = \frac{(1 - \frac{v}{c})(1 + \frac{v}{c})}{1 + (\frac{v}{c})} = \frac{(1 - (\frac{v}{c})^2)}{1 + \frac{v}{c}} \approx \frac{1}{2\gamma^2} \tag{1.39}$$

when $v \approx c$. This approximates Eqn. 1.38 to

$$\Delta T \approx (\gamma^3 \omega_B \sin \alpha)^{-1}. \tag{1.40}$$

The spectrum of radiation is limited by the frequency resolution Δw and the amount of time the waves of radiation are detected. The spectrum is defined by

$$\Delta w \Delta t > 1. \tag{1.41}$$

The term $\Delta\ \omega$ is then approximated to $\Delta\ \omega \sim \frac{1}{T}$. Using this with Eqn. 1.40 and Eqn. 1.41 the critical frequency ω_c is defined as

$$\omega_c \equiv \frac{3}{2}\gamma^3 \omega_B \sin \alpha. \tag{1.42}$$

The critical frequency indicates the median frequency at which the electrons in the field are emitting. A plot of the synchrotron spectrum and critical frequency of a single electron is provided in Fig. 1.11. The electron population *N(E)* with energies between E and $E + dE$ is in the form

$$N(E)dE = CE^{-P}dE, \tag{1.43}$$

where C is a constant that depends on the pitch angle and P is the particle distribution index index. The relationship between γ and E allows Eqn. 1.43 to

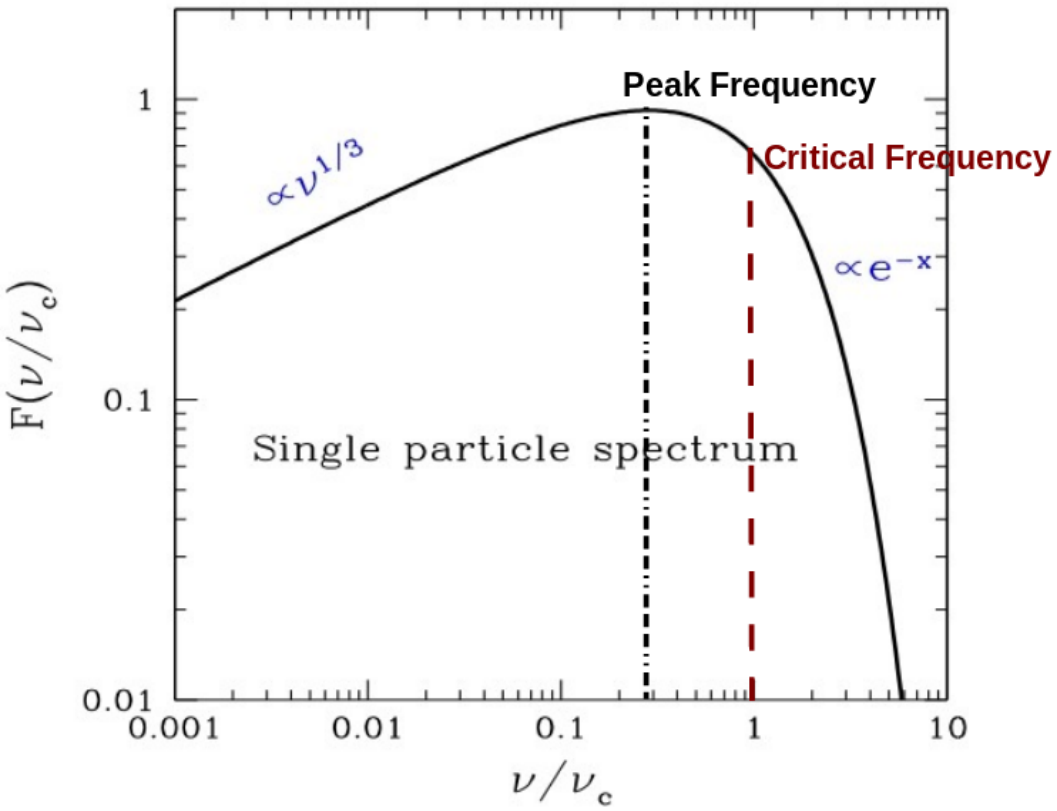

Figure 1.11: Synchrotron spectrum of a single electron in a magnetic field. Higher frequencies have smaller critical angles. Image is reproduced from NRAO.

be written as

$$N(\gamma)d\gamma = C\gamma^{-P}d\gamma. \tag{1.44}$$

The emissivity of a population of electrons at a certain frequency J_ν is given by

$$J_\nu = \int_{\gamma_1}^{\gamma_2} Cj(\nu)\gamma^{-P}d\gamma, \tag{1.45}$$

with j_ν being the emissivity of a single electron. Absorbing C into j_ν as $F(\frac{\omega}{\omega_c})$ and using $x \equiv \frac{\omega}{\omega_c}$, Eqn. 1.45 can be rewritten in the form

$$J(\nu) \propto \omega^{-(p-1)/2} \int_{x_1}^{x_2} F(x)x^{(p-3)/2}dx. \tag{1.46}$$

Completing the integral gives

$$J(\omega) \propto \omega^{-(p-1)/2}. \tag{1.47}$$

The power law index of the electron energy distribution can be expressed as $\alpha = \frac{p-1}{2}$, where α is the spectral index of the spectrum. Flux S_ν over an observed spectrum can be expressed as

$$S_\nu \propto \nu^\alpha. \tag{1.48}$$

Alternatively, α can be defined as

$$\alpha = \frac{\ln(S_1/S_2)}{\ln(\nu_1/\nu_2)}, \tag{1.49}$$

where S_1 and S_2 are the flux densities at frequencies ν_1 and ν_2 respectively (Brown and Burns, 1991). With S_ν, the radio power P_ν can be determined with

$$P_\nu = r_{\text{eff}}^2(1+z)S_{\nu/(1+z)}, \tag{1.50}$$

at a given redshift z and r is derived from Hubble's law (Leahy, 1991).

The lifetime of synchrotron radiating electrons τ_{rad} can be defined as

$$\tau_{rad} = \frac{E}{dE\ /\ dt} \propto E^{-1}B^{-2}. \tag{1.51}$$

Higher energy electrons radiate at higher energies. As shown by Eqn. 1.30, these electrons also cool at a greater rate. Equation 1.51 relates these two ideas by showing that high energy electrons have shorter lifetimes than low energy electrons (Robson, 1996). In some synchrotron sources the energy observed is not consistent with the age of the source. The magnetic field is believed to play a role in re-energizing electrons to high energies at large distances from the object (Robson, 1996; Krolik, 1999).

Chapter 2

Radio Astronomy

Radio interferometers rely on a group of antennas to collect radiation from sources. The processes that enable interferometry to be successful are different from single dish optical counterparts. This chapter will discuss the principles of radio interferometry and the mathematics behind the theory as outlined in Thompson et al. (2017). Thompson et al. (2017) provides a very detailed introduction to radio interferometry, including the mathematical derivations. I will touch upon the key points, leaving out the full derivation. Also discussed are calibration and imaging techniques used to create maps from radio data.

2.1 Principles of Radio Interferometry

2.1.1 Resolution

Angular resolution is the minimum angular separation between two point sources needed to detect two distinct sources. The resolution with a uniformly-illuminated circular aperture θ is given by

$$\theta = 1.22\frac{\lambda}{D}, \tag{2.1}$$

where λ is the wavelength of the observed emission, D is the diameter of the dish, and the factor 1.22 is derived from the position of the first dark circular ring around an Airy disk. A large telescope diameter resolves smaller structures at the same wavelength as smaller dishes. At radio wavelengths, the diameter needed to reach a similar resolution as an optical telescope would be too costly

and would require an impractical amount of land.

Aperture synthesis (Ryle and Hewish, 1960) simulates a large single dish telescope by using a collection of smaller, correlated dishes. The basic principle is that N antennas can be linked together to form an array consisting of N(N−1)/2 two-element interferometers (Ryle and Hewish, 1960). Joining radio telescopes, known as radio interferometry, provides a cheaper and more practical solution to the problems associated with single dishes. The longest baseline b_{max} between all of the two-element interferometer pairs in the array becomes the diameter of the "dish" to give the form

$$\theta \sim \frac{\lambda}{b_{max}}. \tag{2.2}$$

The resolution of an interferometer at b_{max} becomes the synthesised beam of the array. The intensity distribution of sources smaller than the resolution will be broadened to the beam size, thus resembling a point source. Using the smallest baseline in the array b_{min} in place of b_{max} in Eqn. 2.2 gives the maximum angular size observable. An interferometer is sensitive to structures with angular sizes between b_{max} and b_{min} (λ / $b_{max} < \theta < \lambda$ / b_{min}). Sources larger than θ at b_{min} begin to be resolved out. Since the maximum and minimum baselines give the resolution in the direction parallel to the baseline, the beam is typically elliptical.

2.1.2 Two-element Radio Interferometer

From the reciprocity theorem, an antenna can be treated as a transmitting system − sending out electromagnetic waves, or a receiving device − collecting incoming radiation (Burke and Graham-Smith, 1997). In a two-element radio interferometer acting as a receiving device, if the same voltage is applied to antenna A and antenna B, an identical current will be measured at both antennas (Burke and Graham-Smith, 1997).

Consider the two-element interferometer observing a far-field source shown in Fig. 2.1. The radiation from the distant source can be assumed to arrive as planar wavefronts with angle θ representing the angular distance between the baseline and the direction to the point source. The radiation field is received by two spatially separated antennas in the array at different times. Antenna 1 detects the radiation at $\mathbf{r}_1$ before antenna 2 detects the radiation at $\mathbf{r}_2$ by a difference τ_g.

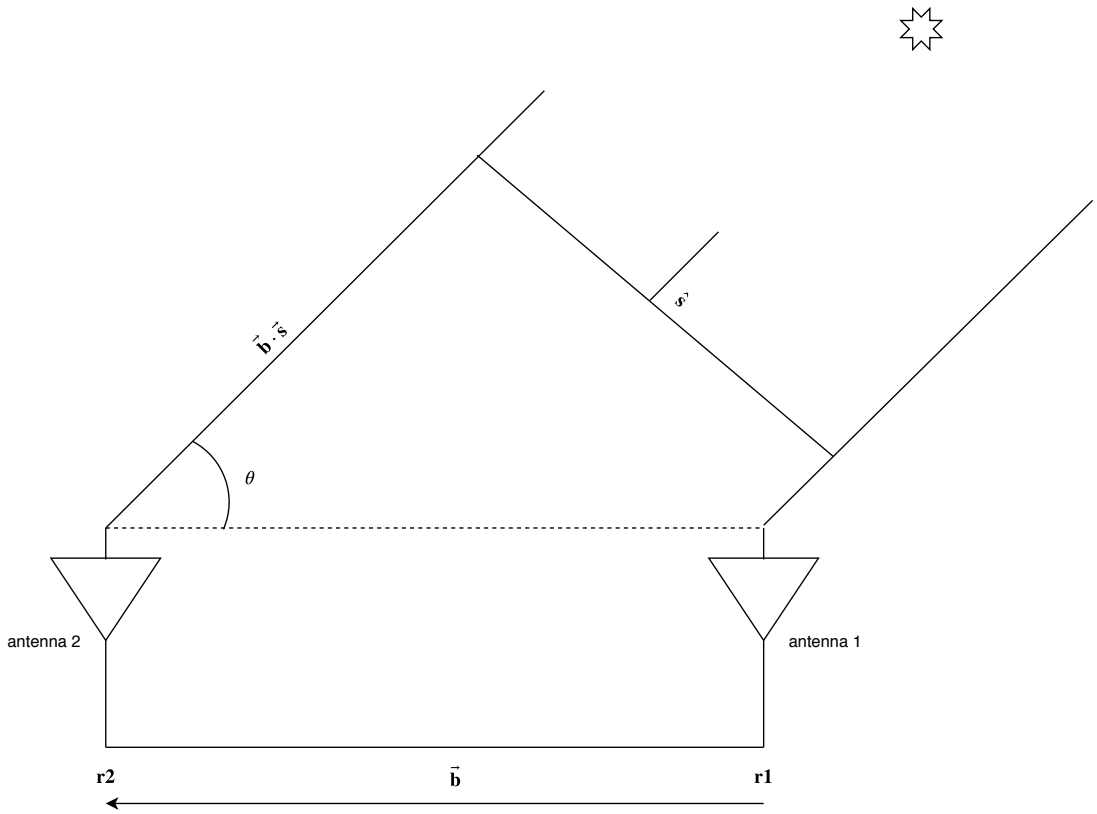

Figure 2.1: A two-element radio interferometer separated by $\vec{\mathrm{b}}$ =**r1**−**r2**.

The geometric delay τ_g is derived from the diagram to be

$$\tau_g = \frac{\overrightarrow{b} \cdot \hat{\mathrm{s}}}{c}, \tag{2.3}$$

where $\vec{\mathrm{b}}$ is the interferometer baseline ($\mathbf{r}_1 - \mathbf{r}_2$) and $\hat{\mathrm{s}}$ is the normal vector to the plane wavefront.

Upon reaching each antenna the incident electromagnetic wave induces a voltage of V_1 and V_2, corresponding to the voltages at antenna 1 and antenna 2 respectively. The signals from the antennas are passed through amplifiers which filter out the desired frequency band, $\Delta\nu$. The interferometer pair is correlated by multiplying the signals and integrating over some time, typically a few seconds. Correlation of the signal is defined as

$$\langle V_1 V_2^* \rangle = \langle \mathrm{E}_\nu(\mathbf{r}_1) \mathrm{E}_\nu^*(\mathbf{r}_2) \rangle \,, \tag{2.4}$$

where $\mathrm{E}_\nu(\mathbf{r1})$ is the electric field and $\mathrm{E}_\nu^*(\mathbf{r2})$ is the complex conjugate of the

electric field at antenna 1 and 2.

Extended sources observed by the interferometer are treated as a collection of many point sources with different intensity and positions on the celestial sphere. Radio interferometers track a phase reference point $\mathbf{s}_0$ which defines the centre of the field. The displacement from various points in the field at $\mathbf{s}$ to the phase centre is represented by $\boldsymbol{\sigma} = \mathbf{s} - \mathbf{s}_0$. From Thompson et al. (2017), the correlated signals from the two antennas can be expressed as visibilities defined as

$$V \equiv |V| e^{i\phi_V} = \int_S \mathcal{A}(\boldsymbol{\sigma}) I(\boldsymbol{\sigma}) e^{-2\pi i \nu \mathbf{b}\cdot\boldsymbol{\sigma}/c} d\Omega, \tag{2.5}$$

where $\mathcal{A}(\boldsymbol{\sigma}) \equiv A(\boldsymbol{\sigma})/A_0$ is the normalised antenna reception pattern, A_0 is the response at the centre of the primary beam, $I(\sigma)$ is the intensity, and $d\Omega$ is the surface area.

2.1.3 Coordinate Systems

In radio astronomy it is useful to define a coordinate system that represents the North-South and East-West components of two planes: (i) a uv plane to represent one on which the array lies and (ii) a second lm plane to represent the one at which the source lies. The convention in radio astronomy is to point the u component along the East-West direction and the v component pointed towards the North-South direction. In 3-dimensions the w component points in the direction towards the phase reference centre $\mathbf{s}_0$. Points within the uvw volume define the baseline vectors $\vec{b}_\lambda$ that describe the orientation and distance between each antenna pair as

$$\vec{b}_\lambda = u\hat{x} + v\hat{y} + w\hat{z}, \tag{2.6}$$

where $\vec{b}_\lambda = \vec{b}/\lambda$ is the baseline vector expressed in wavelengths.

The antenna positions can also be expressed in a Cartesian system with components X, Y, and Z. The coordinates X and Y are part of a plane that runs parallel to the equator and the Z component points toward the geometric North. The corresponding baseline coordinates (u, v, w) can be determined from the transformation matrix given by Thompson et al. (2017):

$$\begin{bmatrix} u \\ v \\ w \end{bmatrix} = \begin{bmatrix} \sin(H) & \cos(H) & 0 \\ -\sin(\delta_d)\cos(H) & \sin(\delta_d)\sin(H) & \cos(\delta_d) \\ \cos(\delta_d)\cos(H) & -\cos(\delta_d)\sin(H) & \sin(\delta_d) \end{bmatrix} \begin{bmatrix} X_\lambda \\ Y_\lambda \\ Z_\lambda \end{bmatrix}, \tag{2.7}$$

where H is the hour-angle of the phase reference position, δ is the declination of the phase reference position, and the terms X_λ, Y_λ, and Z_λ are X, Y, and Z expressed in wavelengths.

The uv coordinates of the uvw volume are measured in a plane perpendicular to the direction of the phase reference position. These points sample the spatial frequencies to produce the sampled visibility function. From Eqn. 2.7 the positions of the antennas in X, Y, and Z are related to the coordinates u, v, and w by:

$$\begin{aligned} u &= X_\lambda \sin(H) + Y_\lambda \cos(H) \\ v &= -X_\lambda \cos(\delta)\cos(H) + Y_\lambda \sin(\delta)\sin(H) + Z_\lambda \cos(\delta) \\ w &= X_\lambda \cos(\delta)\cos(H) - Y_\lambda \cos(\delta)\sin(H) + Z_\lambda \sin(\delta). \end{aligned} \tag{2.8}$$

Combining the expressions for u and v gives the equation of an ellipse in the uv plane as

$$u^2 + \left(\frac{v - (Z_\lambda \cos(\delta))}{\sin(\delta)}\right)^2 = \frac{X_\lambda^2 + Y_\lambda^2}{\lambda}. \tag{2.9}$$

From Eqn. 2.9 it is apparent that the points in the uv plane will form an ellipsoidal shape in their tracks. The declination of the observed source determines the degree of ellipticity. At a declination of 90° the uv points would trace perfect concentric circles. A declination of 0° would result in a horizontal line track. Tracking the field of interest as the Earth rotates allows the uv coverage to increase because the relative position of the antennas changes.

A coordinate system for the source brightness distribution can be specified in terms of directional cosines (l, m, n) with the phase tracking centre considered the reference point. The sky coordinates can then be expressed as

$$\boldsymbol{\sigma} = l\hat{x} + m\hat{y} + n\hat{z}. \tag{2.10}$$

Using the coordinates found in Eqns. 2.6 and 2.10 in place of $\nu\vec{b} \cdot \vec{s}$ in the exponential gives

$$\begin{aligned} \frac{\nu \mathbf{b} \cdot \mathrm{s}_0}{c} &= w \\ \frac{\nu \mathbf{b} \cdot \boldsymbol{\sigma}}{c} &= ul + vm + wn \\ d\Omega = \frac{dldm}{n} &= \frac{dldm}{\sqrt{1 - l^2 - m^2}}, \end{aligned} \tag{2.11}$$

where $n = \sqrt{1 - l^2 - m^2}$. In these coordinates the visibility equation in Eqn. 2.5

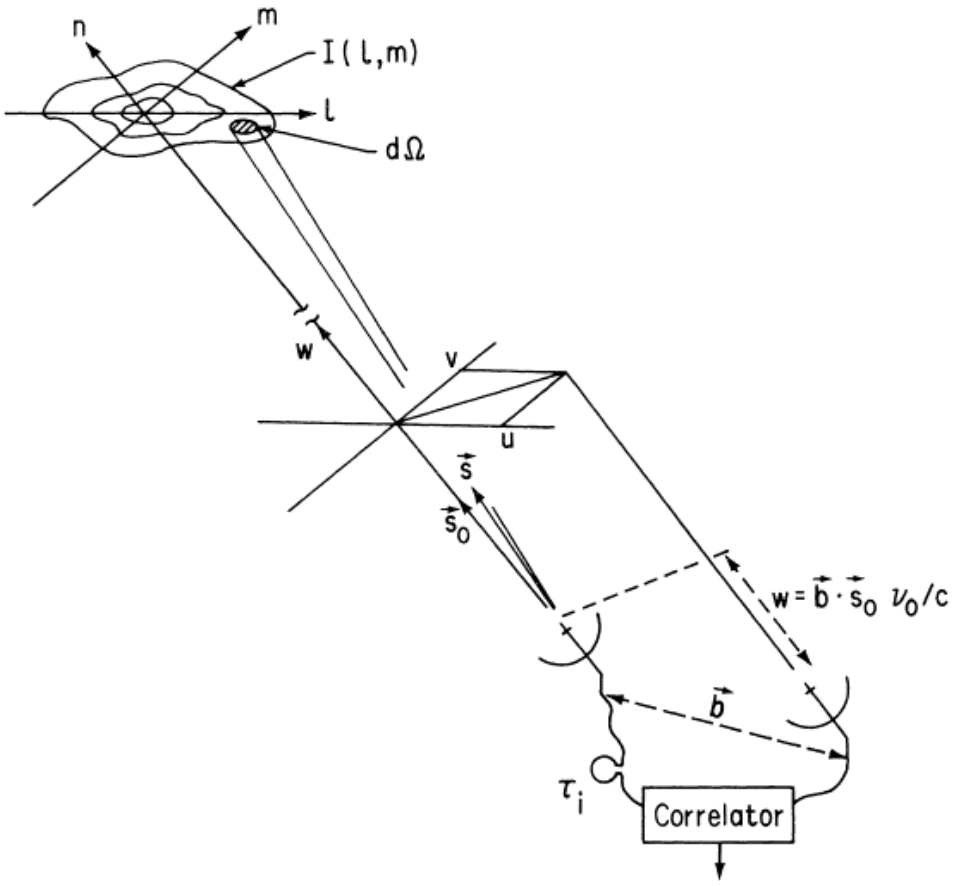

Figure 2.2: The interferometer baselines are expressed in (u, v, w) coordinates and the source brightness distribution is represented by the (l, m, n) coordinates. Image is reproduced from Thompson (1986).

becomes

$$V(u,v,w) = \int_{-\infty}^{\infty}\int_{-\infty}^{\infty} \mathcal{A}(l,m) I(l,m) e^{-2\pi i[ul+vm+w(\sqrt{1-l^2-m^2}-1)]} \frac{dldm}{\sqrt{1-l^2-m^2}}. \tag{2.12}$$

For arrays with components in only u and v planes ($w = 0$), Eqn. 2.12 can be simplified to a two-dimensional equation. If l and m are small, the w term can be approximated to 0 by

$$(\sqrt{1-l^2-m^2}-1)w \approx 0. \tag{2.13}$$

Thus, in two-dimensions Eqn. 2.12 can be written as

$$V(u,v) = \int_{-\infty}^{\infty}\int_{-\infty}^{\infty} \mathcal{A}(l,m)I(l,m)e^{-2\pi i(ul+vm)}dldm, \tag{2.14}$$

and its Fourier transform can be written as

$$\mathcal{A}(l,m)I(l,m) = \int_{-\infty}^{\infty}\int_{-\infty}^{\infty} V(u,v)e^{2\pi i(ul+vm)}dudv. \tag{2.15}$$

Equations 2.14 and 2.15 reveal an important result in interferometry. If $V(u,v)$ is known, that is the baseline length is known and the correlation of voltages is accurate, a map of the source as it appears on the celestial sphere can be obtained from a two-dimensional Fourier transform and vice versa. The Earth's rotation with respect to the source can help maximise uv plane coverage by rotating through the plane without moving an antenna. Unsampled values in the uv plane means the brightness distribution $\mathcal{A}I$ cannot be solved for at every point and the values that are sampled are not solved for accurately. This presents a challenge during deconvolution and will be discussed in §2.4.

2.2 Sensitivity

The system temperature T_{sys} is a measure of the performance of an antenna and is expressed in units of kelvin (K). The T_{sys} is a combination of all noise introduced during an observation of a radio source. Sources that can introduce noise include the cosmic microwave background (T_{BG}), additional atmospheric emission (T_{sky}), calibration signals (T_{cal}), ground radiation scattering (i.e., sidelobes) (T_{spill}), losses in the feed (T_{loss}), and receiver noise (T_{rx}):

$$T_{sys} = T_{BG} + T_{sky} + T_{spill} + T_{loss} + T_{cal} + T_{rx}. \tag{2.16}$$

For simplicity, it will be assumed that the system temperature will include only noise contributions introduced after receiving the signal. In this case, T_{sys} is the sum of noise introduced at the receiver T_R, from the antenna T_A, and from power loss along the transmission line T_L,

$$T_{sys} = T_A + (L-1)T_L + LT_R. \tag{2.17}$$

The L represents some power loss factor of the system ($L = P_{in}/P_{out}$), where P is the power) and T_R includes contributions from the amplifier, the correlator, and the filter (Wrobel and Walker, 1999).

The power collected by the antenna from the radio source P_A is related to the antenna temperature by

$$P_A = k_B T_A \Delta\nu, \tag{2.18}$$

where k_B is the Boltzmann constant. Expressing the antenna temperature as a function of flux density S gives

$$T_A = KS. \tag{2.19}$$

The K term represents $\frac{\eta_A A}{2k_B}$, where η_A is the aperture efficiency and A is the collecting area of the dish. Substituting Eqn. 2.19 into Eqn. 2.18 gives

$$P_A = \frac{1}{2}\eta_A S A \Delta\nu. \tag{2.20}$$

Combining noise from the total number of antennas in the array N and accounting for all noise present in T_{sys} results in a noise level, or sensitivity, of

$$S_{rms} = \frac{2k_B T_{sys}}{A_{\text{eff}}\eta_A\sqrt{N(N-1)\Delta\nu t}}. \tag{2.21}$$

The term A_{eff} is a measure of how effective an antenna is at receiving power in m^2, t is the integration time in seconds, and T_{sys} is given in K. The sensitivity gives the smallest flux detectable with an array.

2.3 Calibration and Editing

Corruption from external sources must be corrected for before the data are usable. Erroneous changes to the phases and amplitudes are introduced as the radio signal travels through media such as the observing instrumentation and the Earth's atmosphere. Calibration is the process of undoing these effects by using other well known sources, referred to as calibrators. The stages of calibration discussed in this section are outlined in Fig. 2.3.

Calibration begins by loading the data set into software designed for radio interferometry processing. The most commonly used programs are Astronomical

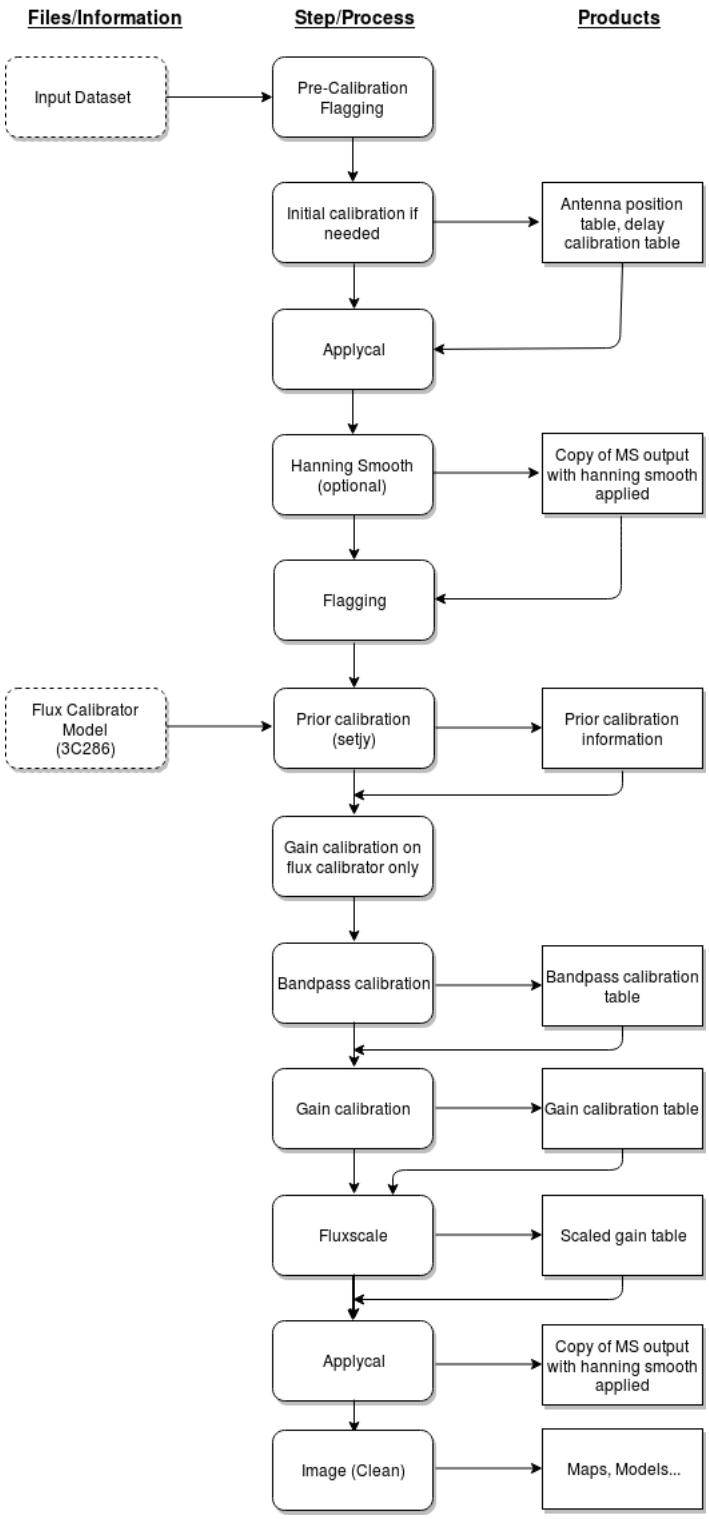

Figure 2.3: A flowchart of a typical calibration routine for radio data observed with a radio interferometer.

Image Processing System (AIPS) and Common Astronomy Software Applications (CASA). Both AIPS and CASA are powerful tools for radio data calibration, as many tasks have equivalent counterparts in both. However, the format of the data loaded into the programs is different. Historically Flexible Image Transport System (FITS) files were the preferred digital files in astronomy. AIPS continues to use FITS files. CASA prefers to use measurement sets to work with. A measurement set is a directory tree that includes important information such as the visibilities, observation date, and antennas used during the observation. More details about the tasks used in CASA and AIPS for this thesis can be found in Ch. 3.

After loading the data into the preferred program, the next step is data editing or *flagging* (Fig. 2.3). Radio frequency interference (RFI) can produce large increases in amplitude during some of the observation and varies by baseline. Visual inspection of the data can be done using a TV data display. Data are typically plotted in AIPS per baseline with time on the y-axis and channel on the x-axis. High amplitude RFI and much lower amplitude data produced from equipment failure will appear as brighter or darker points compared to most of the other data. These points should be discarded.

Corrections to errors in amplitude and phase are done when most of the values of the remaining data seems sensible. The observed visibilities $\tilde{V}$ with variations in amplitude and phase relate to the true visibilities V by

$$\tilde{V}_{ij}(t) = G_{ij}(t)V_{ij}(t) + \epsilon_{ij}(t) + \eta_{ij}(t), \tag{2.22}$$

Where G is the complex gain associated with a baseline formed by antenna i and j, $\eta_{ij}(t)$ is thermal noise, and $\epsilon_{ij}(t)$ is a baseline-based offset term (Thompson et al., 2017). Engineering of the array minimises the offset of ϵ. Unless a correlator is not properly working or some other instrument is malfunctioning it should be ignored. Since most errors are introduced prior to correlating, G_{ij} is a product of the gains $g_i(t)$ and $g_j(t)$ at each antenna,

$$G_{ij}(t) = g_i(t)g_j^*(t) = a_i(t)a_j(t)e^{i(\phi_i(t)-\phi_j(t))}, \tag{2.23}$$

where $a_i(t)$ and $a_j(t)$ are amplitude corrections per antenna and $\phi_i(t)$ and $\phi_j(t)$ are the phase corrections per antenna. The observed visibilities are close to the true visibilities when g_{ij} is close to 1.

The G_{ij} baseline-based corrections can be determined by observing a well-known point source calibrator at regular intervals throughout the observation. The response associated with each baseline to the point source is compared to the response expected for a point source with no errors in phase or amplitude. Differences between the observed and the expected are regularised by solving for N complex gains, g_i.

2.3.1 VLBI Fringe Fitting and Other Initial Calibrations

Some arrays require an additional calibration step prior to beginning calibration processes for amplitude and phase corrections. Corrections to antenna positions for the Very Large Array (VLA) is one example of an initial calibration. It is not unusual for antenna positions to be adjusted to a better position for an observation. The database may not be updated before starting the observation and may need correcting.

Another initial calibration, particularly important for VLBI, is fringe fitting. The correlated signal from larger-baseline arrays are more difficult to correct for delays a priori. As discussed in §2.1.2, geometric delays are introduced as a result of the positions of the interferometer and the source, the atmosphere, and through instrumental hardware. High-resolution data are even more susceptible to these uncertainties. As the ionosphere and troposphere can change the phase rapidly (on time scales less than a minute at times), as well as small changes in Earth's rotation and with the clock, it is important to correct for these offsets prior to any amplitude and phase calibration. Observations from the e-MERLIN array are especially susceptible to delays due to the atmosphere. Fringe fitting determines the antenna-based delays and fringe rates, or rate of change between between expected and actual phases. If the correlation function is plotted as a frequency spectrum, delays are presented as a slope in the phase. If not corrected, these delays will produce larger phase offsets that may not be removable even with self-calibration, see §2.5.

2.3.2 Amplitude and Phase Calibrations

Flux calibration requires observations of a source with a high flux density and a well-known position. The chosen source should be compact and have a flux density well above the noise of the system. Compact sources often have flux densities

that are highly variable, which makes choosing a flux calibrator difficult. A commonly used flux calibrator is the non-varying source 3C 286. Each observation will include a few scans of the calibrator and a model is often provided. The gain is determined between the model and the observed visibilities. Corrections are applied to all other calibrators for all baselines.

Atmospheric disturbances can introduce antenna-based time variations in the gains. As a result, large phase variations on spatial scales of a few degrees can occur. These fluctuations can be reduced by observing another phase calibrator close to the target every few minutes throughout the observation. Unlike the flux calibrator, the phase calibrator can be resolved as long as some of a compact structure is visible on all baselines. Additionally, bright targets can be used to derive their own phase corrections through a process called self-calibration. Self-calibration is discussed later in §2.5.

2.3.3 Bandpass Calibration

Visibilities also show frequency-dependent variations in amplitude and phase. A receiver will have different amplitude responses at each frequency resulting in offsets across the bandpass. If these variations are not corrected, the dynamic range of the final maps may be affected. Frequency-dependent amplitude errors can limit detection of weaker emission, while frequency-dependent phase errors can create positional offsets that may falsely resemble Doppler motion.

Removal of frequency based fluctuations requires observations of a bright bandpass calibrator source. It is necessary that this source has a known spectrum over the frequency observed so that the visibilities can be considered a constant across the channels. If the visibilities should be identical, a correction can be determined and applied to the other calibrators and target.

2.4 Imaging

Equations 2.14 and 2.15 revealed that the visibilities $V(u, v)$ could be Fourier transformed to give the sky brightness $I(l, m)$ and the antenna beam pattern $A(l, m)$. As discussed in §2.3, corruption from instrumental and atmospheric effects are mostly corrected for during calibration. Assuming calibration has minimised errors, the data should be corrected well enough to produce an image of the estimated sky brightness. The process begins by interpolating the data onto

a rectangular grid, referred to as *gridding*, so that a fast Fourier transform (FFT) can be used. This section discuses the theory and techniques behind imaging of uv plane data.

2.4.1 The Sampling Theorem

The Nyquist-Shannon theorem, otherwise known as the sampling theorem, states that a bandwidth-limited continuous function within a frequency range $\Delta\nu$ can be reconstructed exactly from samples separated equally in time by a factor $\leq (2\Delta\nu)^{-1}$. The critical sampling rate, given by $1/\Delta t = 2\Delta\nu$, is used in radio interferometry with the spacing between samples to satisfy the sampling interval $\Delta t \leq 1/(2\Delta\nu)$ seconds. The Nyquist frequency corresponds to the high-frequency cut-off of a system sampling at $\Delta\nu$ and is given by

$$\Delta\nu_{N/2} = \frac{1}{2\Delta t}, \tag{2.24}$$

where N is the length of the Nyquist-sampled signal, ν is the frequency in Hz, and Δt is the length of time sampled in seconds (Thompson et al., 2017).

The sampling theorem has many useful applications for imaging, such as the calculation of the cell size and image size. Cell sizes are chosen by Nyquist-sampling the main lobe of the PSF. The PSF of the beamwidth is given by

$$\theta_{PSF} \sim \frac{\lambda}{b_{max}} \sim \frac{1}{u_{max}} \tag{2.25}$$

in radians. At least 3−5 pixels should fit across one beam but the beam size depends on the full uv distribution and weighting. Similarly, the image size is determined by Nyquist-sampling the uv grid cell size δu using

$$\delta u = \frac{1}{FoV_{rad}}, \tag{2.26}$$

where FoV is the field of view. While this is a good starting point, the image size should be adjusted as needed. For the e-MERLIN array it is often best to choose an initial image size twice the size of δu due to the sparse uv coverage.

2.4.2 Deconvolution in Radio Interferometry

This chapter began discussing the Fourier relationship between Eqns. 2.14 and 2.15 and gridding the data onto a rectangular grid. The uv plane is a collection of sampled points and unsampled points that can be considered as a sampling function $S(u, v)$ given by

$$S(u, v) = \sum_{k=1}^{M} \delta(u - u_k, v - v_k), \tag{2.27}$$

where δ is a two-dimentional dirac delta function and M is on the order of N^2 for and $N \times N$ grid. Grid squares with data are assigned a value of 1 and those without data are given a value of 0. The true source visibility $V(u, v)$ is multiplied with $S(u, v)$ to give the recorded visibility V_r,

$$V_r(u, v) = S(u, v)V(u, v). \tag{2.28}$$

Inversion of the recorded visibilities with a Fourier transform gives a dirty map I^D given by

$$I^D(l, m) = \sum_r V_r(u, v)e^{2\pi i(ul+vm)}\delta u\delta v. \tag{2.29}$$

Substitute Eqn. 2.28 into this equation and using the convolution theorem gives

$$\begin{aligned} I^D(l, m) &= \int_{-\infty}^{\infty} V(u, v)S(u, v)e^{2\pi i(ul+vm)}dudv \\ &= \mathbf{F}V(u, v) * \mathbf{F}S(u, v) \\ &= I(l, m) * B(l, m), \end{aligned} \tag{2.30}$$

where $\mathbf{F}$ denotes the Fourier transform, the point source response to $S(u, v)$ is referred to as the dirty beam or point spread function (PSF) and is given by $B = \mathbf{F}S$, and I is the true intensity distribution. The dirty beam $B(l, m)$ is the Fourier Transform of the uv coverage. The result of Eqn. 2.30 shows that the true intensity distribution convolved with the dirty beam produces a dirty map. The dirty beam will contain sidelobes due to the Fourier transform of unsampled uv points. Sidelobes lead to a lower signal to noise ratio and produce defects in the dirty map. The most obvious solution to minimizing effects due to sidelobes is to fully sample the uv plane so that data exists for every point. This isn't a

realistic solution though. Deconvolving the dirty map using advanced techniques can help remove the effects caused by the convolution. The two most commonly used deconvolution techniques are the CLEAN algorithm (see §2.4.3) and the Maximum Entropy Method, or MEM (Thompson et al., 2017).

2.4.3 The CLEAN Algorithm

The CLEAN deconvolution algorithm works under the assumption that the source is composed of a number of point sources in an otherwise empty field (Thompson et al., 2017). The position and strength of each of the point sources is found, starting from the brightest and iterating down. These points are summed together and convolved with a CLEAN beam, usually a Gaussian, to produce a clean map. The iterative process behind CLEAN is shown as a flow chart in Fig. 2.4. Variations of the CLEAN algorithm have been developed to assist with larger images and may reduce computing time. The original Högbom algorithm and the multi-scale CLEAN algorithm used for this thesis will be discussed in the following sub-sections.

The Högbom Algorithm

The H*ö*gbom algorithm was the first CLEAN algorithm but since has been updated. The procedure is simple. It can be described by the following steps:

1. Locate the strength and position of the pixel with the highest intensity in the dirty image.

2. A gain factor γ between 0 and 1 (typically 0.1) is multiplied to the peaks found in Step 1. This value and the corresponding position are stored in a list of CLEAN components.

3. Multiply the dirty beam by the amplitude and γ. Subtract this value from the dirty image to remove effects caused by the CLEAN component in the dirty map.

4. Repeat the process, starting with Step 1 until no peaks are found above the threshold set for the observation. All regions should be cleaned down to the noise.

5. Convolve the CLEAN components with a CLEAN beam and add in the residual map to produce the final CLEAN map. Without the residuals the CLEANed map would contain no noise. Adding the residuals to the final image provides a more accurate representation of the brightness distribution (Thompson et al., 2017).

To help make CLEAN more efficient and smooth it is necessary to consider a few details about the algorithm. First, CLEAN boxes or windows should be used to restrict the peak emission search region. In simple point-like sources one box may be sufficient. Large, complicated structures may require more than one box. Setting boxes limits the number of degrees of freedom for fitting the data. Secondly, the CLEAN beam is a Gaussian fit to the primary lobe of the dirty beam. It will not contain sidelobes from the dirty beam but sidelobes may still be in the residual map.

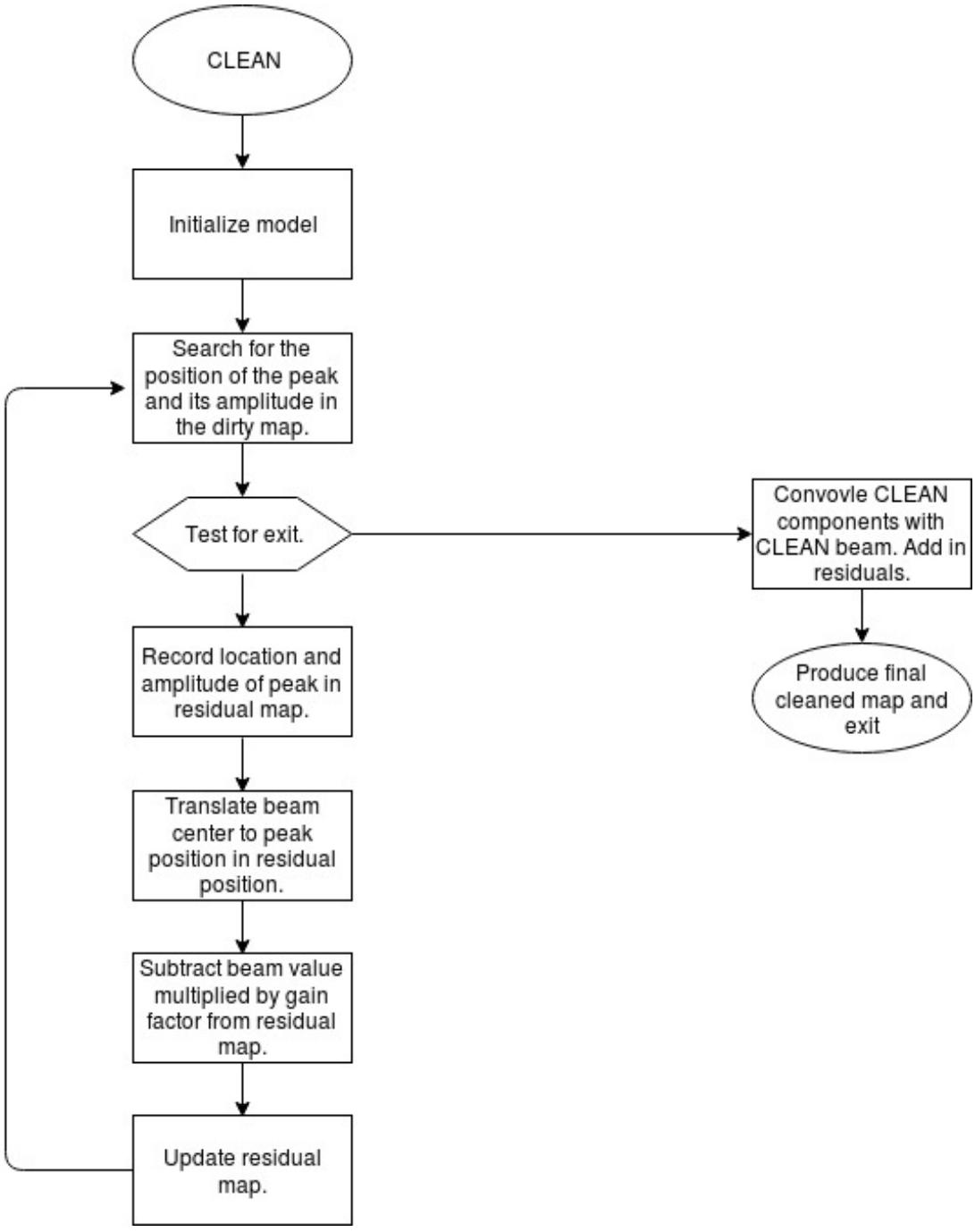

Figure 2.4: A flowchart describing the CLEAN algorithm.

Multi-term Multi-Frequency Synthesis

Multi-term (multi-scale) multi-frequency synthesis (MS-MFS) is an algorithm that was developed to make use of large bandwidths offered by modern arrays while also improving CLEAN techniques for extended emission (Rau and Cornwell, 2011). Traditional CLEAN techniques assumed that the source emission could be modeled by point-source flux components. This does not always work well for large-scale flux components. Classic CLEAN algorithms, such as the Högbom CLEAN algorithm, do a poor job of correcting negative bowls in extended emission. This is because numerous point sources representing the emission must be subtracted (Cornwell, 2008). The MS-MFS algorithm was developed to produce images of large-scale emission while also fitting for the intrinsic source spectrum.

Multi-scale CLEAN (MS-CLEAN) works under the assumption that the sky is composed of emission at various angular scales. A combination of images at these different scales are created simultaneously. The multi-scale CLEAN process created by Cornwell (2008) describes an adaptation of the traditional CLEAN process by the following:

1. Initialise the model to zero: $I^M = 0$.
2. Set the residual image equal to the dirty image: $I^R = I^D$.
3. Convolve the dirty map with pre-selected pixel scales. Pixel scales are chosen somewhat arbitrarily, with a bias towards smaller scales. Choosing larger scales to represent a source that is nearly point-like with a small amount of extended emission will fail to remove the point source from the residuals (Cornwell, 2008; Rich et al., 2008). Locate the pixel with the maximum total flux and record the peak flux, the scale size it occurs at, and its position (Rich et al., 2008).
4. Multiply a gain factor γ to the dirty beam convolved with the scale size corresponding to the peak flux. Subtract this value from all of the scaled imaged created in the step 3 (Cornwell, 2008).
5. Store the component from the step above and the scale at which it was found in a table (CLEAN components) (Rich et al., 2008).

6. Repeat the entire process until a flux threshold is reached, all emission is removed (noise-like within boxes), or the maximum number of iterations set by the user has been reached (Rich et al., 2008).

Wide bandwidth observations can introduce artifacts that increase the rms noise during imaging. The primary and synthesised beams are linearly dependent on wavelength and variations can be observed across the different frequencies at each baseline. Take for instance a single baseline observing over several frequencies in the uv plane (measured in wavelengths). Several ellipses with varying sizes are sampled that correspond to each observed frequency. Multi-frequency (MF) synthesis is a method used to combine the measurements across the bandwidth to obtain a better image fidelity. The MF algorithms work in a similar way to other CLEAN techniques. In the case of MF synthesis, image reconstruction relies on a priori information of the spectral structure of the sky brightness (Rau and Cornwell, 2011). A model with the known frequency-dependence can be combined with the element response function to reconstruct the sky brightness (Rau and Cornwell, 2011).

The multi-scale multi-frequency deconvolution algorithm developed by Rau and Cornwell (2011) allows multi-frequency and multi-scale methods to be processed simultaneously. Identical to those methods, MS-MFS approximates the spectrum using a Taylor-series expansion in frequency at various angular scales:

$$I_\nu^m = \sum_{t=0}^{N_t-1} w_\nu^t I_t^{sky}, \tag{2.31}$$

where $w_\nu^t = [(\nu - \nu_0)/(\nu_0)]^t$, ν_0 is the reference frequency typically at the centre of the frequency of interest (Sault and Conway, 1999). The spectral models chosen to perform a Taylor expansion on is given in the form of a power law:

$$I_\nu^{sky} = I_{\nu_0}^{sky} \left(\frac{\nu}{\nu_0}\right)^{I_\alpha + I_\beta \log(\frac{\nu}{\nu_0})}, \tag{2.32}$$

where I_α is the average spectral index and I_β is the spectral curvature (Sault and Conway, 1999). Wide frequency receivers can detect changes in the spectral index across the band. Sault and Conway (1999) describes spectral curvature as an additional term to smooth turnovers and steepening (spectral breaks) in continuum synchrotron emission. Expanding the first three terms of Eqn. 2.31

gives

$$I_0^m = I_{\nu_0}^{sky}, \tag{2.33}$$

$$I_1^m = I_\alpha I_{\nu_0}^{sky}, \tag{2.34}$$

and

$$I_2^m = \left(\frac{I_\alpha(I_\alpha - 1)}{2} + I_\beta\right) I_{\nu_0}^{sky}, \tag{2.35}$$

corresponding to the sky brightness, spectral index, and spectral curvature respectively (Sault and Conway, 1999). The MS-MFS algorithm in CASA produces images with an extension noted by 'tt*', where the '*' indicates the Taylor term expansion number.

2.4.4 W-projection

Most of the work presented thus far has assumed that the array is coplanar with $w = 0$ in Eqn. 2.12, or that the source is small and close to the phase reference centre. These assumptions allow for the use of a two-dimensional Fourier transform. For cases other than these two conditions the w component should be included in the visibility equations. Consider the case where the antennas in the array are non-coplanar, that is at least one of the antennas is positioned at some offset above or below the uv plane. The wavefront is no longer detected uniformly at each receiver and a phase offset $\phi = 2\pi w(\sqrt{1 - l^2 - m^2} - 1)$ is introduced (Cornwell et al., 2008).

Take the coordinate system for a radiating source as observed by an array shown in Fig. 2.2. While the visibility is dependent on (u, v, w) and (l, m, n), the focus for now is on the dependence of the w-term on directional cosine n. A position on the celestial sphere can be represented by $l^2 + m^2 + n^2 = 1$. If the n-term is confined to one hemisphere, n can be given by

$$n = \pm\sqrt{1 - l^2 + m^2}. \tag{2.36}$$

Substituting Eqn. 2.36 into Eqn. 2.12 results in a visibility equation dependent on n:

$$V(u, v, w) = \int_{-\infty}^{\infty}\int_{-\infty}^{\infty} A(l, m)I(l, m)e^{-2\pi i(ul+vm+w(n-1))}\frac{dldm}{n}. \tag{2.37}$$

Despite the inclusion of the w-term in this equation, the sky intensity distribution

$I(l, m)$ is still restricted to the image plane. The visibilities obtained will not take into account the offset from the lm-plane leading to a distortion in the image during the reconstruction of the sky brightness.

The two most common techniques used to correct the phase offset in wide-field imaging are w-projection and faceting. Faceting assumes the large field can be split into a number of smaller fields with $l = m = 0$. This approximates the image sphere into many smaller tangent image planes that can be imaged using the two-dimensional Fourier transform. Each smaller image can be stitched together to form a larger image in the end. W-projection works in a similar way to faceting, but is more commonly used because of its efficiency. In w-projection the number of distinct w-values is estimated. With these values inserted into the equation gridding using different convolution functions can be done. The final image is a composition of the different w-planes. While it is a quicker method it can require greater memory usage (Cornwell et al., 2008).

2.4.5 Weighting

The sampling function given in Eqn. 2.27 can be written as a weighted sampling function where each cell in the gridded data is assigned a weight:

$$W(u, v) = \sum_{k=1}^{M} R_k T_k D_k \delta(u - u_k, v - v_k), \tag{2.38}$$

where the coefficients R_k, T_k, and D_k are the assigned weights of the visibilities (Briggs et al., 1999). The R_k weight value depends on the integration time, frequency, and system temperature for each data point. D_k is the density weighting function where $D_k = 1$ is natural weighting and $D_k = 1/N$ where N is the number of data points is uniform weighting. The third coefficient T_k is the tapering weight that downweights the data as a function of uv radius. High spatial frequencies are often downweighted compared to lower spatial frequencies to suppress sidelobes induced by sparse uv coverage. Tapering increases the flux sensitivity but is done so at the cost of resolution (Briggs et al., 1999).

The three most commonly used weighting schemes are:

- *Natural*: The weights of each cell is based on the number of measured points within the cell. These are the weights identical to the observed data weights. This means that areas of denser uv coverage will have heavier

weights assigned to the cells. Interferometers typically have more shorter baselines than longer baselines. As a result, the centre of the *uv* distribution (shorter baselines) is weighted more heavily. While the natural weighting scheme produces a higher sensitivity, the angular resolution of the image is reduced.

- *Uniform*: Each cell is assigned the same weight regardless of the number of data points within it. In other words, longer baselines with fewer sampled data points have the same effect on the image as the shorter baselines. This means a higher resolution than natural weighting can be achieved but at the expense of sensitivity. An example of how uniform weighting compares to natural weighting is given in Fig. 2.5.

- *Briggs*: This is an intermediate weighting scheme that compromises between the loss of resolution and sensitivity that uniform and natural weighting produce by specifying a *robust* parameter. In CASA, a robust parameter of -2.0 corresponds to uniform weighting. Natural weighting occurs when robust $= +2.0$. For many cases robust $= 0$ is a good balance between natural and uniform schemes to produce the best results.

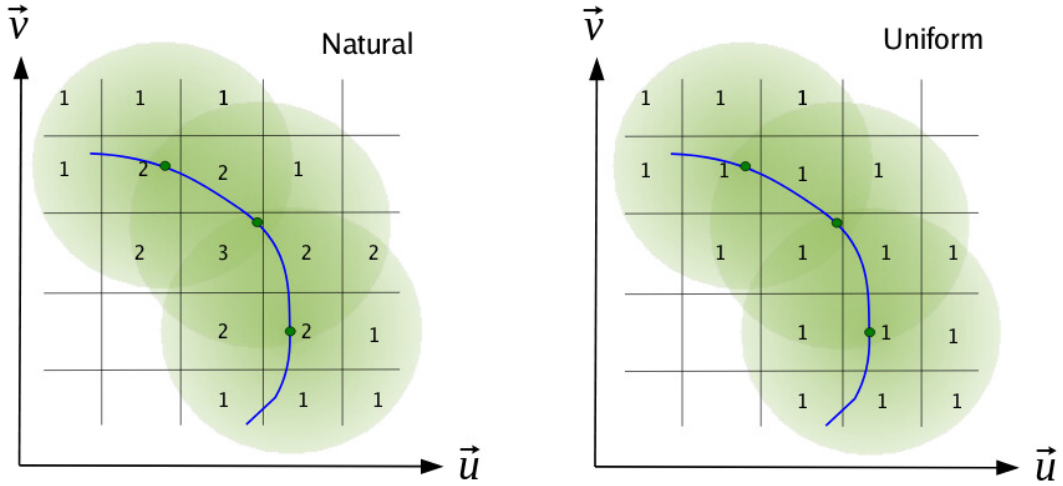

Figure 2.5: Natural weighting (left) weights the more densely-sampled regions heavier. Uniform weighting assigns equal weighting to each cell regardless of the number of data points in each. Robust weighting combines both natural and uniform schemes so that resolution and sensitivity are not negatively affected. Image is reproduced from the Australia Telescope National Facility (Rau, 2012).

2.5 Self-Calibration

Early calibration steps alleviate many of the errors introduced during observation or correlation of the signal but fail to remove all of the variations. These errors scatter power, thus affecting regions of weaker emission more and produce errors in the map. Self-calibration is a technique that further reduces variations in the data by having a target use itself as an amplitude and phase calibrator. Self-calibration uses the CLEAN algorithm to create a model of the target and determine the gain corrections that minimise the function

$$S = \sum_{k} \sum_{i,j \forall i \neq j} w_{ij}(t_k) |\tilde{V}_{ij}(t_k) - g_i(t_k) g_j^*(t_k) \hat{V}_{ij}(t_k)|, \tag{2.39}$$

where w_{ij} is the weighting for antenna i and j in a baseline, g is the gain of an antenna, $\hat{\mathrm{V}}$ is the Fourier transform of the model, and $t(k)$ is the time at which the the observations were done. As g_i and g_j are changed through many iterations of self-calibration, the model improves and becomes accurate enough to improve phase and amplitude measurements.

2.5.1 Closure Quantities

Observations with many antennas are what allows self-calibration to correct antenna based errors. Self-calibration uses closure quantities to correct phase and amplitude errors. Roger Jennison (1958) determined that visibility phases could be obtained when delays were present. This was based on the idea that element related errors cancel when an appropriate number of antennas are used. Consider the phase portion of Eqn. 2.22,

$$\tilde{\phi}_{ij}(t) = \phi_{ij}(t) + \theta_i(t) - \theta_j(t) + \epsilon_{nt}, \tag{2.40}$$

where $\theta_i(t)$ and $\theta_j(t)$ are the phases of the gain terms, ϕ_{ij} is the true phase, $\tilde{\phi}_{ij}$ is the observed phase, and ϵ_{nt} is the noise term. If at least three telescopes (i, j, and k) are operational during the observation, a closed loop is formed that allows

the closure phase $\tilde{C}_{ijk}(t)$ to be calculated from

$$\begin{aligned}\tilde{C}_{ijk}(t) &= \tilde{\phi}_{ij}(t) + \tilde{\phi}_{jk}(t) + \tilde{\phi}_{ki}(t) \\ &= \phi_{ij}(t) + \phi_{jk}(t) + \phi_{ki}(t) + \epsilon_{nt} \\ &= C_{ijk}(t) + \epsilon_{nt}.\end{aligned} \tag{2.41}$$

Similarly, a closure amplitude Γ is derived from Eqn. 2.22 to be

$$\Gamma_{ijkl} = \frac{|\tilde{V}_{ij}(t)||\tilde{V}_{kl}(t)|}{|\tilde{V}_{ij}(t)||\tilde{V}_{jl}(t)|}. \tag{2.42}$$

The closure quantities remain unchanged when the antenna-based gains vary, with the gains canceling out in Eqns. 2.40 and 2.42.

Chapter 3

Observations and Calibration

This chapter discusses data collection, calibration, and imaging techniques for the FRII quasars 3C 334 (1620+1736), 3C 263 (1139+6547), and the FRII radio galaxy Cygnus A (1959+4044). The fields were imaged as part of the e-MERLIN Extragalactic Jets Legacy Project using the e-MERLIN array and the Karl G. Jansky Very Large Array (JVLA) at L-band (centre frequency at 1.5 GHz) and C-band (centre frequency at 5.5 GHz). Data were calibrated using the standard procedures discussed in Ch.2 (see Fig. 2.3 for a summary). In some cases a pipeline designed for calibrating data for the arrays was used. Special techniques for removing Cygnus A's contribution to the overall system temperature had to be considered at L-band for the e-MERLIN array. The procedure for doing so is shown in §3.6. Final calibrated maps produced from the data are provided at the end of each target's imaging section.

3.1 e-MERLIN Jets Legacy Project Observations

The e-MERLIN Extragalactic Jets Legacy Project is utilising the high spatial resolution of e-MERLIN to observe a number of bright radio sources at 1.5 and 5 GHz. The sample includes extragalactic radio sources belonging to one of two classes: (1) low-luminosity FRI jets and (2) powerful FRII jets. Each source chosen for the sample is a quintessential member of its class. Eight twin-jet sources observable only at L-band make up the FRI sample selection. FRII sources were chosen from the bright sample of quasars with redshifts in the range $0.25 \leq z \leq 1$ by Bridle et al. (1994a). The project seeks to resolve jets where they brighten, probe the transverse structure, and measure the magnetic fields

in the environment near the jet. The work done for this thesis focused on a few FRII DRAGNs with bright jets.

Observations were taken separately using the e-MERLIN and JVLA arrays at L-Band to provide the maximum *uv* coverage. The e-MERLIN data at C-band were not supplemented with JVLA data at the time of writing this thesis. The JVLA data, spanning a maximum baseline up to 11.1 km in B configuration to 36.4 km in A configuration, are needed to alleviate errors introduced during the cleaning process as a result of missing short spacings (see Chapter 2 for details) (Perley et al., 1989). The JVLA array, shown in Fig. 3.1, consists of antennas placed on a "Y" shaped track. These antennas can be moved to increase or decrease the baseline lengths to achieve a particular resolution. The e-MERLIN array consists of 7 antennas spread out over England (see Fig. 3.2). Spanning up to 217 km, the e-MERLIN array provides the longest baselines in this project. The longest baselines of the e-MERLIN array provides the spatial scales needed to achieve the highest resolution. The *uv* plots presented in Figures 3.3 and 3.4 show the *uv* coverage of the e-MERLIN and the JVLA arrays separately for the source 3C 334 compared to the *uv* coverage of the two arrays combined (Figure 3.5). Both JVLA and e-MERLIN observations in L-band were concatenated with e-MERLIN's channels averaged to 64 channels per spectral window (SPW). This placed each averaged channel in the e-MERLIN data within 0.1 MHz of the 64 channels observed in the JVLA data. Centre frequencies and bandwith of each of the SPWs in the e-MERLIN and JVLA arrays are provided in Table 3.1.

Table 3.1: Bandwidth (BW) and centre frequencies (ν_c) for each averaged spectral window in the e-MERLIN and JVLA arrays. The e-MERLIN L-band spans frequencies 1.23−1.74 GHz. The e-MERLIN C-band spans 4.5−7.5 GHz but only 512 MHz was used in total. The JVLA array at L-band spans frequencies 1.0−2.0 GHz.

SPW	e-MERLIN (L)		e-MERLIN (C)		JVLA (L)	
	ν_c (GHz)	BW (MHz)	ν_c (GHz)	BW (MHz)	ν_c (GHz)	BW (MHz)
0	1.286	64	4.880	128	1.026	64
1	1.350	64	5.008	128	1.090	64
2	1.414	64	5.136	128	1.154	64
3	1.478	64	5.264	128	1.218	64
4	1.542	64	-	-	1.282	64
5	1.606	64	-	-	1.346	64
6	1.670	64	-	-	1.410	64
7	1.734	64	-	-	1.474	64
8	-	-	-	-	1.526	64
9	-	-	-	-	1.538	64
10	-	-	-	-	1.602	64
11	-	-	-	-	1.666	64
12	-	-	-	-	1.730	64
13	-	-	-	-	1.794	64
14	-	-	-	-	1.858	64
15	-	-	-	-	1.922	64

Figure 3.1: Antennas in the JVLA array are moved every few months to observe with different resolutions. This is an image of the JVLA in C configuration ($b_{max} = 3.4$ km). Photo credit: NRAO, NSF.

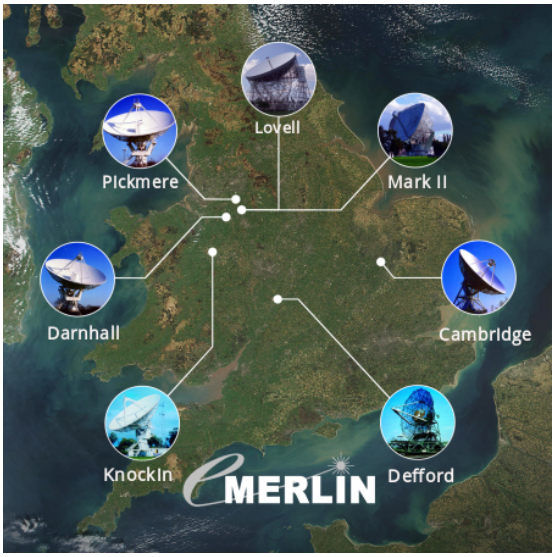

Figure 3.2: Antennas in the e-MERLIN array are spread out over England with $b_{max} = 217$ km. Photo credit: e-MERLIN.

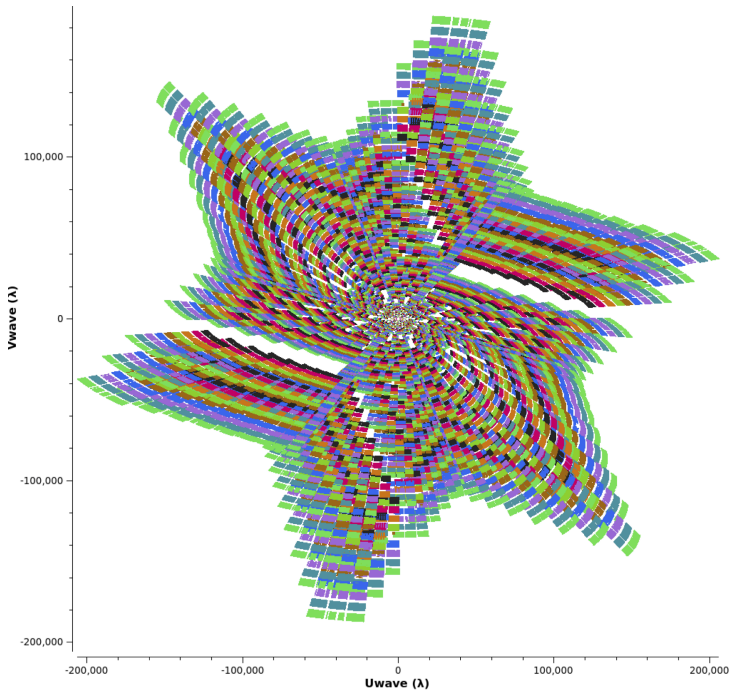

Figure 3.3: The *uv* coverage over the total observing time of 3C 334 with the JVLA array. The *uv* coverage shown includes A and B configuration for a total of 1 hour observation time each. Each color in the plot represents one of the 16 SPWs in the JVLA array.

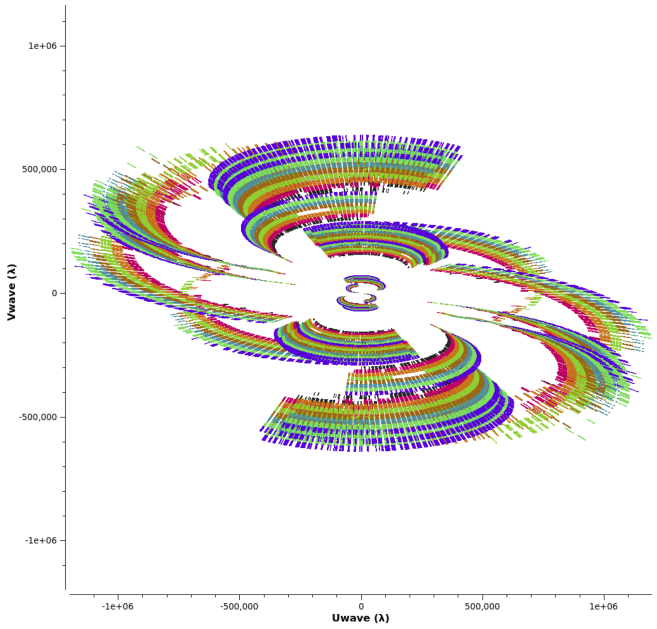

Figure 3.4: The *uv* coverage for the total observing time of 3C 334 using the e-MERLIN array. Each color in the plot represents one of the 8 SPWs in the e-MERLIN array.

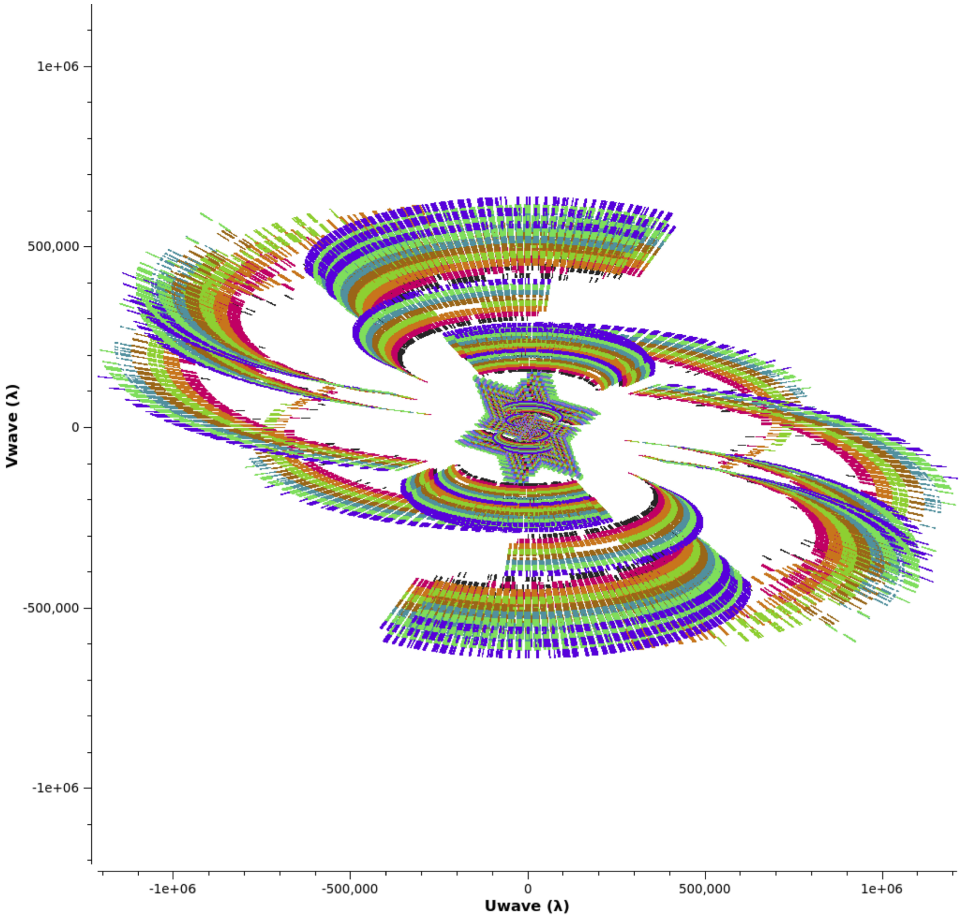

Figure 3.5: The *uv* coverage over the total observing time of 3C 334 by combining both the e-MERLIN and JVLA arrays. Each color in the plot represent one of the 24 SPWs in the e-MERLIN and JVLA arrays.

3.2 3C 334 Calibration

3.2.1 3 C334 e-MERLIN L-Band Calibration

The quasar 3C 334 was observed using the e-MERLIN array on 03 April 2015 for a total of 10 hours as part of the e-MERLIN Jets Legacy Project. Antennas included in this observation were Lovell (Lo), Mark II (Mk2), Knockin (Kn), Defford (De), Pickmere (Pi), Darnhall (Da), and Cambridge (Cm). The Lovell antenna was included in the observation but all Lovell baselines were flagged prior to calibration and imaging. An initial inspection of the data found that the data were largely decorrelated on the Lovell baselines, possibly due to an issue with the phase delays. Information about the antenna diameters (Argo, 2015) and the estimated individual dish temperatures (T_{sys}) can be found in Table 3.2. At L-band, e-MERLIN's upgrade from MERLIN increased its bandwidth from 16 MHz to 512 MHz with a total of 8 SPWs centred at frequencies ranging 1.25 GHz to 1.75 GHz (Argo, 2015). Each of the 8 SPWs is divided into 512 channels, with the first SPW being highly affected by non-astrophysical radio emission in the form of radio frequency interference (RFI). Details of the observational configuration can be found in Table 3.3.

Table 3.2: A list of e-MERLIN antenna diameters (Argo, 2015) and estimated single dish system temperatures (T_{sys}) at 1.5 GHz. The estimated T_{sys} were provided courtesy of Dr. Tom Muxlow and Dr. Robert Beswick (private communication). The telescope gains were obtained from Diamond et al. (2003).

Antenna	Diameter (m)	Telescope Gain g (Jy K^{-1})	Estimated T_{sys} (K)
Lovell	76.2	1.1	∼55
Mark II	24.0	10.0	∼40
Knockin	25.0	9.9	∼45-55
Defford	25.0	9.5	∼35-40
Pickmere	25.0	9.9	∼45-55
Darnhall	25.0	9.9	∼45-55
Cambridge	32.0	6.0	∼40

Table 3.3: The e-MERLIN (e) and JVLA observations for targets observed for this thesis.

Target	Band	Centre ν (GHz)	Array	Channels per SPW	Channels Avg.	SPW	Epoch	τ (hrs)	rms expected (μJy)	HA min (hours)	HA max (hours)
3C 334	L	1.5	e	512	64	8	2015/04/04	10	12	−10	0
3C 334	L	1.5	JVLA	64		16	2015/07/22 2015/12/01	2	74	−1.1 1.6	−0.1 2.6
3C 263	L	1.5	e	512	64	8	2016/12/25	12	6[a]	−12 11	−1 12
3C 263	L	1.5	JVLA	64		16	2012/07/25 (B) 2012/12/02 (A)	2	74	3.5 3.6	4.5 4.6
Cyg A	L	1.5	e	512	64	8	2017/01/09	11	12	−9 4	−2 12
Cyg A	C	5.5	e	256	128	4	2017/07/28	10	13	−9.5	9.8

[a] The sensitivity is improved for 3C 263 due to the inclusion of the Lovell telescope during the observation. Sensitivity can be determined from Eqn. 2.21 in §2.

The e-MERLIN pipeline for Astronomical Image Processing System (AIPS) can automate all steps in the calibration process from loading the data up to self-calibration. The pipeline begins by providing an input file with a list of parameters telling AIPS which tasks to run using ParselTongue, a Python interface for running AIPS tasks. For 3C 334 only the beginning steps for preparing the data for calibration were executed. The initial pre-calibration pipeline tasks executed included the following:

- Loaded the FITS files of the data into AIPS using FITLD.
- Applied a flag mask with all channels known to be affected by RFI with UVFLG.
- Averaged the data in frequency to 128 channels from 512 channels.
- Produced diagnostic plots of amplitudes and phases prior to flagging with SERPent as shown in Fig. 3.6.

L-band is greatly affected by RFI, thus reducing the sensitivity of observations. To reduce the time spent removing bad data, some of the RFI were flagged using SERPent. SERPent, an acronym for *Scripted E-merlin Rfi-mitigation PipelinE for iNTerferomerty*, is an automated flagging tool developed for the Low-Frequency Array, or LOFAR (LOFAR Collaboration, 2013), but helpful for any bands and arrays suffering from strong RFI (Peck & Fenech, 2014). Serpent is integrated into the pipeline and was used before beginning the final pre-processing step in the pipeline: concatenating the data by time and frequency into one file using DBCON (Argo, 2015).

After using the pipeline for pre-processing the data, the tedious task of manually flagging the data began. Data were flagged using QUACK to remove the first 5 seconds of each scan. Due to the slewing of the telescopes between the sources, antennas may still be off source at the beginning of scans. Removing a small interval of a few seconds at the beginning of each scan removes bad data from this off-source time. The beginning and end channels required flagging as well. Ideally the observed bandpass of the spectral window will resemble a top-hat function - a flat response over the interval between the highest and lowest frequencies with a sharp, perfect cutoff to zero at the ends. This, however, is not the case. The signal at the ends will attenuate but will not cut off completely to zero. The task UVFLG was used to remove five channels at the beginning and

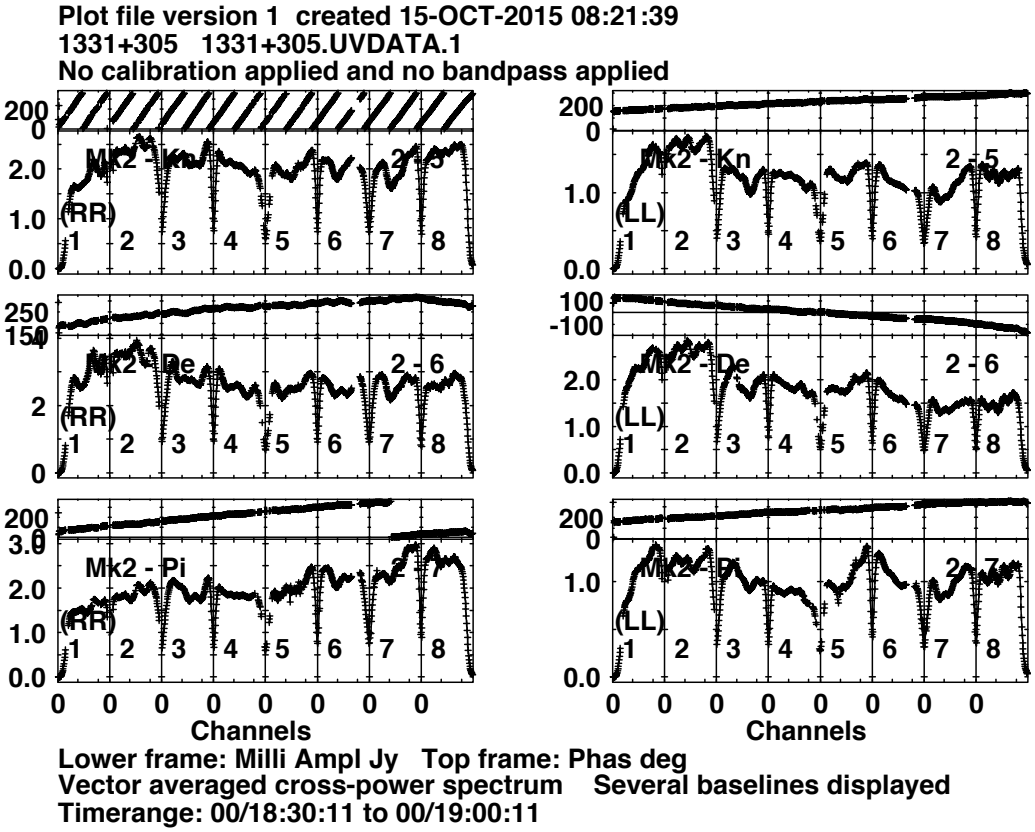

Figure 3.6: Pre-flagging diagnostic plots of calibrator 1331+305 created using the AIPS pipeline. This calibrator was used for flux density calibration for the target 3C 334.

the end of each bandpass for this band edge roll-off. A correction to the data to produce a flatter response is applied in a later step.

Even small amounts of RFI can lead to imperfections in the calibration steps that may have damaging effects during the self-calibration process. Removing as much RFI as possible becomes important for high quality data. The flagging task SPFLG may be the most time consuming and interactive step in the data reduction process. The task SPFLG allows the user to have more control over the flagging of all remaining RFI embedded within good data by using an interactive editing tool. Data were plotted on grids of time versus spectral channel for each baseline/polarization pair with varying levels of pixel brightness to indicate areas of change in amplitude or phase (see Fig. 3.7). Pixels with extreme high or low values were removed during this step. AIPS stores the user selected pixels

containing RFI in a table of flags. Calibrators and the target were flagged separately in one hour blocks with 1 second averaging, creating a new flag table each time. Due to limitations on the number of flags in a table that AIPS can handle without problems, the task UVCOP was used once after the flag table reached many thousands of entries to create a new copy of the data file with flags applied. Flagging then continued on the copied data set with the task SPFLG until it became apparent that flagging could no longer be improved by visual inspection.

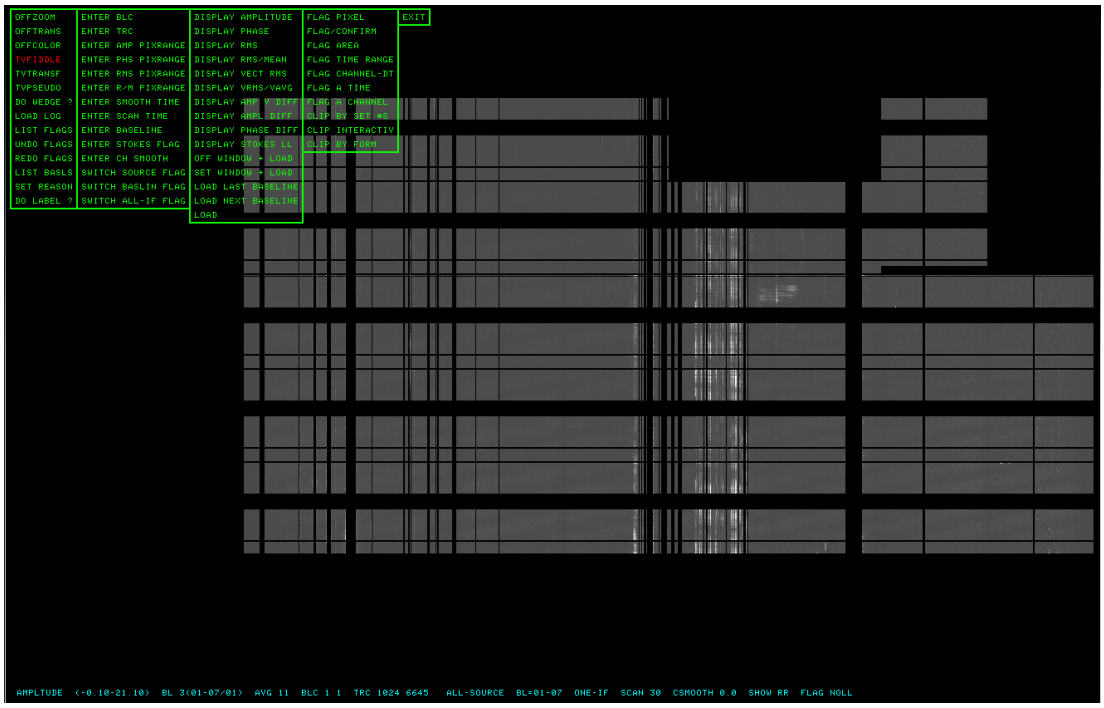

Figure 3.7: An image taken of SPFLG in AIPS. Some areas have been removed by SERPent and UVFLG. The bright contrasting pixels indicate RFI that must be removed.

After flagging the process of calibration began. Calibrators observed during this observation were:

- 3C 286 (1331+305): Often used as a flux calibrator for its well constrained flux. This is e-MERLIN's standard flux calibrator.
- 3C 84 (0319+415): Provided as an additional bandpass calibrator.
- 1407+284 (OQ208): A bright, flat spectrum source used as e-MERLIN's standard bandpass calibrator.
- 1611+1856: An unresolved source near the target used for phase calibration.

The first steps of calibration began with the task FRING to correct for delays expressed as phase displacements in the radio data. Delays are introduced from various external sources including but not limited to: wavefronts arriving at each antenna at different times due to the geometry of the Earth or atmospheric influences; elevation differences between antennas; or introduced through instrumental effects such as temperature changes. In the case of e-MERLIN data, the task FRING is used to correct for differential delays introduced from the atmosphere. Because delays can vary with time, e-MERLIN's delays must be corrected throughout the observation run and corrected as a function of time (Argo, 2015). By fitting delays over all SPWs in all calibrators, a set of corrections in the range of tens of nanoseconds were produced and written into a solution table (SN) with the task FRING. The SN table was then written into a calibration table (CL) using the task CLCAL (van Diepen and Farris, 1994).

In Ch. 2 the process of converting a signal into visibilities is discussed. The correlator, the component of the array that multiplies voltages induced by the signal at two antennas to produce visibilities, can only process the phase and amplitude information provided by the electronics. The amplitude of the visibilities needs to be scaled so that the data represents the sky brightness. To do this, the flux density of 3C 286 was scaled by using a model of the source provided by the e-MERLIN team. The raw flux density was scaled to match the flux densities in the model at each frequency. The flux densities were derived from the model using the task CALIB and then applied to the flux calibrator. The task GETJY is then used to pull the calculated corrections from the flux density calibrator and apply them to the secondary calibrators (1611+1856, 0319+415, and 1407+284). A new source table (SU) containing the bootstrapped flux densities in Stokes I and a CL table (from the task CLCAL) containing corrections in gains of all calibrators were created (see Table 3.4).

After a spectral and spatial model was inserted for 3C 286, and flux densities of all calibrators were bootstrapped, a preliminary bandpass calibration was done. Bandpass calibration solves for frequency-dependent gains across the SPW. The task SETJY must be done prior to bandpass calibration so that the spectral behavior can be determined and all that remains is the unknown response of the receiver. Generally bandpass gains are time-independent, though they may show slight time-dependency during the observation. The task BPASS solves for amplitude and phase corrections per scan by breaking apart baseline-based

Table 3.4: Output of flux densities in Stokes I for all calibrators in the 3C 334 e-MERLIN observation.

Channel Frequency ν (GHz)	3C 286 (Jy)	1611+1856 (Jy)	1407+284 (Jy)	0319+415 (Jy)
1.25	15.97	0.14	0.82	14.48
1.31	15.58	0.14	0.85	15.86
1.38	15.21	0.14	0.92	14.57
1.44	14.86	0.14	0.99	14.10
1.51	14.52	0.13	1.06	14.38
1.57	14.21	0.13	1.13	14.02
1.63	13.91	0.13	1.20	13.89
1.70	13.62	0.13	1.27	13.69

frequency dependent functions into antenna-based functions. With the newly created tables containing corrections to the amplitudes and phases, 3C 334 was extracted into a single-source file using the task SPLIT. The split data were used for imaging. Imaging of 3C 334 will be discussed later in this chapter.

While it was strongly hoped that polarization calibration would be done on the e-MERLIN data, the experimental and uncertain quality of polarization calibration for e-MERLIN at the time meant it was not included in the work for this thesis.

3.2.2 3C 334 A & B array JVLA Data

The Very Large Array (VLA) was created in the 1970s as a 27 element interferometer that can observe at frequencies between 74 MHz and 50 GHz. Each parabolic dish has a 25 m diameter[1]. In 2010 major upgrades were installed that improved the sensitivity and bandwidth of the array. Upgrades included the installation of the Wideband Interferometric Digital ARchitecture (WIDAR) that expanded the observing bandwidth from 100 MHz to 8 GHz in each polarization and provides complete coverage between 1 and 50 GHz (Perley et al., 2011). Any observations taken prior to the expanded VLA upgrade in 2010 will be referred to as VLA data. All observations post the upgrades are referred to as the JVLA.

The JVLA provides additional crucial data that cover the shorter baselines required for the e-MERLIN Jets Legacy Project. JVLA data were necessary to

[1]http://www.vla.nrao.edu

minimise problems associated with resolved-out large extended emission from e-MERLIN's missing short spacings. Observations corresponding to the two highest resolutions were done at L-band: A configuration (baseline extends from 0.68 km to 36.4 km) and B configuration (baseline extends from 0.21 km to 11.1 km). The shorter baselines found in A and B configurations allow large extended emission to be sampled and prove to be excellent complementary arrays to the e-MERLIN array. Resolution at L-band for the JVLA array range from approximately 1 arcsec (A array) to approximately 4 arcsec (B array). JVLA observations of 3C 334 were done for a total of approximately 1 hour on source observing time in two epochs: 22 July 2012 (B configuration) and 01 December 2012 (A configuration) (see Table 3.3). The following section will discuss the steps taken during the data reduction process of the JVLA data.

3C 334 JVLA L-Band Calibration

The steps taken for calibrating A and B arrays were mostly identical and so will be described simultaneously. Any differences in procedures between the A and B configurations will be noted. JVLA data were calibrated using the package Common Astronomy Software Applications (CASA) version 4.7.0 developed with the support of the National Radio Astronomy Observatory (NRAO). Unlike AIPS, CASA's default data format is a measurement set (MS). Using the task BROWSETABLE reveals the subtables included in the MS. Some of the tables included in a MS are:

- ANTENNA: Lists antennas used during the observation and their position in the array.
- HISTORY: Records changes made by the user during calibration.
- POINTINGS: Includes information on telescope pointings.
- SPECTRAL WINDOW: Information regarding the spectral windows of the JVLA array.
- FLAGCMD: Keeps a running table of all flagged data in the measurement set.

Calibration of the JVLA data began with an inspection of the data. The task LISTOBS provided a complete list of observation details such as antennas, scans,

fields observed, and phase centre details. Sources observed for both A and B configuration data included:

- 3C286 (1331+305): Flux and bandpass calibrator for the JVLA.
- J1553+1256: Phase calibrator for the JVLA.
- 3C334: A bright FR II quasar which was the target of interest for this observation.

PLOTMS in CASA is an important, interactive tool for examining both uncorrected and corrected data and applying flags. From PLOTMS it was noted that as with the e-MERLIN data, the first 5 seconds needed to be flagged to account for telescope slewing time. To ensure the measurement set would not be corrupted, the task FLAGMANAGER was used to save a backup copy of the initial state of flags. With the task FLAGDATA, mode set to 'quack', 5 seconds were removed at the start and end of each scan. Setting mode to 'manual' in the task FLAGDATA, the first 5 and last 5 channels were removed on all SPWs.

Antenna-based phase slopes across the bandwidth need to be removed early. This is especially important to do prior to Hanning smoothing data. Significant delays may de-correlate the amplitudes during this step. If corrections are made after Hanning smoothing the data, there is a greater risk of creating a larger de-correlation effect. An example of phase slopes observed in data is shown in the phase versus channel plot from PLOTMS provided in Fig. 3.8. The sub-bands in the JVLA normally have different delays. The delays are calculated from fast Fourier transforms (FFT) of the spectra on baselines including the reference antenna. Visually inspecting the data of 3C 286, an interval of 1 minute with minimal RFI was chosen from which to derive solutions. Using GAINCAL with GAINTYPE set to 'K' (delay), delays were solved and written into a calibration table for one value per SPW per polarization. The calibration table produced is applied using the task APPLYCAL to eliminate gradients in the phase across channels. Figure 3.9 shows the data after the corrections for the phase slopes have been applied. After delay corrections the task HANNINGSMOOTH was used to help smooth the data.

The task FLAGDATA was run with mode set to 'manual' to remove the first scan, field 0. Field 0 in JVLA data is known as a dummy scan and provides time for the array to move to its first calibration source. Each calibrator was flagged

separately and by SPW using mode 'rflag' (Greisen, 2003) in FLAGDATA until no obvious outliers or jumps were seen in PLOTMS. At this point the calibrators were flagged enough for calibration to begin.

The MS will contain three columns of visibilities: DATA, CORRECTED, and MODEL. Before calibration is applied the CORRECTED column is equal to DATA and the MODEL column is set to all ones. Using the flux calibrator 3C 286, amplitudes and phases in Stokes I were scaled using models provided within CASA for JVLA using the task SETJY. An initial gain calibration was done using the middle channels of each SPW for 3C 286 in the task GAINCAL. Bandpass calibration of the flux calibrator followed using the task BANDPASS on all SPWs. Gain tables produced from GAINCAL were solved on the flux calibrator in phase only and then appended to include solutions for the phases of the phase calibrator. Another round of calibration tables produced from GAINCAL were then produced to solve amplitudes using the previous tables created from BANDPASS and GAINCAL. Fluxes from 3C 286 were bootstrapped to the phase calibrator using the task FLUXSCALE. To complete standard calibration, all calibrator tables were applied to the calibrators and the target using the task APPLYCAL. After successful calibration, 3C 334 was split from the multi-source MS into a single source file for imaging and self-calibration.

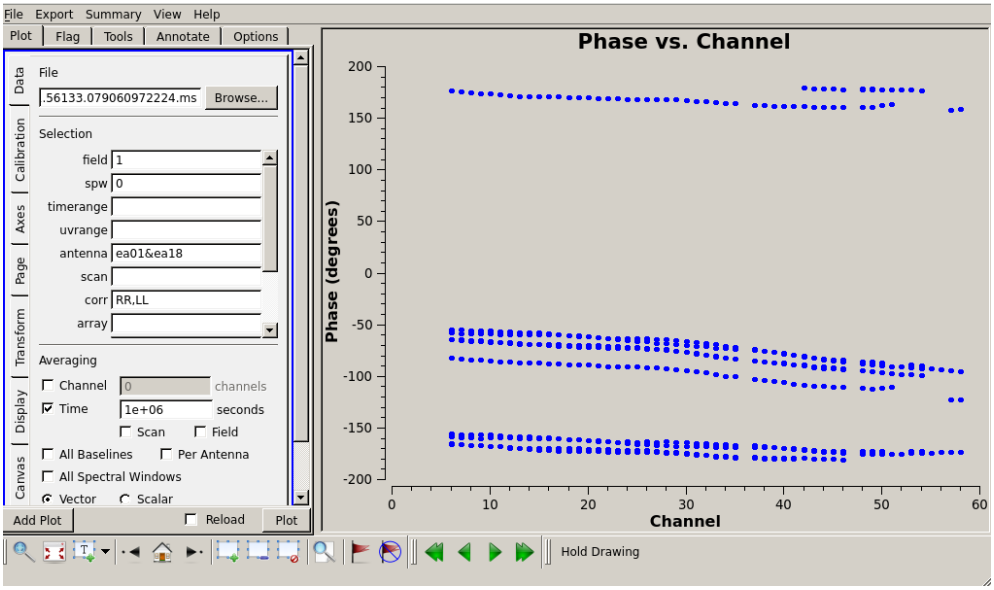

Figure 3.8: A screenshot of PLOTMS to show the antenna-based delays in phase as a function of frequency.

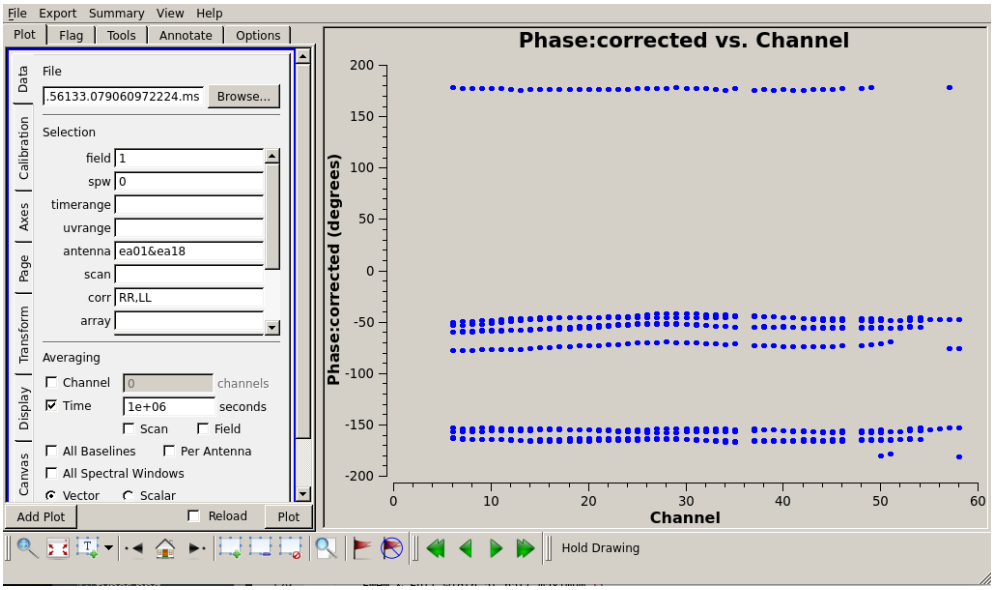

Figure 3.9: A screenshot of PLOTMS to show the corrected antenna-based delays.

3.3 Imaging 3C 334

3.3.1 Imaging e-MERLIN Data

The e-MERLIN observation of 3C 334 was initially imaged in AIPS using the task IMAGR. The task IMAGR provides users with a wide range of options for customising imaging based on the needs of the field. Options within IMAGR include altering the weighting of the telescopes, changing the dimensions of the restoring beam, and setting the phase centre of the fields. Within IMAGR the cell size was set to 0.02 arcsec, the full width at half maximum (FWHM) major axis of the restoring beam (bmaj) was set to 0.1 arcsec, and the FWHM minor axis (bmin) was set to 0.1 arcsec. Without setting bmaj and bmin IMAGR will fit a Gaussian CLEAN beam to the central portion of the dirty beam. However, this poses a problem for e-MERLIN data since the e-MERLIN array typically produces a highly elliptical dirty beam from the predominantly east-west baselines. The fitted beam was $0\farcs26\times0\farcs12$. Details of the parameters given to IMAGR, or CASA's equivalent task CLEAN, are provided in Table 3.6 in §3.8. From Bridle et al. (1994a), it was known that two confusing sources were located near 3C 334. The first, which I will refer to as confusing source 1 (CS1), was an 88 mJy confusing source located at (B1950.0) $16^h18^m18\fs96$, $+17^\circ47'01''$(Bridle et al., 1994a). The second identified confusing source was a 1.8 mJy compact source located at (B1950.0) $16^h18^m4\fs86$, $+17^\circ44'14\farcs1$, from here on referred to as CS2. The B1950.0 coordinates were converted to J2000 coordinates and a test image was made to verify the coordinates of the sources: CS1 was located at (J2000) $\alpha = 16^h20^m33\fs432$, $\delta = +17^\circ29'55\farcs49$; CS2 was located at (J2000) $\alpha = 16^h20^m19\fs375$, $\delta = +17^\circ37'7\farcs57$. Separate fields were imaged for CS1 and CS2 to subtract effects introduced to the target field (see Fig. 3.13). Five fields with an image size of 2048 × 2048 pixels were imaged in total: a field for each of the confusing sources (CS1 and CS2), one for the core, one for the southern jet, and an additional field for the counterjet and northern hotspot. Phase self-calibration was completed 10 times and 10 rounds of phase and amplitude self-calibration were done using maps produced by IMAGR as a model using the task CALIB. The resulting clean maps are shown in Figs. 3.10−3.13. Despite efforts to remove artifacts in the field through the twenty rounds of phase and amplitude self-calibration, calibration errors remained present in the fields near

the core and the confusing source. Sidelobes were also visible around the northern hotspot. The remaining artifacts were a product of the standard CLEAN algorithm's inability to deconvolve extended emission (see Ch. 2). The rms noise reached 44 μJy and a dynamic range of 2,909 was achieved. At this point the calibrated e-MERLIN data were exported as a FITS file and loaded into CASA as a MS file to be multi-scale cleaned, imaged, and combined with the JVLA data.

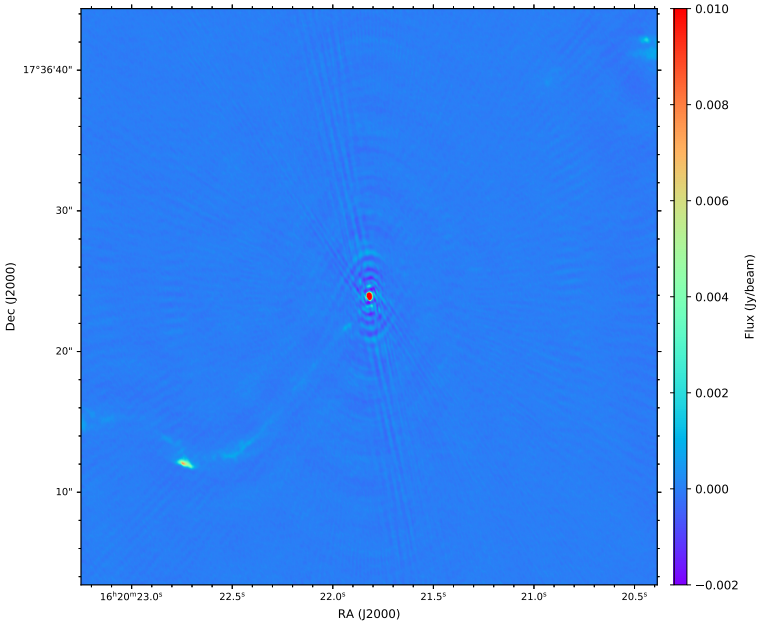

Figure 3.10: The e-MERLIN map of 3C 334's core, jet, and part of the northeast hotspot produced by IMAGR in AIPS after phase and amplitude self-calibration. Image was reproduced in Python. Calibration errors can be seen around the core of the quasar.

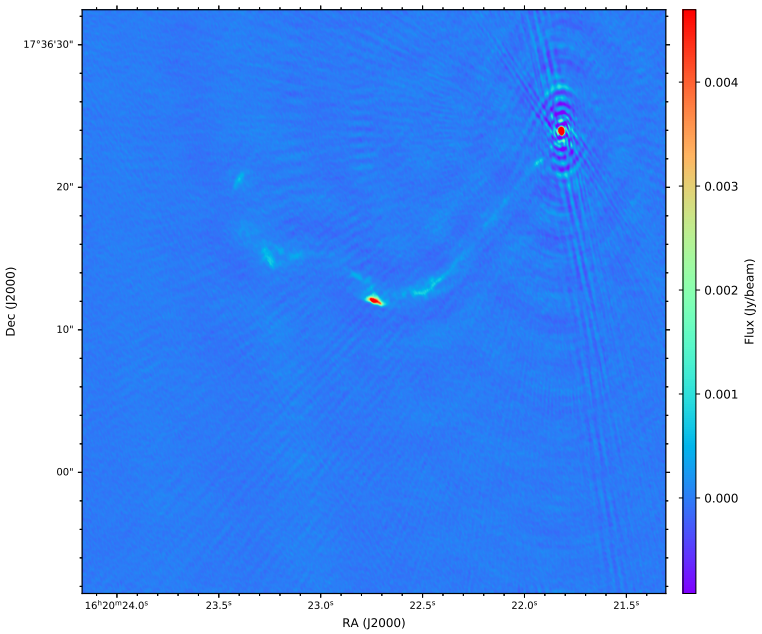

Figure 3.11: The e-MERLIN map produced by IMAGR in AIPS of 3C 334's jet and core. Image was reproduced in Python.

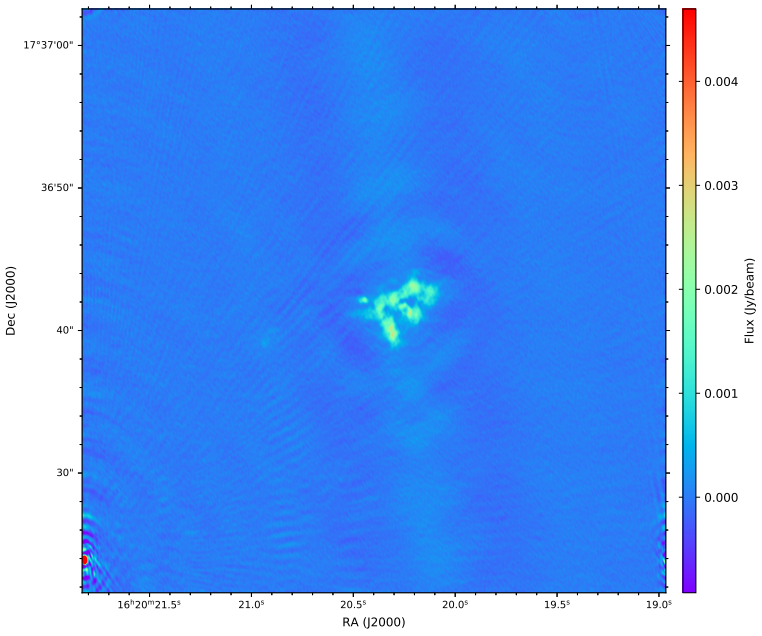

Figure 3.12: The e-MERLIN map produced by IMAGR in AIPS of 3C 334's northern hotspot located on the counterjet side. Image was reproduced in Python.

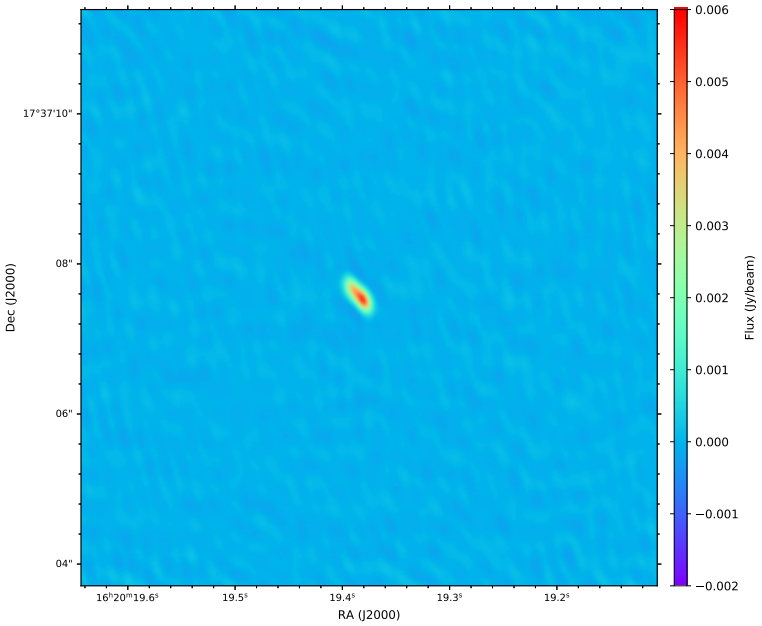

Figure 3.13: The e-MERLIN map produced by IMAGR in AIPS of the confusing source 2 (CS2) located near the north lobe in 3C 334. Calibration errors remain present in the field. Image was reproduced in Python.

An improvement was made to the e-MERLIN maps using the task TCLEAN in CASA. The task TCLEAN was implemented into CASA starting in version 4.7 as a replacement to the traditional CLEAN task. A few improvements made in TCLEAN include having the option to select the data column to image (data or corrected), re-labeling some parameters to make it clearer to the user, and allowing the user to restart an image from the previous input image by specifying "restart=True". The most important upgrades for the quasar data was the combining of multi-frequency CLEAN with multi-scale CLEAN into MS-MFS (see §2.4.3) (Rau and Cornwell, 2011) and the ability to CLEAN two MSs together. MS-MFS streamlines the two independent parameters to reconstruct both spectral and spatial structure of the visibilities (Rau and Cornwell, 2011). Within the task TCLEAN the MS-MFS algorithm was used to deconvolve using both a delta-function, which is the standard clean procedure, and circular Gaussians at different pixel scales. Determining the correct scales to use proved to be a challenge due to the highly elliptical beam shape produced for the e-MERLIN array in TCLEAN. Multi-scale CLEAN was determined by the minor axis of the FWHM of the beam. Ideally scales (the diameter in units of the number of pixels used) should be chosen as a point source (0), on the order of the dirty beam, and

then three to five times the beam size. For 3C 334 multi-scale was set to pixel scales of [0,6,18] that correspond to a point source, the dirty beam size, and three times the beam-size. The number of Taylor terms solved for was 2. The cell size remained 0.″02. A 0.″23 × 0.″12 CLEAN beam with a PA of 28.°0 was used. Using MS-MFS clean produced a map of 3C 334 that reduced the rms noise to 55 μJy beam^{-1} and smoothed some of the calibration errors that remained after imaging in AIPS (see Figs. 3.14 and 3.15).

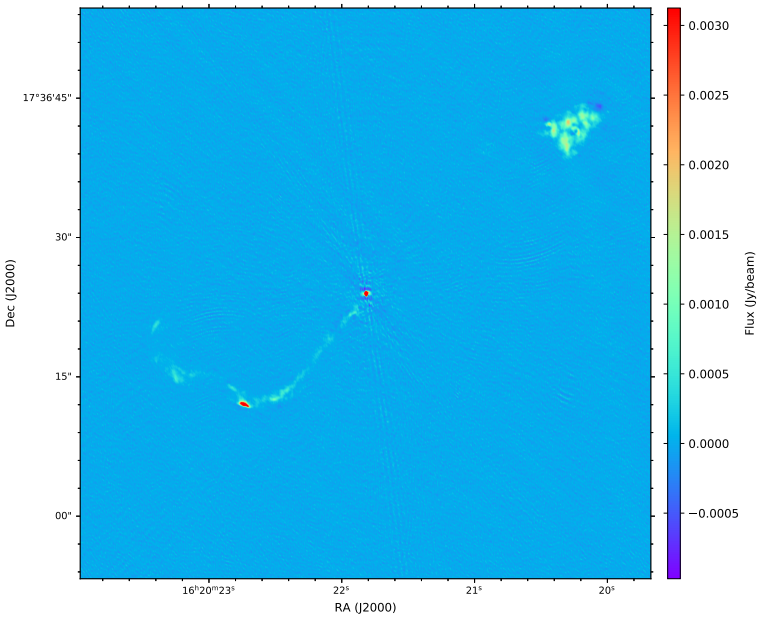

Figure 3.14: The e-MERLIN map produced in CASA with the task TCLEAN. Using multi-scale clean removed some of the calibration errors that were limiting the image fidelity. Sidelobes from the limited *uv* converage remained. Image was reproduced in Python.

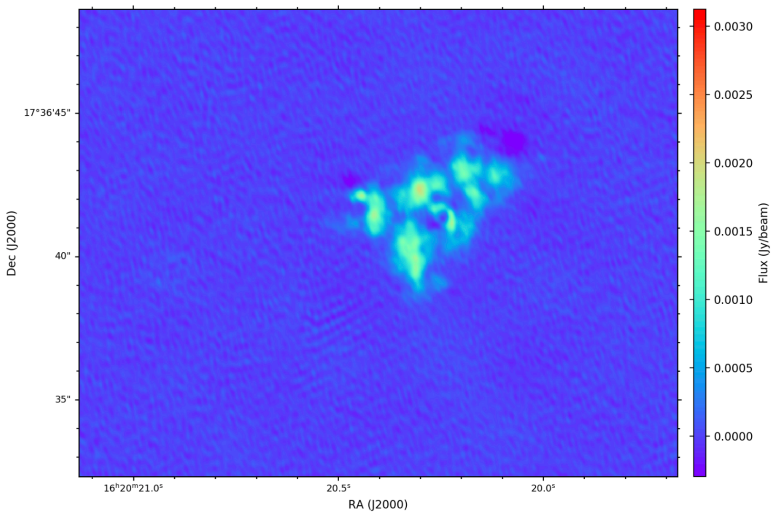

Figure 3.15: A closeup e-MERLIN map of 3C 334's northern hotspot produced in CASA. Negative bowls remain due to missing short spacings in the e-MERLIN array. Image was reproduced in Python.

3.3.2 Imaging JVLA Data

The JVLA observations were cleaned and imaged in CASA using TCLEAN. Data observed using the A configuration were cleaned and imaged while using Briggs weighting with 0.0 robustness and a cell size set to $0\farcs25$. Three rounds of phase self-calibration and three rounds of amplitude calibration reduced the rms noise to 56.23 μJy beam^{-1} away from the nucleus. The beam size of the clean beam was $1\farcs03 \times 0\farcs92$ with a PA of $22\fdg92$. Data observed in B configuration were imaged with cell size set to $0\farcs75$ and using Briggs weighting with a robustness of 0.0. The rms noise was 123 μJy beam^{-1}. The restoring beam size was $4\farcs78 \times 3\farcs34$ with a PA of $55\fdg3$. A and B configuration data were amplitude self-calibrated three times using GAINCAL in CASA. Final images produced by CLEAN can be seen in Fig. 3.16 (A configuration) and Fig. 3.17 (B configuration).

3.3.3 Imaging Combined e-MERLIN with JVLA Data

Separate amplitude and phase self-calibrations for each array were followed by the creation of maps using all of the observations. Prior to this, the visibility weighting needed to be adjusted so that the JVLA data did not dominate and lower the resolution of the maps. Weighting before adjustments were originally

set to nearly 1,000 for the e-MERLIN data and scaled to approximately 2.0E6 for the JVLA data. The CASA toolkit proved to be a useful tool to adjust the weight scale of the JVLA data so that the e-MERLIN array became the primary beam setter. A Python script was used to read in the weights from the data column and rewrite these values. Weights were determined by experimenting and testing the result. A visual inspection of the re-scaled weights was done by producing an image until the desired resolution was achieved. The final weights of the JVLA data were set to nearly one-fourth the e-MERLIN weights.

After re-scaling the weights of the visibilities I attempted to use the task CONCAT to concatenate the data from the e-MERLIN and JVLA arrays. The combined MS of the e-MERLIN and JVLA arrays was cleaned using Briggs weighting with -0.5 robustness and a widefield gridmode. The cell size was set to $0\farcs02$ to be consistent with the e-MERLIN imaging strategies. In the combined e-MERLIN and JVLA 2048×2048 maps, the rms noise reached 68.21 μJy. Images produced from the combined MS had phase errors that extended out near the core. It was apparent from the negative bowl surrounding the core and from attempts to obtain transverse profiles across the jet, the arrays were not aligning properly. It was determined that the task CONCAT resets phase information to the original measurement set source phase centre. All phase information derived during self-calibration of each array was lost. The misalignment of the cores resulted in one peak at the core for the e-MERLIN array and one peak from the JVLA arrays. CLEAN was attempting to deconvolve with the two peaks on different pixels. This resulted in the negative bowl on the southeast side of the core. Using the combined MS from CONCAT was abandoned once this was confirmed.

Observing a source at different epochs and resolutions provided additional complications during imaging. AGN cores are typically variable. Changes in the flux over many years is not unusual. Also, at higher resolution some of the flux begins to be resolved out, leading to variations in the core flux. To correct for the differences in the core's flux between the data, the e-MERLIN data were smoothed to the JVLA resolution. Separate Gaussian fits over the core in the JVLA image and the e-MERLIN image confirmed that the peak of the core in the e-MERLIN image was 128 ± 1.5 mJy/beam and the peak of the JVLA image was 177 ± 0.74 mJy/beam. The CASA toolkit was used to add flux to the brightest pixel in the e-MERLIN data so that it would have the same value as the JVLA data. Doing this removed ambiguity over which pixel is the brightest and which

values to fit a Gaussian over during the CLEAN process.

To produce the best quality map, the task TCLEAN was used to simultaneously CLEAN the visibilities from the e-MERLIN MS and the separate JVLA A&B configurations MS. Doing this produced a map as if the data sets were concatenated. Parameters in TCLEAN used for this image included multi-scale clean with scales set to [0,8,25,43], gridding set to widefield, robustness set to 0.0, and cell size set to $0\farcs02$. The result was a higher quality map with a beam size of $0\farcs29 \times 0\farcs14$ and a PA of $30\fdg5$. The rms reached 50.4 μJy. A well-collimated jet was visible (see Figs. 3.18 and 3.20). Comparing the northern hotspot in Fig. 3.19 to the map created of the e-MERLIN map alone (Fig. 3.15), it is apparent that the negative bowls previously observed are less prominent.

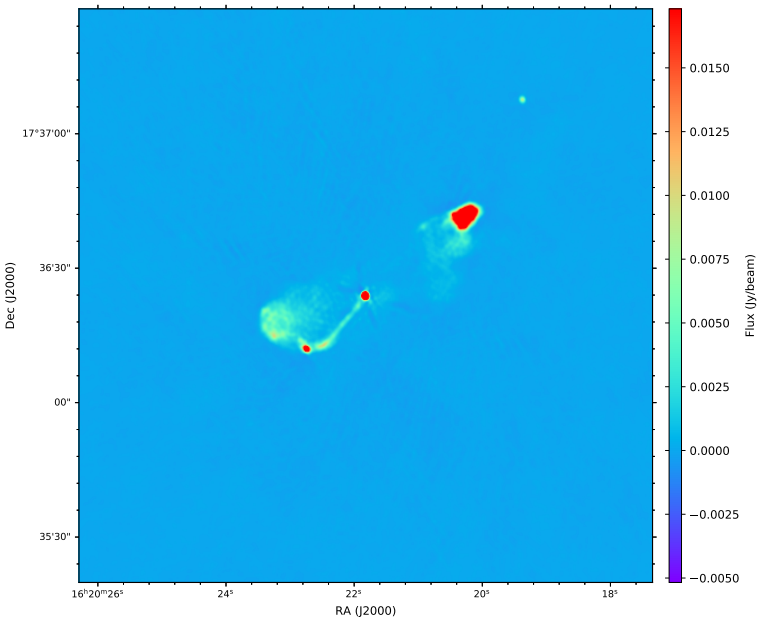

Figure 3.16: Image produced by CLEAN of 3C 334 from the JVLA A configuration data. Image was reproduced in Python.

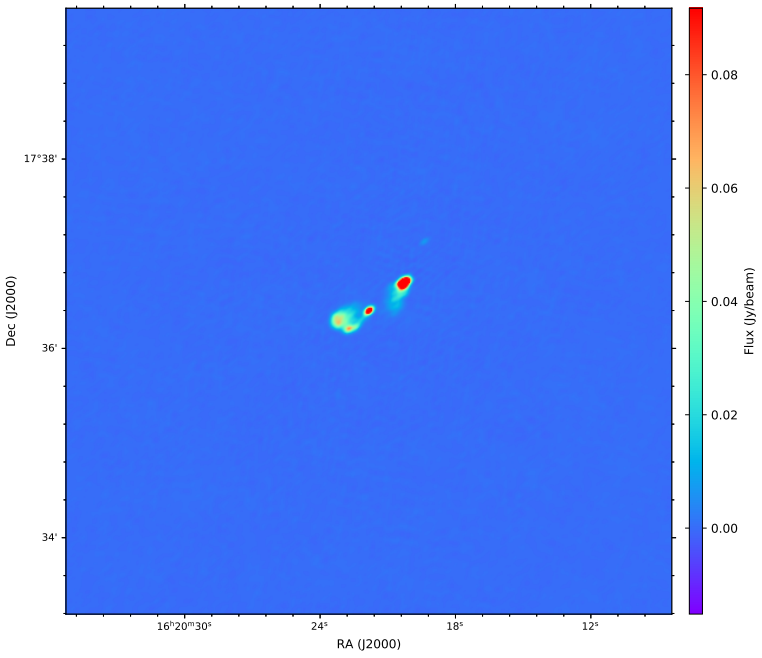

Figure 3.17: Image produced by CLEAN of 3C 334 from the JVLA B configuration array. Image was reproduced in Python.

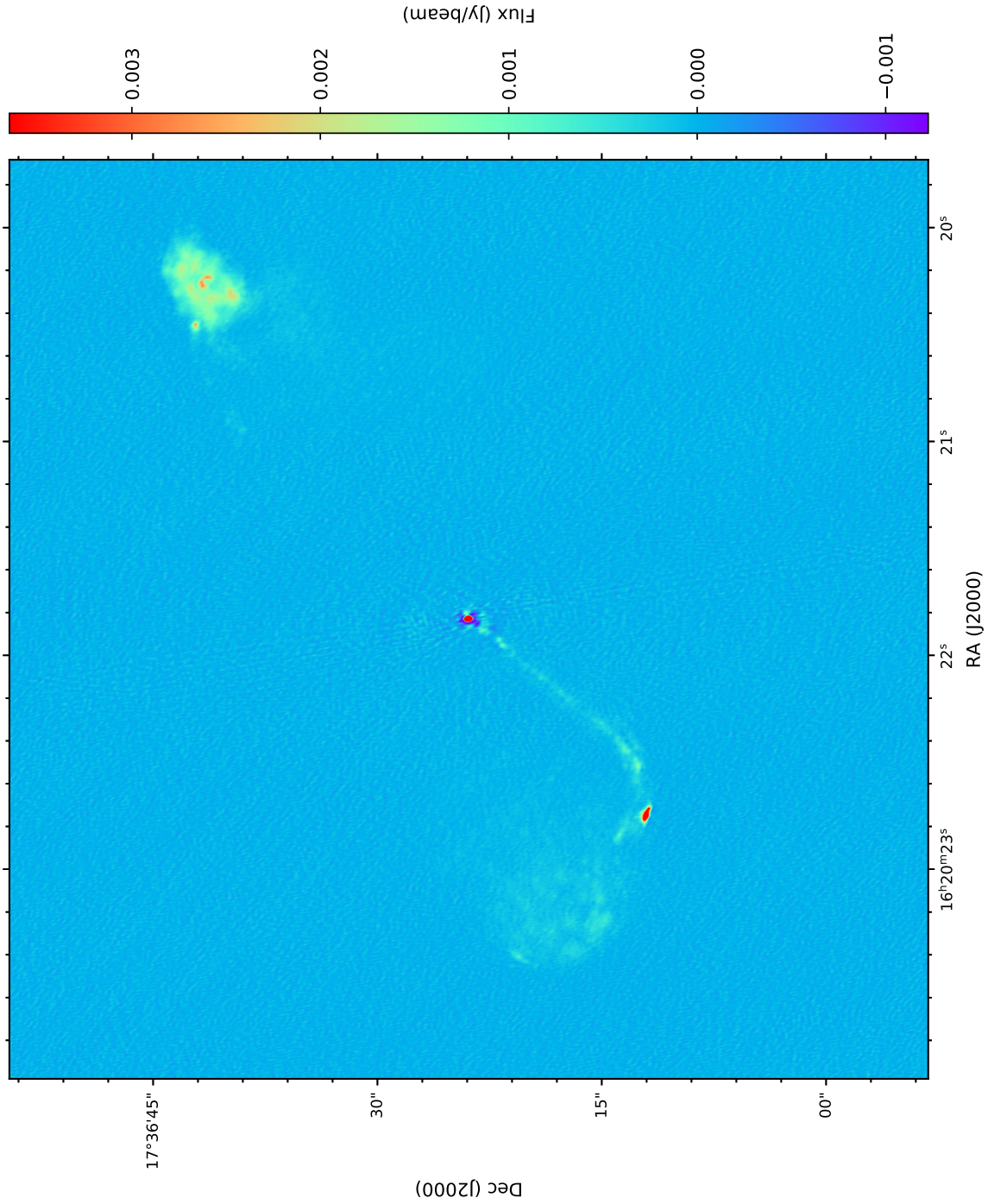

Figure 3.18: Final calibrated image of 3C 334 using both the e-MERLIN and JVLA arrays. Image was originally produced using the task TCLEAN in CASA. Image was reproduced in Python.

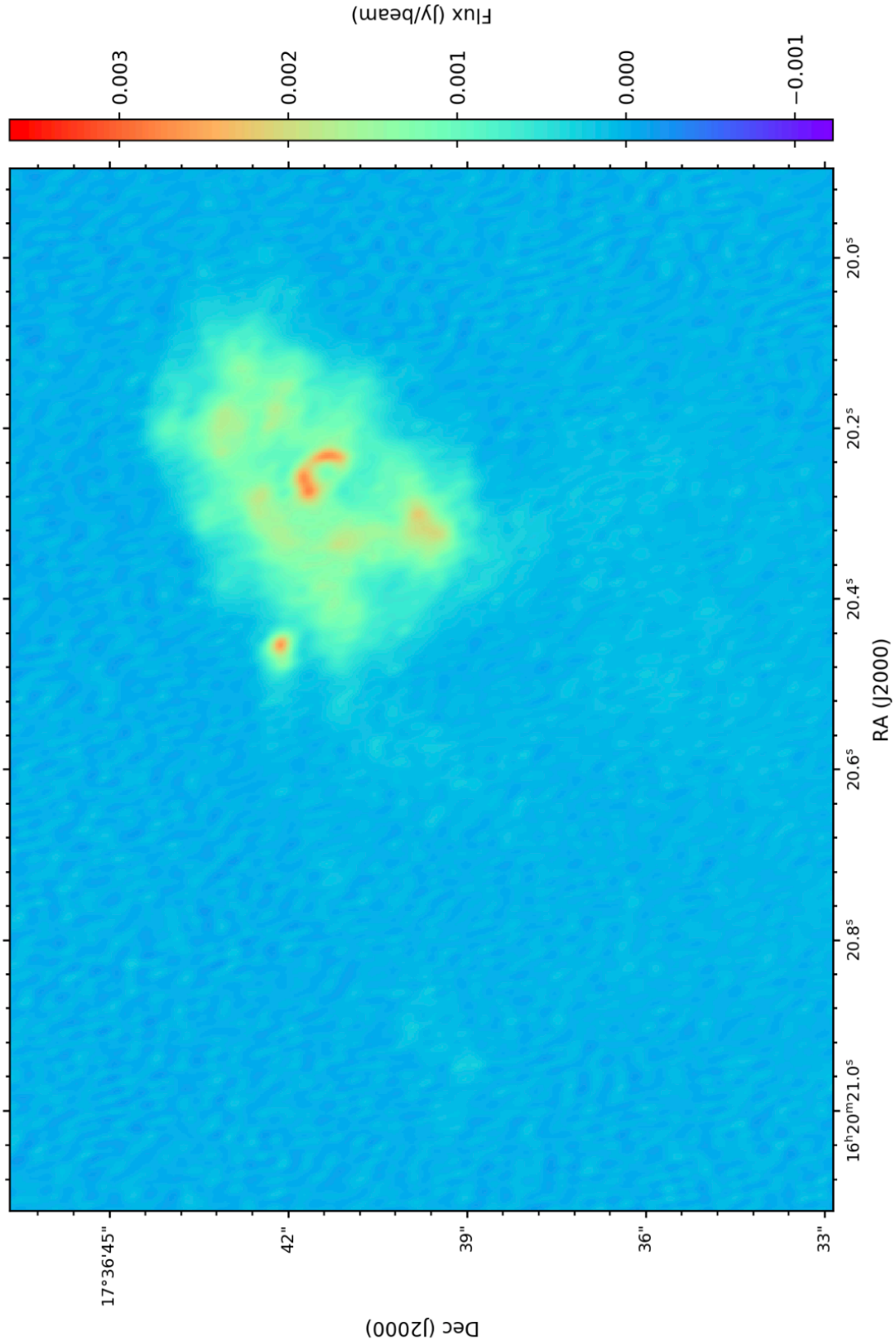

Figure 3.19: Final calibrated image of 3C 334's northern hotspot using both the e-MERLIN and JVLA arrays. Original image was produced using the task TCLEAN in CASA. Image was reproduced in Python.

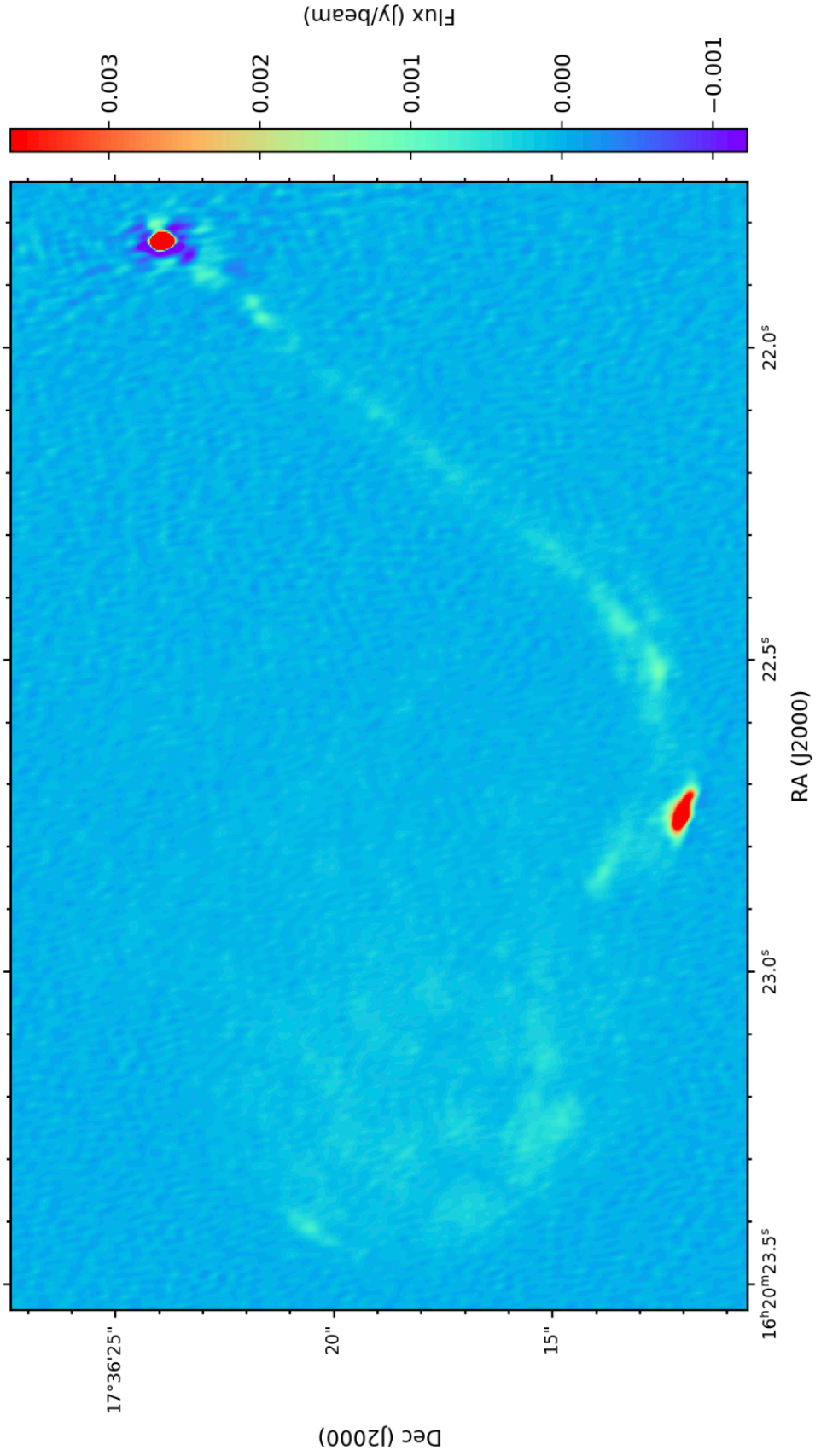

Figure 3.20: Final calibrated image of 3C 334's core and jet using both the e-MERLIN and JVLA arrays. Image was originally produced using the task TCLEAN in CASA. Image was reproduced in Python.

3.4 3C 263 Calibration

3.4.1 3C 263 e-MERLIN L-Band Calibration

Observations of 3C 263 with the e-MERLIN array took place on 25 December 2016 for a total of 12 hours (see Table 3.3). The full e-MERLIN array, including the Lovell telescope, were included in this observation. A plot of the e-MERLIN *uv* coverage is shown in Fig. 3.21. Sources observed during this run include:

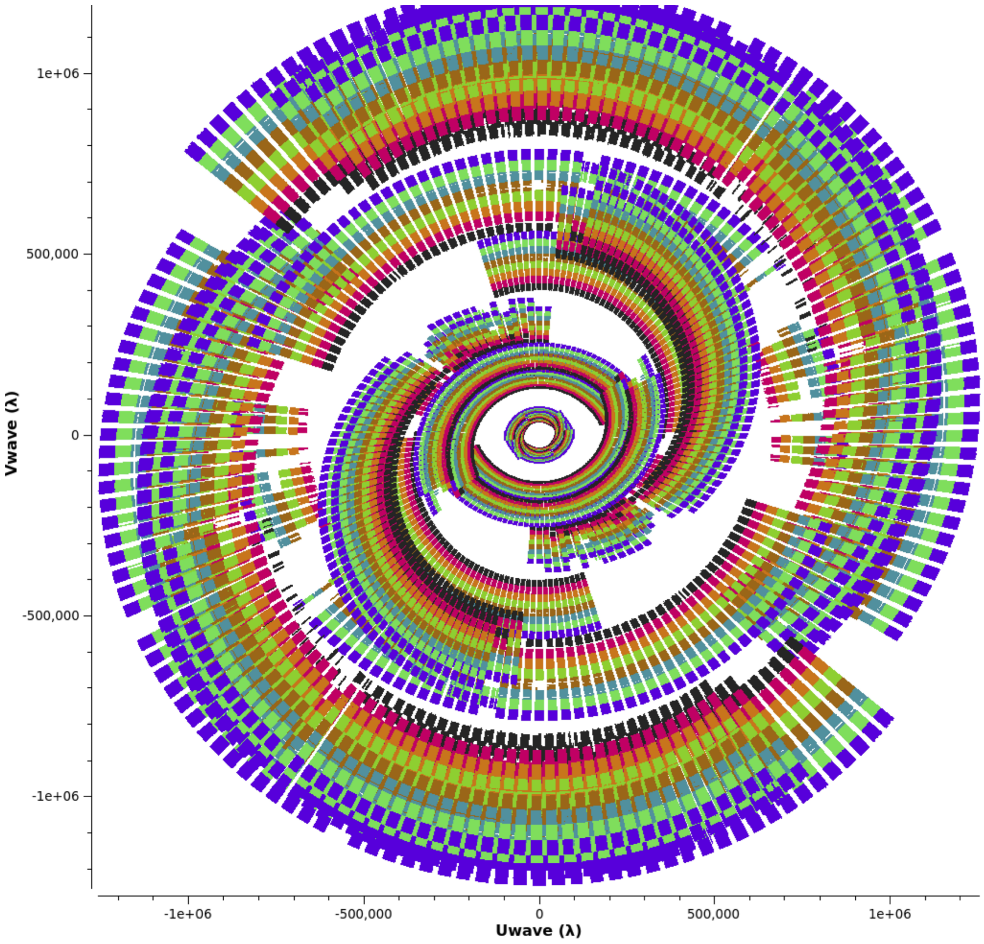

Figure 3.21: The *uv* coverage over the total observing time of 3C 263 with the e-MERLIN array. Each color represents one of the 8 SPWs in the e-MERLIN array.

- 0319+415: Polarization calibrator that was not used but was still calibrated.
- 1139+6547 (3C 263): A bright, FR II quasar that is the target in this observation.

- 1331+305 (3C 286): Standard flux density calibrator.
- 1141+6410: An unresolved point source used for phase calibration.
- 1407+284 (OQ208): Same bandpass calibrator as the 3C 334 observation.

At the time of receiving this data set the e-MERLIN CASA pipeline had been completed and was used to fully calibrate this observation. The same tasks used to calibrate the e-MERLIN data of 3C 263 were used to calibrate the JVLA data of 3C 334. A full description of the tasks can be found in Section 3.2.2. Additional tasks used in this data set will be described as needed. Steps in the e-MERLIN CASA pipeline can be split into two categories: pre-processing/data preparation and calibration. Beginning with pre-processing and data preparation, the pipeline accepted a FITS file input and returned a MS using the task IMPORTFITSIDI and a text file with the details of the observation from the task LISTOBS. On rare occasions the correlator does not record the u,v,w coordinates of a MS correctly. To correct this, the task FIXVIS was used to shift the raw data of the phase calibrator to the true phase centre position. Similar to the JVLA calibration steps, HANNINGSMOOTH was used to smooth the effects of bright RFI. An initial round of flagging was done using the task FLAGDATA to remove the first and last 5 channels of the SPW and the first and last 5 seconds of each scan. For the e-MERLIN array, the Lovell (Lo) − Mark II (MkII) was removed before calibration began. This baseline spans only 400 m, which is considerably shorter the next shortest baseline of 11 km. Diffuse structures on the Lo − MkII baseline cannot be fully recovered due to insufficient data (Peck and Fenech, 2013). Data were averaged to 128 channels per spw from 512 channels and 2 seconds integration time.

Pipeline calibration began with initialising a model in the task SETJY for 3C 286 using the model provided by the e-MERLIN team. The other calibrators were initialised with amplitude set to 1 and phase set to 0. The fluxes were then bootstrapped from 3C 286 to the other calibrators. Following this, an initial bandpass table was created using the task BANDPASS. In the CASA version 5.1.1-5 used for this data no task was available for global fringe fitting. It was determined that solving for delays using a time interval of 300 seconds in GAINCAL gave adequate S/N. Phase and amplitude gain corrections were also solved for using GAINCAL. Corrections were applied to the raw data using the task APPLYCAL. After applying the calibration tables to the data, the target was split into a single MS file and prepared for imaging and self-calibration.

3.4.2 3C 263 JVLA Calibration

Two observations of 3C 263 were done for this project. The A configuration data were taken on 02 December 2012 with 1 hour of on-source observing time. The B configuration observations were done on 25 July 2012 for approximately 1 hour of observations. Plots of the *uv* coverage are provided in Fig. 3.22 (A config.) and Fig. 3.23 (B config.). The following objects were observed for both A and B configuration:

- 1331+305 (3C 286): Standard flux calibrator for all targets in the project. Bandpass calibrator for JVLA data.
- J1048+7143: Unresolved point source that serves as the phase calibrator.
- 3C 263: The target FR II quasar.

Following the steps described in Section 3.2.2, calibration tables were created in CASA and applied to the raw data using the task APPLYCAL.

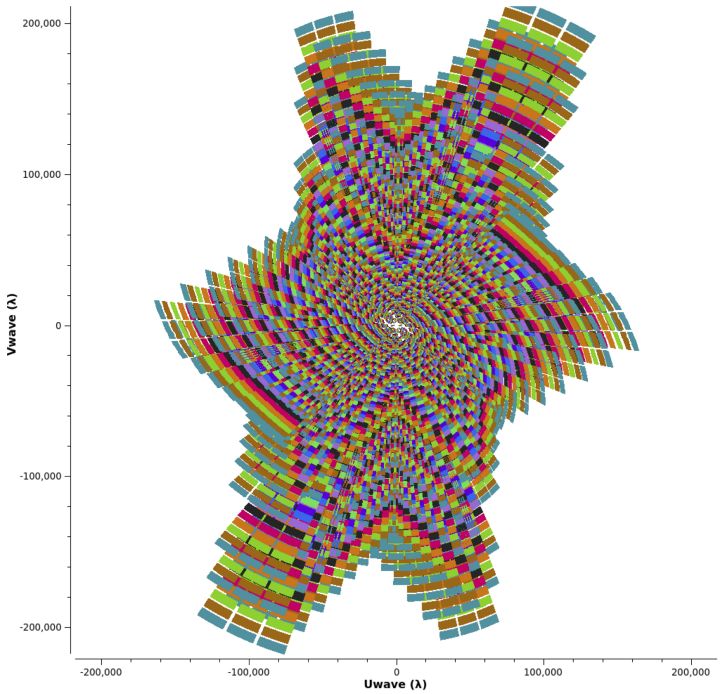

Figure 3.22: The *uv* coverage over the total observing time of 3C 263 with the A configuration of the JVLA array. Each color represents one of the 16 SPWs in the JVLA array.

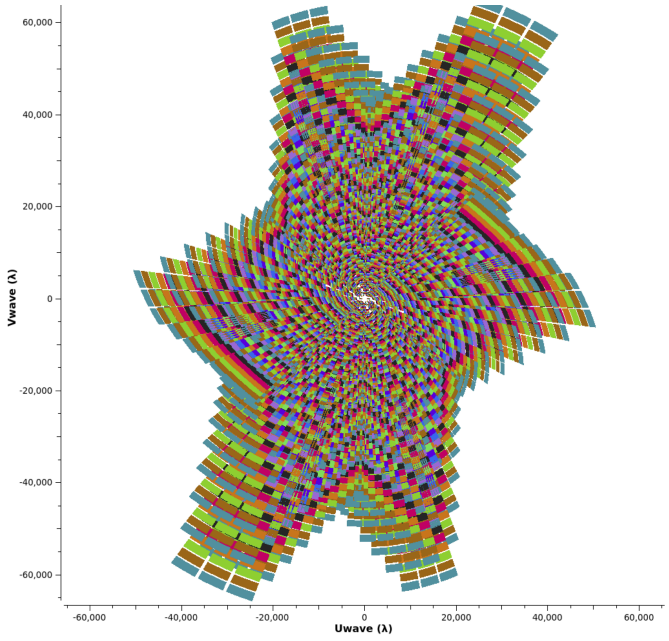

Figure 3.23: The *uv* coverage over the total observing time of 3C 263 with the B configuration of the JVLA array. Each color represents one of the 16 SPWs in the JVLA array.

3.5 Imaging and Self-Calibration of 3C 263

3.5.1 Imaging JVLA Data

The JVLA data for 3C 263 were cleaned and imaged with the task TCLEAN. Data from the A configuration were imaged with the task TCLEAN with the cell size set to $0\farcs2$. Briggs weighting with a robustness of -0.5 and multi-scale clean were used with scales set to [0, 2, 4, 8, 16]. Three rounds of phase self-calibration and three rounds of amplitude and phase self-calibration were done with a restoring beam of $1\farcs23 \times 0\farcs72$. The rms noise reached 157 μJy. The result of the A configuration self-calibration is shown in Fig. 3.24.

The task TCLEAN was used to image the B configuration data. Briggs weighting was used with a robustness of 0.0. Cell size was set to $0\farcs75$ for three rounds of phase self-calibration and two rounds of amplitude and phase self-calibration. For the third and final round of amplitude and phase self-calibration the cell size was set to $0\farcs2$ to prepare for self-calibration with the A configuration. Multi-scale clean was used with scales set to [0,6,19]. Restoring beam for the B configuration was $4\farcs4 \times 2\farcs8$ and the rms noise reached 145 μJy. The map produced from the B configuration self-calibration is shown in Fig. 3.25.

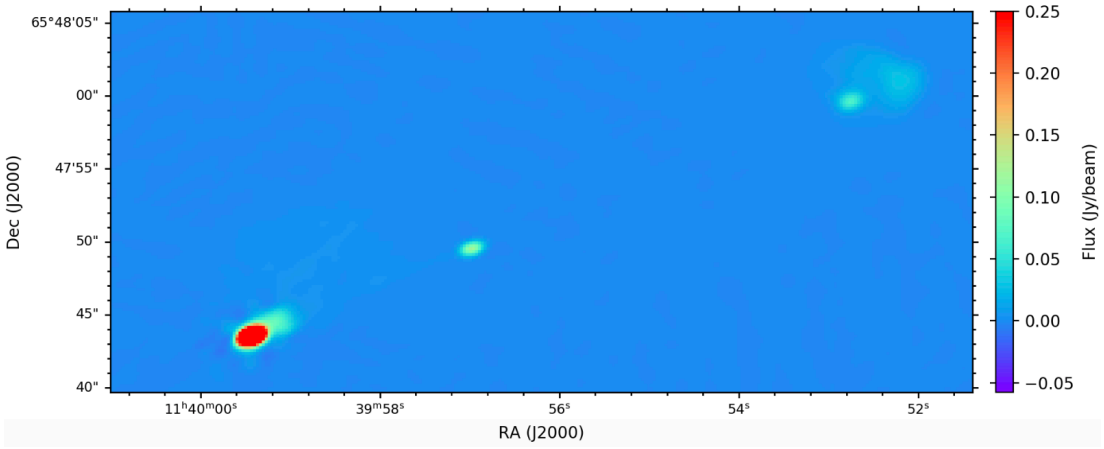

Figure 3.24: The JVLA A configuration map of the field 3C 263 produced with the task TCLEAN in CASA. Image was reproduced in Python.

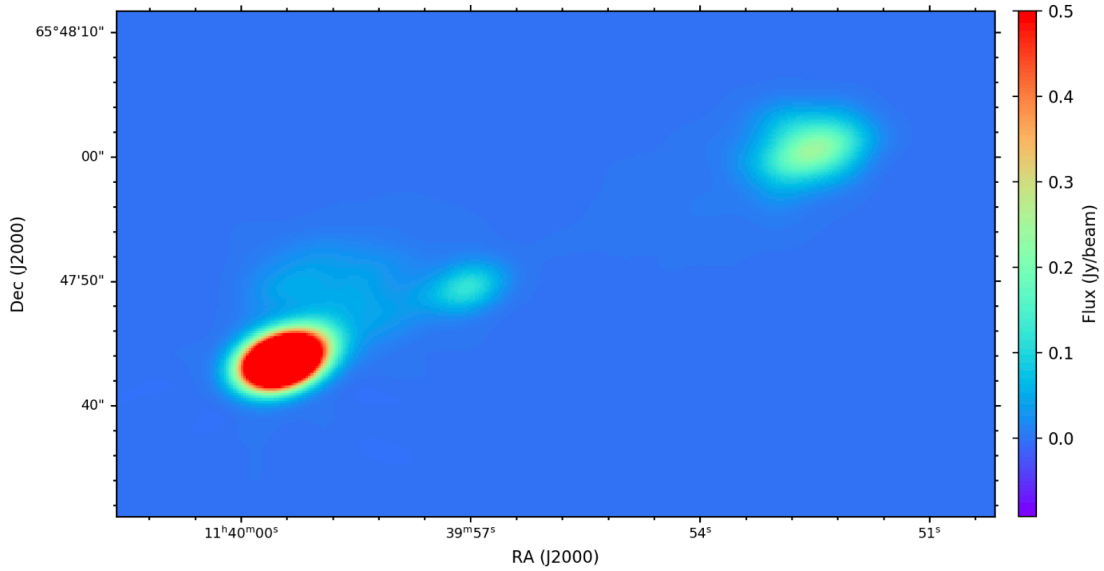

Figure 3.25: The JVLA B configuration map of 3C 263. Originally produced using the task TCLEAN in CASA. Image was reproduced in Python.

3.5.2 Imaging e-MERLIN Data

The e-MERLIN data were cleaned and imaged in TCLEAN with a cell size of 0.″02. Two images with an image size of 2048 × 2048 pixels were cleaned. Figure 3.26 shows the first cleaned field, which includes the southern hotspot and core. The northern hotspot as seen by the e-MERLIN array is shown in Fig. 3.27. Multi-scale cleaning was not used for this data set. The standard CLEAN procedure appeared to image the source adequately. Briggs weighting with a robustness of −0.5 produced an image with a restoring beam size of 0.″13 × 0.″11. The rms noise reached 117 μJy.

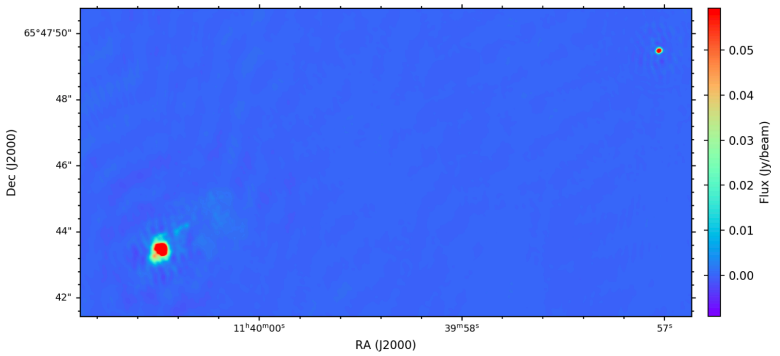

Figure 3.26: Map of 3C 263's southern hotspot and core as revealed by the e-MERLIN array. Image was reproduced in Python.

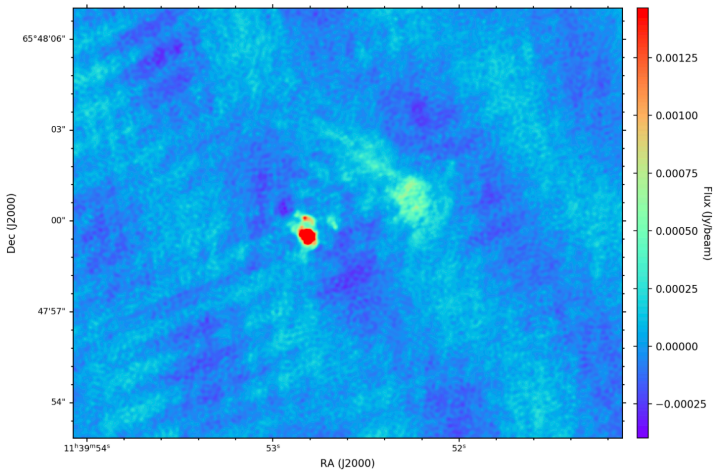

Figure 3.27: Map of 3C 263's northern hotspot and core as revealed by the e-MERLIN array. Image was originally produced using TCLEAN in CASA. Image was reproduced in Python.

3.5.3 Imaging Combined e-MERLIN with JVLA

To correct for a small offset between core positions in the different arrays, data from both JVLA arrays completed two rounds of phase self-calibration starting with the e-MERLIN model. The e-MERLIN model forced the JVLA core to align with the e-MERLIN core, therefore making jet and hotspots align. The weights were re-scaled so that the e-MERLIN data were weighted 9 times more than the JVLA data. This set a weighting that allowed the image to reach a resolution closer to the ideal e-MERLIN resolution. Using both MS files, the data were cleaned together in the task TCLEAN. Cell sizes were set to match the $0\farcs02$ used for e-MERLIN's cell sizes and Briggs weighting was used with robustness set to -0.5. Two 2048×2048 fields of the southern hotspot with core and the northern hotspot were cleaned. The restoring beam size was $0\farcs15 \times 0\farcs12$. After 3 rounds of phase and three rounds of amplitude and phase self-calibration, the rms noise reached 58 μJy. A final CLEANed image including both hotspots and core was made with an image size set to 4096×4096 (see Figs. 3.28, 3.29, 3.30).

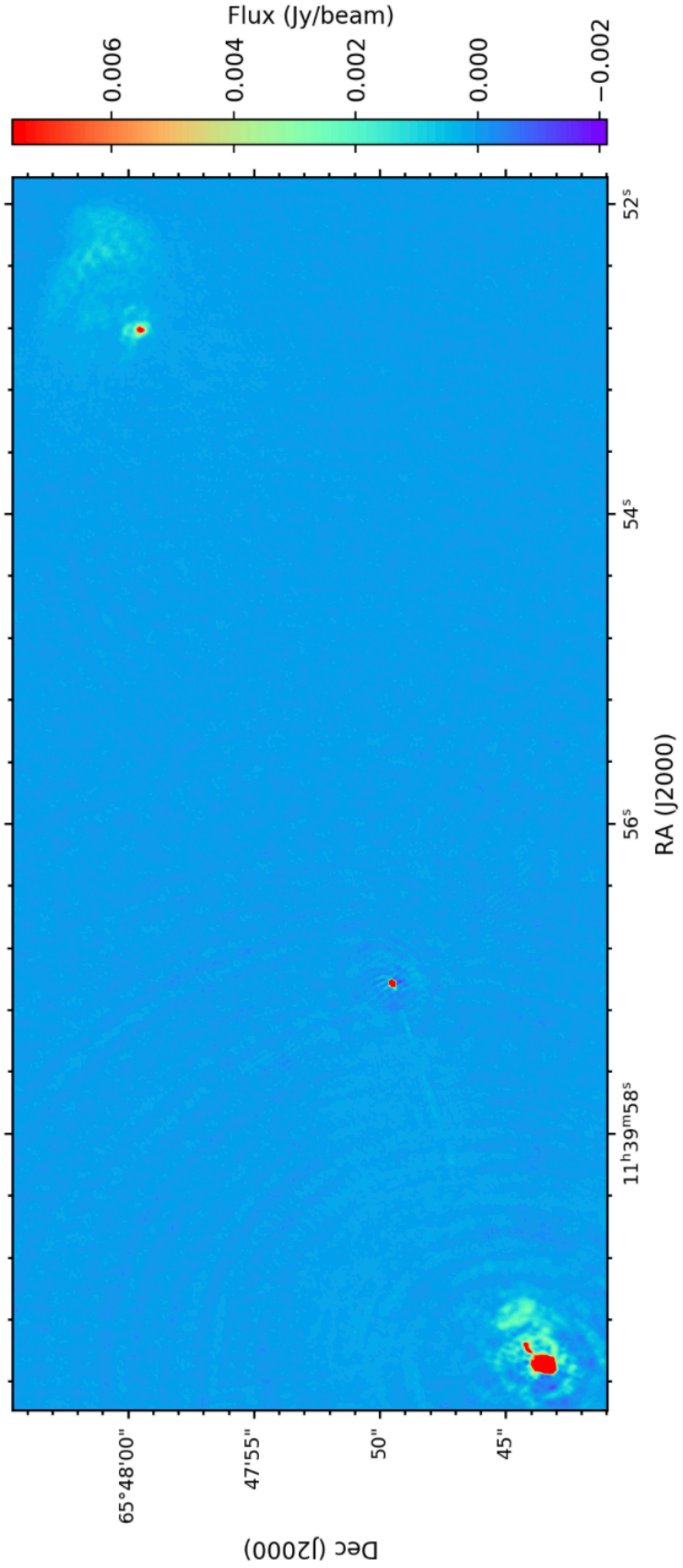

Figure 3.28: Final calibrated map of 3C 263. Image was created from data observed by e-MERLIN + JVLA arrays using the tast TCLEAN in CASA. Image was reproduced in Python.

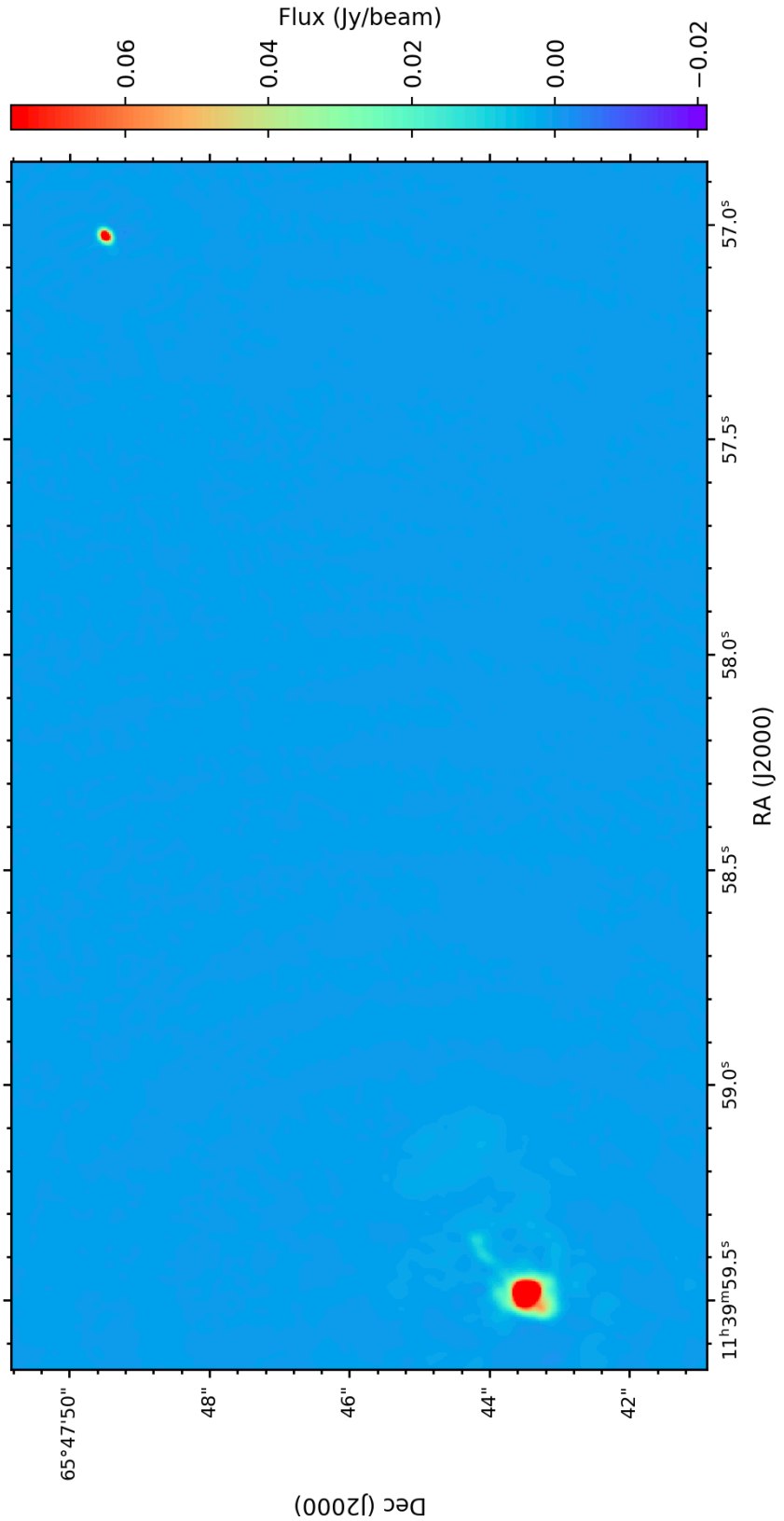

Figure 3.29: Final calibrated map of 3C 263's south hotspot. Image was created from data observed by e-MERLIN + JVLA arrays using the task TCLEAN in CASA. Image was reproduced in Python.

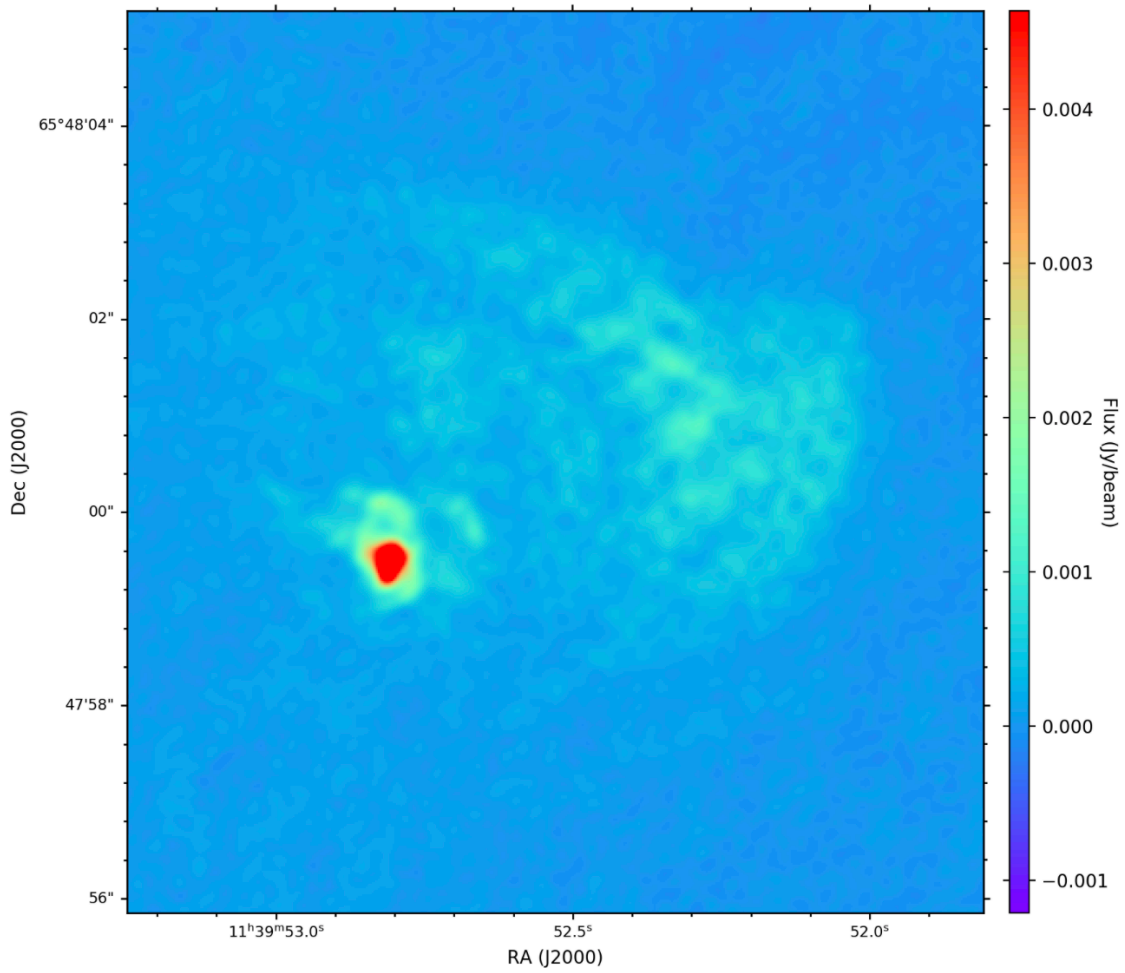

Figure 3.30: Final calibrated map of 3C 263's northern hotspot. Image was created from data observed by e-MERLIN + JVLA arrays using the task TCLEAN in CASA. Image was reproduced in Python.

3.6 Cygnus A L-band Data

The e-MERLIN array observed Cygnus A at L-band on 09 Jan 2017 for approximately 18 hours of total observation time. Full list of observed objects including calibrators and target are:

- 2007+4029: A bright, unresolved phase calibrator.
- 1331+305 (3C 286): Standard flux calibrator for all observations.
- 1407+284 (OQ208): e-MERLIN's bright bandpass calibrator.
- 1959+284 (Cygnus A): A bright, nearby FR II quasar.

Antennas included in the observation were Mk2, Kn, De, Pi, Da, and Cm. Data were provided as a multi-source file and averaged to 128 channels per spectral window prior to receiving them. The *uv* coverage of this observation is shown in Fig. 3.31. Steps taken were a repeat of the 3C 334 e-MERLIN calibration process except the AIPS e-MERLIN pipeline was not executed at any point. Using the task FITLD the data were loaded into AIPS. The first and last 5 channels were flagged using the task UVFLG. The first and last 5 seconds were flagged using the task QUACK. An initial inspection of the data was done using the interactive flagging tool SPFLG. Any obvious bright points were removed and saved to a flag table. The task FRING was used on all calibrators to solve for global delays. The model of 3C 286 was provided by the e-MERLIN team and used to scale the flux of the observed data of 3C 286 using the task CALIB. The flux of each of the other calibrators was bootstrapped from 3C 286 to scale to the correct values. Gain corrections in amplitude and phase were found using the task CALIB and applied to a new calibration table using the task CLCAL. After applying all calibration tables, Cygnus A was split using the task SPLIT into a separate file and exported as a FITS file using the task FITTP. From here all of the remaining procedures were carried out in CASA.

3.6.1 e-MERLIN System Temperature Calibration

Cygnus A at L-band posed a slight challenge for e-MERLIN due to it (i) being one of the brightest radio sources in the sky at this frequency and (ii) having a large extended structure. Cygnus A stretches an impressive $\sim 2'$ and has been known to have flux densities in excess of 1000 Jy at longer wavelengths (Perley

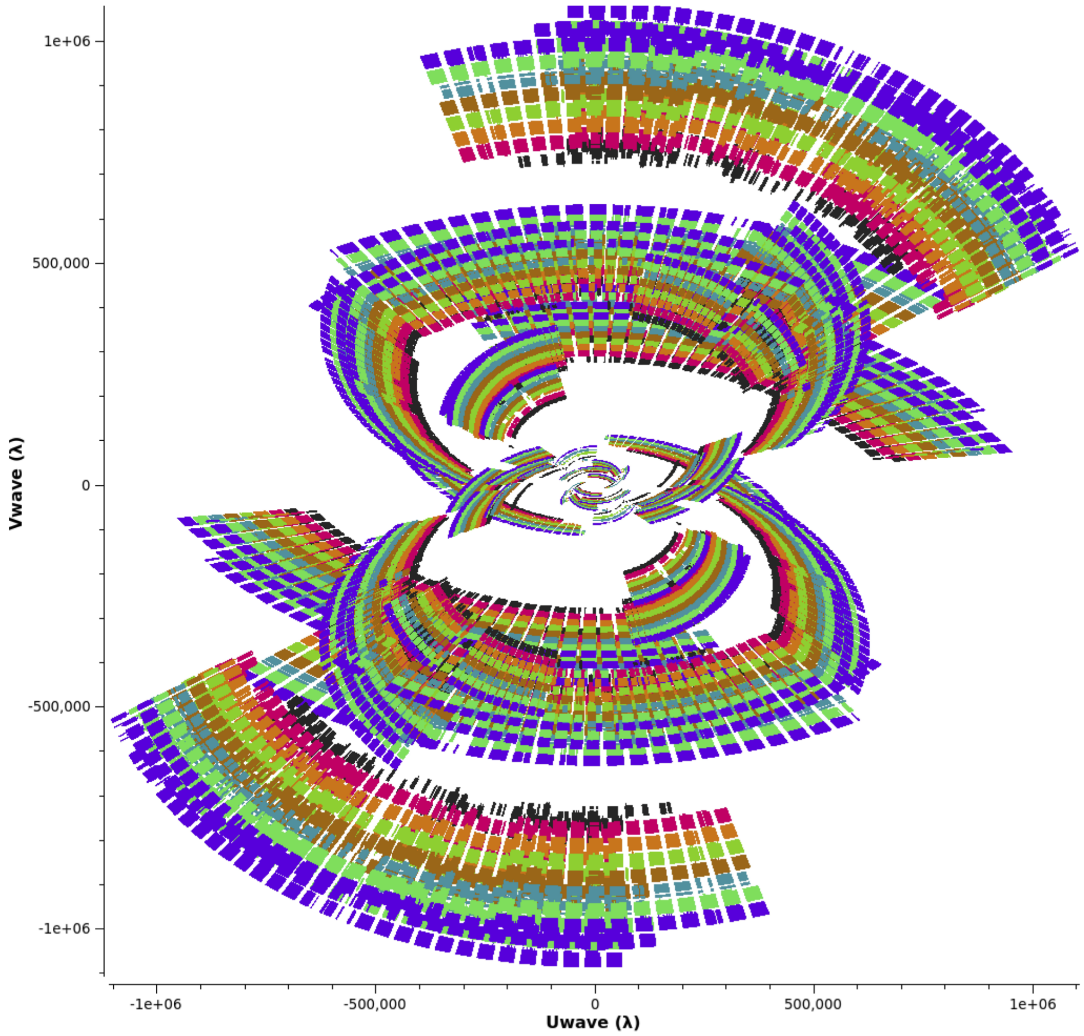

Figure 3.31: Plot of the *uv* coverage over the total observing time for Cygnus A at L-band.

and Butler, 2017). Low-resolution arrays with known gains can accurately measure the flux density. High-resolution arrays struggle to adequately calibrate the bright radio galaxy and remove the added contribution to the system temperature (Perley and Butler, 2017). Therefore, to correct for the fact that Cygnus A makes a measurable contribution to the system temperature, corrections to the flux density needed to be made.

System temperature calibration for the Cygnus A data at L-band followed the process of correcting the raw amplitudes of the flux (3C 286 for e-MERLIN) and point source calibrators described by Diamond et al. (2003). All work described in this section is derived from Diamond et al. (2003) unless otherwise stated.

The amplitude of the point source calibrator does not vary across the different baselines in the e-MERLIN array. However, the amplitude of 3C 286 is resolved with the e-MERLIN baselines. Using only the shortest baselines (Mk2-Pi, Mk2-Da, and Da-Pi) the extended structure of the flux calibrator is less resolved out, making it easier to model. Typically e-MERLIN data uses the Python script DFLUXPY to interpolate and set the flux density values from a model at the observed frequency over these baselines to the flux and point source calibrator. The flux density S of the source scales with the observing frequency by

$$\log(S) = a_0 + a_1 \log(\nu_G) + a_2[\log(\nu_G)]^2 + a_3[\log(\nu_G)]^3 + a_4[\log(\nu_G)]^4, \tag{3.1}$$

where ν_G is the centre frequency of the SPW in GHz, a_0 is the log of the flux density at 1 GHz, a_1 is the spectral slope at 1 GHz, and polynomial fits provided by (Perley and Butler, 2013), and more recently by Perley and Butler (2017), determined the values for all a_i.

The flux density recorded at each of the baselines includes an additional contribution from the background sky brightness. The general automatic voltage correction (AVC or α) corrects for the additional contribution at each antenna by

$$\alpha = \sqrt{\frac{T_{sys} + S/g + T_{sky}}{T_{sys}}}, \tag{3.2}$$

where T_{sys} is the system temperature in K, g is the gain of the telescope in Jy K^{-1}, and T_{sky} is the cosmic microwave background (CMB) temperature (2.7 K). For the flux and point calibrators the AVC terms (α_F and α_P respectively) can be determined from the T_{sys} values in Table 3.2. If we assume the apparent flux density of the calibrators is small ($S = 0$) compared to the T_{sky} and T_{sys} we can approximate α to

$$\alpha = \sqrt{\frac{T_{sys} + T_{sky}}{T_{sys}}}. \tag{3.3}$$

In the case where the flux and point calibrators are corrected for the contribution of the sky brightness, the known flux density values of the flux calibrator S_F and the recorded amplitudes for the calibrators (A_P and A_F) can determine the flux density of the point calibrator (S_P) from

$$S_P = S_F \frac{A_P}{A_F} \frac{\alpha_P}{\alpha_F}. \tag{3.4}$$

The ratio of the AVC terms is typically within 2% of 1 for these two calibrators, and so this additional calibration is not needed. Before considering Cygnus A's contribution it was verified that the ratio of AVCs were within a few percent of 1.

As expressed at the beginning of this section, Cygnus A's contribution to the sky brightness needed to be accounted for by following the same calibration technique described above. From Eqn. 3.1 the apparent flux density of Cygnus A at the centre frequency in each SPW at L-band was determined by using the values of a_i[2]. The calculated apparent flux density at each SPW is provided in Table 3.5.

The S at each centre frequency was used to derive the AVC terms for each antenna. At the time that Cygnus A was observed, e-MERLIN was not fully equipped to provide accurate values for the estimated T_{sys} of each antenna. Values were given as best estimates. Estimated measurements for T_{sys} are provided in Table 3.2. The derived values for the AVC are detailed in Table 3.5. Calibration tables were produced for each antenna per SPW by using the task GENCAL. The calibration tables were then applied to the data using the task APPLYCAL.

3.6.2 Cygnus A L-band Imaging and Self-calibration

Visibilities were cleaned and imaged using the task TCLEAN. Briggs weighting was used with robustness set to 0.0. The target was separated into three fields to account for the large angular size: one field centred on the core at (J2000) $19^h59^m28\overset{s}{.}356104$, $+40°44'02\overset{''}{.}097627$ and two fields centred on the hotspots located at the end of the jet and counterjet: (J2000) $19^h59^m33\overset{s}{.}0$, $+40°43'40\overset{''}{.}0$ and (J2000) $19^h59^m23\overset{s}{.}0$, $+40°44'24\overset{''}{.}0$. All images were constructed with a $0\overset{''}{.}19 \times 0\overset{''}{.}12$ clean beam. Details about the final images are also provided as a summary in Table 3.6. The rms reached 2.9 mJy for the eastern hotspot, 2.3 mJy for the core, and 2.5 mJy for the western hotspot. A map of the core is presented in Fig. 3.32. A map of each hotspot is provided in Figs. 3.33-3.34.

[2]Using the values from Perley and Butler (2017), Eqn. 3.1 is written as
$\log(S) = 3.3498 - 1.0022\log(\nu_G) - 0.2246[\log(\nu_G)]^2 + 0.0227[\log(\nu_G)]^3 + 0.04525[\log(\nu_G)]^4$.

Table 3.5: Expected flux density and automatic voltage correction (AVC) at each antenna for the Cygnus A L-band e-MERLIN data. Expected flux density was calculated and used to determine the AVC that was applied to the data.

Frequency ν_G (GHz)	Flux S (Jy)	Mk2 α	Kn, Da, Pi α	De α	Cm α
1.28	1228.03	1.359	1.253	1.329	1.829
1.35	1070.94	1.314	1.222	1.289	1.725
1.41	955.99	1.281	1.199	1.258	1.648
1.48	840.91	1.248	1.175	1.228	1.571
1.54	755.96	1.224	1.158	1.206	1.515
1.60	681.68	1.202	1.143	1.186	1.465
1.67	606.43	1.181	1.128	1.166	1.415
1.73	550.26	1.165	1.117	1.152	1.378

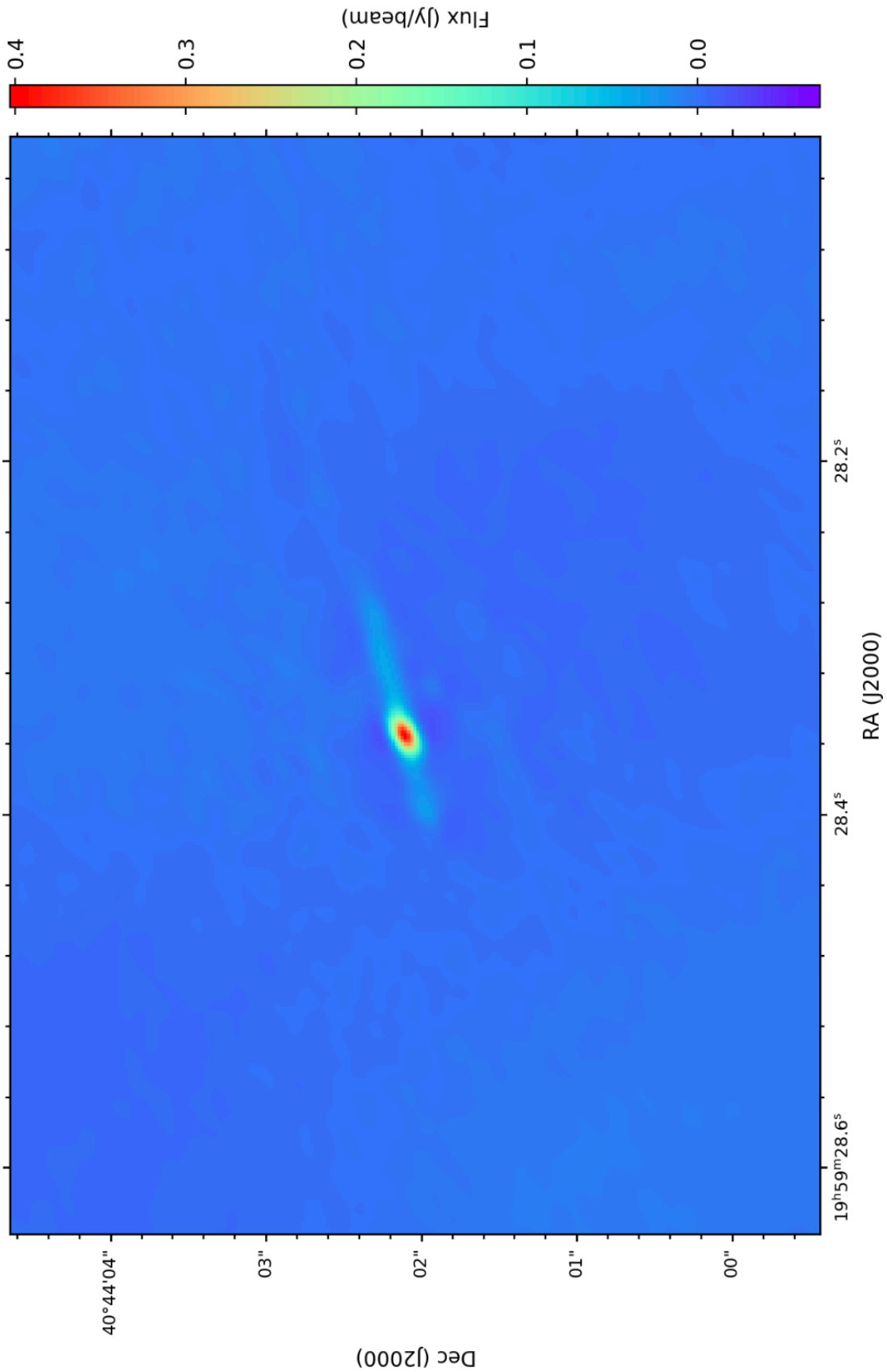

Figure 3.32: Final calibrated map of Cygnus A's core at L-band. Map was produced using data observed by the e-MERLIN array with the tast TCLEAN in CASA.

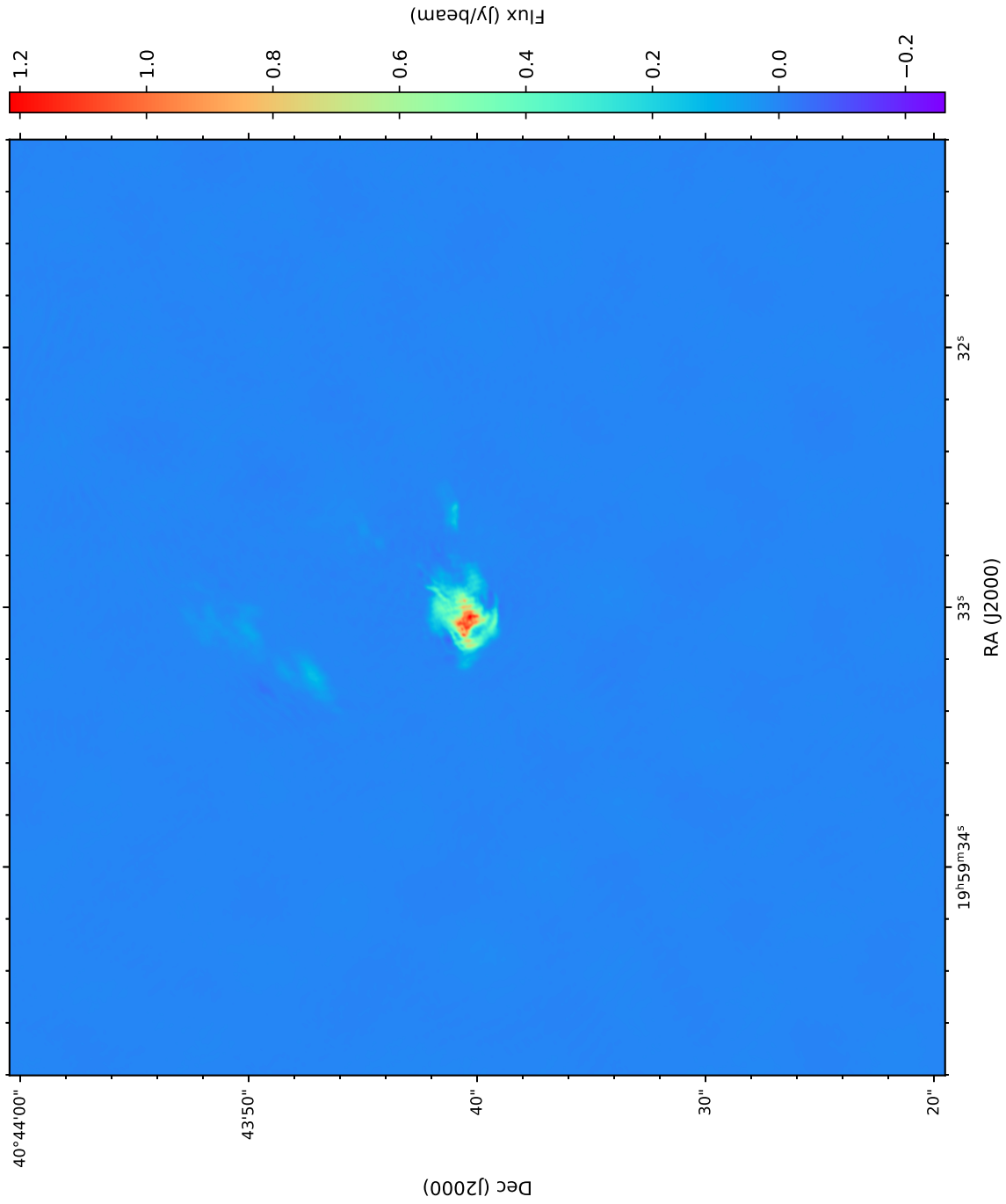

Figure 3.33: e-MERLIN map of Cygnus A's eastern hotspot at L-band. Image was produced using the tast TCLEAN in CASA.

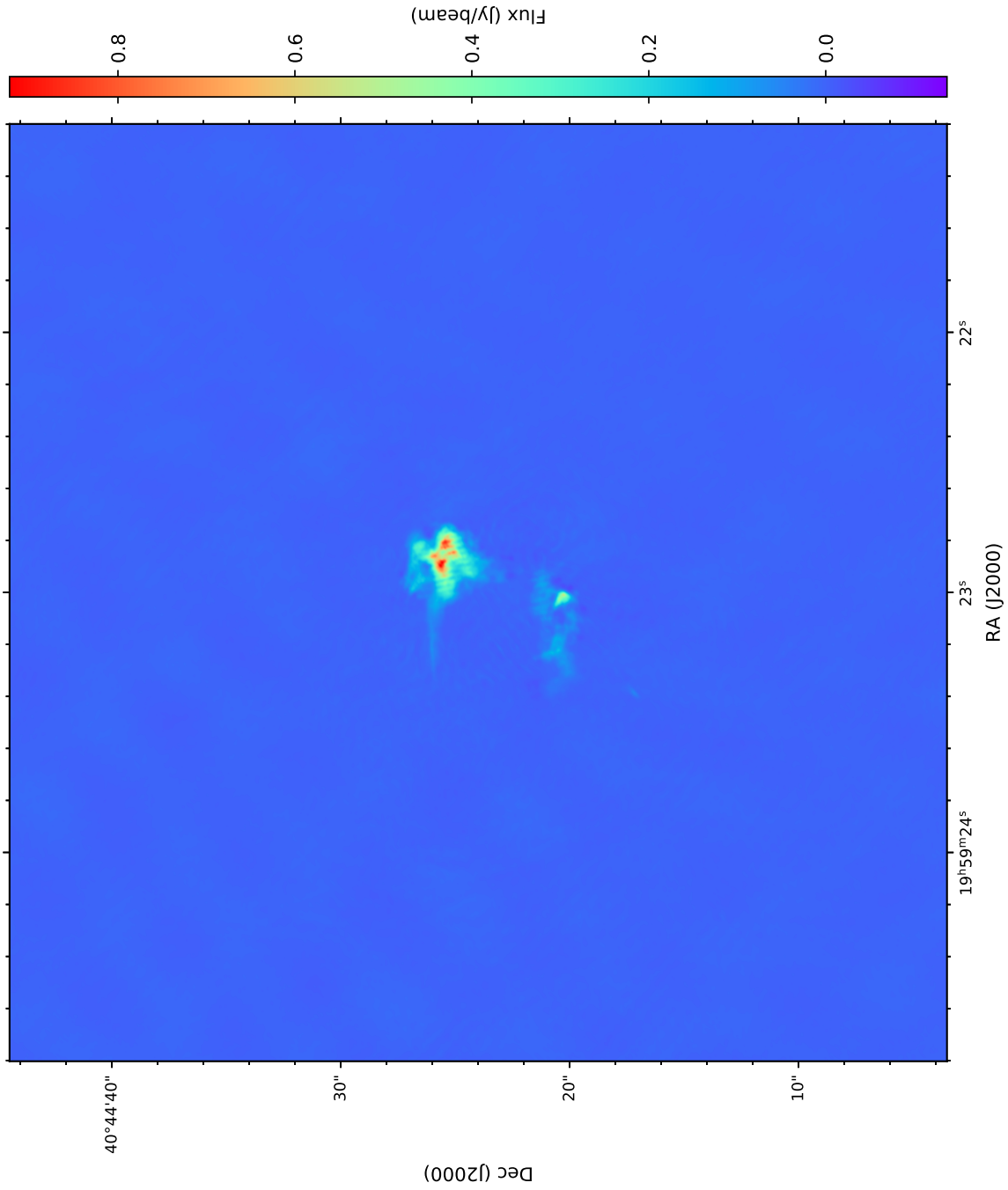

Figure 3.34: e-MERLIN map of Cygnus A's western hotspot at L-band. Image was produced using the task TCLEAN in CASA.

3.7 Cygnus A C-band Data

The observation of Cygnus A at C-band was done on 28 July 2017 using the e-MERLIN array. Sources observed during the observation were:

- Calibrators: 0319+415, 2007+4029, 1331+305, and 1407+284
- Target: 1959+4044.

All e-MERLIN antennas were used in the run except the Lovell telescope. Calibration was done using the e-MERLIN CASA pipeline using the same procedure as that for 3C 263. Figure 3.35 shows the *uv* coverage of Cygnus A during this observation. After converting the FITS file to a measurement set and extracting the observation details into a text file, the pipeline continued by using the task FIXVIS to correct phase centre of the visibilities. Unlike the other targets in this thesis, the task HANNINGSMOOTH was not used on the C-band data because RFI is less of an issue at these frequencies. The pipeline continued with the removal of the first and last 5 channels of the SPW and the removal of the first and last 5 seconds of each scan with the task FLAGDATA. The final pre-processing step of the pipeline was to average the data to 128 channels per spw and 2 seconds of integration time.

The calibration part of the pipeline used the e-MERLIN model of 3C 286 at C-band to bootstrap the fluxes of 3C 286 and the other calibrators (see §3.2). The slope observed across the bandpass was solved for using the task BANDPASS. Delays were then solved for using a time interval of 300 seconds in the task GAINCAL. Phase and amplitude gain corrections were created in the task GAINCAL and all corrections were applied to the data using the task APPLYCAL. Cygnus A at C-band was split off from the multi-source measurement set and self-calibrated.

3.7.1 Cygnus A C-band Imaging and Self-calibration

Cygnus A at C-band was imaged with the task TCLEAN as three fields with a size of 2048 × 2048 each and Briggs weighting with robustness set to 0.0 for each of the fields. Twelve rounds of phase self-calibration were done and four additional rounds of amplitude and phase self-calibration were completed. The maps were centred on the core at (J2000) $19^h59^m28\overset{s}{.}356104$, $+40°44'02''097627$, the eastern hotspot at (J2000) $19^h59^m33\overset{s}{.}0$, $+40°43'40\overset{''}{.}0$, and the western hotspot at

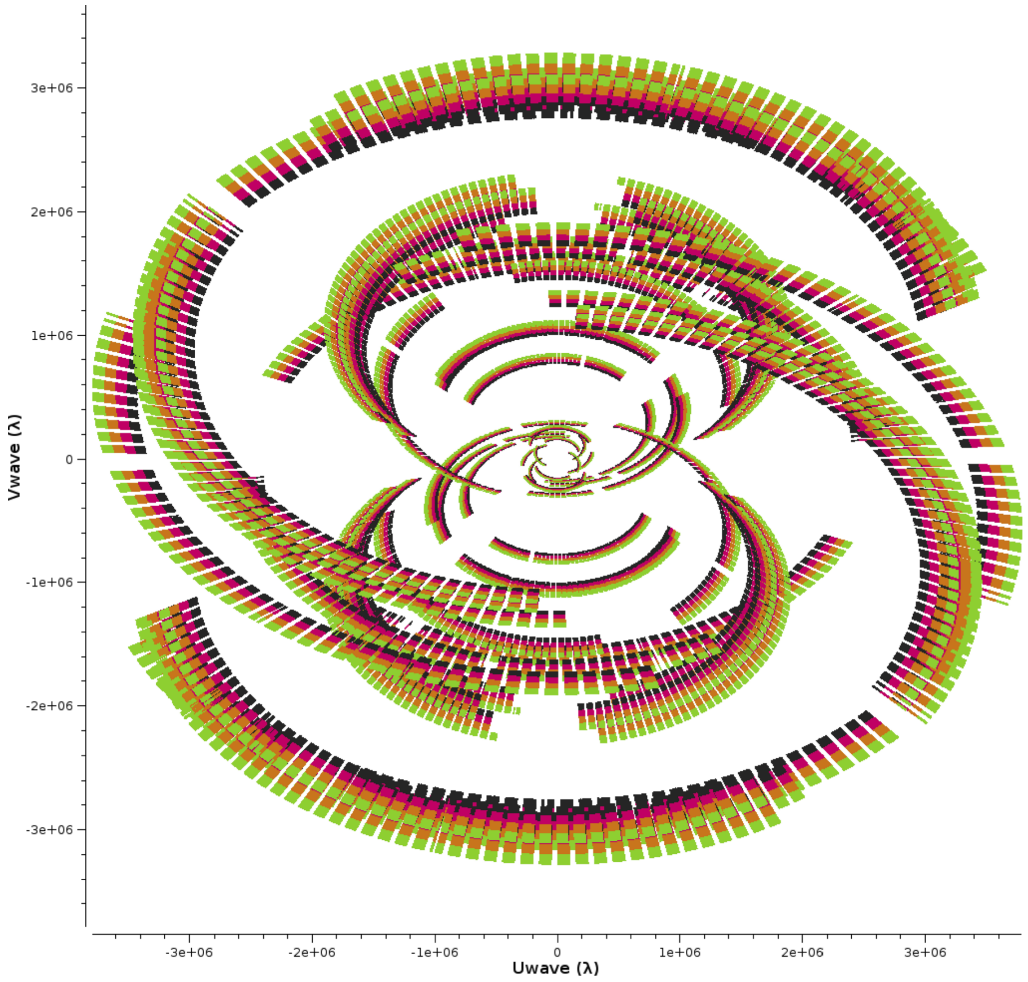

Figure 3.35: Plot of the e-MERLIN *uv* coverage for Cygnus A at C-band. The colors represent one of the 4 SPWs.

(J2000) $19^h59^m23\overset{s}{.}0$, $+40°44'24\overset{''}{.}0$. The CLEANed image of the eastern hotspot, shown in Fig. 3.36, was convolved with a $0\overset{''}{.}042 \times 0\overset{''}{.}037$ clean beam at position angle -18°.64. The rms reached 79 μJy away from the hotspot. A map of the core is shown in Fig. 3.37. The resolution of the core was $0\overset{''}{.}042 \times 0\overset{''}{.}037$ with a position angle of -13°.42. Since the core was the main focus of the project, reducing the rms near the nucleus became the priority. The rms reached close to 91 μJy in the final map around the core. The image of the western hotspot, shown in Fig. 3.38, was convolved with a $0\overset{''}{.}042 \times 0\overset{''}{.}037$ clean beam with a position angle of -18°.65. The rms in the map of the western hotspot reached 77 μJy. A summary of the clean beam information is found in Table 3.6.

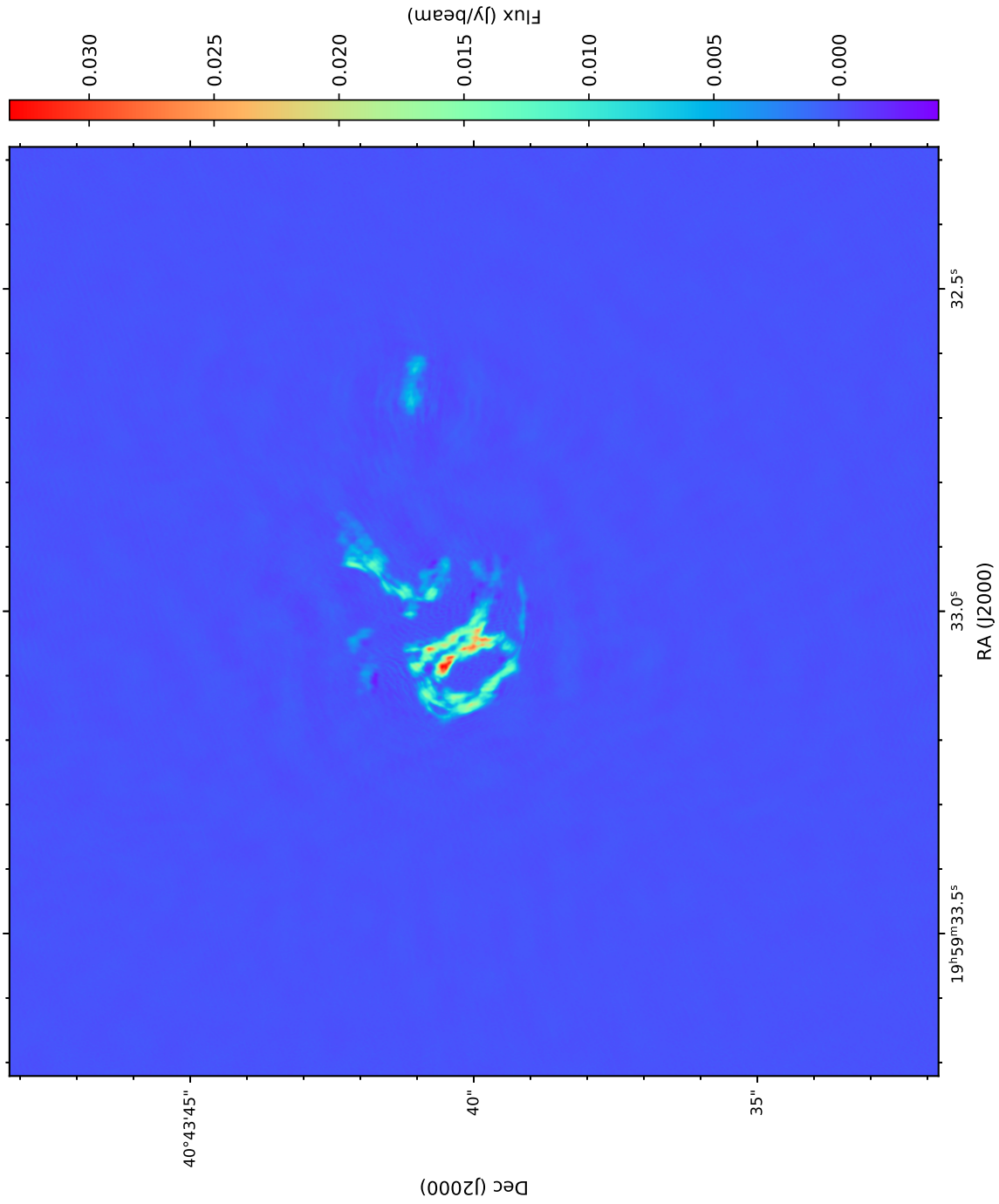

Figure 3.36: Final calibrated e-MERLIN map of Cygnus A's eastern hotspot at C-band. Image was produced using the tast TCLEAN in CASA.

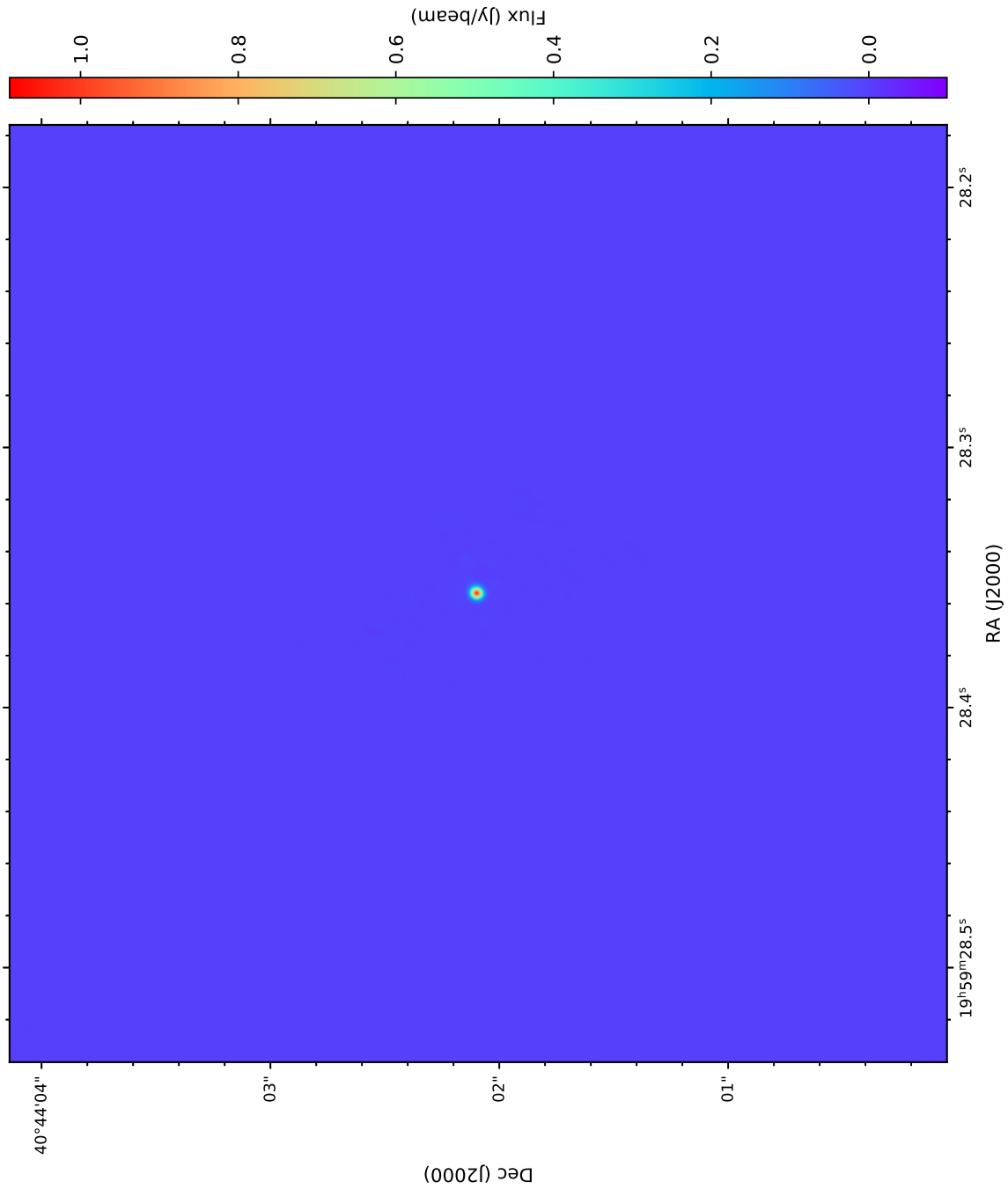

Figure 3.37: Final calibrated e-MERLIN map of Cygnus A's core at C-band. Image was produced using the task TCLEAN in CASA.

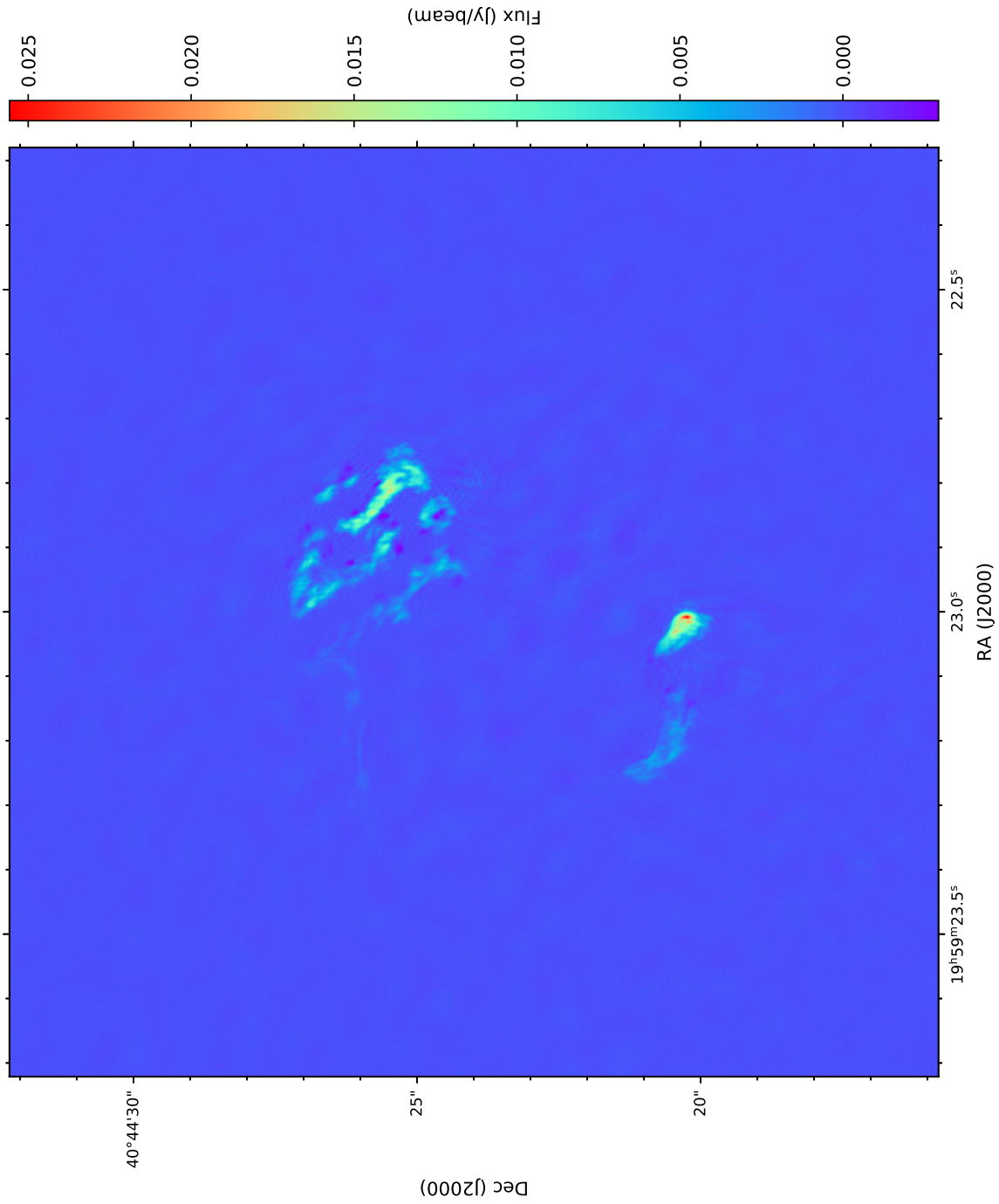

Figure 3.38: Final calibrated e-MERLIN Map of Cygnus A's western hotspot at C-band. Image was produced using the task TCLEAN in CASA.

3.8 Summary of Final Images

Descriptions of the final calibrated images of 3C 334, 3C 263, and Cygnus A are provide in Table 3.6.

Table 3.6: Details of each of the final image produced for each source and array. For array type: VA: JVLA A configuration, VB: JVLA B configuration, VAB: JVLA A and B configurations, and E: e-MERLIN. Final images were either created by: I: "IMAGR" task in AIPS, or T:"TCLEAN" task in CASA. All images are at 1.5 GHz unless otherwise stated. Source names: EHS: east hotspot, N: nucleus, and WHS: west hotspot.

Source	Array	Task	cell size (arcsec)	bmaj (arcsec)	bmin (arcsec)	PA (deg)	Image size (pixels)	Figs.	rms (μJy)	Peak to rms
3C 334	E	T	0.02	0.24	0.12	28.0	2048 × 2048	3.14	44	2,909
3C 334	VA	T	0.25	1.03	0.92	22.9	2048 × 2048	3.16	55	3,218
3C 334	VB	T	0.75	4.78	3.34	55.3	2048 × 2048	3.17	78	3,152
3C 334	E + VAB	T	0.02	0.29	0.14	30.5	2048 × 2048	3.18, 3.19, 3.20	53	2,660
3C 263	E	T	0.02	0.13	0.11	-68.5	2048 × 2048	3.26, 3.27	69	4,115
3C 263	VA	T	0.2	1.23	0.72	-74.4	2048 × 2048	3.24	100	13,900
3C 263	VB	T	0.75	4.4	2.8	-73.4	2048 × 2048	3.25	78	23,076
3C$\dot{2}$63	E + VAB	T	0.02	0.15	0.12	-49.0	4096 × 4096	3.28	45	7,622
Cygnus A EHS	E (1.5 GHz)	T	0.04	0.19	0.12	-57	2048×2048	3.33	1956	2,005
Cygnus A N	E (1.5 GHz)	T	0.04	0.19	0.12	-57	2048×2048	3.32	1341	2,005
Cygnus A WHS	E (1.5 GHz)	T	0.04	0.19	0.12	-57	2048×2048	3.34	1869	2,005
Cygnus A EHS	E (5 GHz)	T	0.007	0.042	0.037	-13.4	2048×2048	3.36	75	4,267
Cygnus A N	E (5 GHz)	T	0.007	0.042	0.038	-13.4	2048×2048	3.37	375	4,267
Cygnus A WHS	E (5 GHz)	T	0.007	0.042	0.037	-13.4	2048×2048	3.38	71	4,267

Chapter 4

The Quasar 3C 334

The first detection of a large scale (>100 kpc) radio jet in 3C 334 was made by Wardle and Potash (1982) using the VLA array at 5 GHz (see Fig. 4.1a). A decade later Bridle et al. (1994a) presented an improved 5 GHz map using the VLA array. The signal to noise significantly improved so that more extended emission could be detected in the northwestern lobe and throughout the total extent of the source (see Figs. 4.1b−4.2b). The improved radio maps showed a ridge corresponding to a jet and likely a counterjet, tracing the boundary of the northwest and southeast lobes (Bridle et al., 1994a). The southeast lobe has a few small features along the ridge while the northwest lobe has a secondary hotspot nearly central to the main lobe component and along the counterjet ridge. Although feature B (see Fig. 4.1b) does not fit the formal definition of a hotspot (see §1.2.3), the work in this chapter will use the term hotspot to describe the feature for simplicity and for reasons that are discussed within this chapter.

3C 334 has a knotty, edge-brightened FRII morphology that extends to a linear size of 326 kpc (Krause et al., 2019). The jet, emanating from the bright core, extends 83 kpc[1] before undergoing a drastic bend ($> 50°$) and terminating into a hotspot on the edge of a diffuse lobe (Wardle and Potash, 1982; Bridle et al., 1994a; Swarup et al., 1984; Krause et al., 2019). The second lobe, located northwest of the bright core, is believed to be connected to the end of a counterjet. A thin trail of emission can be seen tracing out of the northwest lobe back towards the core. This emission is believed to be part of the counterjet.

Since the southeast lobe has a trail of varying emission along the boundary,

[1]A redshift of $z = 0.555$ (Hewitt and Burbidge, 1987) corresponds to a scale of 6.725 kpc arcsec^{-1}.

a research note by Marecki (2012) proposed that 3C 334 may be a restarted quasar. In this explanation for the "gaps" in emission, the activity of the nucleus is believed to have ceased at times in its past (Marecki, 2012). With no more relativistic plasma flowing, the jet and lobe began to take the form of a relic – a diffuse region of synchrotron emission. The northwestern lobe is still perceived as an FRII counterjet lobe with hotspots because the emission is being seen at an earlier phase. The counterjet lobe is located on the far side of the source, requiring additional light travel. Despite the northwest lobe being seen at an earlier time due to the light-travel time effect, it is still further from the core than the southeast lobe. This implies that the northwest end is moving out faster than the southeast for some reason (see Ch. 5). A consequence of intermittent relativistic plasma flows is that the restarted central engine may not be aligned with the previous flow. This can lead to misalignment of the new lobe with the old lobe and may create an illusion of minor bends in the jet (Marecki, 2012).

More recent studies have suggested a more likely scenario where a binary supermassive black hole may contribute to jet precession in 3C 334. Observations have been supported with hydrodynamical simulations by modeling the effects of jet precession. The complementary studies concluded that many features seen in 3C 334 may be explained by this mechanism. In these studies the researchers compared the morphological features associated with a precessing jet to those of a non-precessing jet (e.g., Cox et al., 1991; Wagner and Bicknell, 2011; Monceau-Baroux et al., 2014; English et al., 2016; Donohoe and Smith, 2016; Krause et al., 2019). If precession of the jet and counterjet occurs, the emission will appear to curve into an S-shaped stream of emission (Krause et al., 2019). Due to the large difference between the flow speed closer to the core and the speed of advancement of the lobe, the jet can appear misaligned to the lobe axis. Simulations of interactions of a jet with a lobe boundary suggest the presence of high-pressure features along the boundary advancing along the most current jet direction (e.g., English et al., 2016; Krause et al., 2019). In a more recent study of jet precession by Krause et al. (2019), it is suggested that 3C 334 has a 22° angle of misalignment observed between the jets and lobe axis. This suggests that the host galaxy may contain a binary black hole.

In FRII quasar models it is predicted that emission from the approaching relativistic jet is beamed towards the observer. Emission in the counterjet is beamed away as material flows away from the observer. As a result the structure

is asymmetrically bright with one side of the source distinctly brighter than the other. One prediction of this model is that the lobe on the side of the brighter jet should be less depolarized than the lobe on the counterjet side (e.g., Laing, 1988; Garrington et al., 1988, 1991; Fernini, 2001). The orientation of the lobes to the line of sight and the surrounding interstellar medium play a key role in the Laing-Garrington effect, as the asymmetric depolarization effect is now known. Emission from the weaker jet travels through more material before reaching the observer. Irregularities in the magnetic field of this material results in Faraday rotation that depolarizes the lobe (Laing, 1988; Garrington et al., 1988, 1991). The depolarization ratio DP is

$$DP = P_{20}/P_6, \tag{4.1}$$

where P_{20} and P_6 are the fractional polarization at 20 cm and 6 cm (Garrington et al., 1991). Polarization studies from Garrington et al. (1991) found that for 3C 334, the brighter jet is less depolarized than the weaker jet. Depolarization ratios are provided in Table 4.1. A full discussion on how the surrounding lobe environment impacts the jet length and the amount of depolarization is found in Ch. 5.

In this chapter I present the total intensity maps of the quasar 3C 334 from the e-MERLIN and the JVLA arrays (see Fig. 3.18). Maps were created by the calibration and imaging process described in §3.2. I have also included spectral index maps and transverse profiles along the straight jet. The work presented in this chapter aims to make use of the high-resolution total intensity e-MERLIN with JVLA images by investigating how the spectral index changes along the jet and probing the radio structure of the lobes and jet at the e-MERLIN resolution. Table 4.1 provides redshift and other observational properties derived for 3C 334.

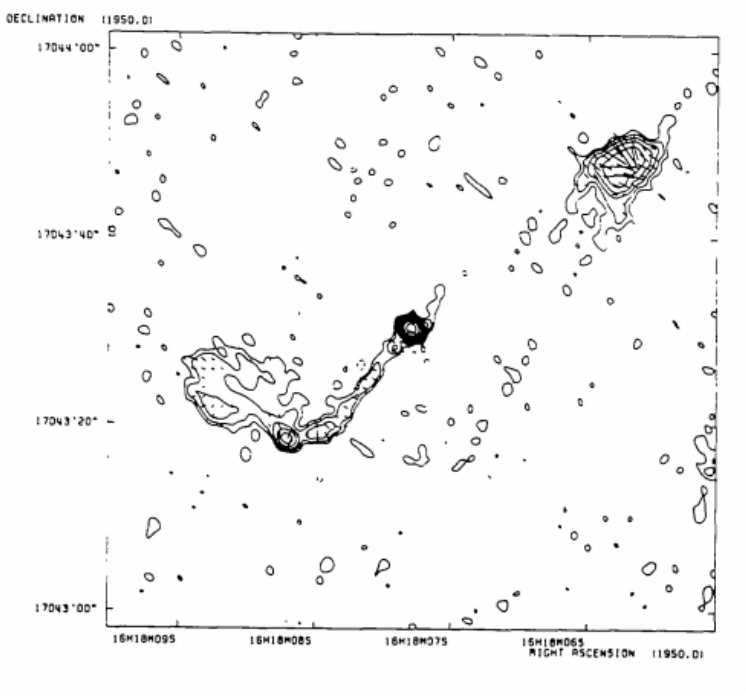

(a)

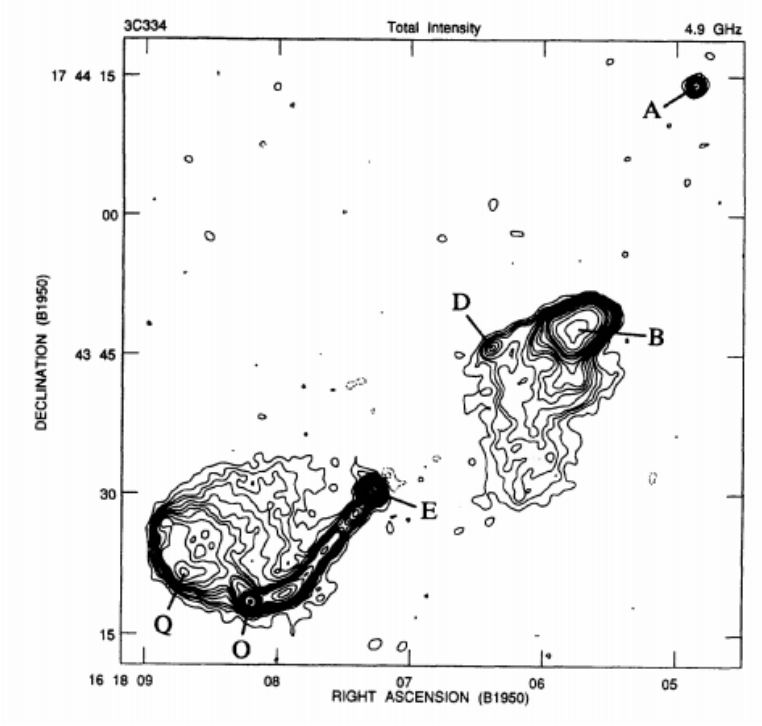

(b)

Figure 4.1: (a) The 5 GHz VLA map of 3C 334 reproduced from Wardle and Potash (1982). (b) A 5 GHz, B configuration VLA map of 3C 334 at 1.″15 resolution. Image is reproduced from Bridle et al. (1994a). Early images are in B1950 coordinates.

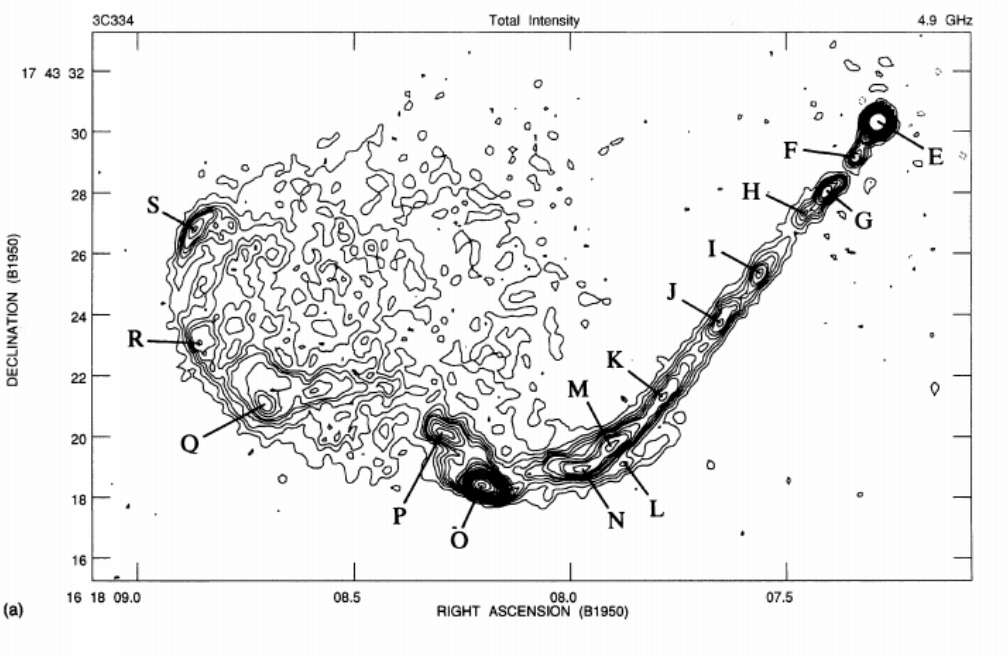

(a)

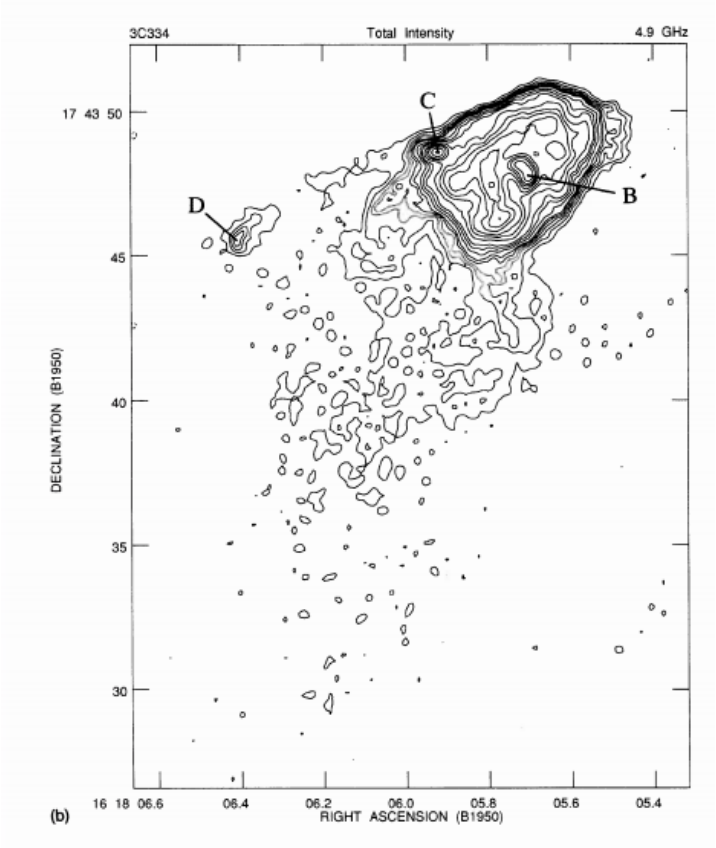

(b)

Figure 4.2: The 5 GHz, A and B configuration VLA map of 3C 334. Map is reproduced from Bridle et al. (1994a). Early images are in B1950 coordinates. Top image (a) shows the jet and southeast lobe and bottom image (b) shows the northwest lobe at 0.″35 resolution.

Table 4.1: Properties of 3C 334. Values were derived from the e-MERLIN plus JVLA map at 1.5 GHz unless otherwise stated.

Property	Value	Reference
IAU name	1618+177	Bridle et al. (1994a)
Optical type	Q[a]	Bridle et al. (1994a)
RA core (J2000)	16h20m21.83	
Dec core (J2000)	+17°36′23.″91	
z	0.555	Hewitt and Burbidge (1987)
Proj. source size (kpc)[b]	326±3.3	Krause et al. (2019)
Proj. straight Jet (kpc)	83±2	Krause et al. (2019)
S_{peak} core (mJy/beam)	141±14	
S_{int} core (mJy)	204± 20	
DP_j	0.86±0.05	Garrington et al. (1991)
DP_{cj}	0.62 ± 0.03	Garrington et al. (1991)
α_{app} (°)[c]	2.°78±0.°52	

[a] Q denotes quasar.

[b] The projected angular size of the source, θ, was taken from the largest contours using the ruler tool in CASA's viewer. The straight jet size was taken from the base of the core until the jet begins to bend.

[c] The apparent jet opening angle α_{app} is calculated using Eqn. 4.2 of §4.3 and is the apparent opening angle at the end of the straight jet.

4.1 Results

4.1.1 Total Intensity Maps at 1.5 GHz

The fidelity of the total intensity image at 1.5 GHz shown in Fig. 3.18 of §3.3 was limited near the centre of the map due to the presence of the bright core and sidelobes. Despite extensive phase and amplitude self-calibration, residual calibration errors remained. The negative bowl was especially pronounced on the southeast side of the core. The artifacts were positioned $> 45°$ from the straight jet axis, thus it did not appear to significantly affect the jet or hotspot properties. The peak flux density of the core is 141±14 mJy. Properties of 3C 334 are given in Table 4.1.

The total intensity distribution of the jet and lobes of 3C 334 at 1.5 GHz is presented in Fig. 4.3. Since the resolution of the image is high ($0\farcs24 \times 0\farcs14$), many of the contour features are indistinguishable from each other when viewed as a full-field. However, a few features are worth noting in this map. A distinct well-collimated jet is shown extending to the southeast from a bright, compact core. At high resolution some of the features in the southeast lobe are still observable. The more diffuse emission is below the noise level. Only a "head" of the northwest lobe is identifiable. Most of the bridge emission tracing back towards the core is not identifiable. A closer inspection of the total intensity map is described below and shown in Figs. 4.4a−4.6. Contours superimposed with grey-scale representation of the surface brightness are also provided in Fig. 4.7−4.9.

Figure 4.4a shows the total intensity distribution of the jet and southeast lobe of Fig. 4.3 also at $0\farcs24 \times 0\farcs14$ resolution. Features are labeled following the notation from Bridle et al. (1994a). A jet composed of several knots (F,G,H1,H2,I1,I2,J1,J2,K,L,M1,M2,N1,N2) is shown extending from a region near the core E. The first evidence of a jet is at knot F.

A small deviation from the straight path occurs between knots G and H1. The jet then returns to a path mostly aligned with knot G at H2. From H2 the jet remains mostly straight with only minor variations in direction through K. Between knots K and M1 the jet begins to bend. At hotspot O the projected direction of the jet is $\sim 90^\circ$ from the axis of the straight jet (F-K). A thin line of emission L extends nearly parallel to the jet between knots M1 and N1. Features P1 and P2 trace an internal structure that does not form the boundary of the lobe (see Fig. 4.2a for lobe structure). The structure at P2 follows a path towards Q where Q, R, and S trace the boundary of the lobe (see Fig. 4.10). A closer view of hotspot O, the line of emission L, and the nearby knots is shown in Fig. 4.4b.

Figure 4.6 shows the total intensity distribution of the head in the northwest lobe region at $0\farcs24 \times 0\farcs14$ resolution. Feature D is identified in the VLA map as a candidate for counterjet emission. At e-MERLIN resolution the feature is composed of several small compact features that trace a path to knot C. Hotspot B is the peak of the head of the northwest lobe that is resolved by the e-MERLIN maps into a twin-peak structure. Smaller features surround hotspot B.

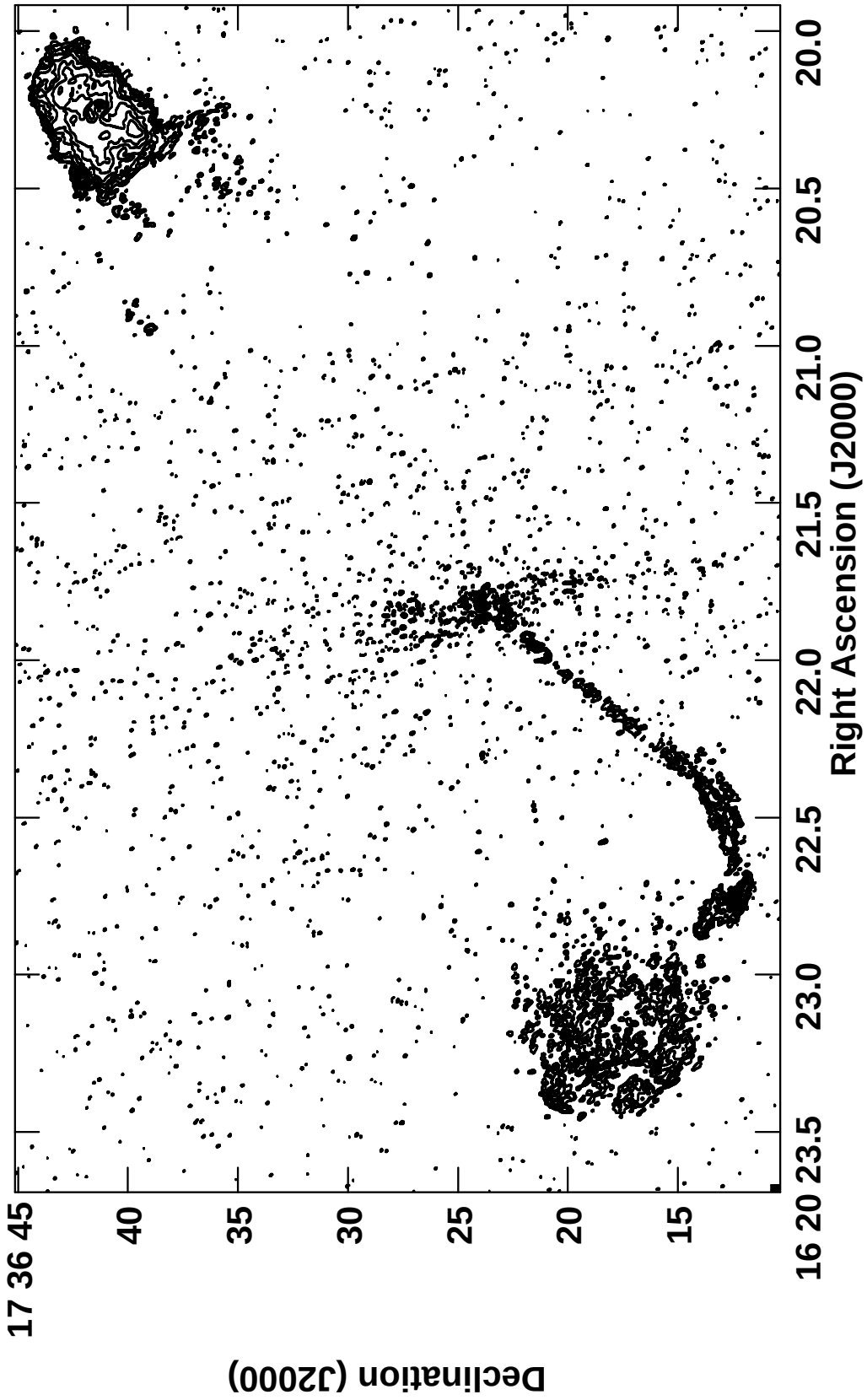

Figure 4.3: Total intensity distribution over the quasar 3C 334 with a resolution of $0''.24 \times 0''.14$. The peak intensity is 139 mJy per CLEAN beam area. Contours are drawn at -4, -2, -1 (dotted), 1, 1.414, 2, 2.828, 4, 5.657, 8, 11.31, 16, 22.63, 32, 45.25, 64, 90.51, 128, 181.0, 256, 362.0, 512, 724.1, 1024, 1450, 2048, 2900, 4096, and 5790 times 150 μJy per CLEAN beam area.

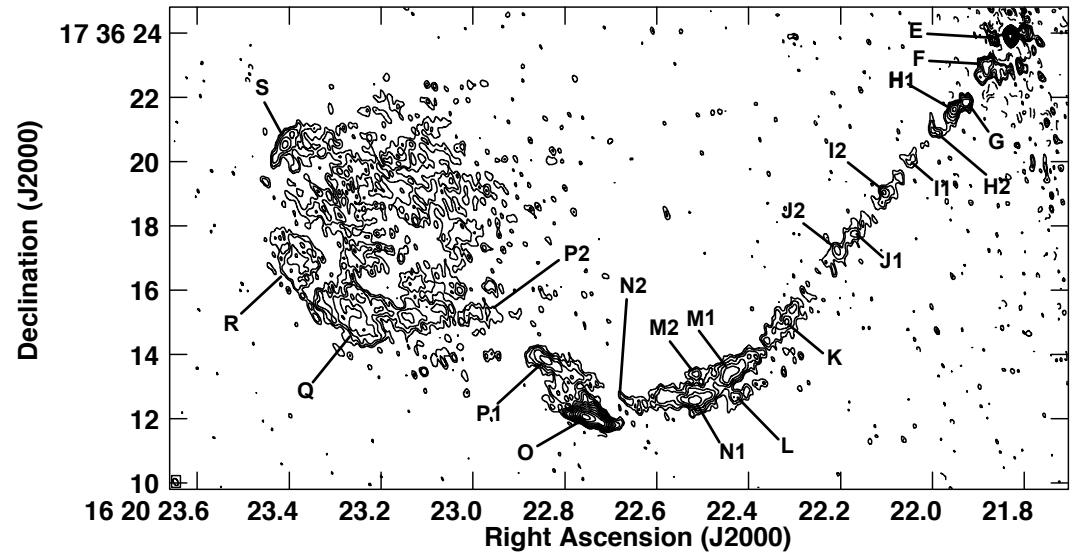

(a)

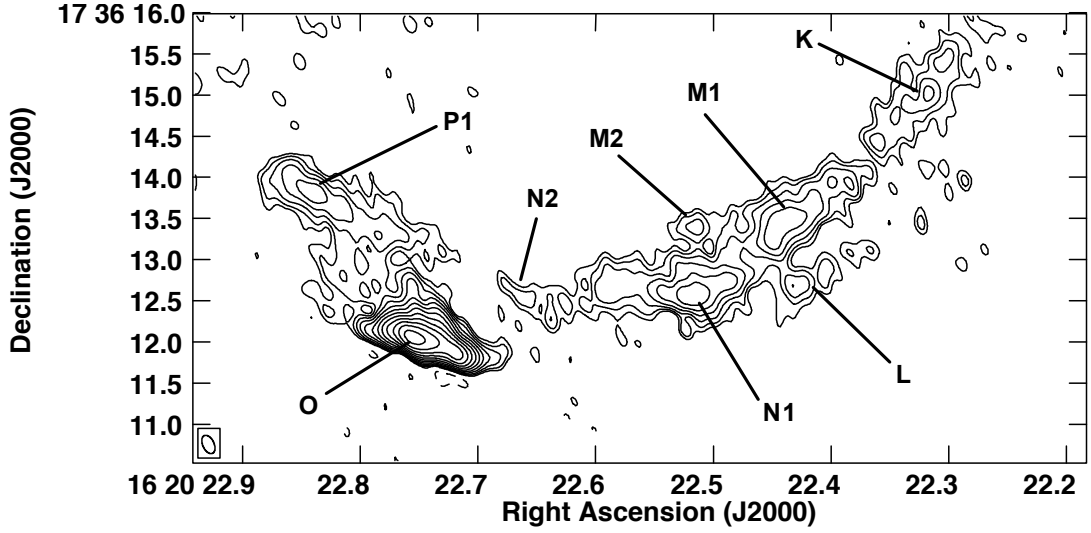

(b)

Figure 4.4: (a) Total intensity distribution of 3C 334 over the southeast lobe and jet with a resolution of 0.″24 by 0.″14. Contours are drawn at -4, -2, -1 (dotted), 1, 1.414, 2, 2.828, 4, 5.657, 8, 11.31, 16, 22.63, 32, 45.25, 64, 90.51, 128, 181.0, 256, 362.0, 512, 724.1, 1024, 1450, 2048, 2900, 4096, and 5790 times 150 μJy per CLEAN beam area. (b) Distribution of the total intensity of the hotspot and nearby knots which are connected to the straight jet.

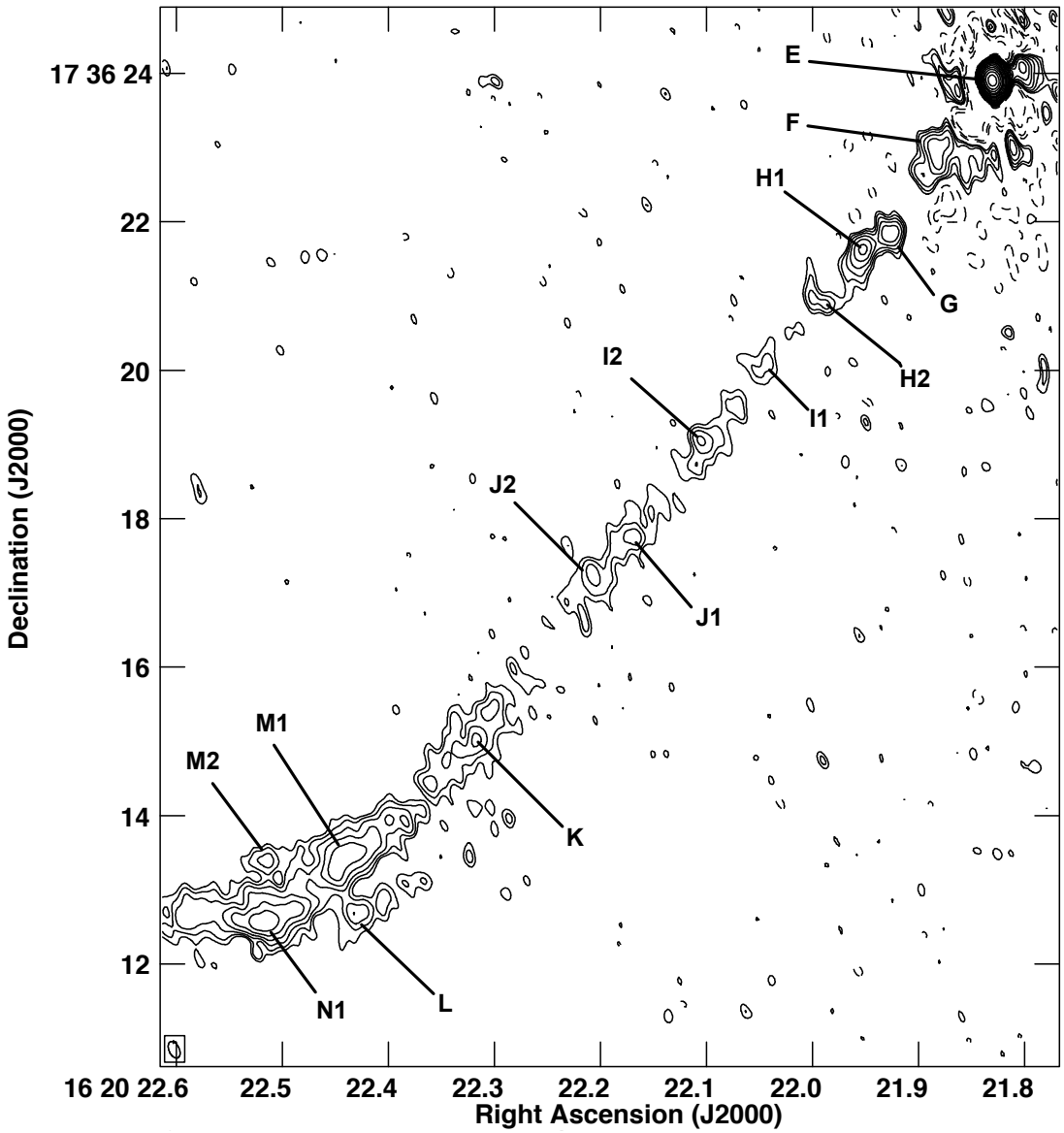

Figure 4.5: Total intensity distribution of 3C 334 over the straight jet with a resolution of 0.″24 by 0.″14. Contours are drawn at -4, -2, -1 (dotted), 1, 1.414, 2, 2.828, 4, 5.657, 8, 11.31, 16, 22.63, 32, 45.25, 64, 90.51, 128, 181.0, 256, 362.0, 512, 724.1, 1024, 1450, 2048, 2900, 4096, and 5790 times 150 μJy per CLEAN beam area.

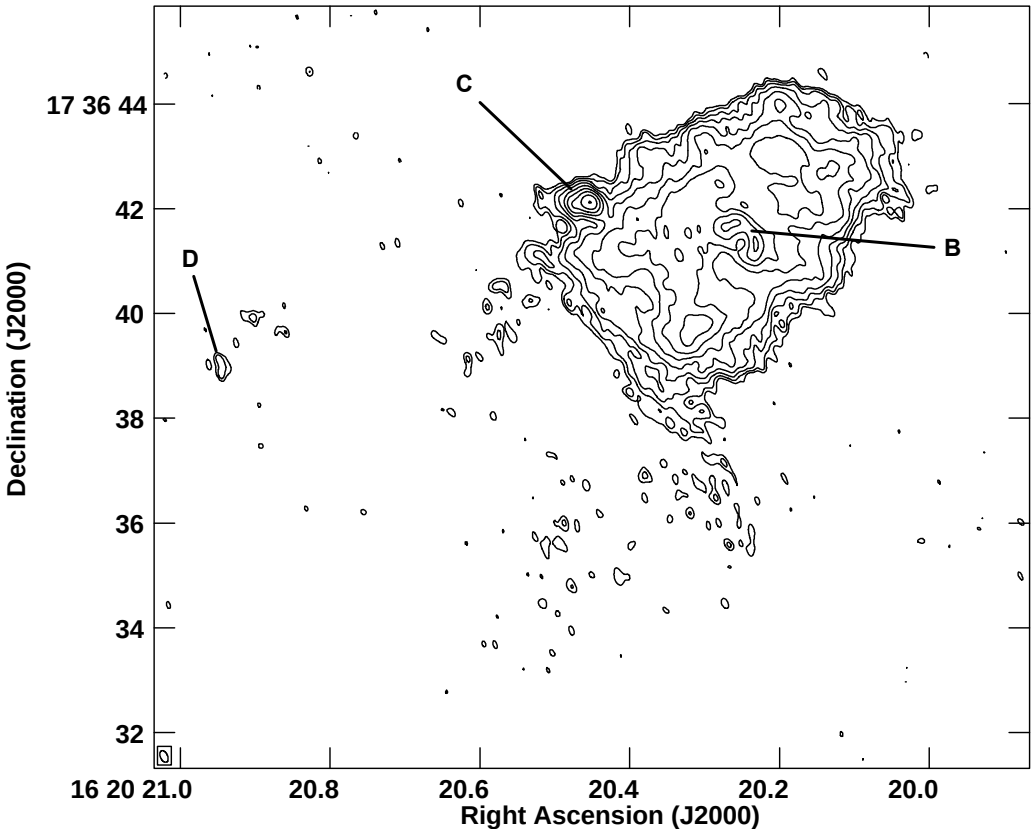

Figure 4.6: Distribution of the total intensity over the "head" component of the northeast lobe in quasar 3C 334 with a resolution of $0\farcs24 \times 0\farcs14$. Contours are drawn at -4, -2, -1 (dotted), 1, 1.414, 2, 2.828, 4, 5.657, 8, 11.31, 16, 22.63, 32, 45.25, 64, 90.51, 128, 181.0, 256, 362.0, 512, 724.1, 1024, 1450, 2048, 2900, 4096, and 5790 times 150 μJy per CLEAN beam area.

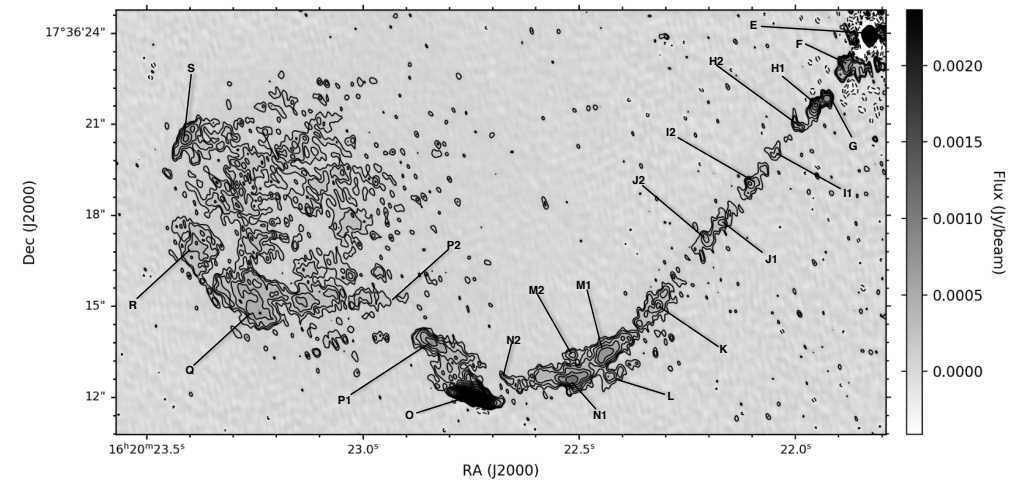

(a)

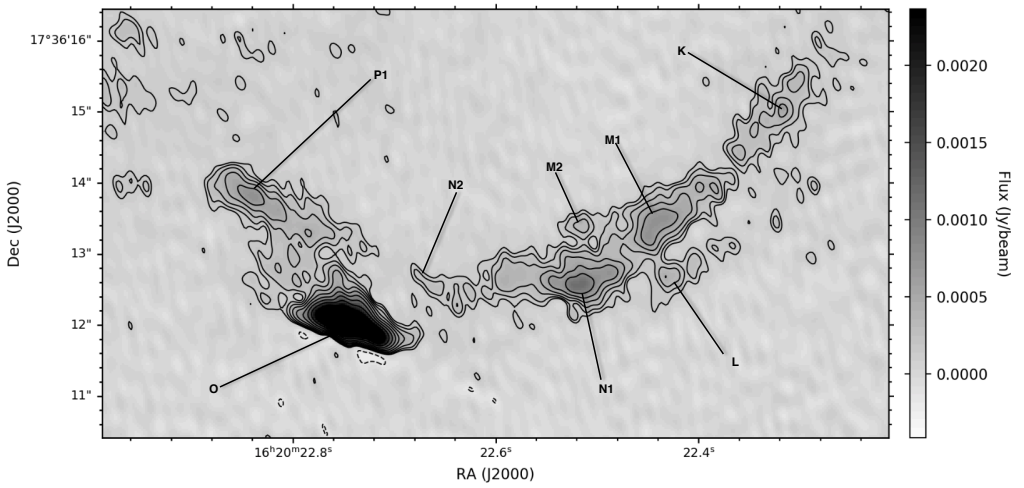

(b)

Figure 4.7: (a) Distribution of total intensity with grey-scale representation over the southeast lobe in quasar 3C 334 with a resolution of 0.″24 × 0.″14. Contours are drawn at -4, -2, -1 (dotted), 1, 1.414, 2, 2.828, 4, 5.657, 8, 11.31, 16, 22.63, 32, 45.25, 64, 90.51, 128, 181.0, 256, 362.0, 512, 724.1, 1024, 1450, 2048, 2900, 4096, and 5790 times 150 μJy per CLEAN beam area. (b) Total intensity distribution with grey-scale of hotspot O.

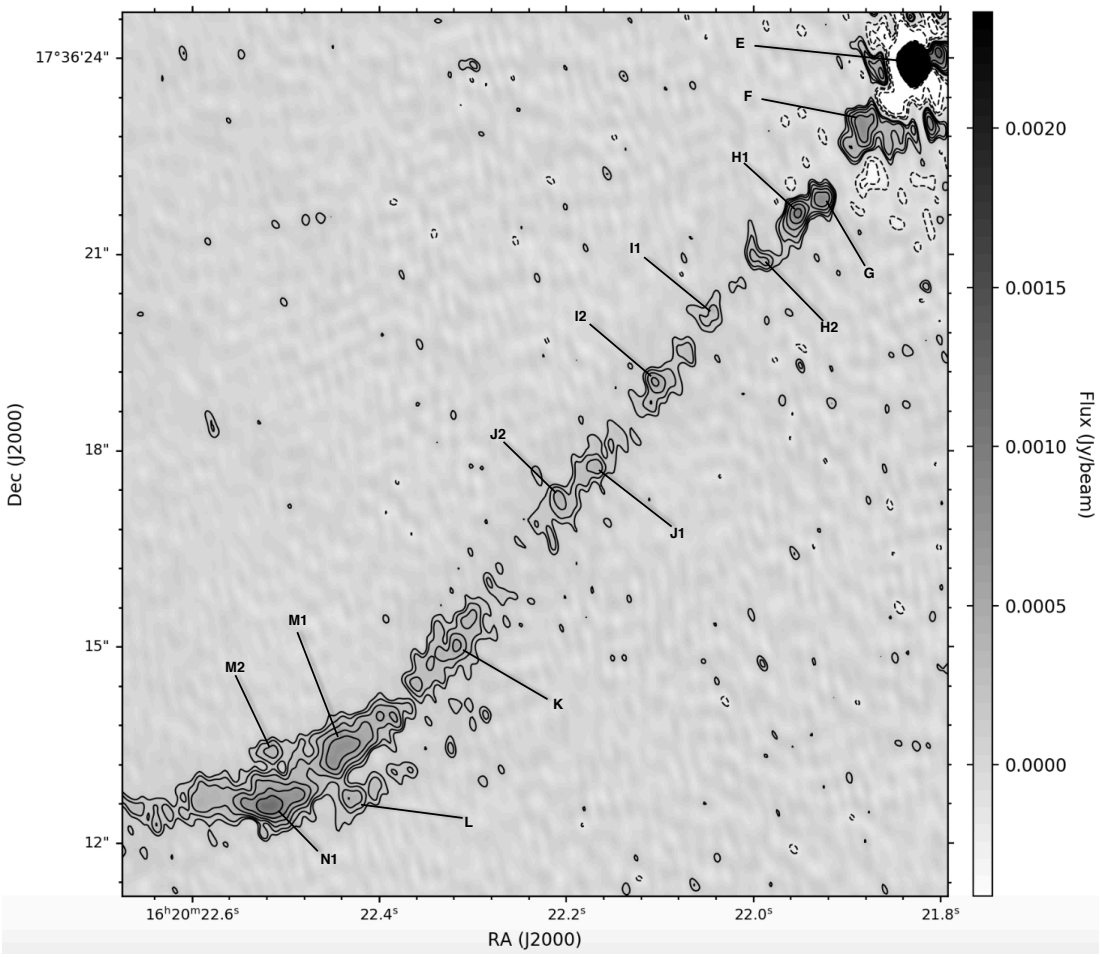

Figure 4.8: Total intensity distribution with grey-scale representation of 3C 334 over the straight jet with a resolution of 0.″24 by 0.″14. Contours are drawn at -4, -2, -1 (dotted), 1, 1.414, 2, 2.828, 4, 5.657, 8, 11.31, 16, 22.63, 32, 45.25, 64, 90.51, 128, 181.0, 256, 362.0, 512, 724.1, 1024, 1450, 2048, 2900, 4096, and 5790 times 150 μJy per CLEAN beam area.

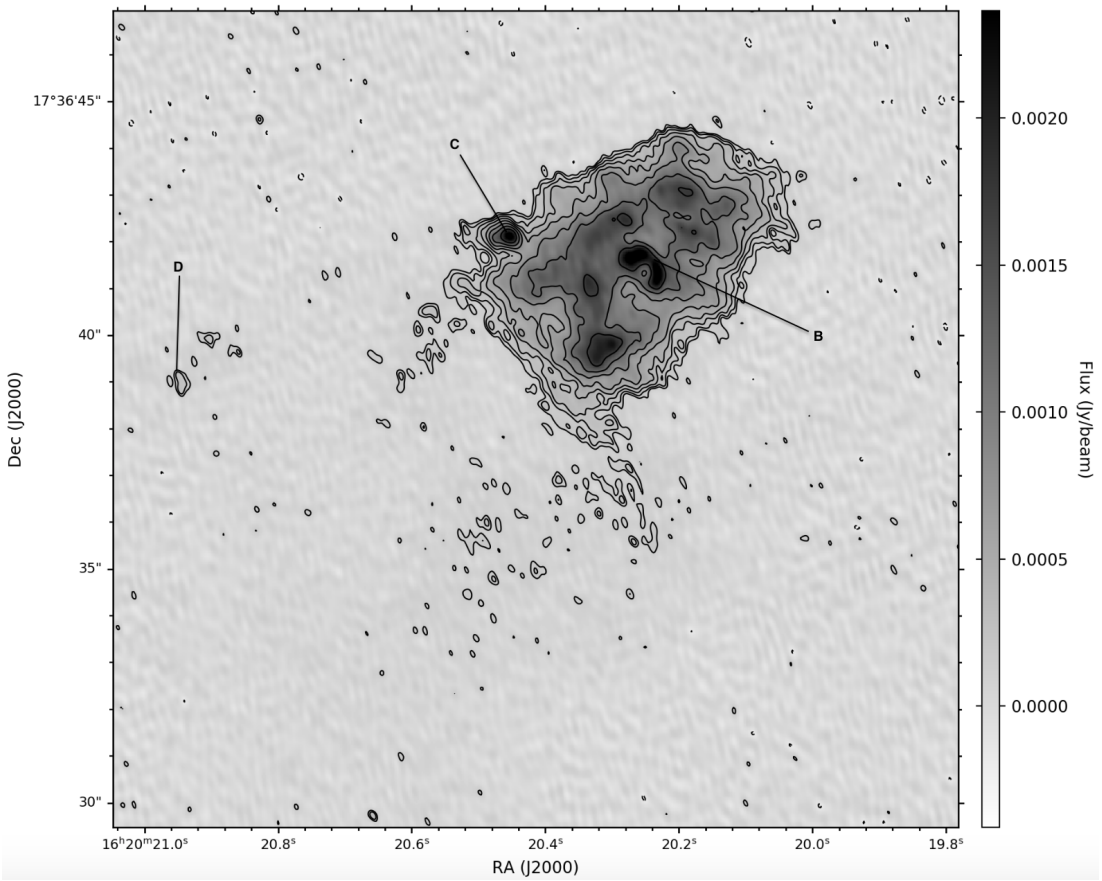

Figure 4.9: Total intensity distribution (contours) superimposed on the surface brightness (grey-scale) of the head of 3C 334 at the northwest lobe with a resolution of $0\farcs24 \times 0\farcs14$. Contours are drawn at -4, -2, -1 (dotted), 1, 1.414, 2, 2.828, 4, 5.657, 8, 11.31, 16, 22.63, 32, 45.25, 64, 90.51, 128, 181.0, 256, 362.0, 512, 724.1, 1024, 1450, 2048, 2900, 4096, and 5790 times 150 μJy per CLEAN beam area.

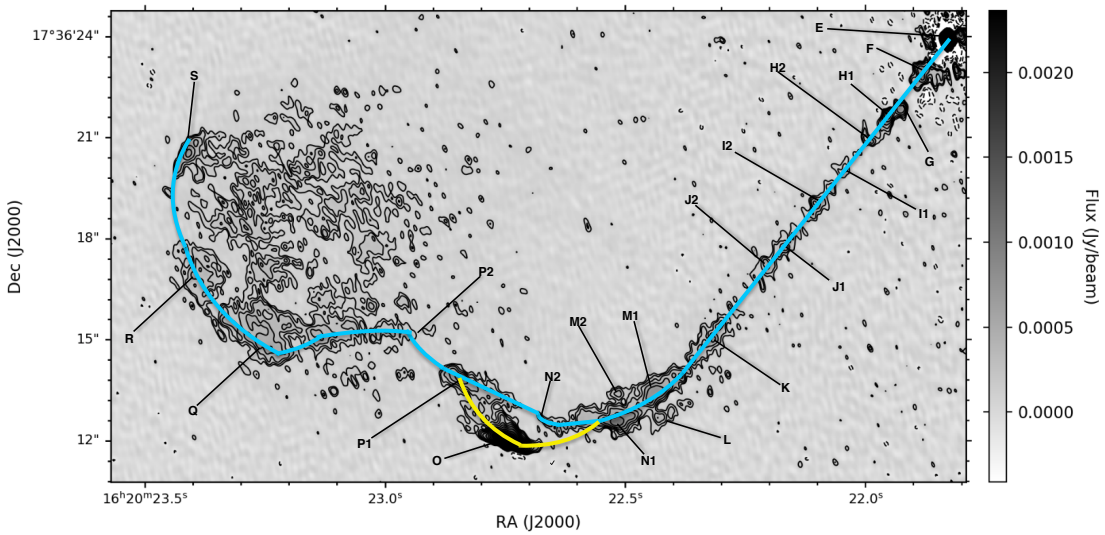

Figure 4.10: An outline of the emission from the end of the jet through the south-east lobe in 3C 334. The blue line traces the emission boundary observed from N2 through S. The yellow line shows the emission boundary observed between N1 and N2 that traces through hotpot O.

4.1.2 The C-band VLA Map

The calibrated VLA map from Bridle et al. (1994a) was provided courtesy of Dr. Robert Laing. The Bridle et al. (1994a) data were observed on 05 May 1986 at A configuration and on 19 July 1986 at B configuration. Details of the observation are provided in Table 4.2. Additional observation details and calibration strategies are described in Bridle et al. (1994a). The final image shown in Fig. 4.11 was produced using a restoring beam size of $0\farcs35 \times 0\farcs35$ and is reproduced from Bridle et al. (1994a).

Table 4.2: Observation details for 3C 334 at C-band data taken by the VLA array in A and B configurations. The calibrated FITS image was provided courtesy of Dr. Robert Laing.

Observation Info.	Value
Obs. ν	4.9 GHz
Configuration	A & B
Obs. Date (A)	1986/05/04
Obs. Date (B)	1986/07/19
b_{maj}	$0\farcs35$
b_{min}	$0\farcs35$
PA	135°
σ_{rms} (μJy/beam)	17
S_{peak} core (mJy/beam)	127
Image size (pixels)	589×591

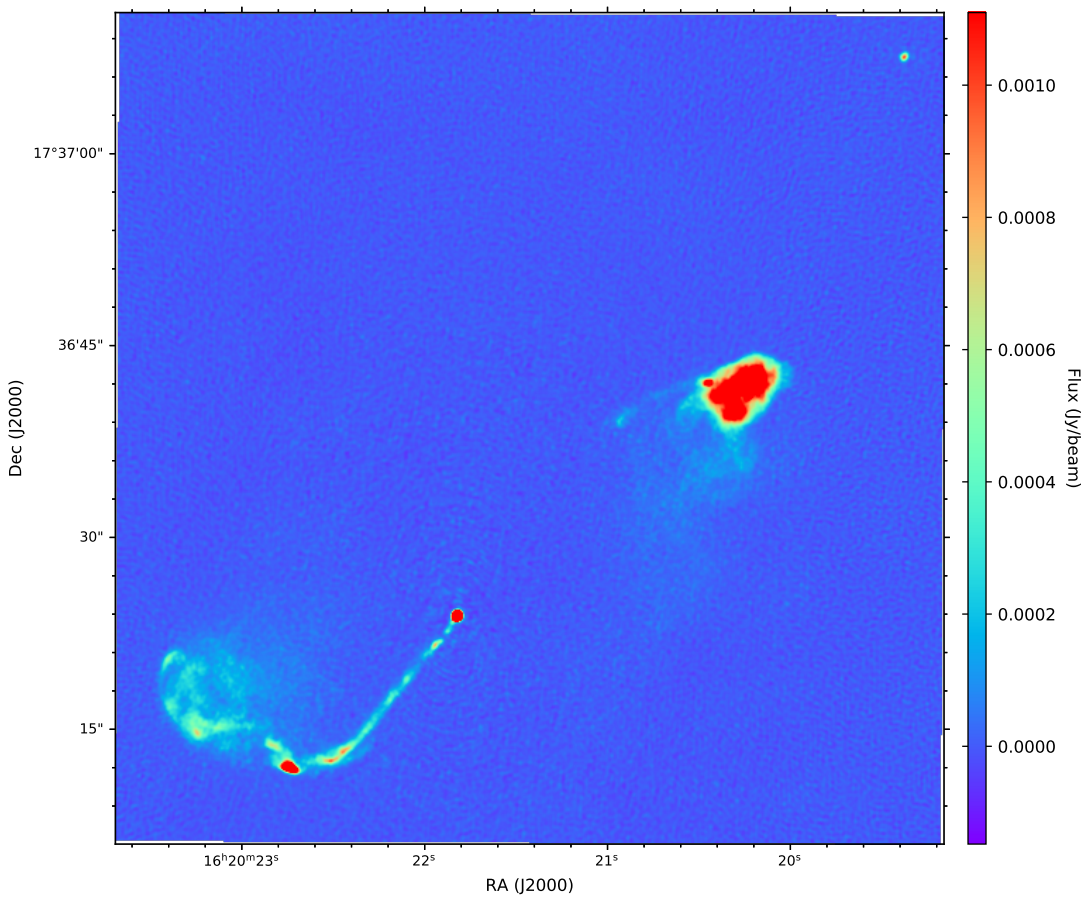

Figure 4.11: Total intensity map of 3C 334 produced from VLA observations at 4.9 GHz with A and B configurations. The FITS image was provided by Dr. Robert Laing (private communication) from his work on Bridle et al. (1994a).

4.1.3 The Spectral Index Map

Before creating a spectral index map, the C-band VLA map was regridded to J2000 coordinates. The L-band e-MERLIN plus multi-configuration JVLA image was smoothed to the VLA C-band resolution (0.″35) in CASA using the task IMSMOOTH. The smoothed 1.5 GHz e-MERLIN with JVLA image was then regridded to match the 5 GHz VLA image shape (see Table 4.2). A plot of the intensity distribution along the jet from the core E down to N1 for both the 1.5 GHz and 5 GHz maps is shown in Fig. 4.12. With the task COMB the C-band and L-band data were combined to create the spectral index map of 3C 334 shown in Fig. 4.13. The error map of the spectral index is provided as Fig. 4.14. A comparison between the spectral index map and the total intensity distribution at the southeast lobe and the northwest head at 0.″35 resolution is shown in Fig. 4.15a and Fig. 4.15b.

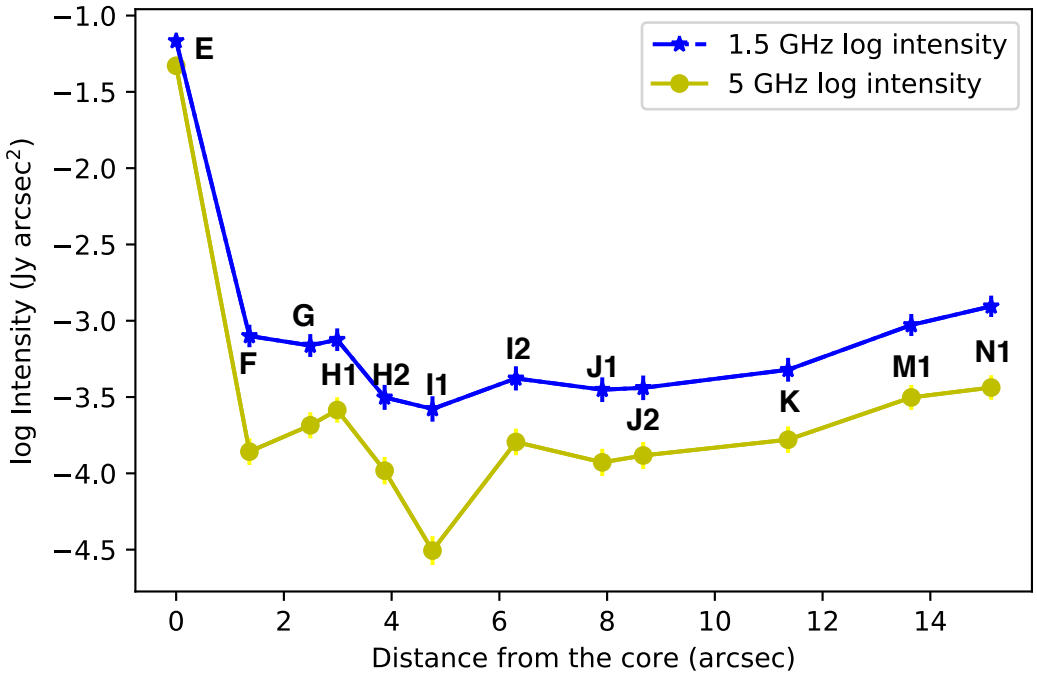

Figure 4.12: This plot shows the change in intensity along the straight jet in the 1.5 GHz and 5 GHz radio maps at a common resolution (0.″35 FWHM). Intensity values were taken at the centre of each feature from the core E through knot N1. The yellow circles represent data from the 5 GHz VLA map. The blue stars represent data from the 1.5 GHz e-MERLIN and JVLA map. Labels on the peaks correspond to the knots shown in Fig. 4.5.

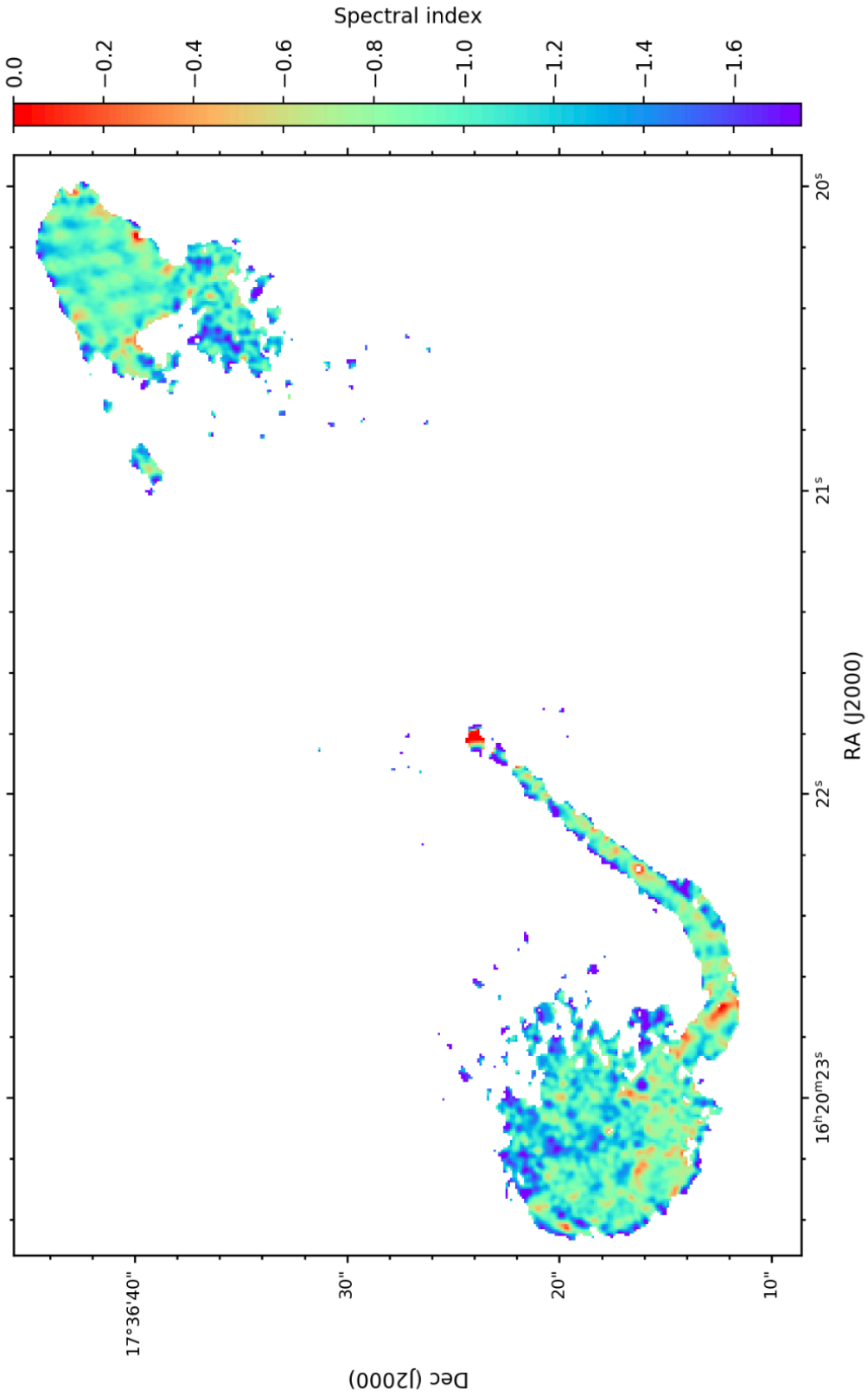

Figure 4.13: Spectral index map of 3C 334 using the 1.5 GHz e-MERLIN with JVLA data and the 5 GHz VLA data at a resolution of 0.″35 by 0.″35. The cut level of the 5 GHz map was 45 μJy and the 1.5 GHz map was clipped at 60 μJy.

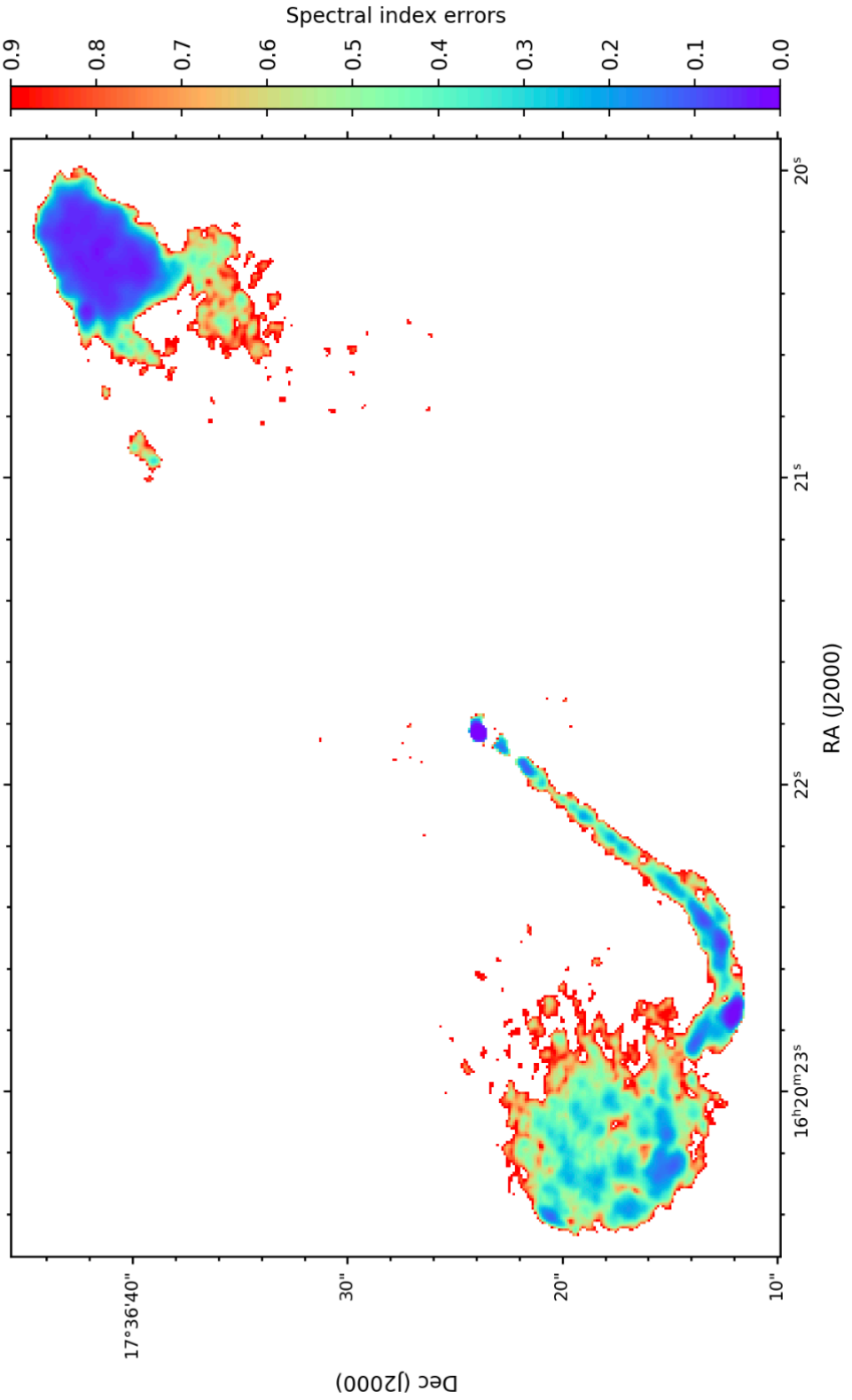

Figure 4.14: Spectral index eror map of 3C 334 using the L-band e-MERLIN with JVLA data and C-band VLA data at a resolution of 0.″35 by 0.″35.

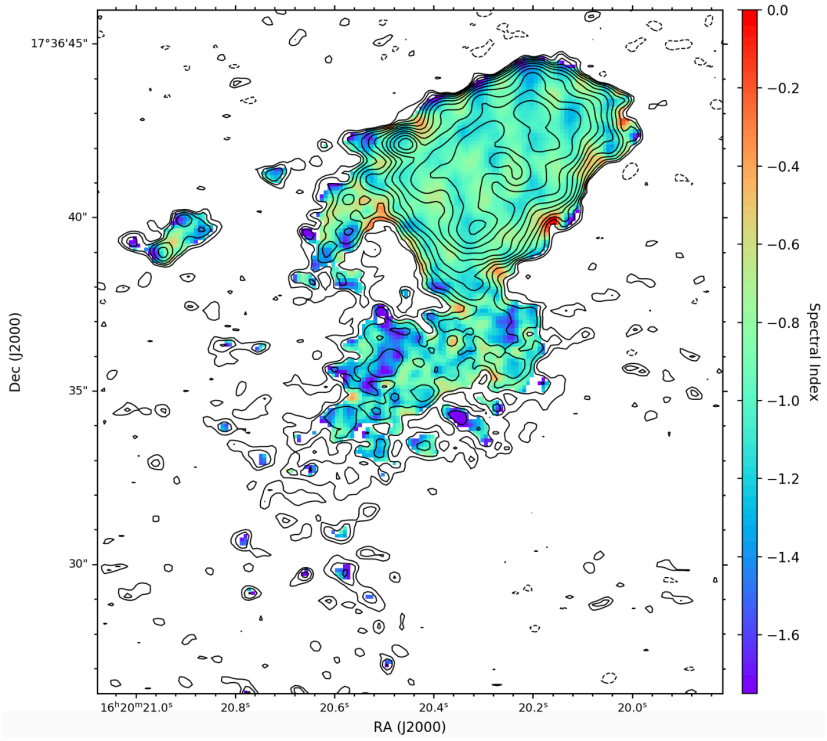

(a)

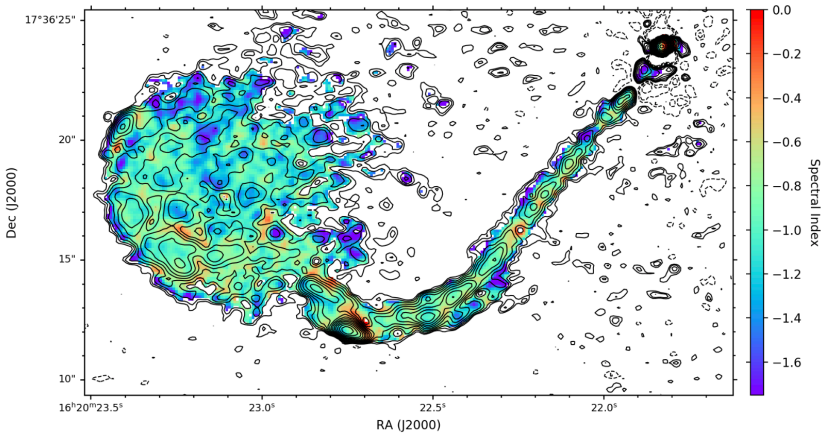

(b)

Figure 4.15: (a) Total intensity distribution (contours) superimposed on spectral index (colour) for the head of 3C 334 at the northwest lobe with a resolution of 0.″35 by 0.″35. Contours are drawn at -4, -2, -1 (dotted), 1, 1.414, 2, 2.828, 4, 5.657, 8, 11.31, 16, 22.63, 32, 45.25, 64, 90.51, 128, 181.0, 256, 362.0, 512, 724.1, 1024, 1450, 2048, 2900, 4096, and 5790 times 150 μJy per CLEAN beam area. (b) Total intensity distribution (contours) superimposed on spectral index (colour) for the southeast lobe and jet.

4.1.4 Transverse Profiles of the Jet

In order to derive accurate transverse intensity profiles, it was necessary to smooth the image of the jet along its length. The final calibrated e-MERLIN plus JVLA image was smoothed to a resolution of $1\overset{''}{.}01 \times 0\overset{''}{.}24$ at a position angle of -37°.09 using the task IMSMOOTH (see Fig. 4.16a). Transverse profiles of total intensity I along the straight jet were produced using the interactive image viewing tool VIEWER in CASA. A line profile of the surface brightness was taken at 29 points along the jet, with slice 1 located closest to the core and slice 29 located near hotspot O in the southeast lobe. Slices were taken orthogonal to the local jet direction, as shown in Fig. 4.16b. Beginning near slice 25, the close proximity of feature L to the jet required a way to separate the emission of the two peaks. Smaller slices were taken so as not to include L when possible. In cases where the emission was too close to isolate without losing information on the jet, deconvolved FWHM values were obtained from a Gaussian fit to the brightest peak. Plots of the surface brightness across the jet are shown in Fig. 4.17. A Gaussian has been fitted to the data and is shown as a dotted blue line in the plots. Errors on the flux densities were derived from

$$\sigma_S = \sqrt{(0.1 * S_\nu)^2 + (\sigma_{rms})^2},$$

where $0.1S_\nu$ is a 10% calibration error on the flux density measurements S_ν and σ_{rms} is the rms noise measured within CASA.

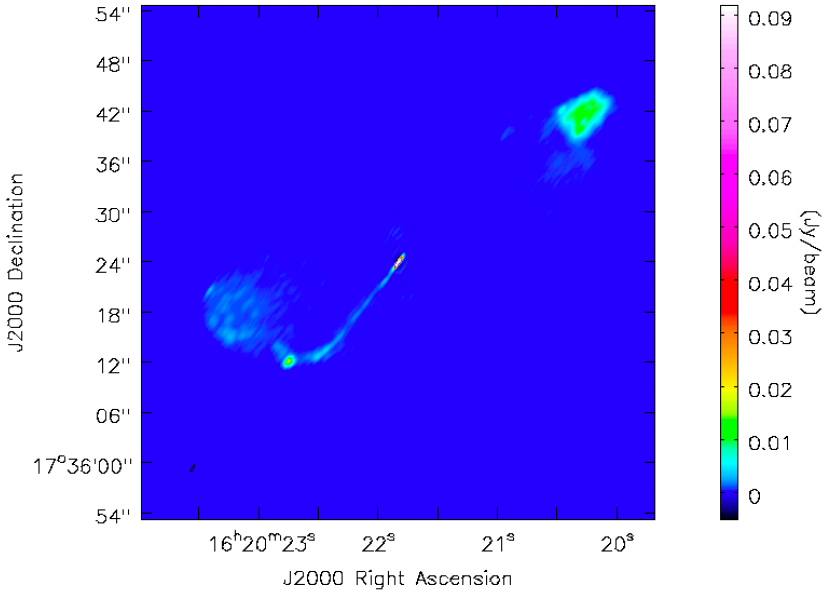

(a)

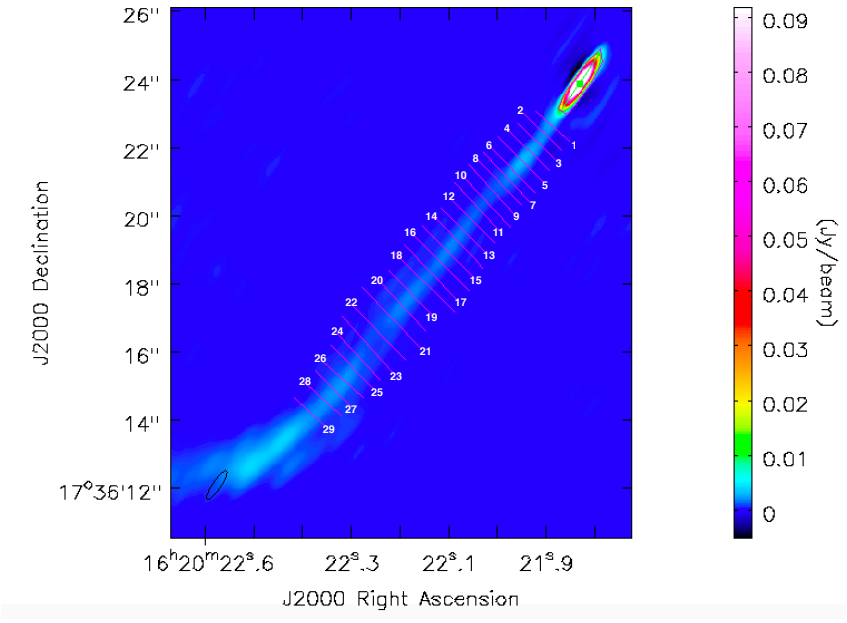

(b)

Figure 4.16: (a) Total intensity map of 3C 334 smoothed to a resolution of $1\farcs01 \times 0\farcs24$ resolution. (b) Locations of the 29 line slices used for 3C 334's transverse jet profile.

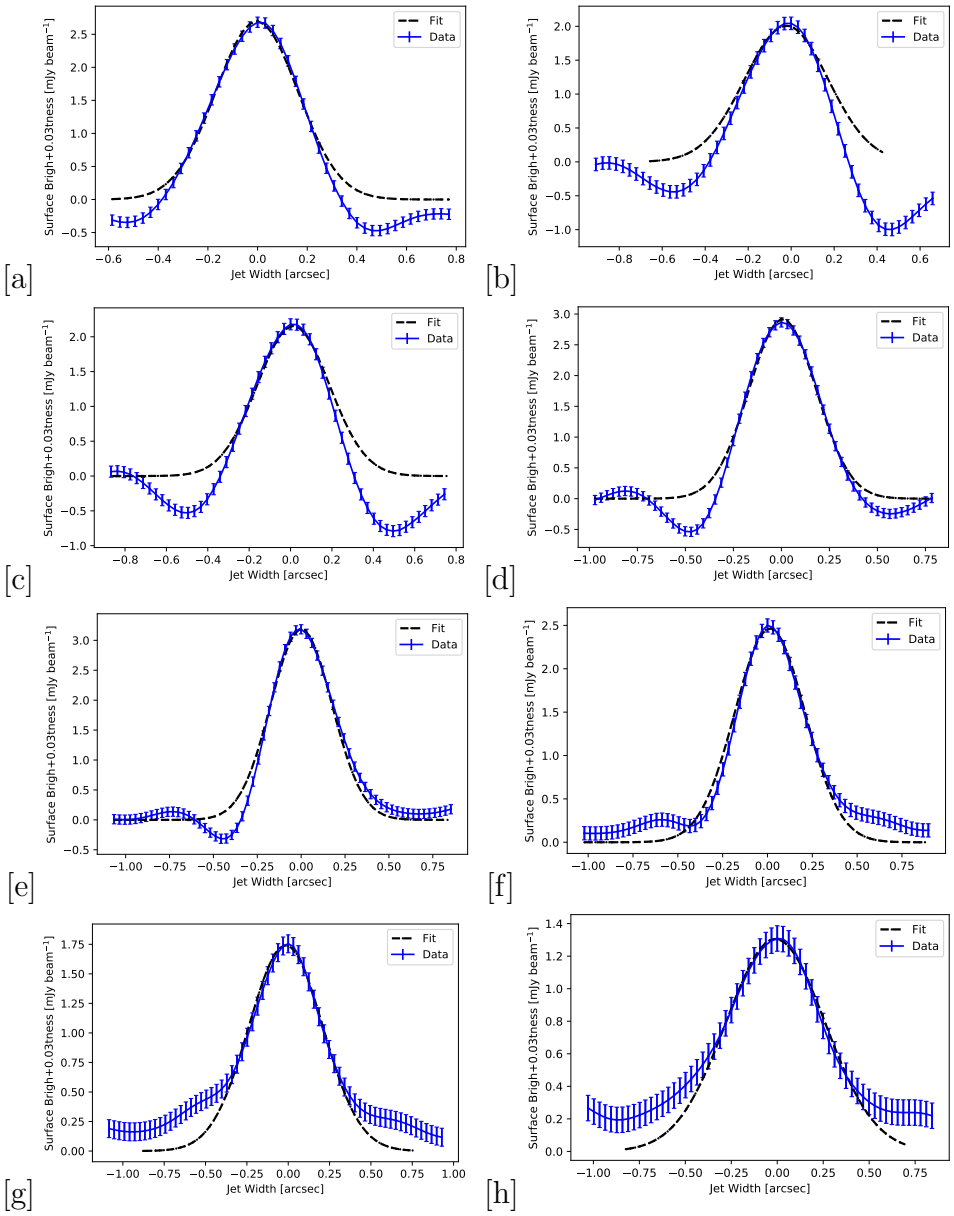

Figure 4.17: 3C 334 total intensity transverse profiles corresponding to slices 1−8 in Fig. 4.16b, (a) slice 1, (b) slice 2, (c) slice 3, (d) slice 4, (e) slice 5, (f) slice 6, (g) slice 7, and (h) slice 8.

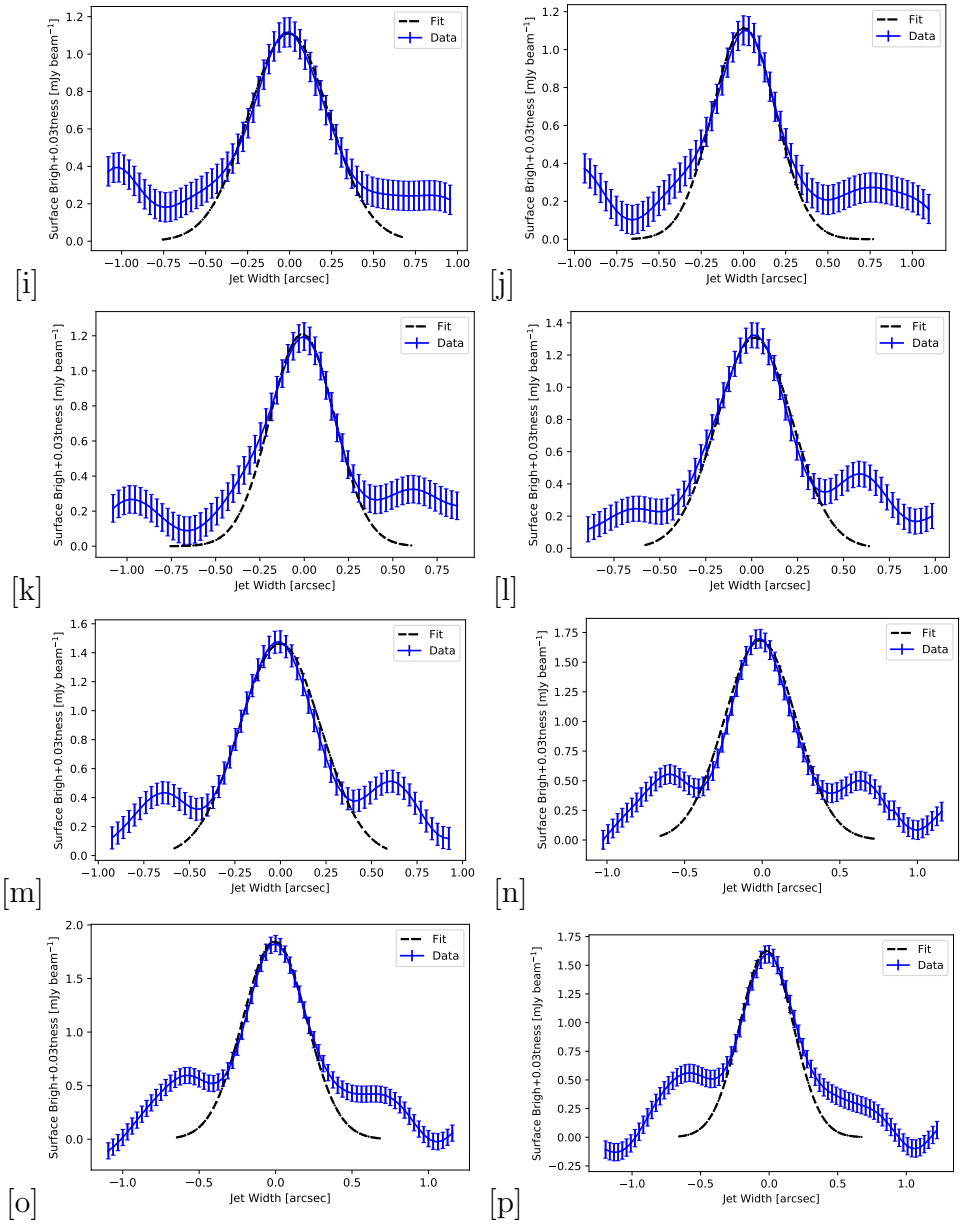

Figure 4.17: 3C 334 total intensity transverse profiles corresponding to slices 9−16 in Fig. 4.16b, (i) slice 9, (j) slice 10, (k) slice 11, (l) slice 12, (m) slice 13, (n) slice 14, (o) slice 15, and (p) slice 16.

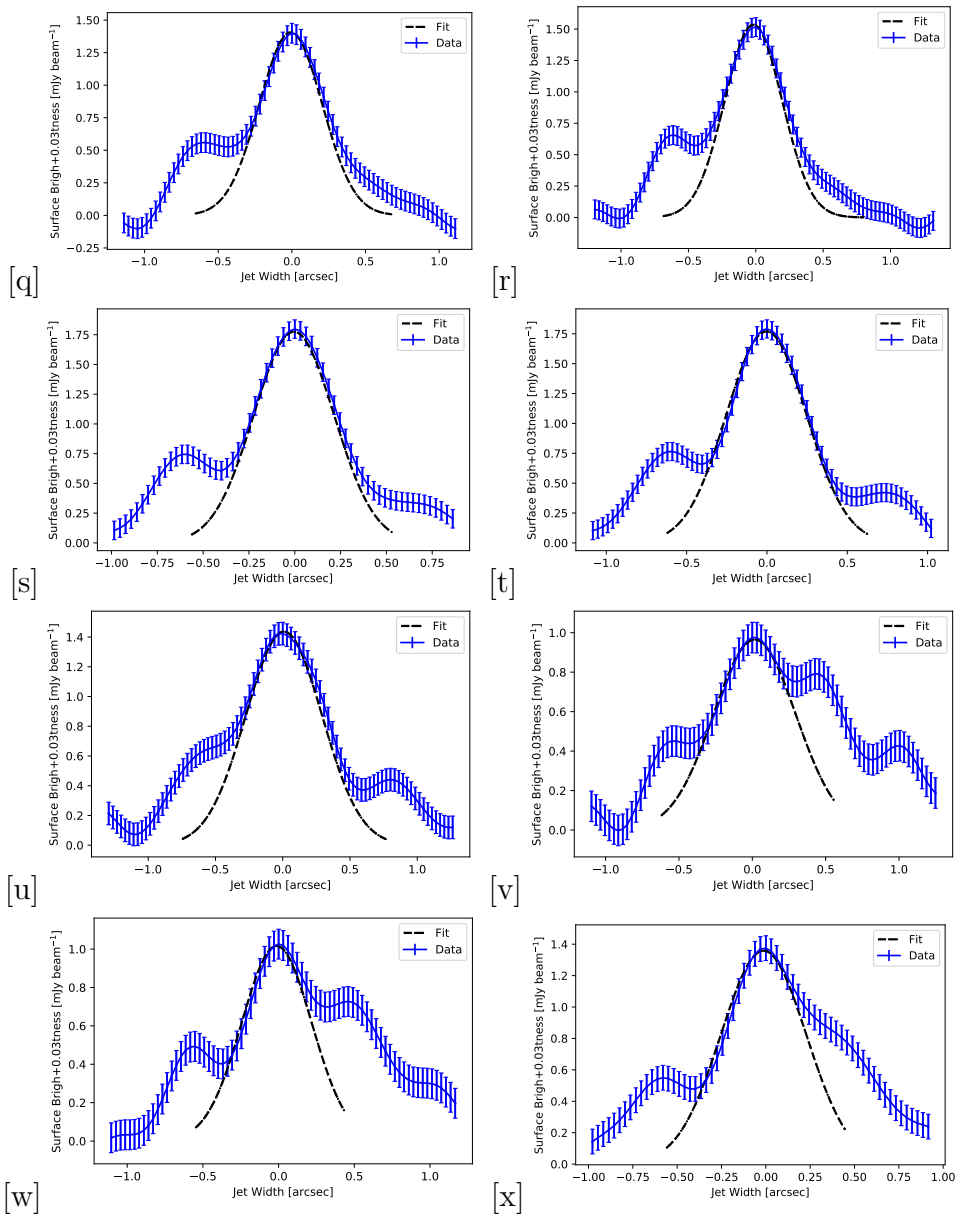

Figure 4.17: 3C 334 total intensity transverse profiles corresponding to slices 17−25 in Fig. 4.16b, (q) slice 17, (r) slice 18, (s) slice 19, (t) slice 20, (u) slice 21, (v) slice 22, (w) slice 23, and (x) slice 24.

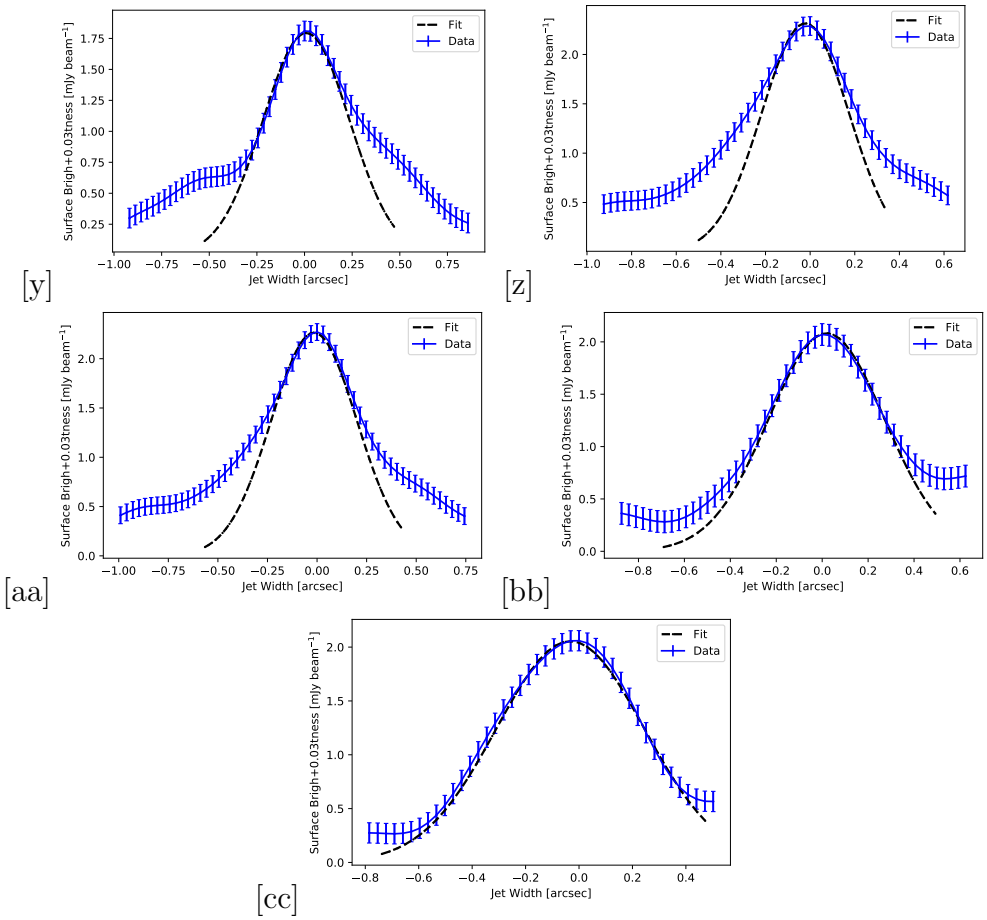

Figure 4.17: 3C 334 total intensity transverse profiles corresponding to slices 25−29 in Fig. 4.16b, (y) slice 25, (z) slice 26, (aa) slice 27, (bb) slice 28, and (cc) slice 29.

4.2 Discussion

4.2.1 Total Intensity Maps

Details regarding structure sizes at 1.5 GHz with a resolution of $0\farcs24 \times 0\farcs14$ are provided in Table 4.3. Discussion of the FRII type quasar can be split into three parts corresponding to the morphological components of the source: (1) the large-scale emission and hotspots, (2) the knots and structure along the jet, and (3) the core.

Lobes and Hotspots

Figures 4.3−4.6 reveal a distinct difference between the northwest and southeast lobes. While the southeast lobe appears to be composed of fragments of emission, the head of the northwest lobe has a well-defined outer boundary. The main body of the head begins ∼175 kpc from the core and extends to ∼ 215 kpc at its most northern point. The southeast boundary of the head is surprisingly straight. The suggestion by Bridle et al. (1994a) that features C and D are evidence of a counterjet is reasonable as it mostly aligns with core and hotspot C (see Fig. 4.6). At e-MERLIN resolution, component B is the brightest feature embedded in the northwest hotspot. Compared to the VLA 5 GHz map, B and the surrounding structure is more complex in the e-MERLIN with JVLA 1.5 GHz map. In the Bridle et al. (1994a) map B is an unresolved structure. In the e-MERLIN maps this feature is resolved into two peaks. North of B are small features that weave into the edge-brightened boundary. From the radio maps it is clear there is asymmetry in the jet and counterjet side lengths. Environmental factors can produce shorter jet side lobes (see Ch. 5).

Table 4.3: Sizes of various structures in 3C 334.

Region	Deconvolved FWHM	size (kpc)
Total source size[a]	$48\farcs5\pm0\farcs19$	326±1.3
Straight jet (length)[a]	$12\farcs3\pm0\farcs1$	83±0.75
Straight jet (avg. width)[a]	$0\farcs66\pm0\farcs23$	4.44±1.5
Northwest head (major)	$4\farcs08\pm0\farcs09$	32 ± 0.6
Northwest head (minor)	$2\farcs9\pm0\farcs06$	19 ± 0.4
Southeast lobe (major)	$10\farcs1\pm0\farcs23$	67.9±1.5
Southeast lobe (minor)	$7\farcs16\pm0\farcs17$	48.2 ± 1.1
Core (major)	148±6.7 mas	0.99±0.05
Core (minor)	35±22 mas	0.23±0.15
Hotspot O (major)	760 ± 39 mas	5.1 ± 0.26
Hotspot O (minor)	242 ± 17 mas	1.6 ± 0.11

[a] Projected source sizes were measured using the ruler feature integrated in CASA viewer.

I have estimated the length of the southeast lobe to be 67.9±1.3 kpc and the width to be 48.2±1.1 kpc in the 1.5 GHz map. In the vicinity of the southeast lobe there is only one major hotspot O (see Fig. 4.4a). The emission at O is highly elongated along the curve of the jet and brighter along the boundary of the curve. The peak flux density at O is 7.1±0.71 mJy beam^{-1}.

Hotspot O is interpreted to be the high-pressure region where the jet impacts a cavity wall (Wilson, 1989). In this picture, a strong shock begins in the direction of the jet and then undergoes a sharp directional change. In Fig. 4.10 a V-shaped feature of dense contours is visible from the start of the hotspot that traces around the edges. At $\sim0\farcs34$ beyond the peak of the hotspot is the fainter feature P1. There is a small gap in emission between N2 and O. The direction of the emission at N2 does not point directly towards O but instead points towards P1. This suggests that the jet shock does not go across the whole of the jet, thus only part of the jet is illuminated as a hotspot. The emission from P1 and P2 are embedded within the southeast lobe. This is consistent with claims by Gilbert et al. (2004). There is another gap in emission between P1 and P2. For reasons discussed on the following page, P2 may align with the position of the jet at an earlier time (see Fig. 4.18). If so, feature P2 may be positioned where the old jet terminated (Cox et al., 1991).

The presence of the secondary hotspot B in the northwest lobe is not unusual for FRII quasars and radio galaxies (e.g., Laing, 1982; Leahy et al., 1997). Assuming the primary hotspot C is the bright, compact feature located where the jet terminates (see §1.2.3), a different process is thought to be forming secondary hotspots. Several models have been developed to explain secondary hotspots by considering jet precession and the escape of material from the primary hotspot. In the first generally accepted model, often referred to as the 'dentist's drill' model, a jet terminating into a hotspot can alter its direction before the hotspot has had time to fade to the surrounding environment's surface brightness (Scheuer, 1982). The time required to do so has been found to be $\approx 10^5$ years due to expansion losses (Carilli et al., 1988). In this scenario the jet will extend and widen the lobe from its original position towards its new direction, creating a more complex structure (e.g., Lonsdale and Morison, 1983). The newest hotspot becomes the primary hotspot and the disconnected secondary hotspot represents the site of the previous termination point of the jet. Secondary hotspots no longer have an energy supply, thus no longer have particle acceleration. This produces a steeper spectrum in the secondary hotspot compared to the primary hotspot. Since hotspots are overpressured regions within a lobe, the secondary hotspot will rapidly expand, creating a more diffuse structure than the primary hotspot. In numerical simulations produced by Cox et al. (1991), secondary hotspots produced by means of the 'dentist-drill' model may be supplied with energy and material long after the jet has disconnected from the former hotspot. Hotspots produced via the dentist-drill model typically are in sources characterised by: (i) wider lobes than models predict (e.g., Cox et al., 1991), (ii) jets that deviate from a straight path, and (iii) recessed hotspots, that is hotspots embedded within the lobe away from the leading edge (e.g., Cox et al., 1991; Fernini, 2019).

Additional models suggest secondary hotspots may be energised through processes induced by the jet, which continues to be a strong component to secondary hotspot formation in all models. Variations of this model include the the beam-deflection model (Lonsdale and Barthel, 1986) and the 'splatter-spot' model (Williams and Gull, 1985). In the case of the former, the jet is forced to alter its direction of motion when it collides with a cloud. In the splatter-spot model the jet's direction is changed once the jet collides with the opposite wall of the previously created cocoon (Williams and Gull, 1985). The defection of the jet allows some material to escape the primary hotspot like a splatter to

provide energy to the secondary hotspot. This may assist with particle acceleration in secondary hotspots (e.g., Williams and Gull, 1985; Hardcastle et al., 2007). Splatter-spots create secondary hotspots that are larger and weaker than hotspots created in a process like the dentist-drill model (Cox et al., 1991). The magnetic fields of primary hotspots will point towards the secondary hotspot when created by splatter-spots (Lonsdale and Barthel, 1986). Simulations have shown that a disconnected hotspot previously formed at the end of a jet (like the dentist drill model) can be powered by an inflow of jet material from the new primary hotspot (similar to the splatter-spot model) (Cox et al., 1991). Hotspots formed through the splatter-spot process will show signs of particle acceleration (a spectral index typically flatter than $\sim \alpha = -1.0$) due to the continuous supply of material (Looney and Hardcastle, 2000). These structures are elongated parallel to the cocoon wall and perpendicular to the path leading to the primary hotspot (Cox et al., 1991).

Figure 4.18 shows a comparison between features in the northwest and southeast lobes at e-MERLIN resolution that may provide additional clues to jet precession and hotspots. In the high-resolution e-MERLIN maps the primary hotspot C is elongated towards the jet, which curves slightly from the core at some point near feature D. Although the counterjet is not detected in any of the maps, the low-resolution VLA map (see Fig. 4.1b) shows that D is elongated towards the core. As it enters the lobe the counterjet begins to curve around the edge of the diffuse lobe. The S-shape is consistent with jet bending models and observations (e.g., Bridle and Perley, 1984; Ekers et al., 1978; Cox et al., 1991; Hardee and Norman, 1990). The primary hotspots O (southeast lobe) and C (northwest lobe) are aligned through the core axis. The secondary hotspot B aligns with feature P1 with only a small deviation from the straight axis. There are notable differences between the structures P1 and B though. The secondary hotspot B forms a C-shaped structure embedded in the head of the lobe that is disconnected from the primary hotspot and recessed from the leading edge of the head structure (similar to the dentist-drill model). The curve of B runs somewhat parallel to the boundary of the northwest head and perpendicular to the line of sight to C. These characteristics are observed in splatter-spot models (Cox et al., 1991). Feature P1 is elongated towards the jet at N2 and hotspot O near the edge of the southeast lobe boundary. Drawing a line from features P2 and Q towards the location of where the trail of emission opposite the counterjet is in low-resolution

maps, there appears to be an alignment between the features. This also suggests that Q and P2 could be remnants of an old hotspot, although there is no former hotspot in the northwest lobe that corresponds to Q or P2. Secondary hotspots produced by splatter-spots tend to be edge-brightened away from the primary hotspots (Laing, 1982). However, this does not appear to be the case for the secondary hotspots of 3C 334. The polarization vectors from Bridle et al. (1994a) (see Fig. 4.19) show a gradual change in direction from the primary hotspot C towards the secondary hotspot B. This is even more evident in the polarization vectors from hotspot O to P1 (see Fig. 4.20), which is consistent with splatter-spot models. Because there is evidence that P1 is in the path of some of the jet, P1 is not a true secondary hotspot based on the formal definitions. Since hotspot B in 3C 334 appears to have mixed characteristics, the secondary hotspot may best be described by a process similar to the modified dentist-drill model by Cox et al. (1991). A precessing jet created the new primary hotspot C, while C may still be feeding the old primary hotspot B during short events.

Jet

As stated in §4.1.1, a counterjet is not visible in the contour maps until feature D in the northwest lobe. A ratio of the integrated flux over the straight jet (S_J) to the integrated flux in the counterjet (S_{CJ}) gives $S_J/S_{CJ} = 9.2 \pm 2.2$. This ratio was based on the assumption that the jet and counterjet are symmetric. Additional length was added to the counterjet side to account for a longer counterjet and included flux until feature D (see Fig. 4.21). A comparison of Fig. 4.5 to the 5 GHz VLA map shown in Fig. 4.2a reveals more complex substructures in features M1, N1, and L. In the rest of this section, the discussion refers to the 1.5-GHZ e-MERLIN + JVLA map unless otherwise stated. The higher resolution image features I1, I2, J1, and J2 correspond to components not resolved clearly in the 5 GHz map. Before reaching hotspot O the jet widens around knot M1 into intricate, smaller knots (M2,N2) that surround the main components M1 and N1. Extending nearly parallel to knot M1 is a line of small features that make up the nearly straight line of emission L. Similar features have been observed in other astrophysical jets such as those produced in HH 34 (Herbig-Haro object) and the radio galaxy 3C 33.1 (Bally, 2016; Clarke and Burns, 1991). In both cases a bow shock leading a supersonic jet produces the "swept-back wings" features. Feature L is embedded within the lobe though.

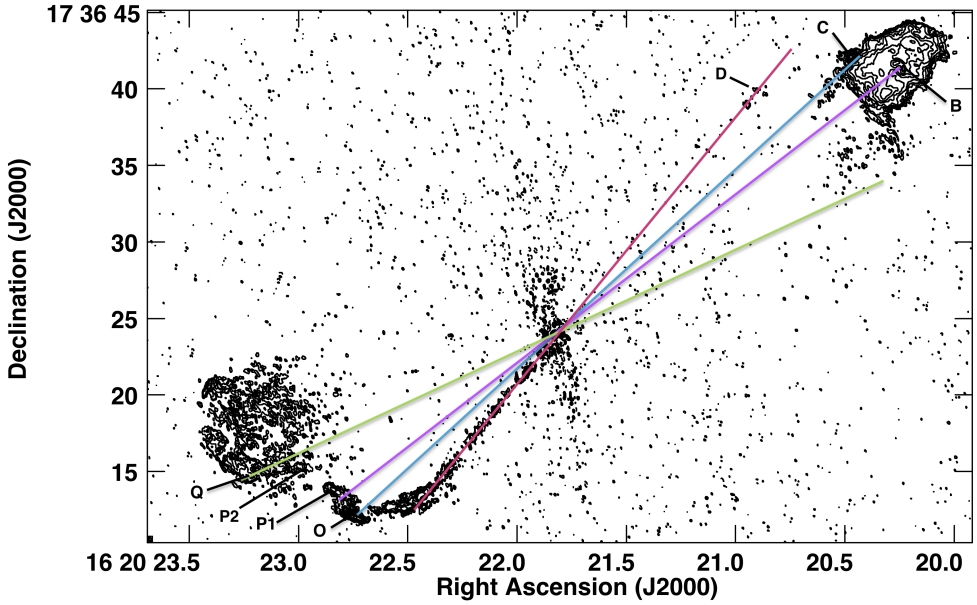

Figure 4.18: Many features in the southeast lobe in 3C 334 show some alignment with features in the northwest lobe. The primary hotspot C shows alignment with the primary hotspot O. The secondary hotspot B corresponds to feature P1 with only a small deviation from the axis. Although features P2 and Q in the southeast lobe and the northwest faint, diffuse lobe are not as noticeable in the e-MERLIN map, there appears to be a correlation between P2/Q and the edge of the northwest lobe where the jet may have have previously been positioned. Also shown is the alignment of the jet with feature D, believed to be a knot in the counterjet.

Core

With the e-MERLIN resolution the core in 3C 334 is resolved. Between the core and knot F is a small gap of emission. The structure has an angular size of $148 \pm 6.7 \times 35 \pm 22$ mas. The configuration of the e-MERLIN array results in an elongated beam. The core lies at position α =16h20m21.83, δ =+17°36′23.″91 with a peak flux of 141 ± 14 Jy beam^{-1}.

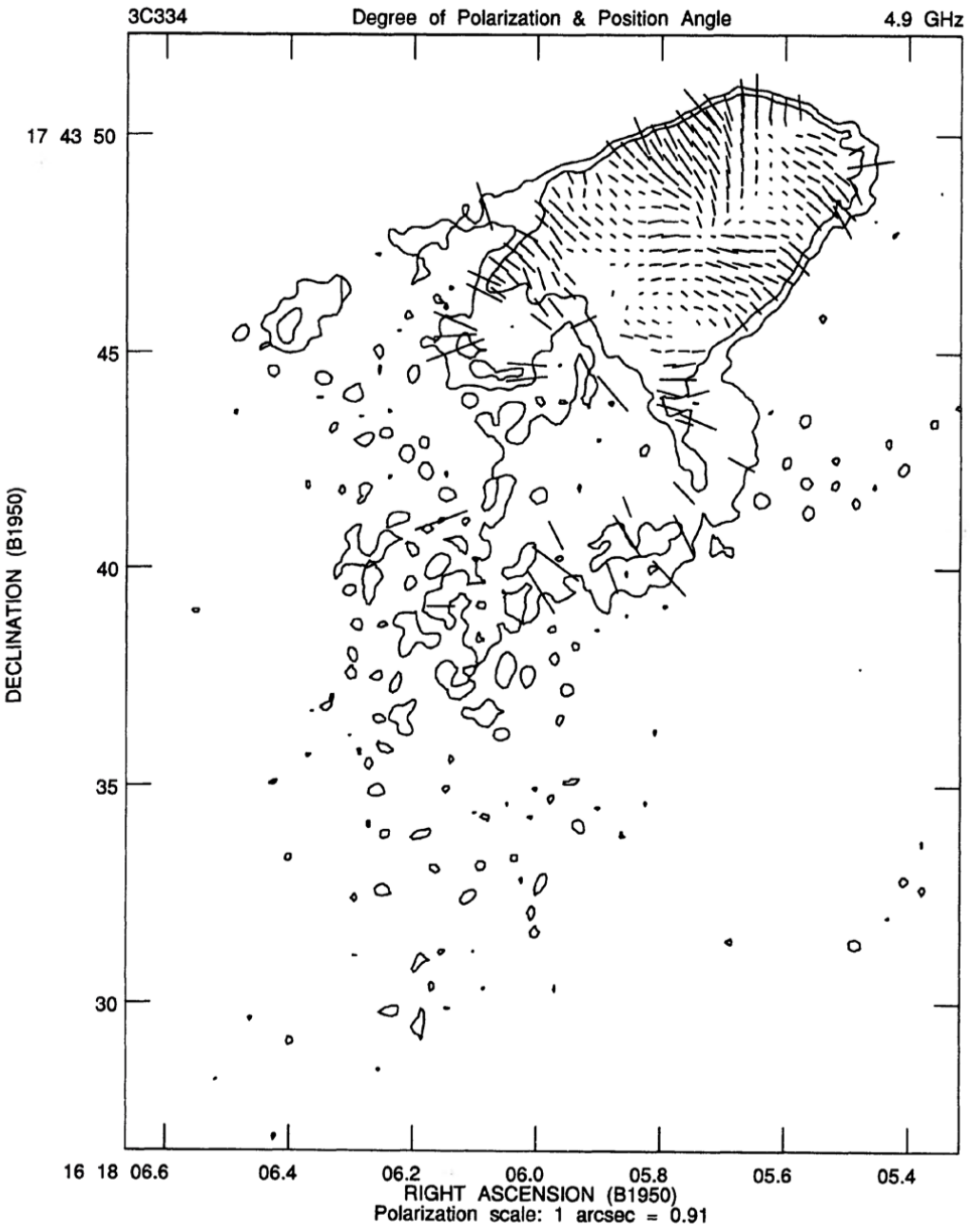

Figure 4.19: Linear polarization map of the northwest head of 3C 334 at VLA resolution. The polarization vectors near the inner boundary of hotspot C begin to align parallel to the lower head boundary. Before the vectors turn to point towards hotspot B. Image is reproduced from Bridle et al. (1994a).

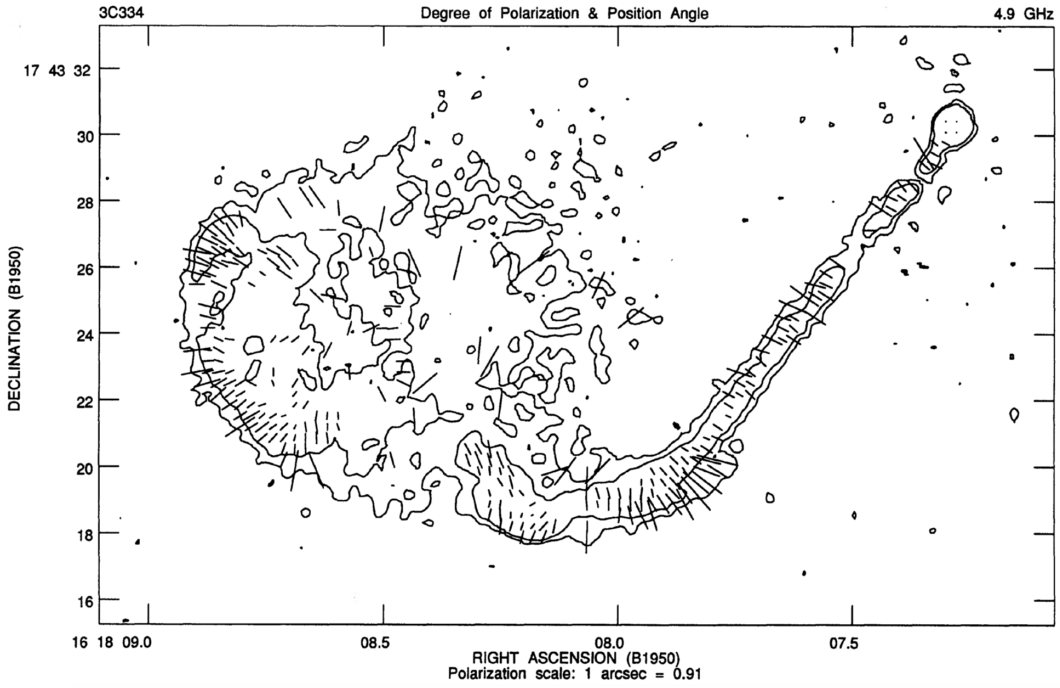

Figure 4.20: Linear polarization map of the southeast lobe of 3C 334 at VLA resolution. The polarization vectors at P1 are pointed in the direction of the primary hotspot O. Image is reproduced from Bridle et al. (1994a).

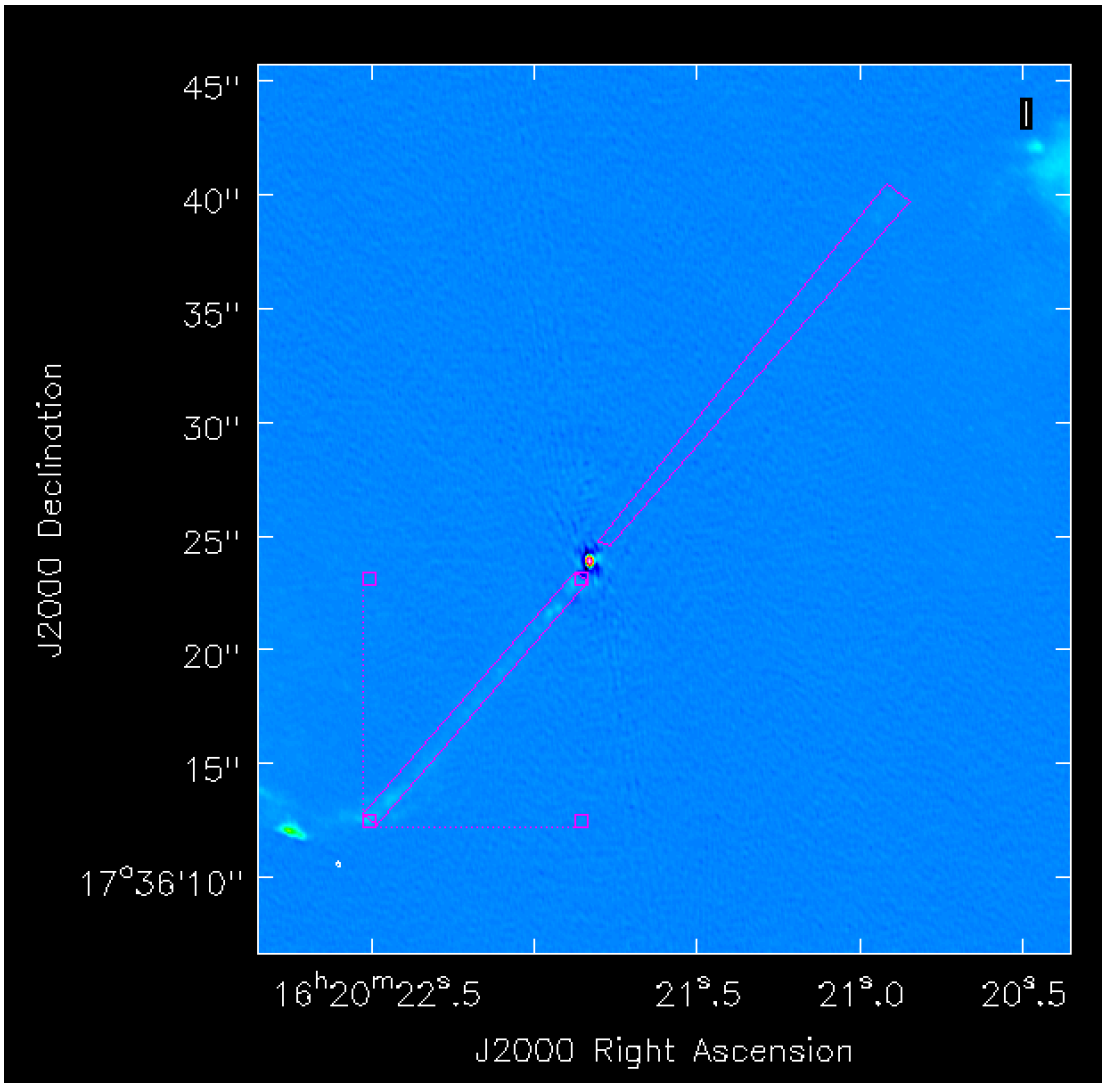

Figure 4.21: The straight portion of the counterjet was assumed to be symmetric with the straight part of the jet so that an upper limit on the ratio of fluxes could be calculated. The integrated regions were equal in width but extra length was added to the counterjet.

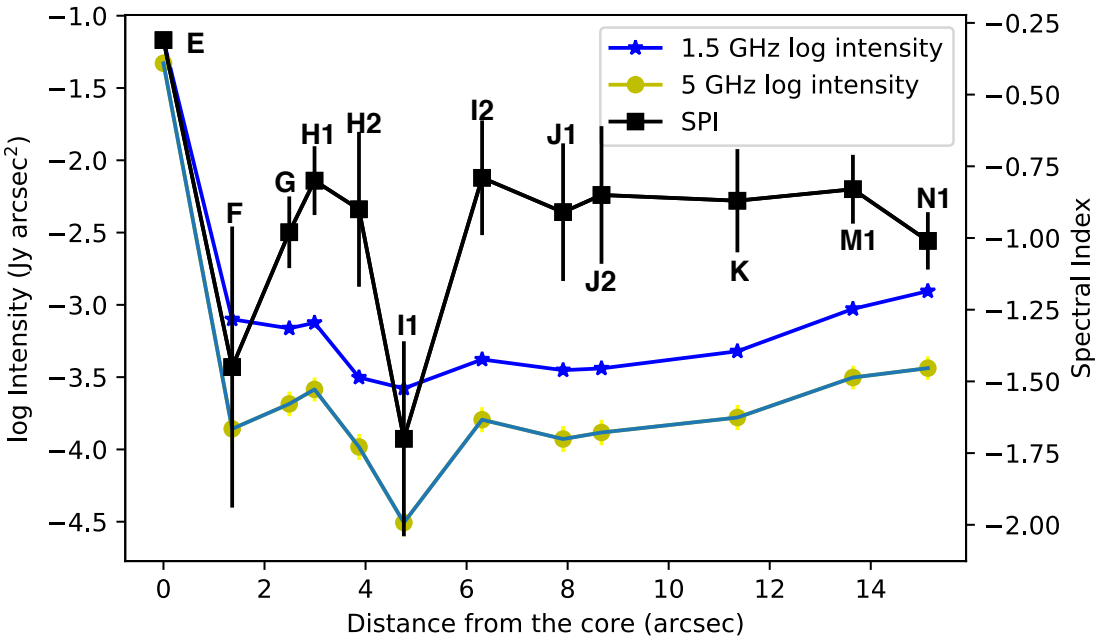

Figure 4.22: The black squares represent the change in spectral index α at features along the jet in 3C 334 at 0.″35 resolution. The blue stars represent the change in intensity at 1.5 GHz along the same path. The yellow dots represent the 5 GHz data from Bridle et al. (1994a). Locations of the corresponding knots are labeled. Data were taken from images convolved with a 0.″35 resolution beam.

4.2.2 The Spectral Index Map

A detailed map of the spectral index of 3C 334 is shown in Fig. 4.13. Figure 4.22 is provided to give better insight into how the spectral index changes along the jet from the core (E) to N1. The changes in the spectral index along the jet, shown as a black line, are compared to changes in intensity along the jet with the knots labeled for the 1.5 GHz map, shown as blue stars. A very small misalignment of the target between two epochs can produce steeper spectral indices in many features along the jet. Therefore, the spectral index values presented in this thesis should be taken cautiously.

The spectral index map reveals:

(i) On average the spectral index of the core is $\alpha \approx -0.31 \pm 0.01$. This value should not be fully trusted because of calibration errors surrounding the core in the two maps.

(ii) From knots G−H2 and I2−N1 the spectral indices range from ~ -0.65

to ~ -1.0. Feature F and I2 are the exceptions with spectral indices between-1.25 and -1.75. The steep spectral index at F is due to its close proximity to the core and at I1 because it is much fainter than the other knots.

(iii) The spectral index of hotspot O was determined to be $\sim -0.6 \pm 0.1$. The edge along the path from N2 to P1 has the flattest-spectrum of the hotspot. The central region of hotspot O lies southeast of the flat spectral feature pointing towards P1. This feature in the spectral index map is also present in Dennett-Thorpe et al. (1997), indicating it is real.

(iv) P has a spectral index between $\alpha \sim -0.8 \pm 0.2$ and $\alpha \sim -0.9 \pm 0.2$.

(v) The emission within the lobe shows $\alpha \approx -1.1 \pm 0.3$ but increases around the edges furthest from the jet. Emission in the extended lobe is below the noise in the e-MERLIN+JVLA map. The errors increase where the emission is weakest in the 1.5 GHz map.

(vi) The edge of the straight jet appears to have steeper values for α. There is a slight spectral gradient across the jet that is likely the result of a small misalignment between the jets in the e-MERLIN and JVLA maps.

Figure 4.15a compares the total intensity distribution with the spectral index of the northwest lobe at $0\farcs35$ resolution. Spectral index features of the northwest lobe are:

(i) The secondary hotspot B has a spectral index of $\alpha \sim -0.8 \pm 0.06$. Because B is relatively faint, quite a lot of emission at the "B" pixels is from the underlying lobe emission. The spectral index value from the maps is then an intermediate value between the lobe spectral index and the hotspot B by itself. This means that the emission is even flatter than the quoted value. Therefore, the spectral index indicates that particle acceleration is still ongoing in B. This is additional evidence in support of B being a secondary hotspot that is still being energised by the primary hotspot C.

(ii) Most of the diffuse emission in the head of the northwest lobe shows that $\alpha \sim -1.0 \pm 0.06$. Similar to the southeast lobe, spectral indices near the edge should not be trusted as the errors are larger.

(iii) The spectral index of the primary hotspot C is -0.5 ± 0.2.

4.3 Analysis of Transverse Profiles

Transverse profile of total intensity at slices along the jet are given in Fig. 4.17. Table 4.4 gives the maximum flux and deconvolved FWHM at each slice as well as the distance from the slice to the peak flux position in the core. Slice 5 is the brightest in the straight jet, with a peak flux of $\sim 3.18 \pm 0.32$ mJy beam^{-1} at a distance of $\sim 2\farcs83$ from the core.

The apparent opening angle of the jet α_{app} was calculated from

$$\alpha_{app} = 2 \arctan[0.5(D^2 - b_p^2)^{1/2}/\theta], \tag{4.2}$$

where D is the FWHM of the Gaussian fitted to the transverse profiles, θ is the angular distance from the slice to the core, and b_p is the beam size along the position angle p of the jet slice (Pushkarev et al., 2011). The quantity $(D^2 - b_p^2)^{1/2}$ is the deconvolved FWHM transverse the jet. Plots of the deconvolved FWHM ϕ and opening angle at each transverse profile's angular distance from the core are provided in Fig. 4.23. The apparent opening angle is $\sim 2\fdg8$ at the end of the straight jet. The jet widened at $\sim 4''$ and $\sim 9''$ from the core. These locations correspond to regions downstream from H2 and J2. Between $4'' \leq \theta \leq 7''$ the jet width is nearly constant. Overall, Fig. 4.23 shows that the opening angle is on average decreasing along the jet; thus, the jet is recollimating. This indicates that the jet is confined either by the lobe pressure or by magnetic forces (if there is a net current along the jet), and not in free expansion. It is most likely that 3C 334's jet is recollimated by lobe pressure, as this is more common for radio jets (e.g., Nalewajko and Sikora, 2008). A jet expanding freely in a low-pressure environment will suffer a decrease in thermal pressure. Jets are then reconfined when the internal pressure of the jet becomes lower than the external pressure (e.g., Gourgouliatos and Komissarov, 2018).

Table 4.4: Maximum flux, deconvolved FWHM (ϕ), and the distance from the core (θ) of the transverse profiles shown in Fig. 4.17. Values were taken at $1\farcs01\times0\farcs24$ resolution.

Slice	θ (arcsec)	Peak flux (mJy beam^{-1})	ϕ (arcsec)
1	$1\farcs32$	2.68±0.27	0.307±0.01
2	$1\farcs79$	2.043±0.2	0.362±0.02
3	$2\farcs17$	2.18±0.22	0.334±0.02
4	$2\farcs49$	2.86±0.29	0.336±0.02
5	$2\farcs83$	3.18±0.32	0.339±0.02
6	$3\farcs24$	2.49±0.25	0.401±0.02
7	$3\farcs49$	1.75±0.18	0.461±0.02
8	$3\farcs76$	1.31±0.13	0.562±0.03
9	$4\farcs07$	1.12±0.11	0.515±0.02
10	$4\farcs42$	1.10±0.11	0.445±0.02
11	$4\farcs77$	1.19±0.12	0.447±0.02
12	$5\farcs12$	1.32±0.13	0.465±0.02
13	$5\farcs49$	1.48±0.15	0.439±0.02
14	$5\farcs84$	1.69±0.17	0.458±0.02
15	$6\farcs25$	1.83±0.18	0.449±0.02
16	$6\farcs59$	1.59±0.16	0.437±0.02
17	$6\farcs98$	1.39±0.14	0.453±0.02
18	$7\farcs14$	1.52±0.15	0.498±0.03
19	$7\farcs89$	1.79±0.18	0.516±0.03
20	$8\farcs30$	1.79±0.18	0.547±0.03
21	$8\farcs81$	1.42±0.14	0.708±0.03
22	$9\farcs35$	0.98±0.10	0.661±0.03
23	$9\farcs93$	1.02±0.10	0.507±0.02
24	$10\farcs33$	1.37±0.14	0.478±0.02
25	$10\farcs61$	1.81±0.18	0.521±0.02
26	$11\farcs14$	2.29±0.23	0.473±0.02
27	$11\farcs54$	2.27±0.23	0.479±0.02
28	$11\farcs92$	2.01±0.20	0.553±0.02
29	$12\farcs29$	2.06±0.021	0.649±0.03

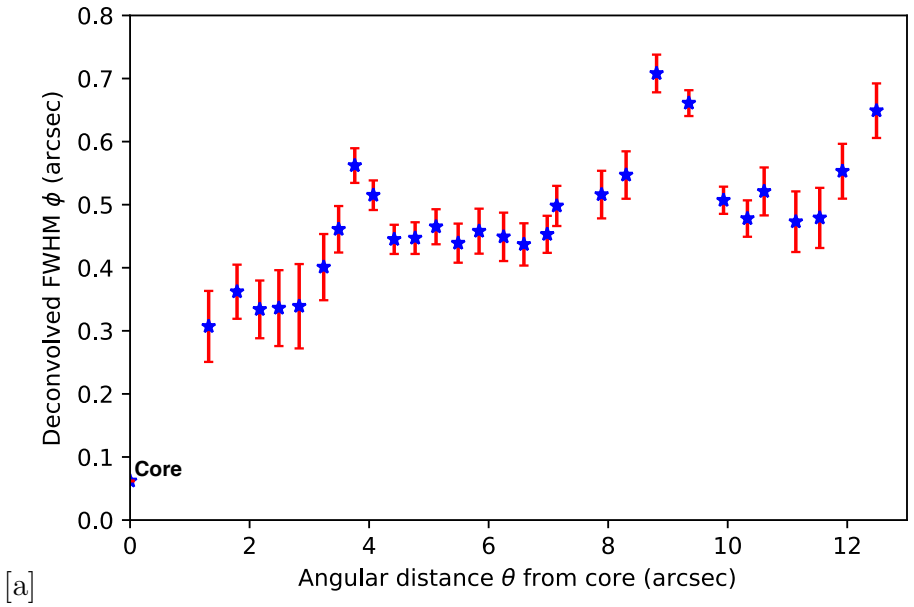

[a]

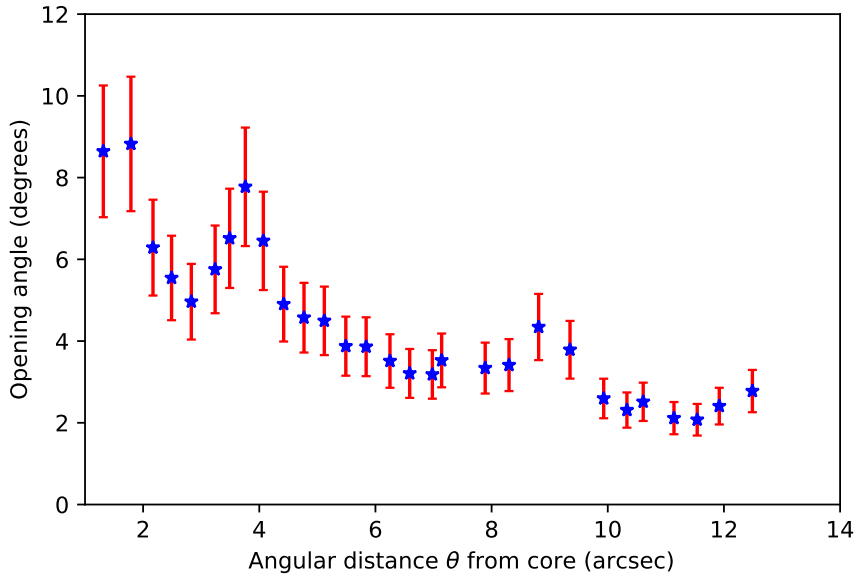

[b]

Figure 4.23: (a) The deconvolved FWHM (ϕ) versus angular distance from the core (θ). Values were taken from the transverse profiles at $1\farcs01\times0\farcs24$ resolution in Fig. 4.17. The deconvolved FWHM of the core is labeled on the plot. (b) A plot showing the apparent opening angle (α_{app}) along the jet from the core.

4.4 Summary

The high resolution e-MERLIN and JVLA map of 3C 334 shows an overall similar structure as the 5 GHz VLA map. A few properties that the e-MERLIN+JVLA map of 3C 334 revealed are:

(i) Knots H, I, J, M, and N in the Bridle et al. (1994a) map are resolved into two structures (H1,H2,I1,I2,J1,J2,M1,M2,N1,N2) at higher resolution.

(ii) Emission is traced through the jet and hotspot O (see Fig. 4.10). The jet at N2 is pointed in the direction of P1 with a gap in emission between N2 and P1 and N2 and O. This indicates the shock does not cross the whole of the jet.

(iii) Emission appears to trace a path through P1, P2, Q, R, and S. P1 is pointed in the direction of P2 but in between is a gap in emission (see Fig. 4.10). There is a fainter trail of emission that connects hotspot O to P2. From P2 emission follows a path back towards the boundary of the lobe at Q.

(iv) Feature B in the northwest lobe is resolved into two peaks. While B did not fit the formal definition of a hotspot by Bridle et al. (1994a), the new map indicates that B is a secondary hotspot in the northwest lobe. At one point in the quasar's evolution the jet terminated into B. It has since changed directions and now terminates into C. The spectral index maps suggest hotspot B may not be a dying hotspot and is still being fed by a flow of material from hotspot C.

(v) Additional evidence for jet precession is presented in Fig. 4.18. Features P2/Q align with the placement of an old jet that may have formed the outer boundary of the northwest head (opposite side of the hotspot). This indicates they may also be remnants of old primary hotspots. No distinguishable counterjet side features are associated with them though.

(v) The average spectral index of the core is $\alpha = -0.31 \pm 0.01$. Phase calibration errors around the nucleus limit the accuracy of the spectral index in this region.

(vi) Along the straight jet the average spectral index is between ~ -0.6 and -1.0. The spectral index gradually steepens from the jet to the lobe. The

exception to this is at hotspot O and feature P (as labeled in the lower resolution map).

(vii) The apparent opening angle of the jet decreased along the straight jet. From this, we know that the jet is being recollimated, likely by lobe pressure.

(viii) A ratio between the integrated flux of the jet and the integrated flux of the counterjet gives $S_J/S_{CJ} = 9.2 \pm 2.2$.

The primary goal of the e-MERLIN observation of 3C 334 was to map the jet and hotspots at high resolution. The high-resolution maps revealed a strikingly flat boundary to the northwestern head as well as a central secondary hotspot. Given that it is a quasar, the angle to the line of sight is quite small compared to radio galaxies. Projection effects due to an inclined angle are known to create illusions in the morphology of quasars and so should also be considered. Like many other quasars, the primary hotspot C is located on the side of the lobe slightly back from the leading edge (Laing, 1989) with the start of the secondary hotspot B recessed from the leading edge. Few radio galaxies have internal hotspots like B in 3C 334; one example of a radio galaxy with this structure is 4C 14.11 (Hardcastle et al., 1997). A comparison of B in 3C 334 to a hotspot in 3C 263 is discussed in §5.3. The southeast and northwest lobes show evidence of jet precession in not only the S-shaped morphology but in the alignment of features and identification of the secondary hotspots B and P1.

Many of the knots in the jet were resolved into smaller knots. Feature L was resolved into a knotty, linear structure that runs nearly parallel to the jet close to its termination. Feature L could be shock propagating through the lobe material. Similar features have been observed in other jets with bow shocks. However, there is no evidence to suggest that L is produced by a classical bow shock. If L were a bow shock it would be outside of the lobe boundary. If L is a shock within the lobe material, this is evidence against a steady flow in 3C 334.

The spectral index map is mostly consistent with the map created at lower resolution by Dennett-Thorpe et al. (1997). There appears to be a flat spectral "bar" feature northwest of O between N2 and P1. Only a steep boundary of O is seen in the contour maps, but no physical bar feature is visible. This also coincides with the region where the emission is traced along (1) a path through hotspot O and P1 and (2) a path through N2 and P1 (see Fig. 4.10). Hotspots with accelerated material have spectral indices < -1.

Chapter 5

The Quasar 3C 263

Early low-resolution radio maps of 3C 263 by MacDonald et al. (1968) first identified two broad regions of radio emission. With high-resolution radio observations, 3C 263 is now known to be comprised of three distinct features: (1) an east lobe, (2) a west lobe, and (3) a core positioned between the two lobes. Improvements in resolution and instrumentation have provided a detailed look at the bright hotspots and a jet between the core and the brightest hotspot (e.g., Bridle et al., 1994a). Much of the work done for this thesis used the 5 GHz VLA map produced by Bridle et al. (1994a) (see Figs. 5.1a and 5.1b) to compare to structural features observed in the 1.5 GHz e-MERLIN with JVLA map .

Modern high-resolution images of 3C 263 reveal that the source is an edge-brightened quasar with an FRII morphology. The core appears asymmetrically positioned between the two lobes, appearing to be closer to the jet side. At VLA resolution a well-collimated jet begins near the core and ends $\sim$ 110 kpc away in a bright, eastern hotspot[1] (Bridle et al., 1994a). The jet is strikingly straight and narrow. A diffuse bridge of emission is observed between the east lobe and the core (see Fig. 3.24). A secondary lobe is visible but a counterjet is not easily identifiable. The total projected linear size of the structure is $\sim$ 340 kpc.

Orientation effects described by the unified model are believed to lead to asymmetry in brightness between the two lobes in quasars. The Laing-Garrington effect, discussed at the beginning of Ch. 4, describes an additional orientation effect on the polarization of these radio sources - relativistic sources beamed near the line of sight are less depolarized than the more distant lobe (Garrington et al.,

[1]A scale of 7.170 kpc arcsec^{-1} corresponds to a redshift of 0.646 (Hewitt and Burbidge, 1987).

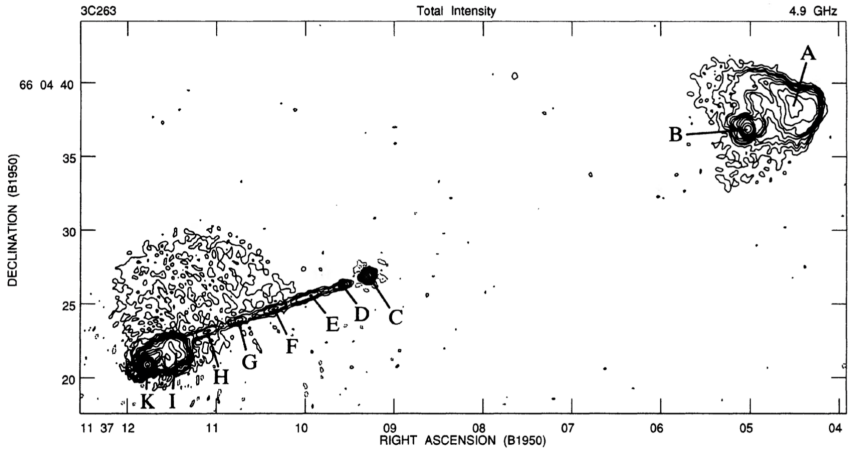

(a)

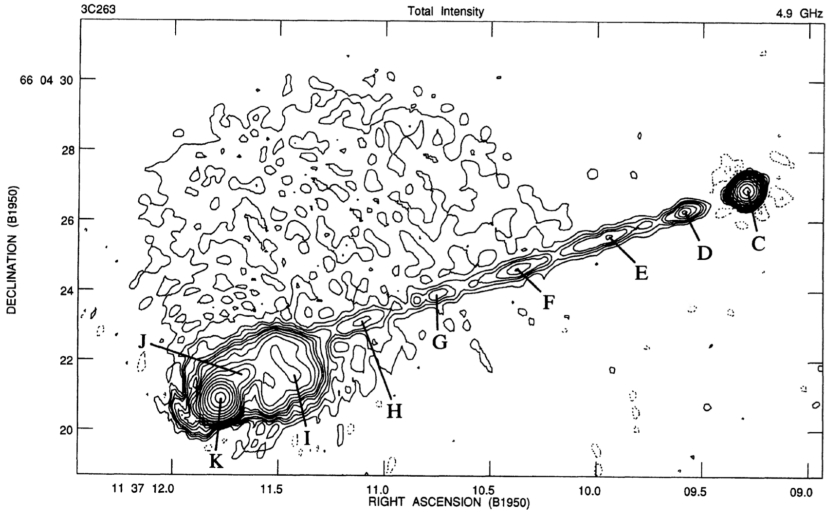

(b)

Figure 5.1: (a) 5 GHz VLA map of the quasar 3C 263 reproduced from Bridle et al. (1994a). (b) 5 GHz VLA map showing the total intensity from the core to the east lobe at 0.″36 resolution. Image is reproduced from Bridle et al. (1994a)

1991). Work done by Bridle et al. (1994a) found evidence for a flatter integrated lobe spectrum in 7 out of 8 sources, with the exception being 3C 263. In polarization studies 3C 263 revealed a steeper lobe spectrum and greater depolarization in the jet side lobe (Bridle et al., 1994b). Bridle et al. (1994b) suggests environmental factors from having a shorter lobe on the jet side can be a suitable explanation for spectral index differences between the two largest lobe structures. The link between a steeper spectrum and a shorter lobe in radio galaxies was shown by Pedelty et al. (1989) and Liu and Pooley (1991).

In this chapter I present the total intensity map of the quasar 3C 263, shown in Fig. 3.28, created with the e-MERLIN and JVLA arrays. The high-resolution image is used to investigate sub-arcsecond structures along the jet and in the environment in and around the hotspots. A spectral index map is included to identify changes in the spectral index along the total extent of the source. Redshift values and other derived observational properties of 3C 263 are found in Table 5.1.

Table 5.1: Properties of 3C 263. Values were derived from the e-MERLIN+JVLA map at 1.5 GHz unless otherwise stated.

Property	Value	Reference
IAU name	1137+660	Bridle et al. (1994a)
Optical type	Q[a]	Bridle et al. (1994a)
RA core (J2000)	11h39m57.026	
Dec core (J2000)	$+65°47'49\overset{''}{.}481$	
z	0.646	Hewitt and Burbidge (1987)
LLS (kpc)	358	
Straight Jet (kpc)	47	
S_{peak} core (mJy beam^{-1})	121±12	
S_{int} core (mJy)	120± 12	
α_{app} [b]	$\sim 0\overset{\circ}{.}5-5°$	

[a] Q denotes a quasar.

[b] The apparent opening angle of the jet was calculated with Eqn. 4.2 in §4.3.

5.1 Results

5.1.1 Total Intensity Maps at 1.5 GHz

Using the calibration steps described in Ch. 3, the total intensity image of 3C 263 shown in Fig. 3.28 was produced from observations done with the e-MERLIN and JVLA arrays. Sidelobes originating from the hotspot in the east lobe remained in the image after multiple rounds of phase and amplitude self-calibration. The image fidelity is also limited by artifacts near the core, with most of the errors positioned nearly perpendicular to the direction of the jet. The peak flux of the source is 338±34 mJy beam^{-1} and is located in the east hotspot. The peak flux of the core is 121±12 mJy beam^{-1}. Image statistics are found in Table 3.6 of §3.8 and physical properties of 3C 263 are found in Table 5.1.

A full-field contour map at resolution 0.″16×0.″12 is provided in Fig. 5.2. In the image two large regions of emission corresponding to the east and west lobes are visible. The lobes are intrinsically asymmetric likely due to their host environment. Embedded in the ring-shaped sidelobes is a jet extending from the core to the east hotspot.

Figures 5.3a and 5.3b show the total intensity distribution in the region between the core and the east lobe. Feature C1 is the compact core of the AGN. East of the core is the first knot in the jet (C2). There is a gap in emission between knot C2 and the next knot D2. The image fidelity near the jet is limited by (i) emission from the diffuse lobe and (ii) sidelobes from the bright, compact hotspot opposite the core (see Fig. 5.3b). Emission from the east lobe is observed by the JVLA array but lies mostly below the noise level in the e-MERLIN and JVLA map. Artifacts from the sidelobes of the hotspot were difficult to separate from real emission near the jet. A well-collimated thin jet is observed until ∼5.″6 (∼ 40 kpc) from the core at 0.″16 × 0.″12 resolution. After F2 the jet is not visibly detected until feature H and J. Feature I points in the direction of the core but lies south of the axis of the straight jet by ∼0.″68.

The total intensity distribution at 0.″16 × 0.″12 resolution of the west lobe is shown in Fig. 5.4. The west lobe is significantly less affected by sidelobes than the east lobe. One hotspot is identified in the e-MERLIN and JVLA map with significant features labeled (B1,B2,B3). Feature A in the Bridle et al. (1994a) map is resolved into smaller features spread out over the western edge of the lobe. B1 and B2 outline the bright boundary of the hotspot. A is the brightest

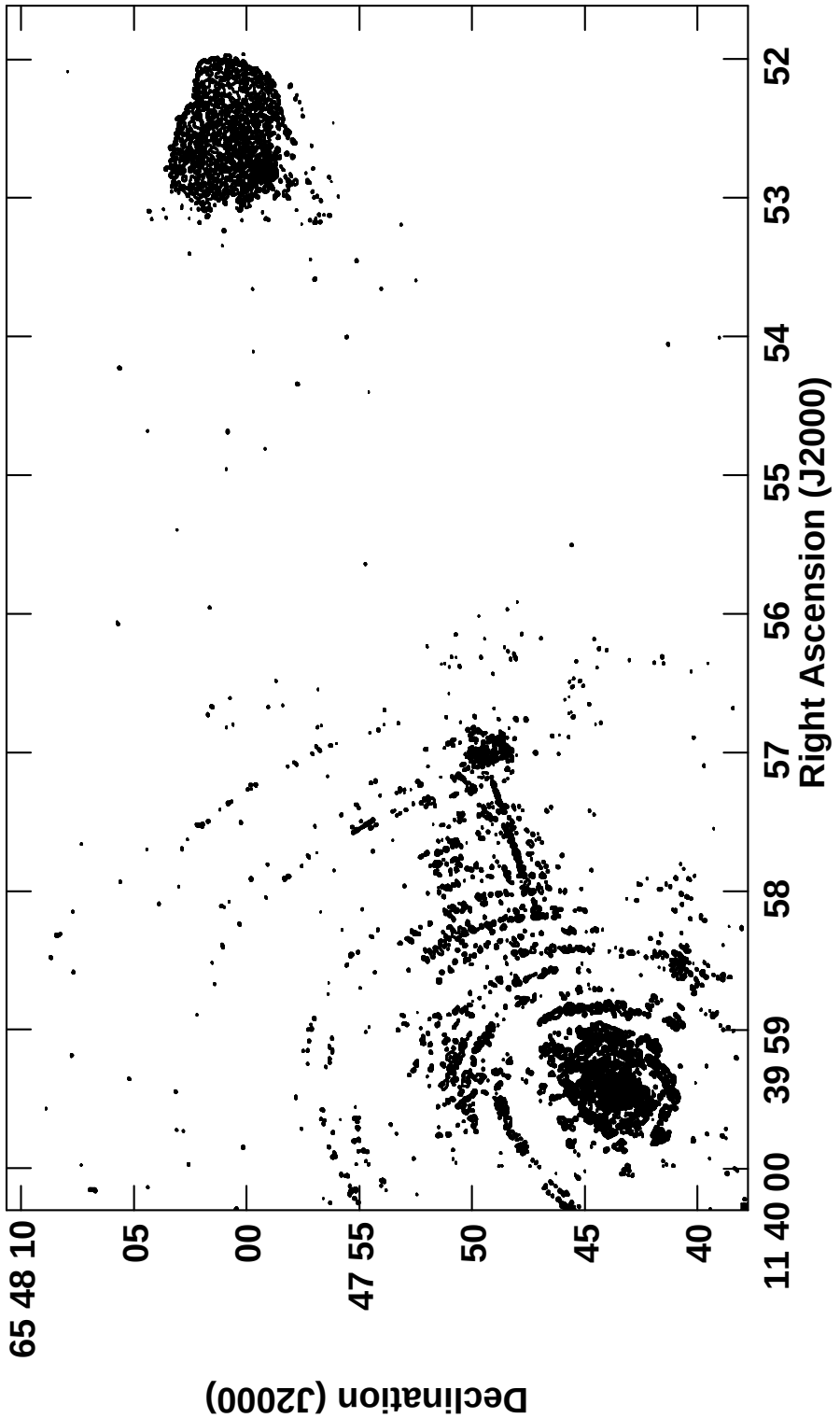

Figure 5.2: Distribution of total intensity over the quasar 3C 263 with a resolution of $0\farcs16 \times 0\farcs12$. Contours are drawn at -4, -2, -1 (dotted), 1, 1.414, 2, 2.828, 4, 5.657, 8, 11.31, 16, 22.63, 32, 45.25, 64, 90.51, 128, 181.0, 256, 362.0, 512, 724.1, 1024, 1450, 2048, 2900, 4096, and 5790 times 145 μJy per CLEAN beam area.

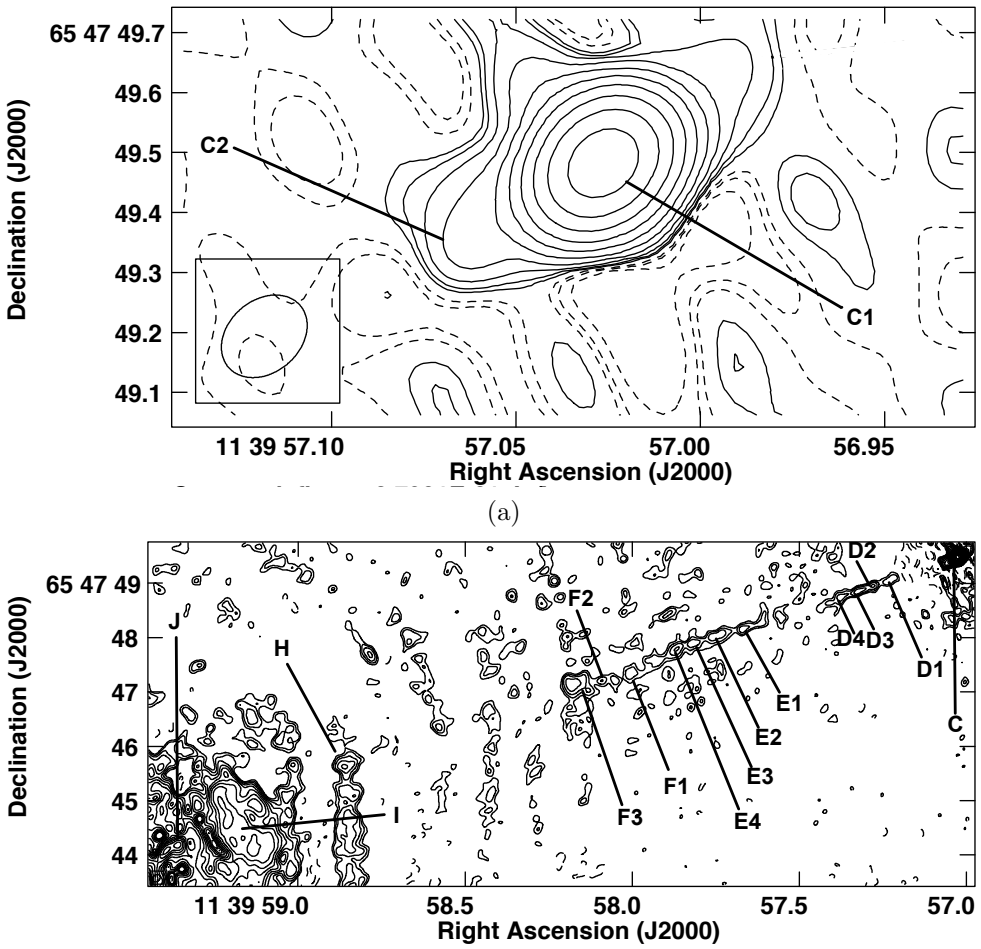

Figure 5.3: (a) Distribution of the total intensity over the nucleus of quasar 3C 263 with a resolution of 0.″16 × 0.″12. Contours are drawn at at -4, -2, -1, (dotted) 1, 2, 4, 8, 16, 32, 64, 128, 256, 512, 1024, and 2048 times 145 μJy per CLEAN beam. (b) Total intensity distribution from the core (C) to feature J. Contours are drawn at -4, -2, -1 (dotted), 1, 1.414, 2, 2.828, 4, 5.657, 8, 11.31, 16, 22.63, 32, 45.25, 64, 90.51, 128, 181.0, 256, 362.0, 512, 724.1, 1024, 1450, 2048, 2900, 4096, and 5790 times 145 μJy per CLEAN beam area.

region outside of hotspot B; it is too diffuse and not bright enough in the map to be considered a secondary hotspot. The western edge is well-defined and bright with most emission contained within the lobe structure.

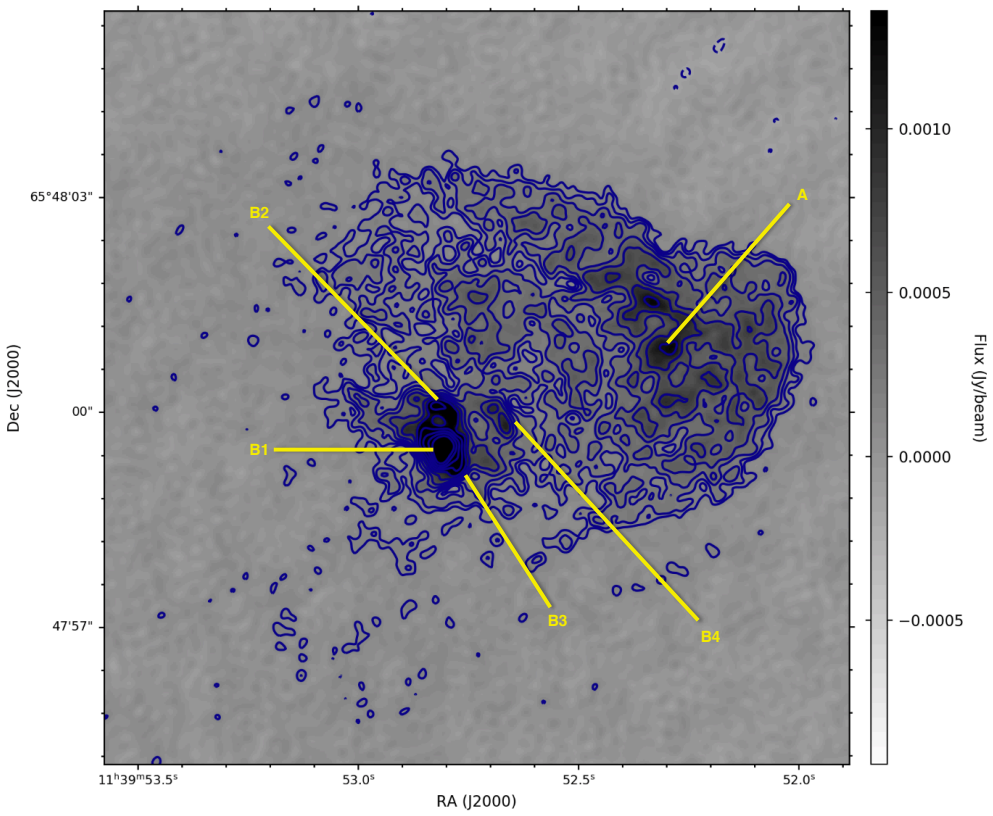

Figure 5.4: Total intensity distribution superimposed on the total intensity of the west lobe in 3C 263 at a resolution of $0''.16 \times 0''.12$. Contours are drawn at -4, -2, -1 (dotted), 1, 1.414, 2, 2.828, 4, 5.657, 8, 11.31, 16, 22.63, 32, 45.25, 64, 90.51, 128, 181.0, 256, 362.0, 512, 724.1, 1024, 1450, 2048, 2900, 4096, 5790, and 8192 times 145 μJy per CLEAN beam area.

A contour map of the east lobe is provided in Figs. 5.5a and 5.5b. Feature K is the main hotspot in the east lobe and the brightest feature in the source. It does not directly align with the axis of the straight jet shown in Fig. 5.3b. The curved shape of feature J is evidence in support of a deflecting jet before terminating in hotspot K. Most of the emission surrounding K is likely attributed to sidelobes from the hotspot. Northwest of J and K by $\sim 2''$ is a bar of emission (I1 and I2) positioned perpendicular to the jet axis.

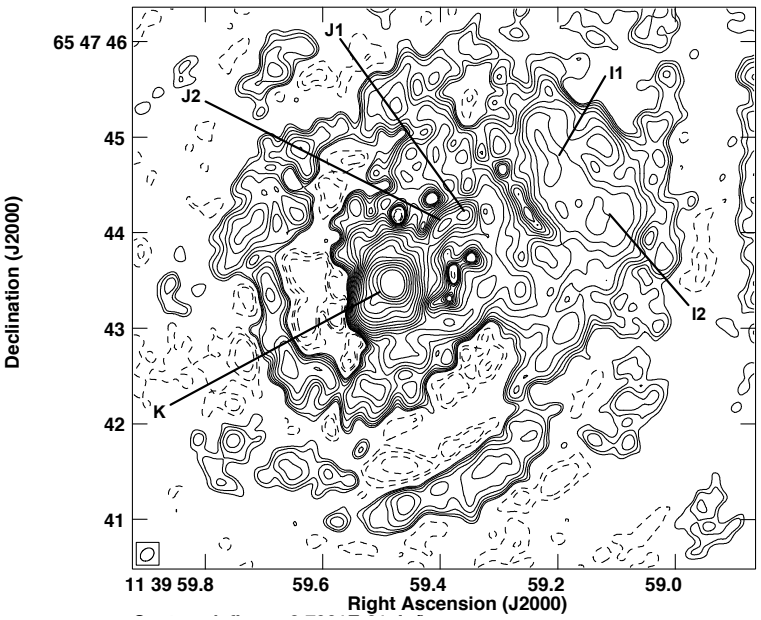

(a)

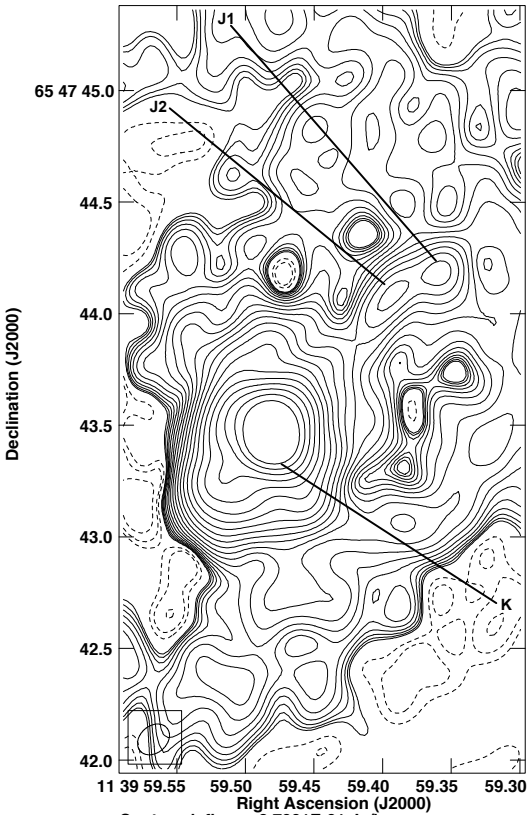

(b)

Figure 5.5: (a) Distribution of total intensity over 3C 263's east lobe with a resolution of $0\farcs16 \times 0\farcs12$. Contours are drawn at -4, -2, -1 (dotted), 1, 1.414, 2, 2.828, 4, 5.657, 8, 11.31, 16, 22.63, 32, 45.25, 64, 90.51, 128, 181.0, 256, 362.0, 512, 724.1, 1024, 1450, 2048, 2900, 4096, and 5790 times 145 μJy per CLEAN beam area. (b) A close of the hotspot in the east lobe.

5.1.2 The C-band Map

The calibrated 5 GHz VLA map of 3C 263 from Bridle et al. (1994a) was provided courtesy of Dr. Alan Bridle (see Fig. 5.6). The C-band data were observed on 11 July 1987 in A configuration and 06 December 1987 in B configuration. The final calibrated image was made with a restoring beam size of $0\farcs36 \times 0\farcs36$. A short summary of observing details is provided in Table 5.2. For more details about the observations and calibration procedure see Bridle et al. (1994a).

Table 5.2: Observation details for 3C 263 at C-band data taken by the VLA array in A and B configurations. The calibrated FITS image was provided courtesy of Dr. Alan Bridle via email correspondence.

Observation Info.	Value
Obs. ν	4.9 GHz
Configuration	A & B
Obs. Date (A)	1987/07/11
Obs. Date (B)	1987/12/06
b_{maj}	$0\farcs36$
b_{min}	$0\farcs36$
PA	0°
σ_{rms} A config. (μJy)	25
σ_{rms} B config. (μJy)	57
S_{peak} core	158 mJy/beam
Image size (pixels)	525×267

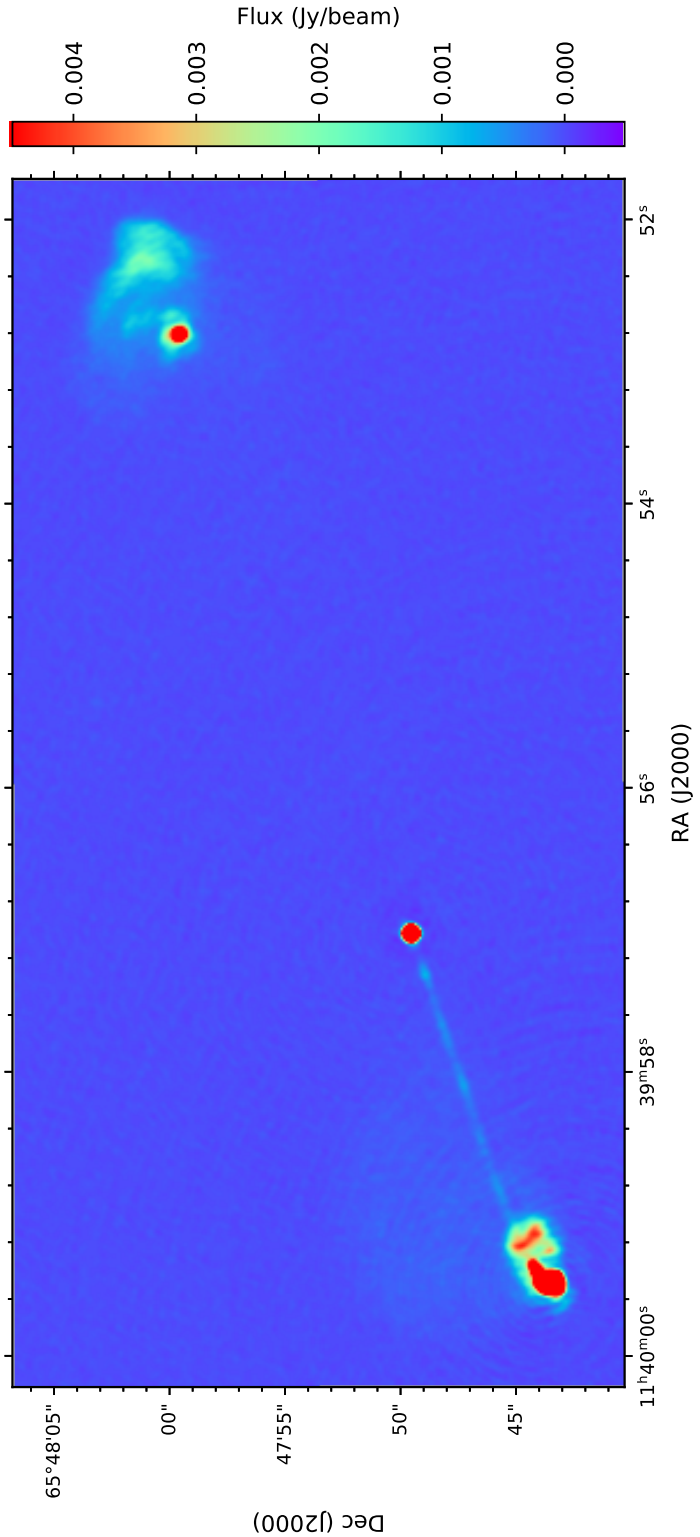

Figure 5.6: 5 GHz total intensity map of 3C 263 from VLA observations. The calibrated FITS image is reproduced from Bridle et al. (1994a) and was received from Dr. Alan Bridle via email correspondence.

5.1.3 The Spectral Index Map

The combined e-MERLIN and JVLA data at L-band were smoothed to the JVLA C-band resolution (0.″36). The 5 GHz map was regridded from B1950 coordinates to J2000 coordinates. Using the 5 GHz map in J2000 coordinates as a template, the smoothed 1.5 GHz map was regridded to match the shape of the 5 GHz map. A plot of the total intensity versus distance from the core (C1) through I at 1.5 and 5 GHz is shown in Fig.5.7. Intensity values with corresponding spectral index errors > 1 were not included in this or any α analysis of 3C 263. Using the steps described in §4.1.3, a spectral index map was produced from the 1.5 and 5 GHz data (see Figs. 5.8, 5.10a, and 5.10b). A spectral index error map for 3C 263 is shown in Fig. 5.9.

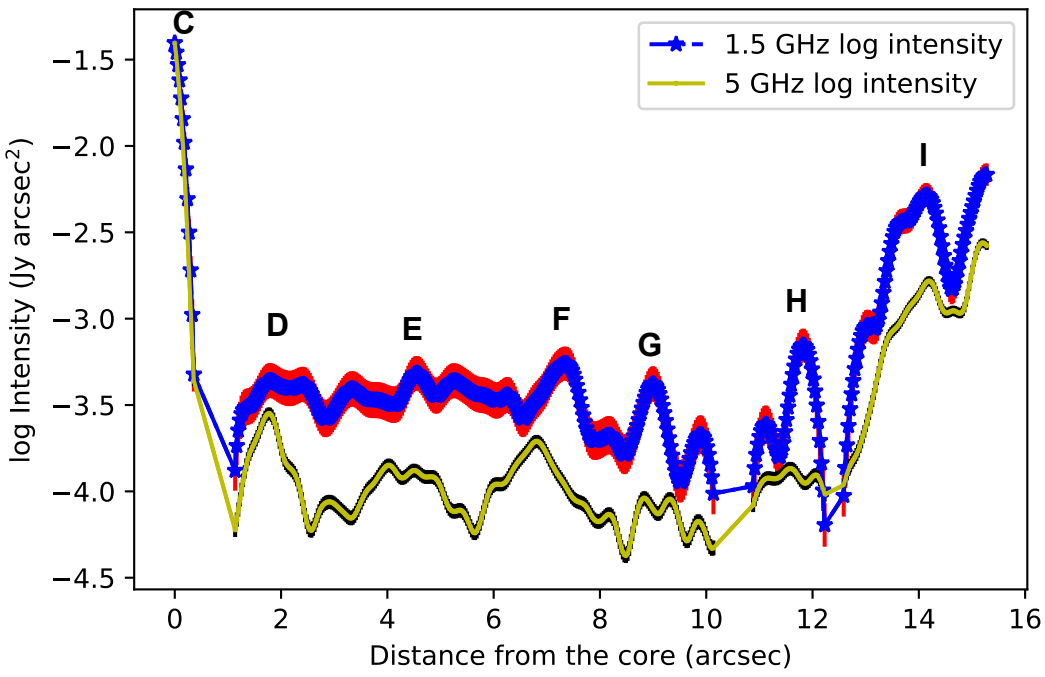

Figure 5.7: This plot shows the change in intensity along the jet from the core through feature I at 0.″36×0.″36. Values were taken from the task SLICE in AIPS. The blue stars represent the 1.5 GHz from the e-MERLIN plus JVLA array map and the yellow line represents the 5 GHz VLA map. The positions of the knots in the 1.5 GHz smoothed map are labeled.

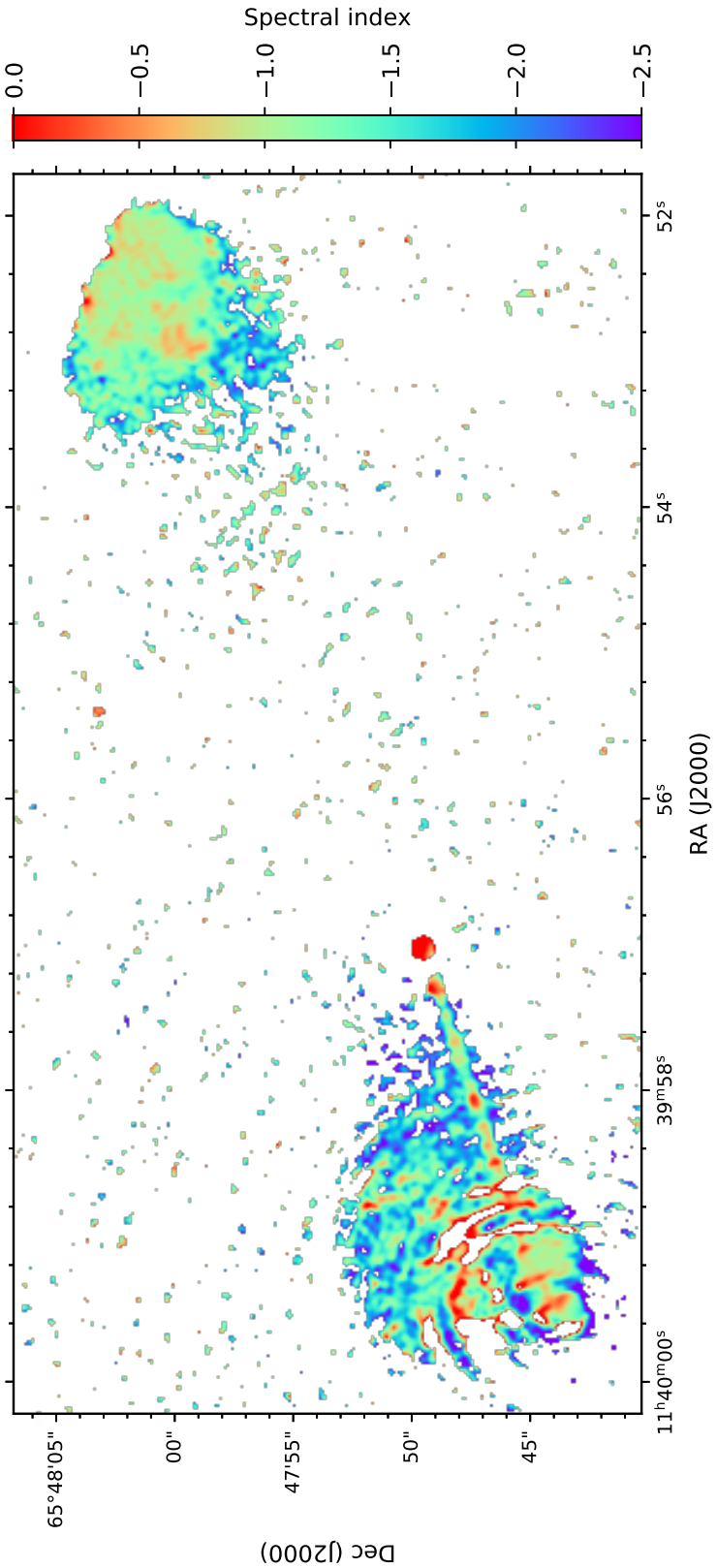

Figure 5.8: Spectral index map of 3C 263 using the 1.5 GHz data from the e-MERLIN and JVLA arrays and the 5 GHz data from the VLA array. Spectral index is shown for maps with a resolution of 0.″36×0.″36. The 5 GHz map was clipped at 35 μJy and the 1.5 GHz map was clipped at 75 μJy.

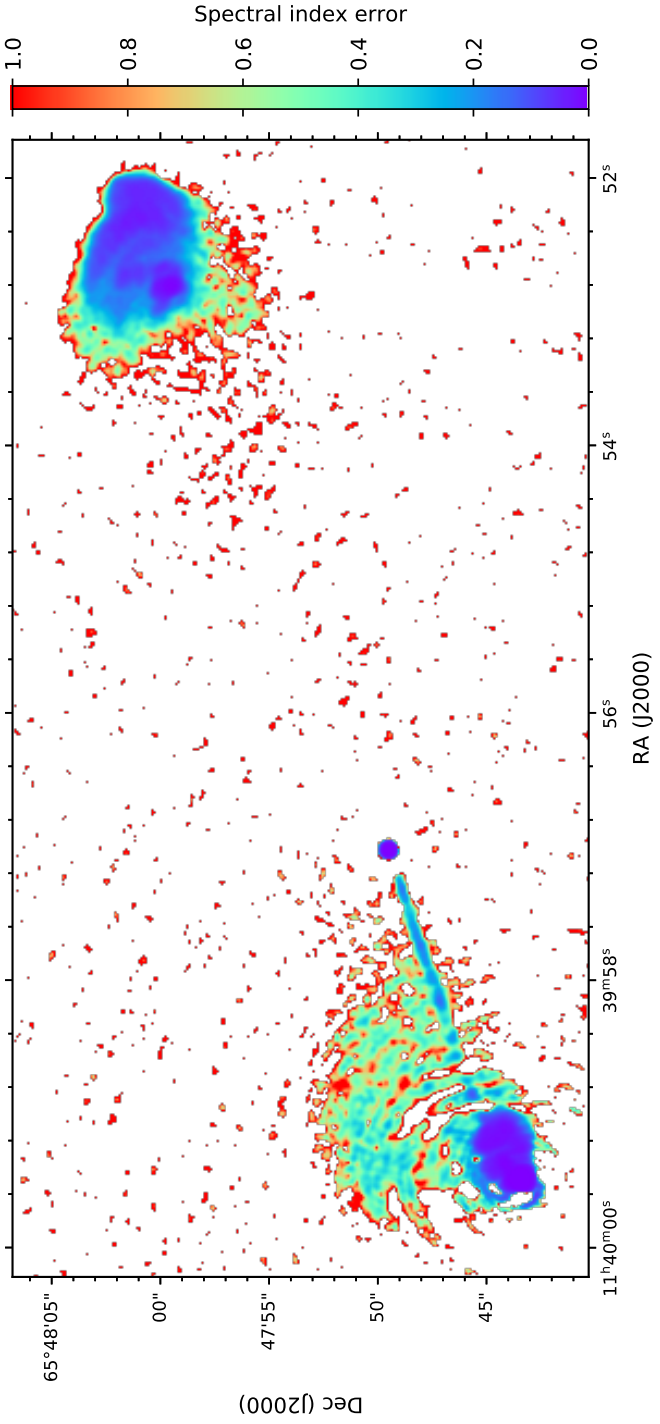

Figure 5.9: Spectral index error map of 3C 263 using the 1.5 GHz data from the e-MERLIN and JVLA arrays and the 5 GHz data from the VLA array. Error in spectral index is shown for maps with a resolution of 0.″36×0.″36.

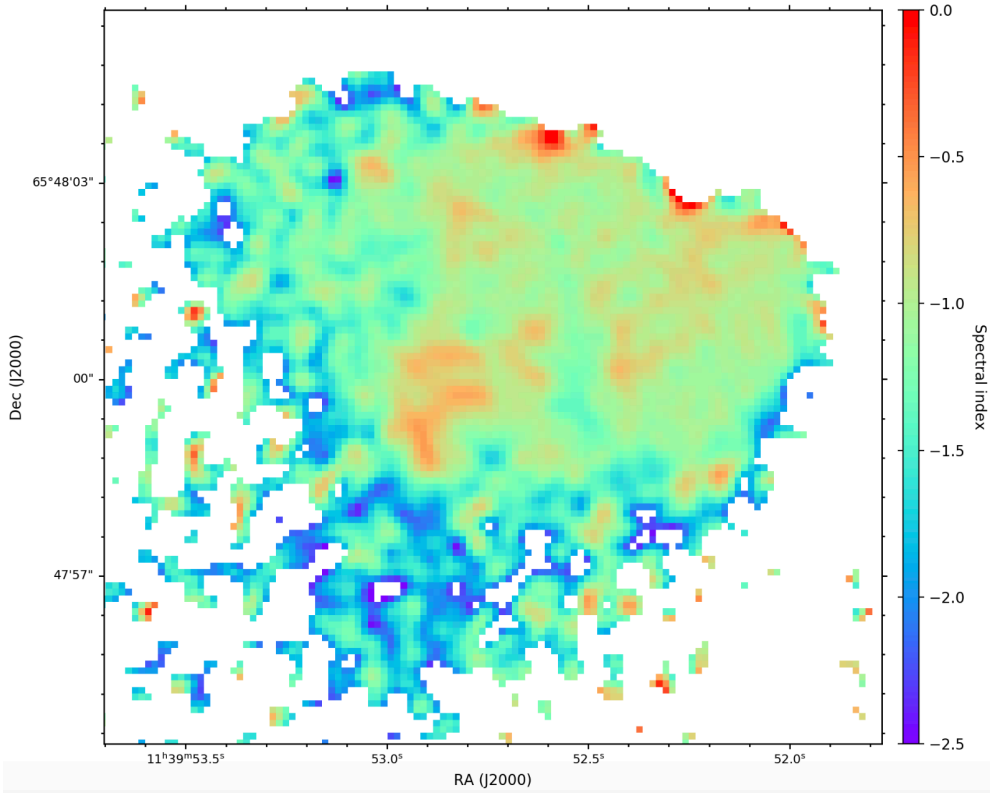

(a)

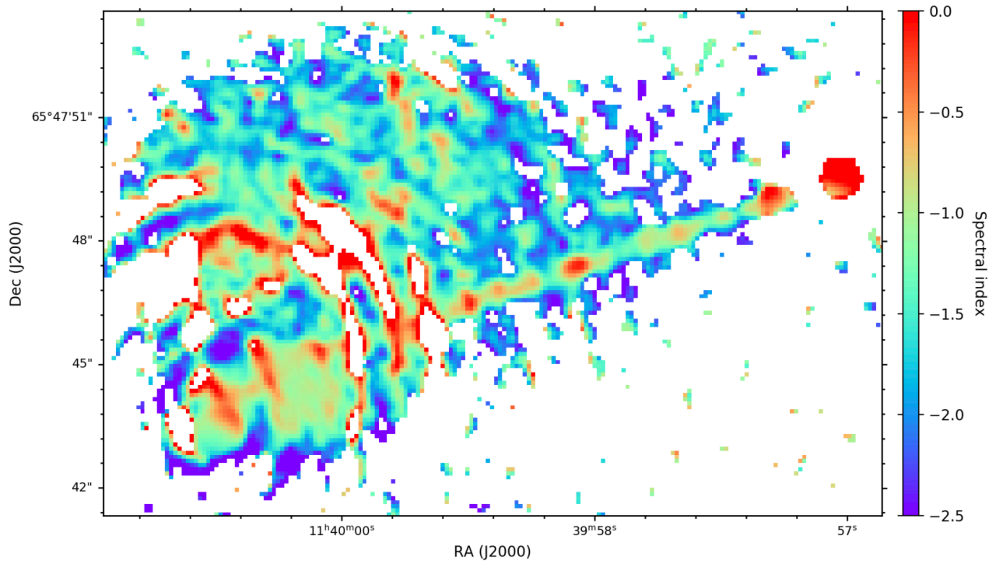

(b)

Figure 5.10: (a) Spectral index map of the west lobe at 0.″36 resolution. (b) Spectral index map of the east hotspot and jet. The spectral index maps were created with 1.5 GHz combined e-MERLIN and JVLA data and 5 GHz JVLA data.

5.1.4 Transverse Profiles of the Jet

The final calibrated image from the e-MERLIN and JVLA observations was smoothed with a restoring beam of $1\farcs0 \times 0\farcs15$ at a position angle of $-70°$. The smoothed map of 3C 263 is provided in Fig. 5.11a. From the smoothed map flux density measurements were taken as slices across the jet to produce transverse profiles of surface brightness. The locations of the 28 slices across the jet are shown in Fig. 5.11b. Slices were taken along the jet until emission surrounding the hotspot was greater than the emission from the jet. Slice 1 is taken closest to the core while slice 28 was taken furthest downstream from the core. Plots of the surface brightness across the jet are shown in Fig. 5.12. The black line represents the data and the blue line represents a Gaussian fit to the data. In regions where the jet emission was weak compared to the rms, a Gaussian fit was to the position of the peak surface brighteness.

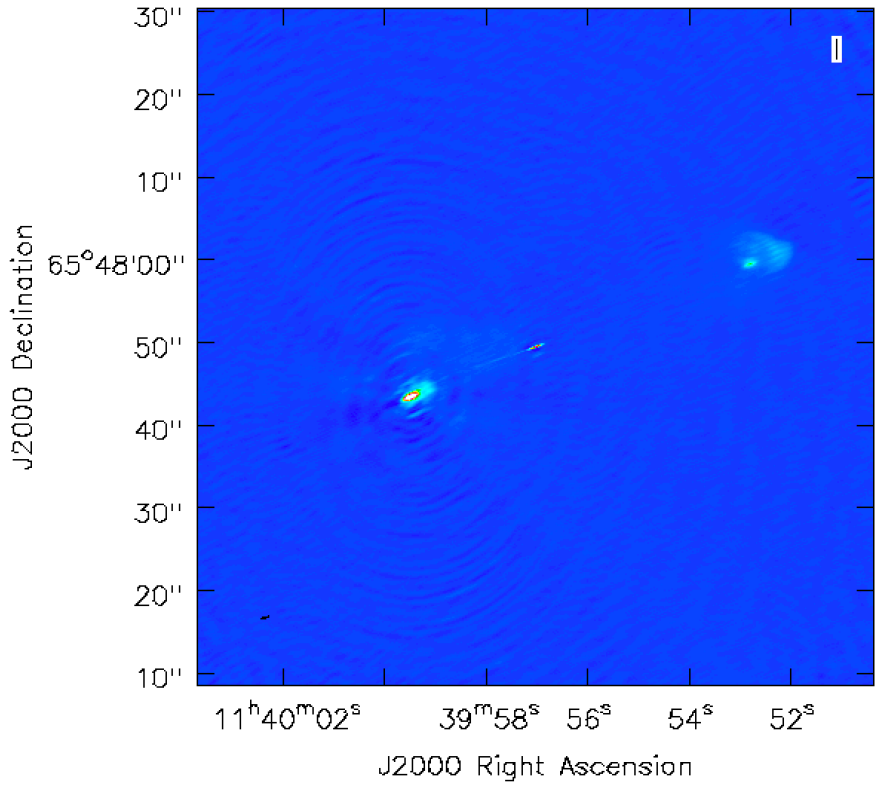

(a)

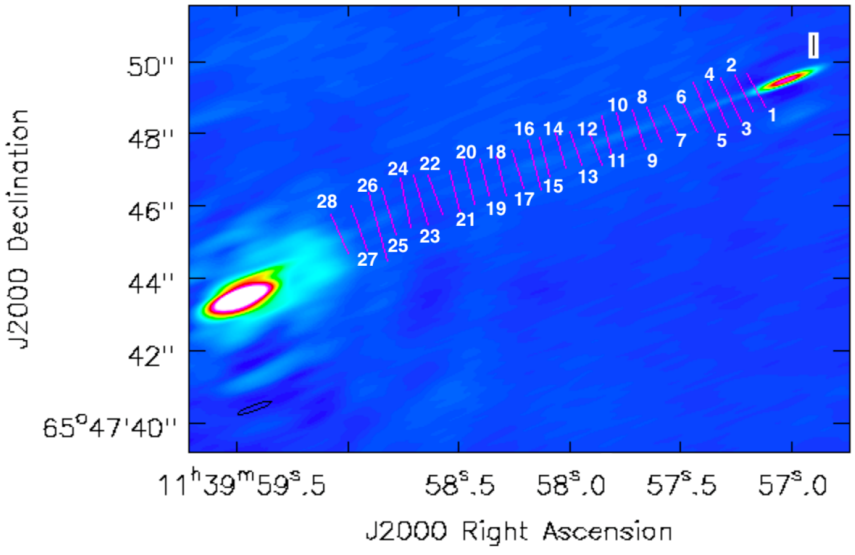

(b)

Figure 5.11: (a) Map of 3C 263 smoothed to a resolution of 1.″0 × 0.″15 at a position angle of −70°. (b) Locations of line segments across the jet at 1.″0 × 0.″15 resolution. Slices were taken from near the core until the emission surrounding the hotspot was greater than emission in the jet.

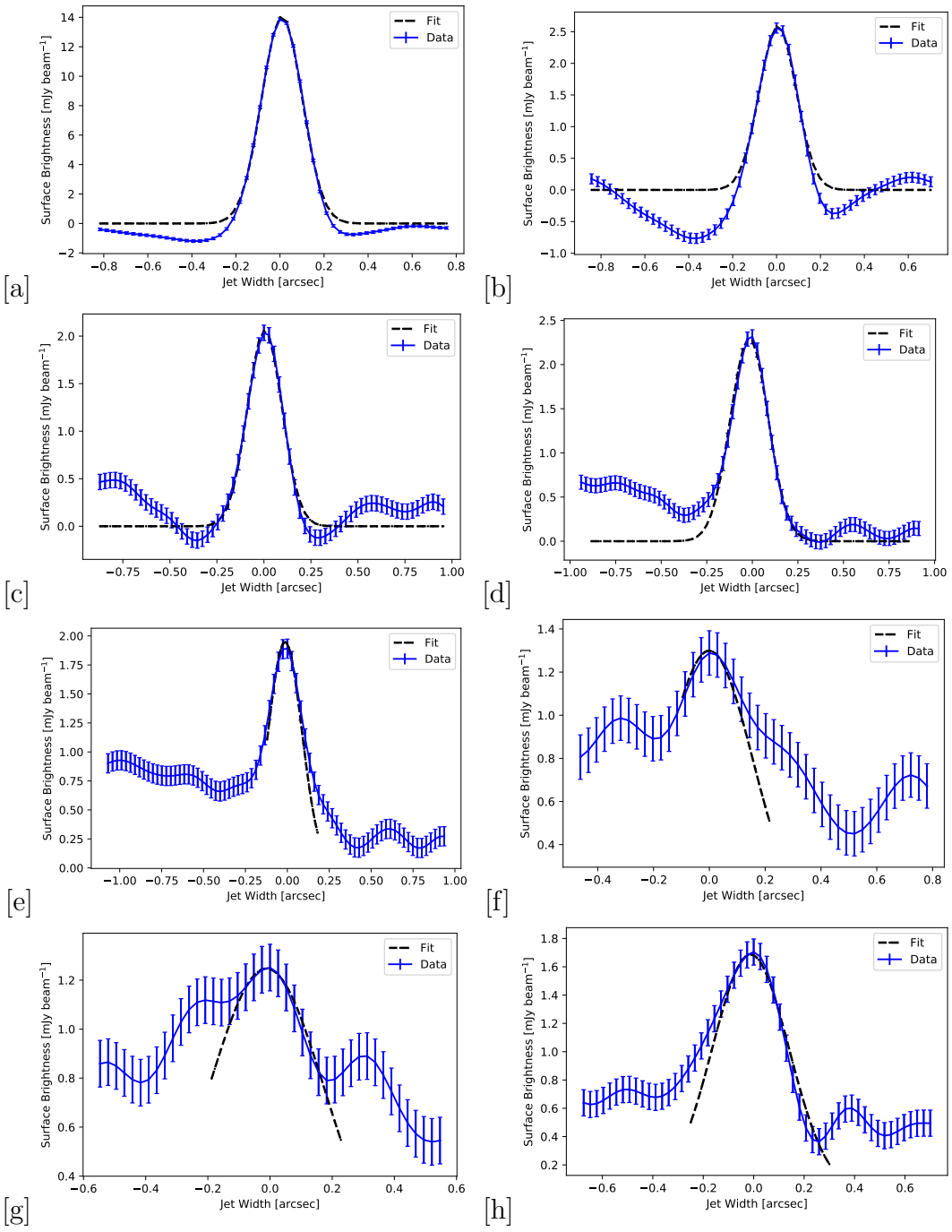

Figure 5.12: 3C 263 total intensity transverse profiles corresponding to slices 1−8 in Fig. 5.11b, (a) slice 1, (b) slice 2, (c) slice 3, (d) slice 4, (e) slice 5, (f) slice 6, (g) slice 7, and (h) slice 8.

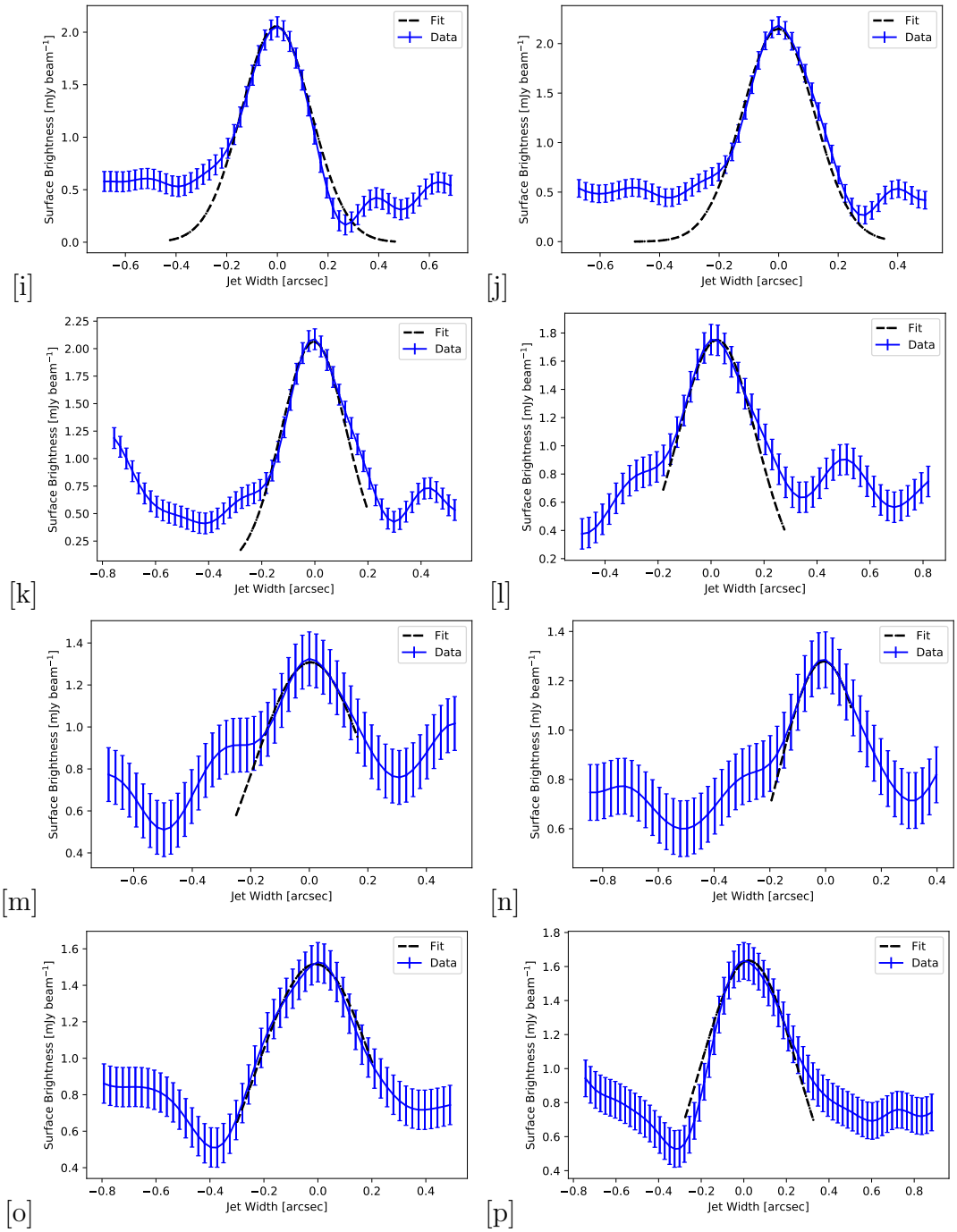

Figure 5.12: 3C 263 total intensity transverse profiles corresponding to slices 9−16 in Fig. 5.11b, (i) slice 9, (j) slice 10, (k) slice 11, (l) slice 12, (m) slice 13, (n) slice 14, (o) slice 15, (p) slice 16.

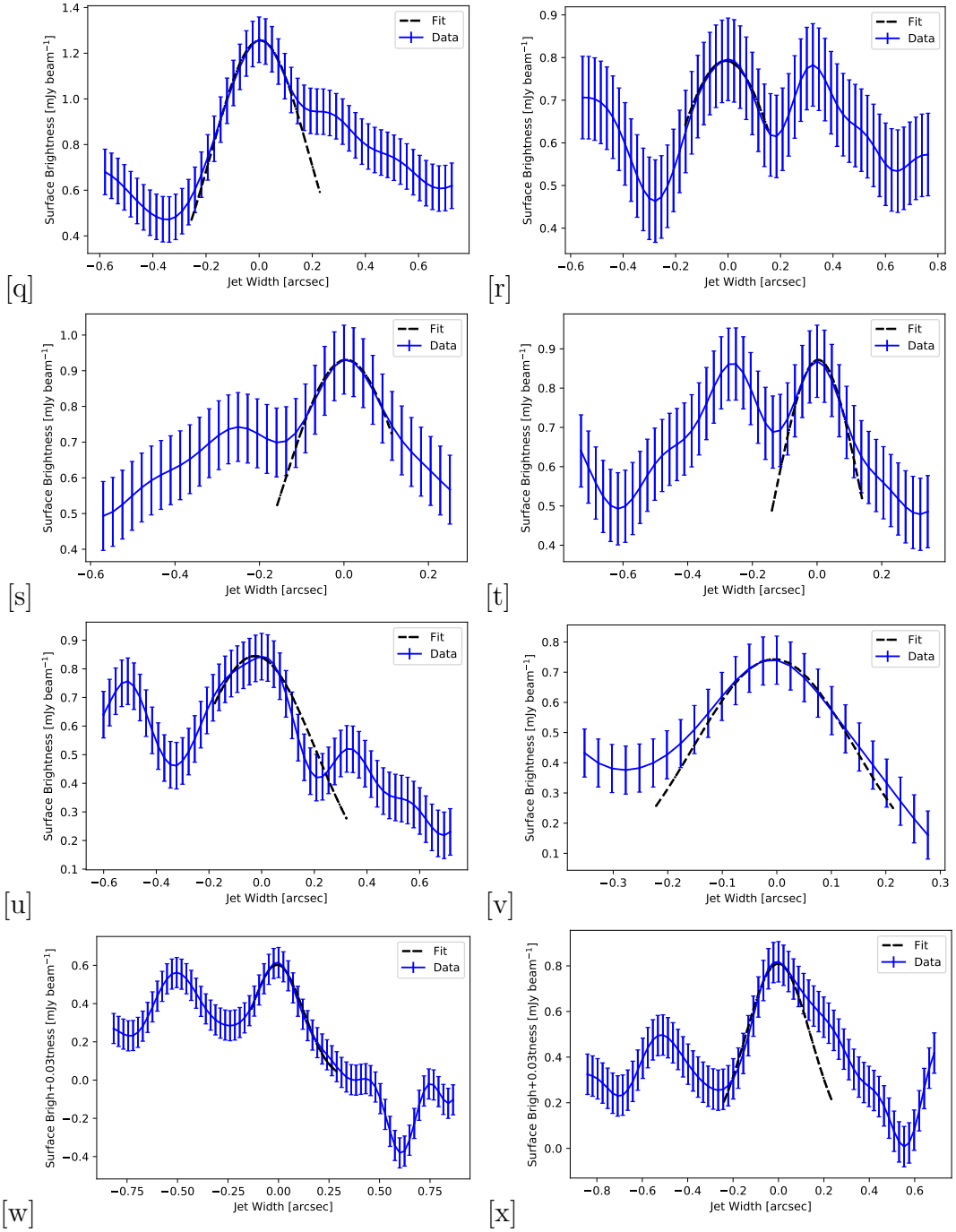

Figure 5.12: 3C 263 total intensity transverse profiles corresponding to slices 17−24 in Fig. 5.11b, (q) slice 17, (r) slice 18, (s) slice 19, (t) slice 20, (u) slice 21, (v) slice 22 (w) slice 23, and (x) slice 24.

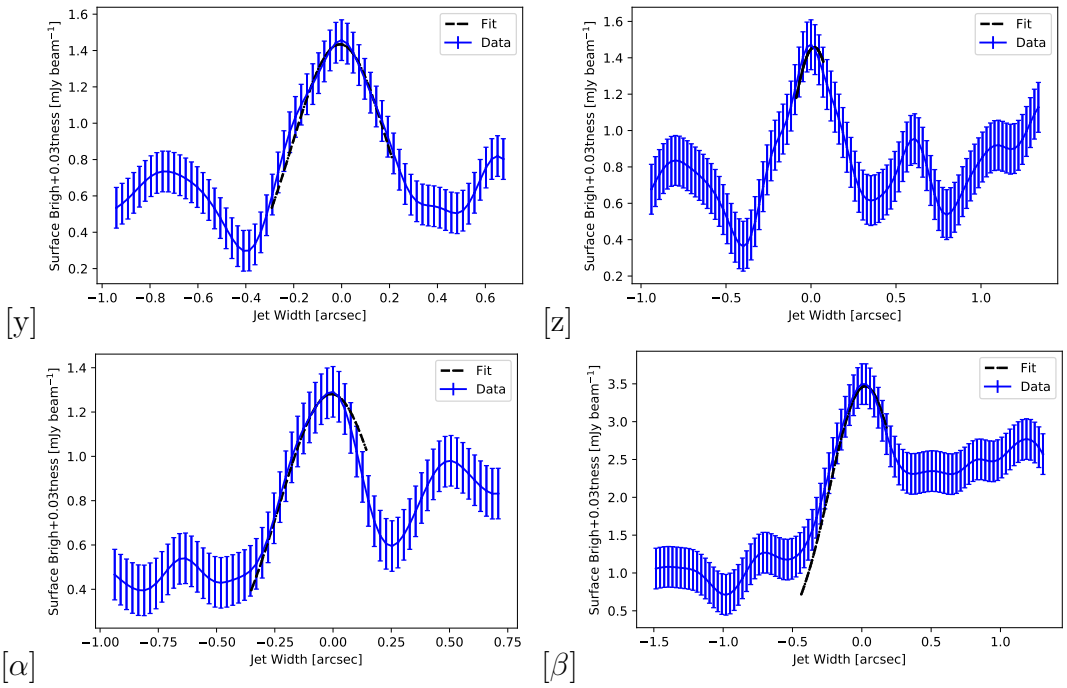

Figure 5.12: 3C 263 total intensity transverse profiles corresponding to slices 25−28 in Fig. 5.11b, (y) slice 25, (z) slice 26, (α) slice 27, and (β) slice 28.

5.2 Discussion

5.2.1 Total Intensity Maps

The total intensity map of quasar 3C 263 shown in Fig. 5.2 reveals that the largest linear size (LLS) of the source is $\sim$ 358 kpc ($\sim 50''$). Table 5.3 details the projected sizes of the lobes, hotspots, and jet at $0''.16 \times 0''.12$ resolution at 1.5 GHz.

Table 5.3: Projected sizes of various structures in 3C 263. In all cases (except for the the jet length and width) the deconvolved FWHM was taken from the CASA task IMFIT. The projected jet length was calculated from the ruler in CASA's viewer. The average deconvolved FWHM of the jet was taken from the transverse profiles. The size of the hotspot was estimated from the most compact and central region of B1.

Region	size	size (kpc)
Total source size	$49''.9 \pm 0.4$	358 ± 2.9
Straight jet (length)	$15''.8 \pm 0.3$	113 ± 2.2
Straight jet (avg. width)	$0''.14$	1.0
West lobe (major)	$6''.73 \pm 0.31$	48 ± 2.2
West lobe (minor)	$3''.05 \pm 0.14$	22 ± 1.0
East hotspot (major)	219 ± 14 mas	1.6 ± 0.1
East hotspot (minor)	165 ± 16 mas	1.2 ± 0.11
West hotspot (major)	313 ± 22 mas	2.2 ± 0.16
West hotspot (major)	231 ± 19 mas	1.65 ± 0.15

Lobes and Hotspots

Figure 5.4 shows the west lobe at $0\farcs16 \times 0\farcs12$ resolution. There is little difference in the large-scale morphology between the low-resolution VLA map and the high-resolution e-MERLIN+JVLA map. The hotspot complex (B1,B2,B3) is positioned slightly back from the leading edge. Feature B4 is an interesting feature as it is a close but separate region from the hotspot (B1). Although not comparable in flux to B1 ($S_{B1} \sim 9$ mJy and $S_{B4} \sim 0.7$ mJy), B4 is brighter than the immediate surrounding emission. The emission between B4 and A dims before brightening again at feature A ($S_A \sim 1$ mJy).

In Figure 5.5a an emission "bar" (I1,I2) nearly perpendicular to the jet, a part of the deflected jet (J1,J2) , and the hotspot (K) are all observed. The peculiar jet-crossing feature (I1,I2) is resolved into two peaks in the 1.5 GHz map. Similar features have been observed in 3C 249.1 (Bridle et al., 1994a) and 3C 381 (Hardcastle et al., 1997). The appearance of a curved jet in between the hotspot and the bar makes it unlikely for the feature to be sudden spot of jet broadening. It is clear that the path of the jet is bent between H and J, and also occurs in 3C 249.1 right before a bend in the jet (see Fig. 5.15). In the case of 3C 381, the bar is explained as a strong backflow from the termination shock (Hardcastle et al., 1997). The position of a jet-crossing bar in 3C 381 and 3C 263 suggests that a similar mechanism could explain the creation of the feature in 3C 263.

3C 263 and 3C 334 share remarkable similarities in their counterjet side lobes and hotspot. In both sources emission at the edge closest to the core is mostly well-defined at high resolution. Both show similar "head" morphology on the counterjet side. It is in these heads that most of the emission is confined even at high resolution. This could be influenced by the angle to the line of sight though. It is known that projection effects, even non-relativistic projection effects, can alter the shape of many of these relativistic extragalactic sources (e.g., Pushkarev et al., 2011). Feature A in 3C 263 is similar to the secondary hotspot B in 3C 334 in that it is further back from the leading edge and somewhat curls into a curved shape directed towards the core. The polarization vectors (see Fig. 5.13) near hotspot B are pointed directly towards feature A (Bridle et al., 1994a). Despite having a few similarities, there are notable differences between the two quasars as well. The primary hotspot C in 3C 334 is positioned on the wall of the lobe, where as primary hotspot B in 3C 263 is centrally located and aligned with the

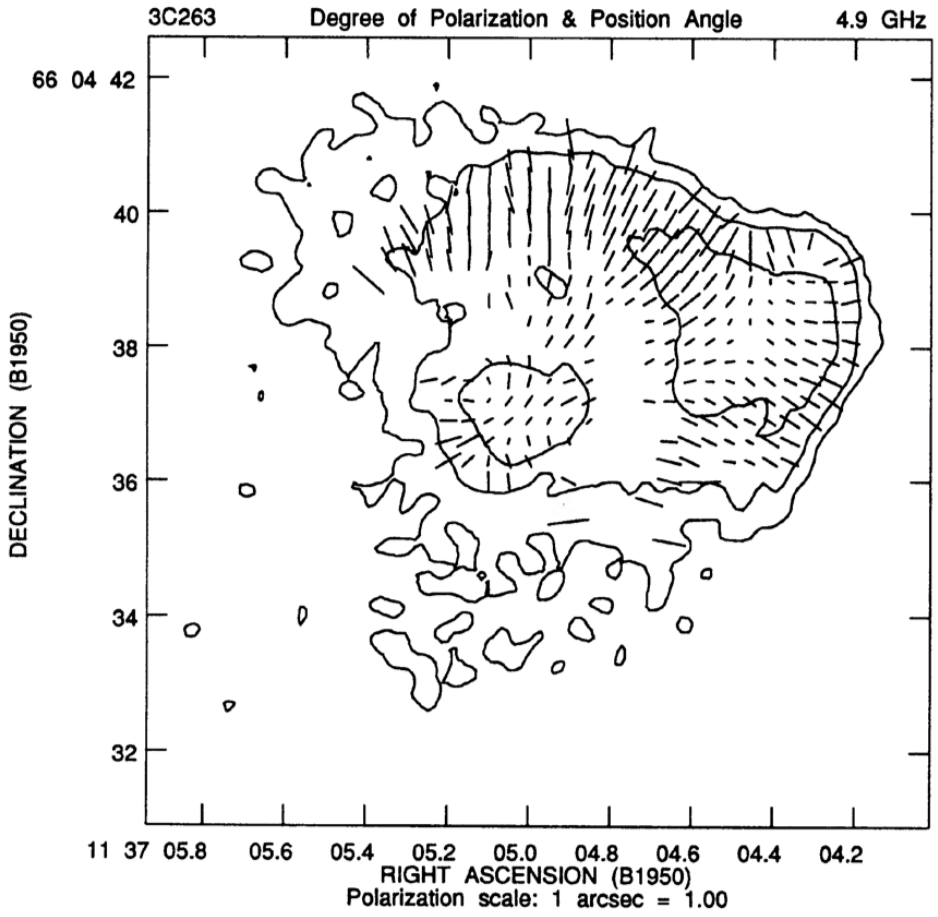

Figure 5.13: The 5 GHz polarization map of the west lobe of 3C 263. Polarization vectors at the primary hotspot B are pointed towards feature A. Image is reproduced from Bridle et al. (1994a).

core and feature A. Feature A in 3C 263 is significantly more diffuse and less defined than the secondary hotspot B in 3C 334. Again, the shape and presence of features can be attributed to projection effects. The quasar 3C 263 also shows significantly less compact features than 3C 334 around an extended jet side lobe (see Fig. 4.7 and Fig. 5.5a). The primary hotspot K maintains a well-defined compact structure at high resolution.

Jet

From the closeup of the jet provided in Fig. 5.3b it is obvious that a well-collimated jet is visible but there is no obvious sign of a counterjet. The ratio of the integrated flux of the jet over the integrated flux of the counterjet gives

$S_J/S_{CJ} > 3$. A description of the final region used to determine the flux ratio is provided in Fig. 5.14. The hotspot in the east lobe produced large sidelobes that affected the image fidelity for both the 1.5 GHz and 5 GHz maps. From the high-resolution e-MERLIN + JVLA map it was estimated that the jet length from near the core to the end of feature J to be $\sim\ 113 \pm 2.2$ kpc.

In the low-resolution VLA maps, the jet appears narrow and mostly continuous from the first knot closest to the core to a region close to the hotspot. Bridle et al. (1994a) showed that the knots in the jet are semi-periodic, with periods close to $2\farcs5$ (excluding the core). At e-MERLIN resolution many of the knots are resolved into multiple, semi-continuous components that are also semi-periodic, with periods between $\sim 0\farcs25 - 0\farcs3$. A surprising result from the e-MERLIN+JVLA map was how narrow and unresolved the jet appears at high resolution. Knots are identifiable but the jet appears as a strikingly narrow and nearly intact trail of emission for a significant portion of the jet. The influence of the sidelobes on some of the emission cannot be completely ruled out. However, the jet structure is much more linear than the sidelobes appear to be in the environment surrounding the jet. There is little evidence (e.g., additional secondary hotspots, S-shaped structure) for jet precession in 3C 263. Figure 5.15 shows the projected straight path of the jet from the core C (black line is extrapolated from the visible jet) to the jet and counterjet hotspots. Assuming the jet and counterjet are linear, symmetric features, there appears to be a slight bend in the counterjet into hotspot B. Without the identification of a counterjet it is difficult to identify where, if at all, the jet does bend. One alternative option is that the jets are misaligned. The alignment of hotspots B and K through the core (yellow line in Fig. 5.15) suggests this may be less likely. A bend in the jet is visible in feature J, although it is unclear at what point in the path prior to this that the jet deviates from the straight path.

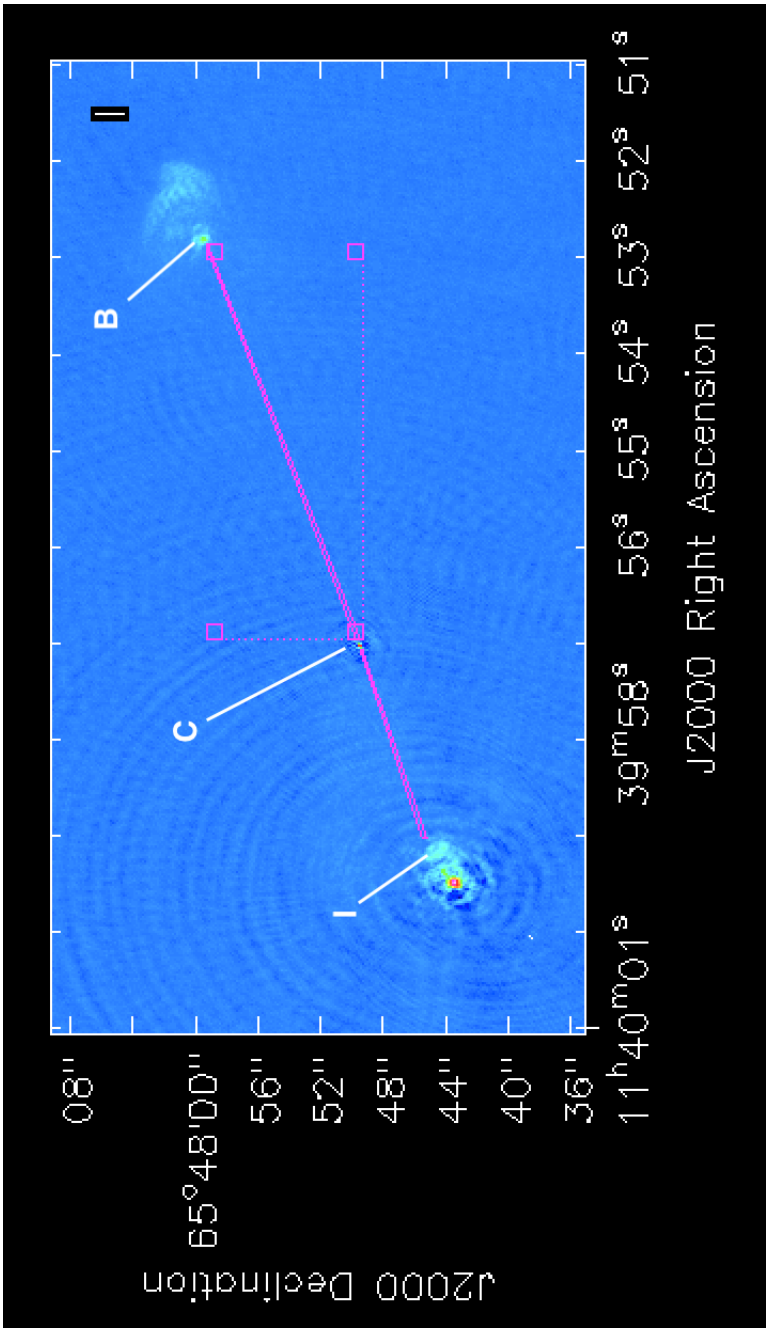

Figure 5.14: The pink boxed regions were used to determine the flux ratio between the jet and counterjet. The jets were assumed to be asymmetric because a straight alignment between the jet and counterjet hotspot was not possible. A region from the first knot nearest to the core to just before feature I was included in the straight jet flux. The counterjet region included emission from just after the core to just before hotspot B.

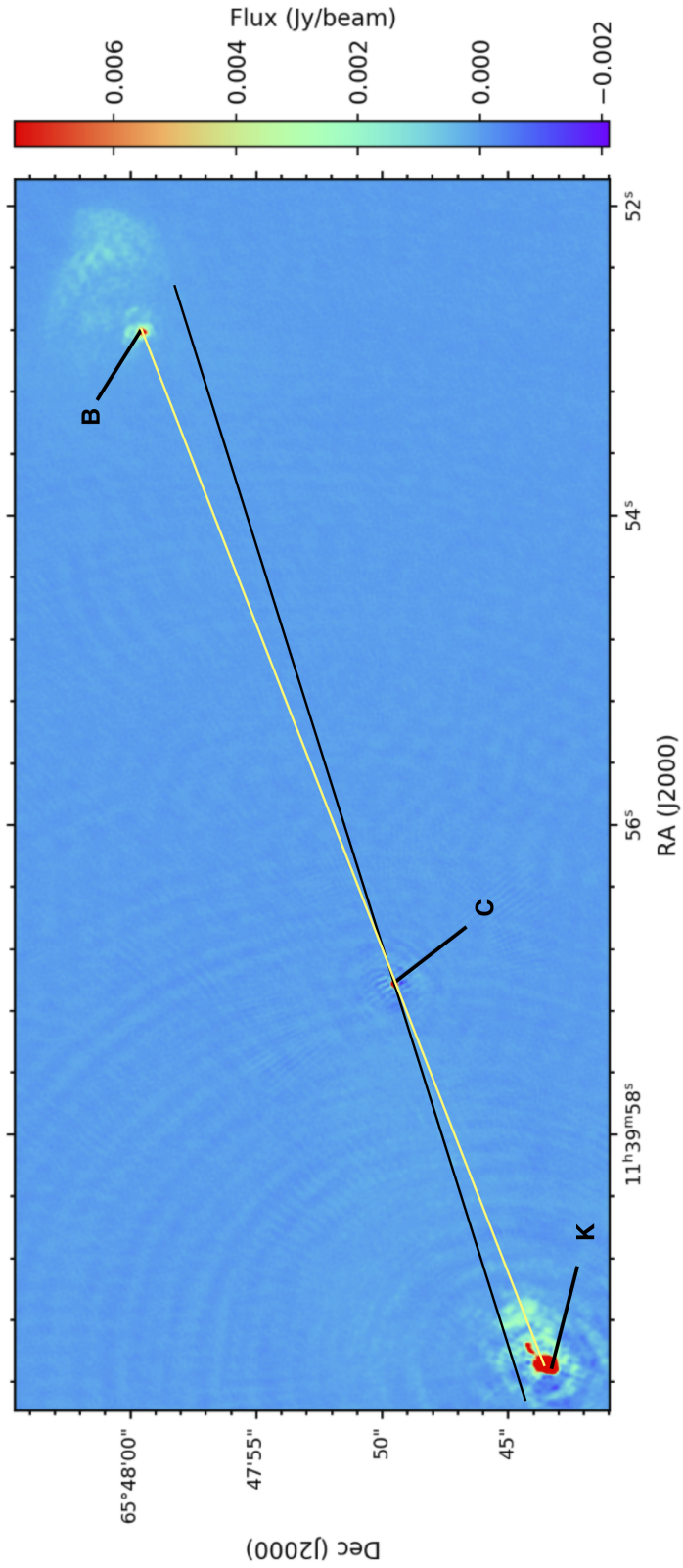

Figure 5.15: The straight path of the visible jet (below the black line) is extrapolated to hotspot distances under the assumption that the jet is linear. The yellow line highlights the alignment of hotspots K and B through the core axis. The offset between the black (visible jet) and the yellow (hotspot axis) indicates that the jet and counterjet are bending at some point in their paths.

5.2.2 The Spectral Index Map

Hotspot B1 in Fig. 5.4 gives $\alpha = -0.65 \pm 0.03$. At A $\alpha = -0.85 \pm 0.05$. Throughout the rest of the lobe the emission ranges from $-1.0 \pm 0.2 \leq \alpha \leq -1.5 \pm 0.2$. Figure 5.10b shows the changes in the spectral index from the core to the east lobe. The extended eastern lobe is corrupted by sidelobes from the hotspot. However, errors on the known real features are low enough to determine α. Important spectral index features include:

(i) At knot D (D1,D2,D3,D4) $\alpha = -0.4 \pm 0.18$. Knot E (E1,E2,E3,E4) correspond to $\alpha = -0.69 \pm 0.17$. Knot F (F2,F3) shows $\alpha = -0.55 \pm 0.22$. At H the spectral index steepens to $\alpha = -1.15 \pm 0.12$ before increasing to $\alpha \sim -0.74 \pm 0.01$ at J.

(ii) The position of hotspot K in Fig. 5.3b corresponds to $\alpha \sim -0.90 \pm 0.01$

(iii) On average the emission bar has $\alpha = -1.25 \pm 0.02$.

5.2.3 Analysis of Transverse Profiles

The changes in flux density across the jet are shown in the transverse profiles in Fig. 5.12. Table 5.4 gives the distance between the slice and the peak position of the core and the maximum flux density at each slice. Slice 1 is part of the core so was not included in the jet analysis. The brightest point along the jet is in slice 2, which corresponds to the first knot (C2). The peak of slice 2 is $\sim$ 2.56 mJy beam^{-1} at a distance of 1$''$.25 ($\sim$ 14 kpc). The dimmest point is at slice 23, where the surface brightness is 0.615 mJy beam^{-1} at a distance of 10$''$.77 from the core. A plot of the deconvolved FWHM versus angular distance from the core is provided in Fig. 5.16a.

The transverse profiles revealed just how narrow and bright knots in the jet are. Knot G from the Bridle et al. (1994a) map ($\sim$9$''$.5 from the core) is difficult to identify in the 1.5 GHz total intensity map. The flux around this knot was close to the rms level. The transverse profiles of the smoothed map show that in the regions where the emission is weak compared to the surrounding emission, there are secondary peaks comparable to the first (e.g., r and w in Fig. 5.12). Since the fidelity of the image is corrupted by the bright sidelobes, some emission peaks were difficult to separate from noise and residual sidelobes.

From Eqn. 4.2 the apparent opening angle was found to be between 0°.5 and 5°. The jet shows the largest expansion in width from the core until $\sim 3''$ from the core. The jet then begins to recollimate until increasing the spreading rate at $\sim 5.5''$ from the core. At $\sim 8''$ from the core the jet continues to expand. The maps produced by (Bridle et al., 1994a) show flaring in 3C 263 close to $14''$ from the core as the jet approaches the hotspot. Measurements were not taken across the jet at this distance in the e-MERLIN+JVLA map since the sidelobes and emission from the hotspot made it difficult to differentiate between real emission and artifacts.

Table 5.4: A list of the peak flux at each slice along the jet, the distance from the core (θ), and the deconvolved FWHM (ϕ). Transverse profiles are given in Fig. 5.12.

Slice	θ (arcsec)	Peak flux (mJy beam^{-1})	ϕ (mas)
1	0.85	13.8715	0.211
2	1.25	2.557	0.198
3	1.60	2.034	0.217
4	1.91	2.315	0.261
5	2.26	1.89001	0.306
6	2.87	1.289	0.355
7	3.42	1.25	0.377
8	3.78	1.704	0.358
9	4.20	2.0513	0.350
10	4.91	2.18169	0.317
11	5.15	2.085	0.291
12	5.58	1.75312	0.390
13	6.02	1.325	0.427
14	6.48	1.285	0.522
15	6.98	1.5267	0.495
16	7.42	1.633	0.502
17	7.79	1.2591	0.487
18	8.38	0.7959	0.349
19	8.78	0.9311	0.253
20	9.18	0.868	0.425
21	9.71	0.843	0.806
22	10.22	0.7399	0.319
23	10.77	0.615	0.398
24	11.19	0.8178	0.372
25	11.66	1.457	0.465
26	12.04	1.47169	0.454
27	12.43	1.291	0.468
28	13.12	3.496	0.664

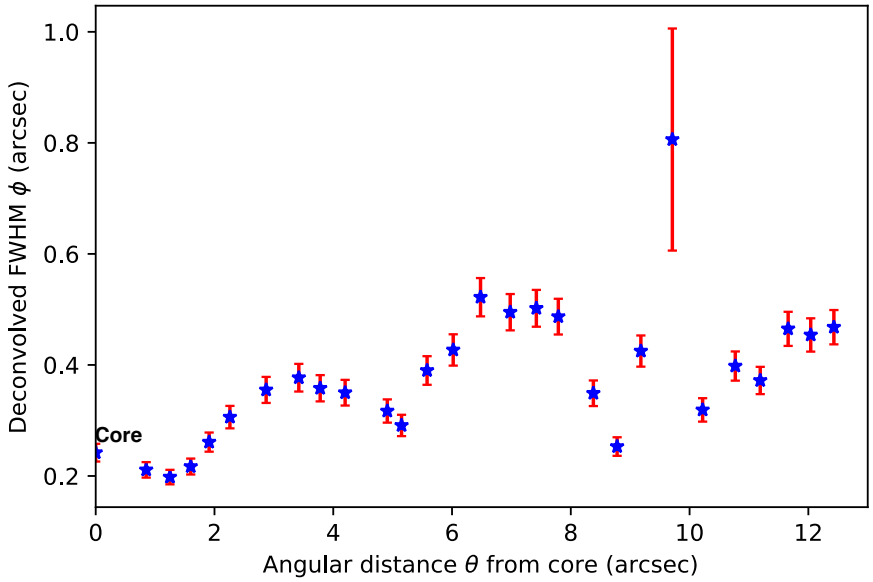

(a)

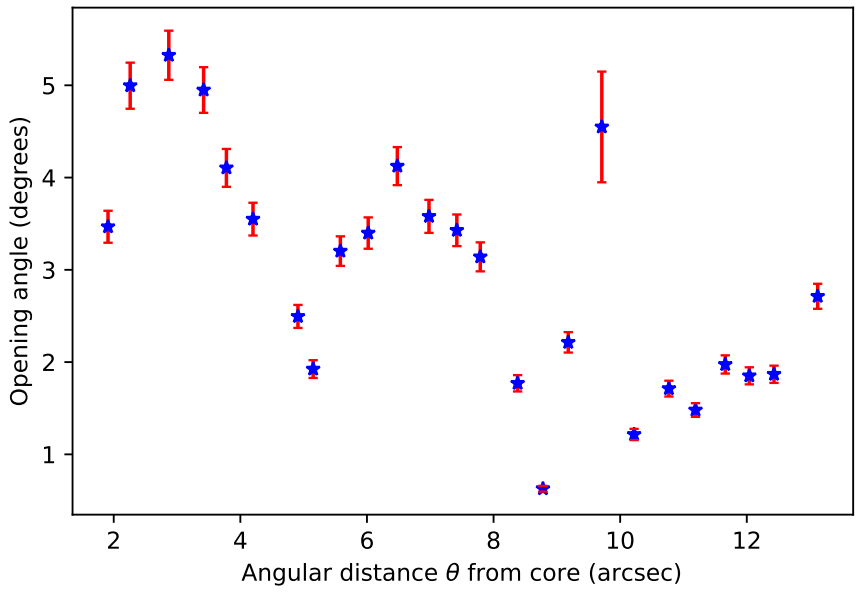

(b)

Figure 5.16: (a) Map of 3C 263 smoothed to a resolution of 1.″0 × 0.″15 at a position angle of −70°. (b) Locations of line segments across the jet at 1.″0 × 0.″15 resolution.

5.2.4 The Environment of 3C 263

The appearance of a bright, compact hotspot in the jet side lobe of 3C 263 is not a complete surprise. A large sample of powerful FRII quasars have been observed having compact hotspots on the jet side (e.g., Laing, 1989; Mullin et al., 2008). This is generally accepted as an indication of relativistic flow around the hotspot (e.g., Mullin et al., 2008). However, there are a few peculiarities about this structure. One of those being the depolarization of the jet side lobe. Of the large sample of DRAGNs known the number observed to have a large depolarization effect on the jet side lobe remains low (e.g., Laing, 1988; Garrington et al., 1988; Bridle et al., 1994b). The other being that the lobe on the jet side is much shorter and the hotspot placed closer to the nucleus than typically observed (e.g., Bridle et al., 1994b). The radio maps of 3C 334 (see Ch. 4) reveal a shorter jet than the counterjet as well, suggesting 3C 263 is not entirely unique.

It is evident that there is some interaction between jets and the local environment on both large and small scales (e.g., Bicknell, 1995; Laing, 1993, 1994, 1996; Garrington et al., 1988). Optical observations with HST and spectroscopy show evidence for clusters of galaxies in the vicinity of quasars at $0.3 < z < 1.0$ (Hardcastle, 2001). The quasar 3C 263 is no exception to this trend. Optical images position the quasar at the centre of a rich galaxy cluster (e.g., Yee et al., 1986; Crawford et al., 1991; Fabian et al., 1991). Clusters are dense, turbulent regions of gravitationally bound galaxies and gas (ionised gas making $\approx 90\%$ of the cluster's composition) (e.g., Roncarelli et al., 2018; Bonafede, 2010). Based on the Laing-Garrington effect, the counterjet side lobe should be more depolarized than the jet side lobe due to the extra distance the light has traveled through a magnetised medium (e.g., Laing, 1988; Garrington et al., 1988). The depolarization of the jet side lobe indicates that there is much more gas on the jet side of the quasar than the counterjet side (e.g., Laing, 1988; Garrington et al., 1988). If hot gas from the intracluster medium (ICM) is more densely found in the jet side region, there should be evidence of extended X-ray emission produced by thermal radiation from the cluster atmosphere (e.g., Hardcastle et al., 2002; Crawford and Fabian, 2003). Early ROSAT satellite data were unsuccessful in this search. These maps were dominated by the bright nuclear X-ray component (Hall et al., 1995). X-ray maps by Chandra provided the resolution necessary to make deep observations to probe the cluster environment (see Figs. 5.17a and 5.17b). The X-ray study by Hardcastle et al. (2002) looked at a small sample

comprised of two quasars and a radio galaxy to identify sources of X-ray emission. In only 3C 263 and the radio galaxy 3C 330 did they find evidence for extended X-ray emission (that is X-ray emission that is larger than than the radio lobes) (Hardcastle et al., 2002). A clear difference in X-ray emission distribution can be seen between the two DRAGNs. The extended X-ray emission in 3C 330 is nearly symmetrically distributed between the two lobes. Whereas in 3C 263, the X-ray emission is greatly lopsided. It is clear from the X-ray maps that the east lobe of 3C 263 is in a region surrounded by hot gas.

Being situated in a dense environment can greatly influence the brightness and morphology of the lobe (e.g., Ishwara-Chandra et al., 1998). The first characteristic in this environment to consider is the asymmetry between the lobe lengths. The east lobe of 3C 263, which sits at the end of the jet, is much closer to the nuclear component than the west lobe. Observations of the radio galaxy 3C 254 may offer some clues to unravel the mystery of this asymmetry (e.g., Thomasson et al., 2006) (see Fig. 5.19). Although a much more extreme case of asymmetry, the nuclear component in 3C 254 lies much closer to the east lobe. There is no detection of a jet or counterjet but emission lines in the east lobe are blueshifted (Thomasson et al., 2006). Two scenarios involving an approaching jet are thought to be responsible for these emission lines. In the first case, the jet drives shocks into the nearby gas. This is thought to increase the ionisation state of the gas (Bremer, 1997). In the second case, the interaction between the jet and the gas can result in the cloud breaking into smaller clouds that allow these emission lines to be visible (Bremer, 1997). In either case the closer east lobe likely lies at the end of the jet (e.g., Bremer, 1997; Thomasson et al., 2006). In both 3C 263 and 3C 254 the lobes are in asymmetric environments with depolarized approaching lobes (e.g., Bremer, 1997; Thomasson et al., 2006). A polarization study of DRAGNs (Ishwara-Chandra et al., 1998) found other sources with similar properties. In a sample of 17 DRAGNs showing evidence of depolarization in lobes, 13 are more depolarized in the shorter lobe (Ishwara-Chandra et al., 1998). In 26 out of 35 DRAGNs the closer components are significantly brighter than any components further away (Ishwara-Chandra et al., 1998). This suggests that the bright jet-side hotspot components (like K in Fig. 5.5a) in other DRAGNs and as seen in 3C 263 have a greater dissipation of energy as it advances through a much denser environment than the counterjet side material (e.g., Eilek and Shore, 1989; Gopal-Krishna and Wiita, 1991; Ishwara-Chandra et al., 1998).

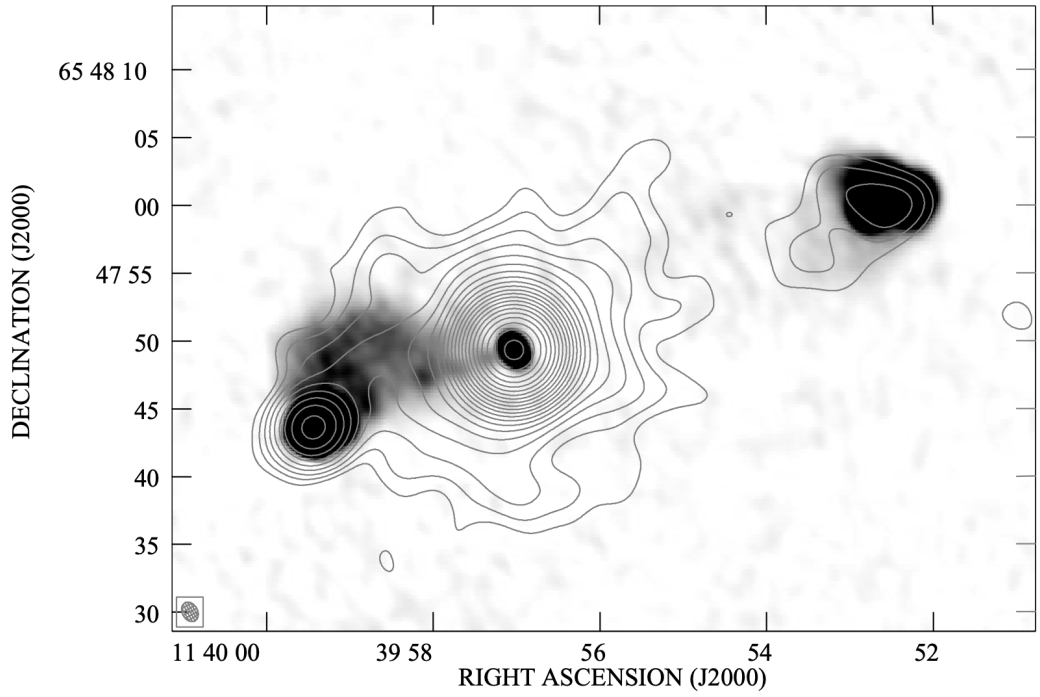

(a)

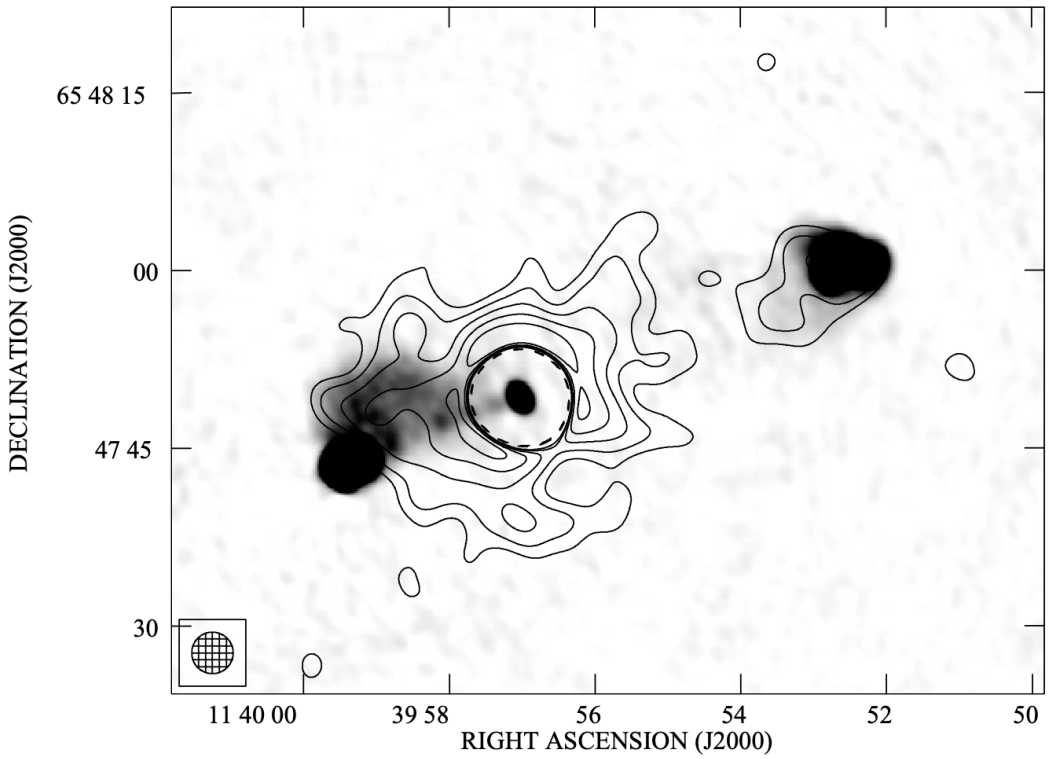

(b)

Figure 5.17: (a) A map of the X-ray emission around 3C 263 as observed by Chandra. The X-ray contours are superimposed on a 1.4 GHz VLA map. Image is reproduced from Hardcastle et al. (2002). (b) The Chandra X-ray map above with the nuclear and hotspot components removed in the X-ray band.

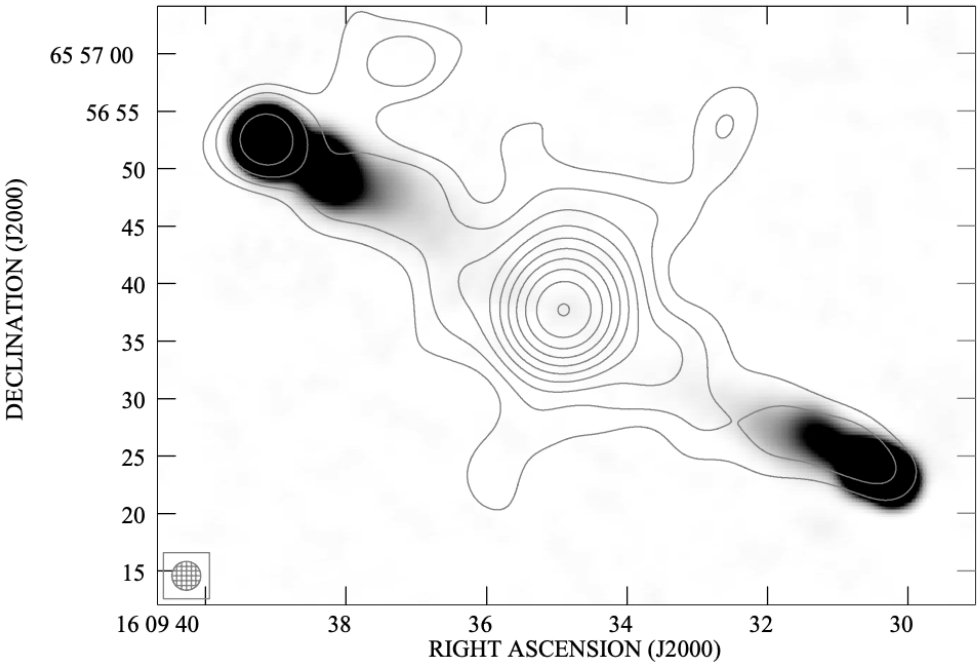

Figure 5.18: A radio map of the radio galaxy 3C 330 with X-ray contours. Image is reproduced from Hardcastle et al. (2002).

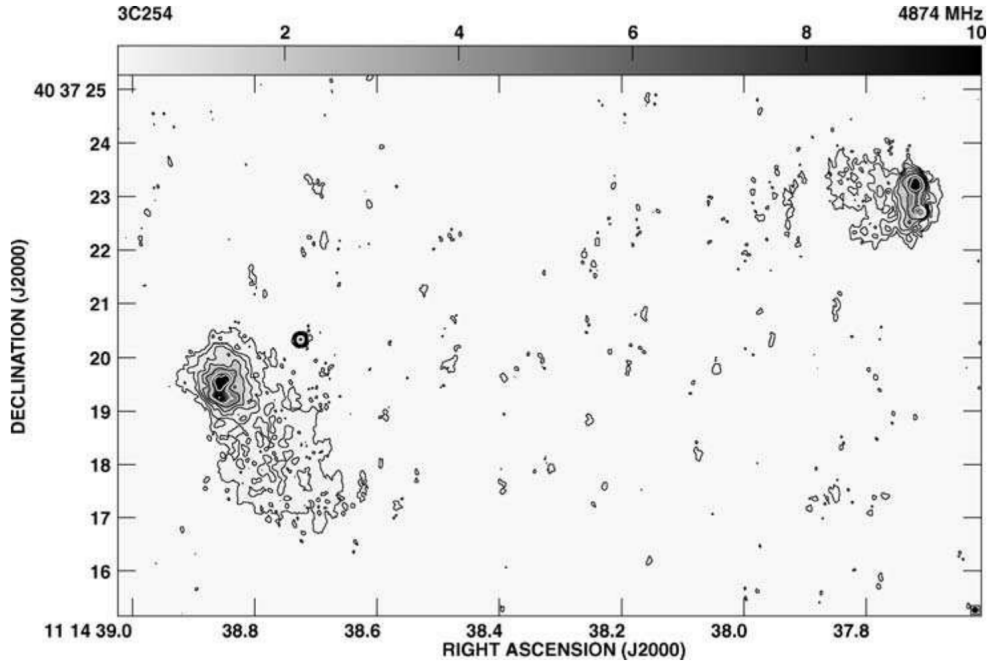

Figure 5.19: An e-MERLIN+VLA radio map of the radio galaxy 3C 254. The radio lobes are asymmetrically placed with respect to the nuclear component. Image is reproduced from Thomasson et al. (2006).

5.3 Summary

The high-resolution 1.5 GHz e-MERLIN+JVLA map shows many similarities to the 5 GHz map in the west lobe. Although severely affected by sidelobes, the east hotspot and the deflected jet is well-defined in the high-resolution map. Overall, the 1.5 GHz map from the e-MERLIN + JVLA arrays has shown:

(i) There is a remarkable similarity in the structure between 3C 334 and 3C 263 that becomes more apparent at high resolution. The two quasars are comprised of an intense, bright 'head' in the counterjet side lobe. The lobe feature is well separated from the host galaxy. Both e-MERLIN maps reveal a straight boundary along the side nearest the core. The heads of the counterjet lobes contain similar features (B - 3C 334, A - 3C 263) that appear embedded in the head of the lobes. Both show polarization vectors from the primary hotspot directed towards the faint feature. This is more obvious in 3C 263. The hotspot in 3C 263 is more centrally placed at the end of the lobe. Faint and diffuse emission fills the space between B and A, especially at low resolution.

(ii) 3C 263 has a strikingly narrow jet. Even at high resolution the knots are not completely resolved. The opening angle of the jet is between $\sim 0\overset{\circ}{.}5$ and $\sim 5^{\circ}$. Three regions of localised spreading are identified. The jet appears to recollimate at least twice between $0''-12''$ from the core. Even in regions where the jet is starting to expand, the jet appears quite narrow along its path.

(iii) Feature J is the final appearance of the jet before terminating in K. The straight jet (D,E,F) do not align with feature J. Astrophysical jets with a jet-crossing feature similar to the emission bar I (e.g., 3C 249.1 and 3C 381) are thought to be formed by a backflow from the termination shock.

(iv) The high resolution of the e-MERLIN+JVLA map revealed the first knot in the jet which was previously undetected at VLA resolution.

(v) The morphology and brightness are very different between the east and west lobes and hotspots. This suggests that there is asymmetry in gas density in the environment around the approaching and receding lobes. The Chandra X-ray maps reveals hot gas around the east lobe. The bright, compact

hotspot is likely a result of greater dissipation of energy as it travels through a denser environment created by the hot gas. Other sources (e.g., 3C 254, 3C 334) have similar properties including a shorter jet side lobe.

The shared similarities between 3C 263 and 3C 334 are not completely unique (e.g., 3C 154 (Bogers et al., 1994), 3C 254 (Thomasson et al., 2006)), but the number of similar FRII DRAGNs is few. In the unified scheme we should also expect to see radio galaxies sharing similar features at different angles. The radio galaxies 4C 14.11 (Hardcastle et al., 1997) and 3C 219 (Brocksopp et al., 2007) are examples of radio galaxies with a hotspot embedded within the lobe. Still, the number of radio galaxies sharing similar properties such as a faint, diffuse, steep-spectrum lobe on the jet side and a bright lobe on the counterjet side is quite low.

Observations and simulations suggest that a binary black hole in the heart of the quasar can explain the "s" shape and misalignment of the lobes in 3C 334 as well as the misalignment of the east lobe in 3C 263 (e.g., Krause et al., 2019). While the jet is remarkably straight in 3C 263, there is some evidence of bending in the lobes. Jet precession could explain the secondary hotspots and the trail of emission likely tracing previous jet locations in 3C 334. In fact, most of the evidence proposed by Marecki (2012) can be explained by a precessing jet (e.g., the spectral gradient across the jet in 3C 334). In 3C 263 there is very little evidence for jet precession except for a misaligned lobe axis. This is not to say jet precession has not occured. It simply does not have the overwhelming evidence that 3C 334 has.

Increasing the sensitivity in the e-MERLIN+JVLA map, which can be done by including the Lovell telescope in the observations or taking more data, will help improve the image fidelity in 3C 334. Additional self-calibration techniques for 3C 263 could also improve the fidelity of the e-MERLIN+JVLA map. Improving the image fidelity could lead to additional evidence in support of an unsteady flow and may aid attempts to resolve the counterjet in these DRAGNs.

Chapter 6

The Radio Galaxy Cygnus A

The very powerful radio source Cygnus A was first linked to two merging galaxies by Baade and Minkowski (1954), although it was later discovered to be a giant elliptical with a dust lane. A two-element interferometer at Jodrell Bank revealed that the single radio source was actually composed of two large radio lobes separated by nearly 2′.12 (Jennison and Das Gupta, 1953). Improved optical observations revealed a peculiar elongated object near the core but no definitive sign of a quasar until the early 1990's. It was then Antonucci et al. (1994) used the Hubble Space Telescope (HST) to detect broad emission lines from Mg II and high polarization perpendicular to the observed radio axis around the nucleus. From this it was discovered that a powerful quasar was residing within the nucleus. Since Cygnus A is relatively close for a radio galaxy ($\sim$ 600 million light-years away) and is the second strongest radio source in the sky, Cygnus A is an excellent source for probing properties of FRII radio sources and comparing theories to observations. More details regarding Cyg A's very early history and importance in developing the field of radio galaxies are given in §1.2.3.

Despite being extensively studied over the years, continuous improvements to sensitivity and bandwidth provide the necessary tools to probe structures within the large extended emission in Cygnus A. The most recent discoveries exceptionally important for this thesis are (i) the discovery of a $\sim$4 mJy radio source 460 pc from the nucleus of Cygnus A by Perley et al. (2017), and (ii) the first direct imaging of the torus around the nucleus of Cygnus A by Carilli et al. (2019). Images showing the transient and torus are provided in Figs. 6.1a and 6.1b.

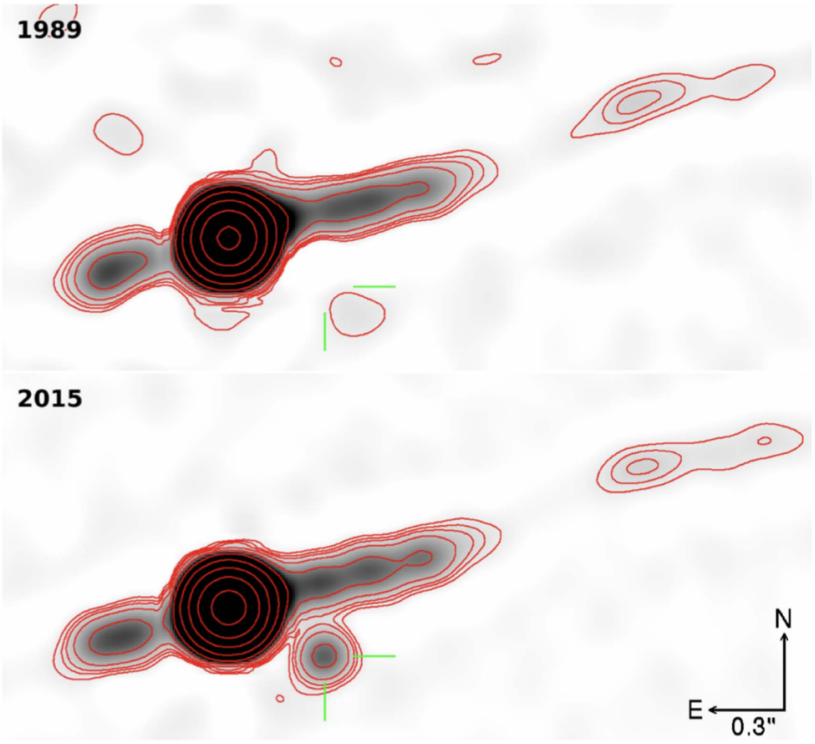

(a)

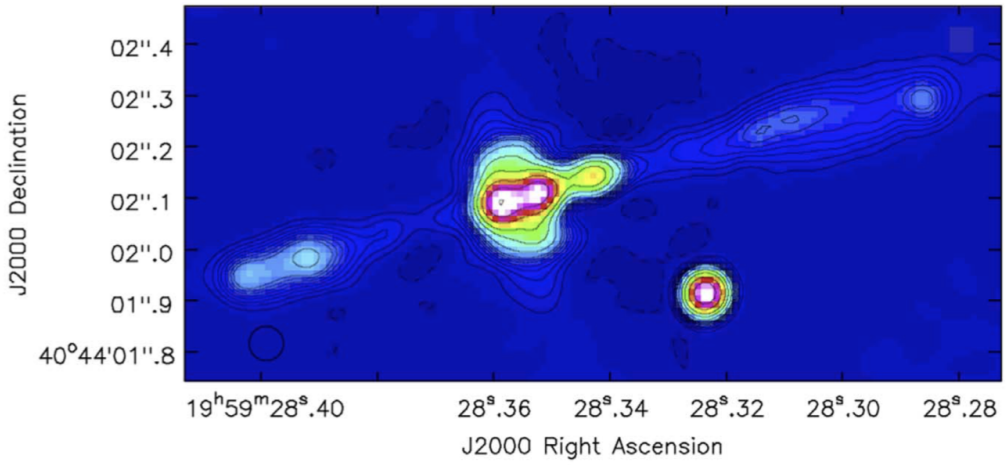

(b)

Figure 6.1: (a) Radio maps of the nucleus of Cygnus A at 5 GHz from 1989 and 2015 compared to show the brightening of the transient. Image reproduced from Perley et al. (2017). (b) Radio Map of the nucleus of Cygnus A at 22 GHz to show the torus and transient. In this image emission from the core has been subtracted to highlight the newly identified features. Image reproduced from Carilli et al. (2019).

This chapter describes the work done for this thesis on the powerful radio galaxy Cygnus A (Cyg A). Total intensity maps of Cyg A from the e-MERLIN array at 1.5 GHz and 5 GHz are discussed. Maps and analysis presented in this chapter seek to supplement work regarding the recent discoveries of features near the core and to provide new insight into the emission seen in Cyg A at e-MERLIN resolution. Redshift and other derived observational properties of Cygnus A are found in Table 6.1.

Table 6.1: Properties of Cygnus A at 1.5 GHz and 5 GHz. Values where the frequency is not expressed were derived from the 1.5 GHz e-MERLIN map.

Property	Value	Reference
Alt. name	3C 405	
IAU name	1957+41	
Optical type	RG[a]	Antonucci et al. (1994)
RA core (J2000)	19h59m28.355	
Dec core (J2000)	$+40°44'02''.11$	
z	0.056	NED
Distance	232 Mpc	Graham (1970)
Source size[b] (kpc)	143	
S_{peak} core at 1.5 GHz (mJy beam^{-1})	401±12	
S_{peak} core at 5 GHz (Jy beam^{-1})	1.03±0.004	
S_{int} core (mJy) at 1.5 GHz	450±25	
S_{int} core (Jy) at 5 GHz	1.11±0.06	
S_{peak} east hotspots at 1.5 GHz (mJy/beam)[c]	911±20	
S_{peak} east hotspots at 5 GHz (mJy/beam)[c]	17.9±0.34	
S_{peak} west hotspots at 1.5 GHz (mJy/beam)[c]	648±17	
S_{peak} west hotspots at 5 GHz (mJy)[c]	17.2±0.3	

[a] RG indicates a radio galaxy.

[b] All projected source sizes used the cosmological calculator by Wright (2006) to determine that $z = 0.056$ corresponds to a scale of 1.129 kpc arcsec^{-1}.

[c] Values refer to the brightest hotspot at each frequency.

6.1 Results

6.1.1 Total Intensity Map at 1.5 GHz

Cygnus A at 1.5 GHz is a great challenge for the e-MERLIN array. The source extends an impressive 2′.1 across and has large diffuse lobes. At e-MERLIN resolution much of the diffuse structure is resolved out but the lobes and hotspots still affect the system temperature. The increase in flux due to the rise in system temperature was corrected using the steps described in §3.6. The fidelity of the total intensity image at 1.5 GHz shown in Figs. 3.32, 3.33, and 3.34 was limited by the phase and amplitude calibration and the presence of diffuse emission not easily reconstructed by CLEAN.

At e-MERLIN resolution, Cygnus A at L- and C-band is composed of three distinct regions:(i) the nucleus, (ii) east hotspots, and (iii) west hotspots. From the furthest point of the most eastern hotspot to the furthest point of the most western hotspot the total extent of the source is ∼128″ (∼143 kpc). Observational properties derived from the maps are provided in Table 6.1. A complete list of source sizes is also provided in Table 6.2.

A map of the total intensity distribution of the east hotspots is provided in Fig. 6.2a. From these maps it was clear that untangling real features from sidelobes around the hotspots would be a challenge in the e-MERLIN maps. To verify the fidelity of the images, the contours from each of the hotspots were superimposed on the high-resolution total intensity maps presented in Dabbech et al. (2018) (see Figs. 6.3 and 6.5). The emission at 0″.19×0″.12 resolution is composed of four main regions of emission: G, H, I, and J. A small nearly linear feature composed of G1 and G2 is pointed in the direction of the core and the brightest feature H (H1,H2,H3,H4). Feature G1 in Fig. 6.2b shows a slight bend and a bright boundary in the feature directed toward hotspot H. Early radio observations identified G as the primary hotspot and H as the secondary hotspot in the east lobe (Hargrave and Ryle, 1974). Hotspot H has a peak flux density of 911±182 Jy beam^{-1}. A small, faint region is embedded in the main hotspot between the large, bright region (H4) and the hook-like feature near the edge of the hotspot (H3). Feature H2 is a bright line of emission protruding from the hotspot in the direction of feature J. Regions J and I (I1,I2) are north of hotspots G and H and reveal less intense but equally complex sub-features.

Table 6.2: Deconvolved FWHM of various structures in Cygnus A at 1.5 and 5 GHz. Projected source sizes and errors were estimated using the task IMFIT in CASA.

Region	size[a]
Total source size	$120''$
Feature G at 1.5 GHz (major)	$1''.047\pm0.057$
Feature G at 1.5 GHz (minor)	$0''.384\pm0.022$
Feature G at 5 GHz (major)	$1''.004\pm0.008$
Feature G at 5 GHz (minor)	$0''.245\pm0.008$
Core at 5 GHz (major)[b]	13.60 ± 0.89 mas
Core at 5 GHz (minor)	$7.72\pm$ mas

[a] Angular sizes were calculated using the ruler feature in CASA's viewer or by fitting a Gaussian over the source with the task IMFIT.
[b] The deconvolved FWHM at 1.5 GHz for this source could not be calculated.

The total intensity distribution of the west hotspots is shown as two main regions: K and L (see Fig. 6.4). As with the east hotspots, the C-band VLA maps were superimposed with the L-band e-MERLIN data to test image fidelity (see Fig. 6.5) (Dabbech et al., 2018). Early observations with a 5 km radio telescope identified L as the primary hotspot and K as the secondary hotspot (Hargrave and Ryle, 1974). A long feature K1 is seen extending from the largest hotspot towards the east. West of K1 is a larger, brighter region K2 that makes up one hotspot. The peak of the west hotspot K2 is $S_\nu = 648 \pm 130$ mJy/beam. South of hotspot K is the bright hotspot L. L is a complex region composed of sub-features and convoluted boundaries. Many of the features surrounding L1 and L2 are from the sidelobes due to the sparse *uv* coverage. Yet L1 is clearly defined as a bright, compact hotspot. Feature L2 forms a fainter, bent trail of emission. Detectable also in old VLA radio maps and X-ray maps (e.g., Carilli et al., 1989; Pyrzas et al., 2015), feature M appears to be a knot from the jet that is elongated in the direction of hotspot L1.

Figure 6.6 shows the total intensity distribution of the nuclear region of Cygnus A at 1.5 GHz. In this map the core, inner jet, and counterjet are one

continuous structure. At the centre of feature A is the core with a flux density of 450±90 mJy. The small bump of emission to the east (E) corresponds with the direction of the counterjet. The longer, elongated emission to the west (D) points in the direction of the jet. These are the only visible remnants of a jet or counterjet in the 1.5 GHz map. Below A is a compact radio source B with a flux density of 5.2±2.2 mJy.

6.1.2 Total Intensity Map at 5 GHz

The 5 GHz maps of the total intensity distribution with grey-scale representation of each of the significant regions in Cygnus A are provided in Figs. 6.7, 6.9, 6.11, 6.12a, and 6.12b. The nucleus of the radio galaxy is shown in Fig. 6.7. An additional map showing the core and inner knot positions with respect to the inner jet in the 1986 1.6 GHz EVN-VLBI maps by Krichbaum et al. (1998) is provided in Fig. 6.8. Since the rms noise around the nucleus decreased the signal detection, comparing the two maps served as a way to minimize problems with feature identification. Feature A on the 5 GHz map is the bright, compact core. Most of the elongated jet emission seen in Fig. 6.6 is resolved out at 5 GHz. A remnant of this emission along the jet is shown as feature D1. Feature B aligns with the radio source also found in the 1.5 GHz map (see Fig. 6.6). Feature E appears to coincide with the counterjet in the 1.5 GHz map, indicating it could be a knot in the counterjet. Features C1 and C2 are discussed in §6.3.3.

Only fragments of the brightest components of the east hotspot (G and H) are observed in the 5 GHz map (see Fig. 6.9). A comparison between the e-MERLIN 5 GHz e-MERLIN east hotspot map and the 43 GHz map produced by Carilli et al. (1999) is shown in Figs. 6.10. At 5 GHz features G1 and G2 are pointed towards feature H2. The region between the hook (H3) and H4 is also resolved out. The ridge of emission (I1,I2) and J are not identifiable in the 5 GHz map.

The west hotspot shown in Figs. 6.11, 6.12a, and 6.12b reveals fragmented remnants of the hotspot. At the northern end of the hotspot is a thin linear structure (K1) pointed due east. Most of the east-west emission is resolved out at 5 GHz. West of K1 is a larger region of emission (K2) that is resolved into multiple complex sub-regions. The southern hotspot (L) is split into L1 and L2. Although feature M is not large or very bright, it does align with knot M in the 1.5 GHz map (see Fig. 6.4). A comparison to the 43 GHz VLA maps is shown in Fig. 6.13.

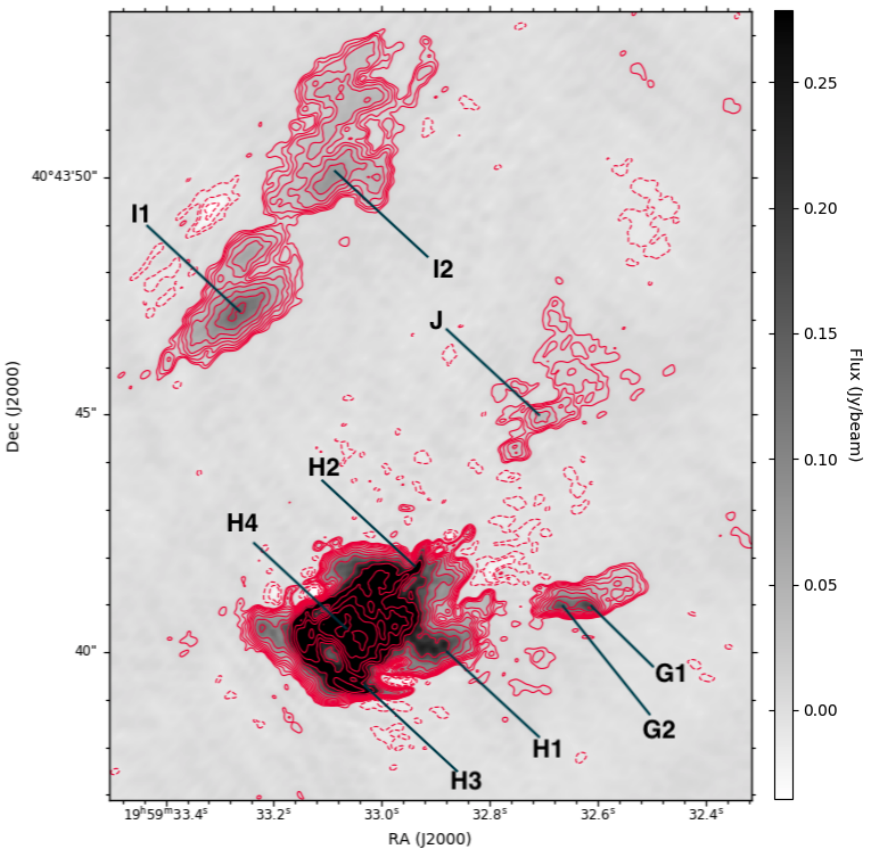

(a)

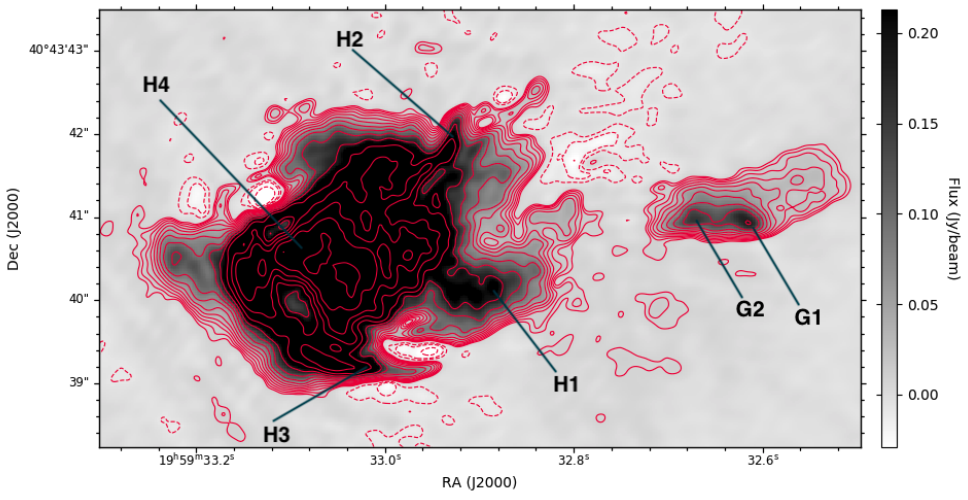

(b)

Figure 6.2: (a) A map of the total intensity distribution of the east hotspot of Cygnus A at 1.5 GHz. Contours are superimposed on a grey-scale representation of the total intensity. Contour levels are drawn at -4, -2, -1 (dotted), 1, 1.414, 2, 2.828, 4, 5.657, 8, 11.31, 16, 22.63, 32, 45.25, 64, 90.51, 128, 181, 256, 362, 512, 724, and 1024 times 8.0 mJy per clean beam area. (b) A closeup of the complex regions G and H.

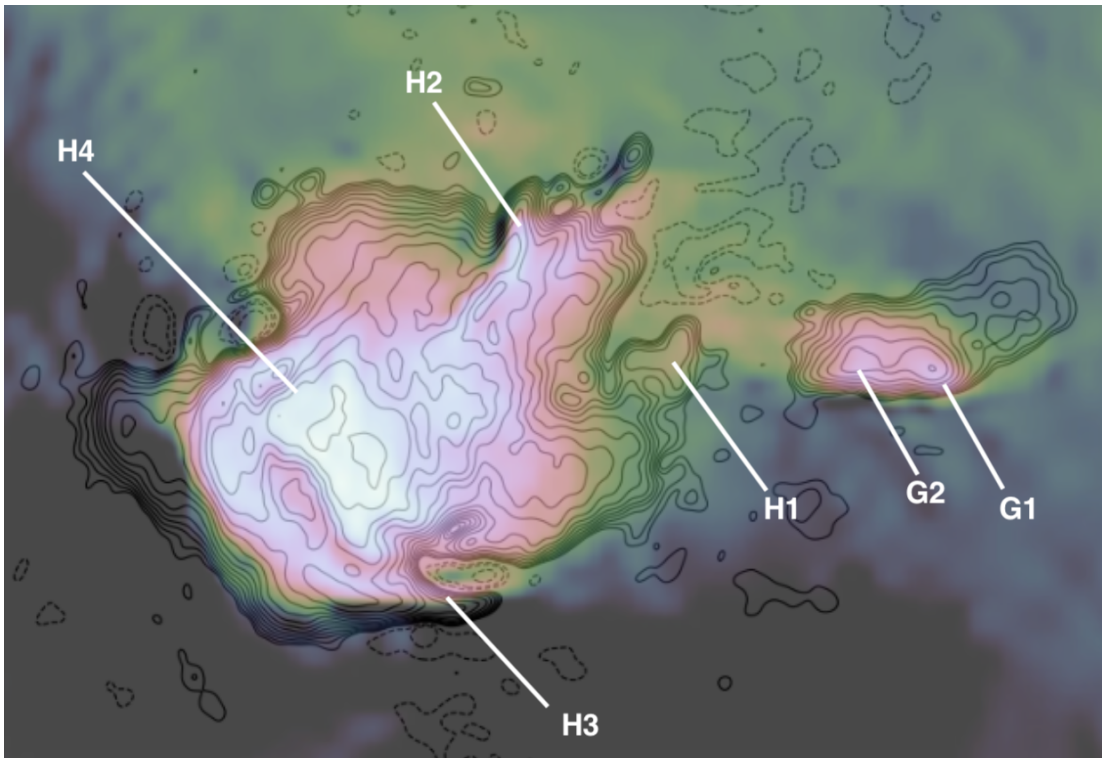

Figure 6.3: Total intensity distribution (black contours) of the east hotspots in the L-band e-MERLIN maps superimposed on high-resolution VLA coloured C-band maps from Dabbech et al. (2018). The C-band VLA images are not precisely to scale but served as a guide to test the fidelity of the e-MERLIN maps. Contours are drawn at -4, -2, -1 (dotted), 1, 1.414, 2, 2.828, 4, 5.657, 8, 11.31, 16, 22.63, 32, 45.25, 64, 90.51, 128, 181, 256, 362, 512, 724, and 1024 times 8.0 mJy per clean beam area.

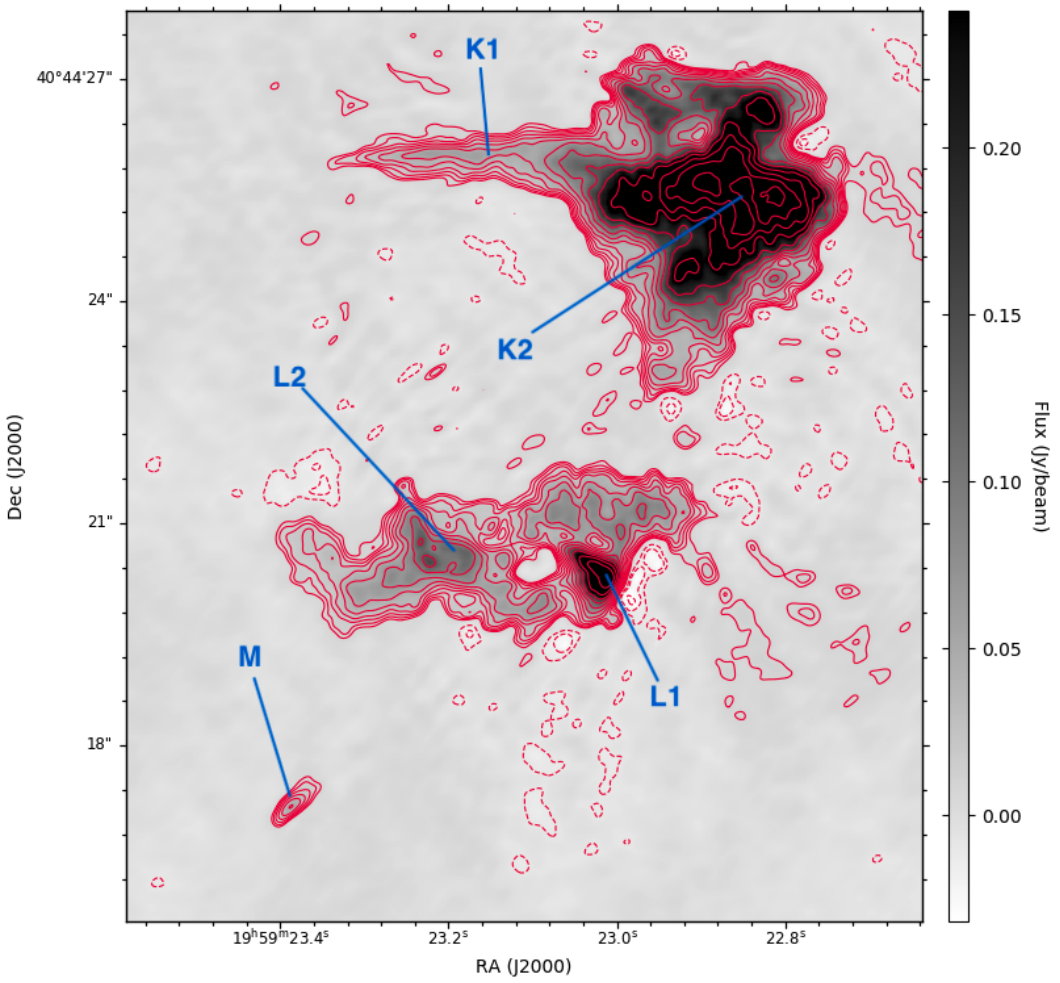

Figure 6.4: A map of the total intensity distribution of the west hotspots of Cygnus A at 1.5 GHz. Contours are superimposed on a grey-scale representation of the total intensity. Contour levels are drawn at -4, -2, -1 (dotted), 1, 1.414, 2, 2.828, 4, 5.657, 8, 11.31, 16, 22.63, 32, 45.25, 64, 90.51, 128, 181, 256, 362, 512, 724, and 1024 times 8.4 mJy per clean beam area.

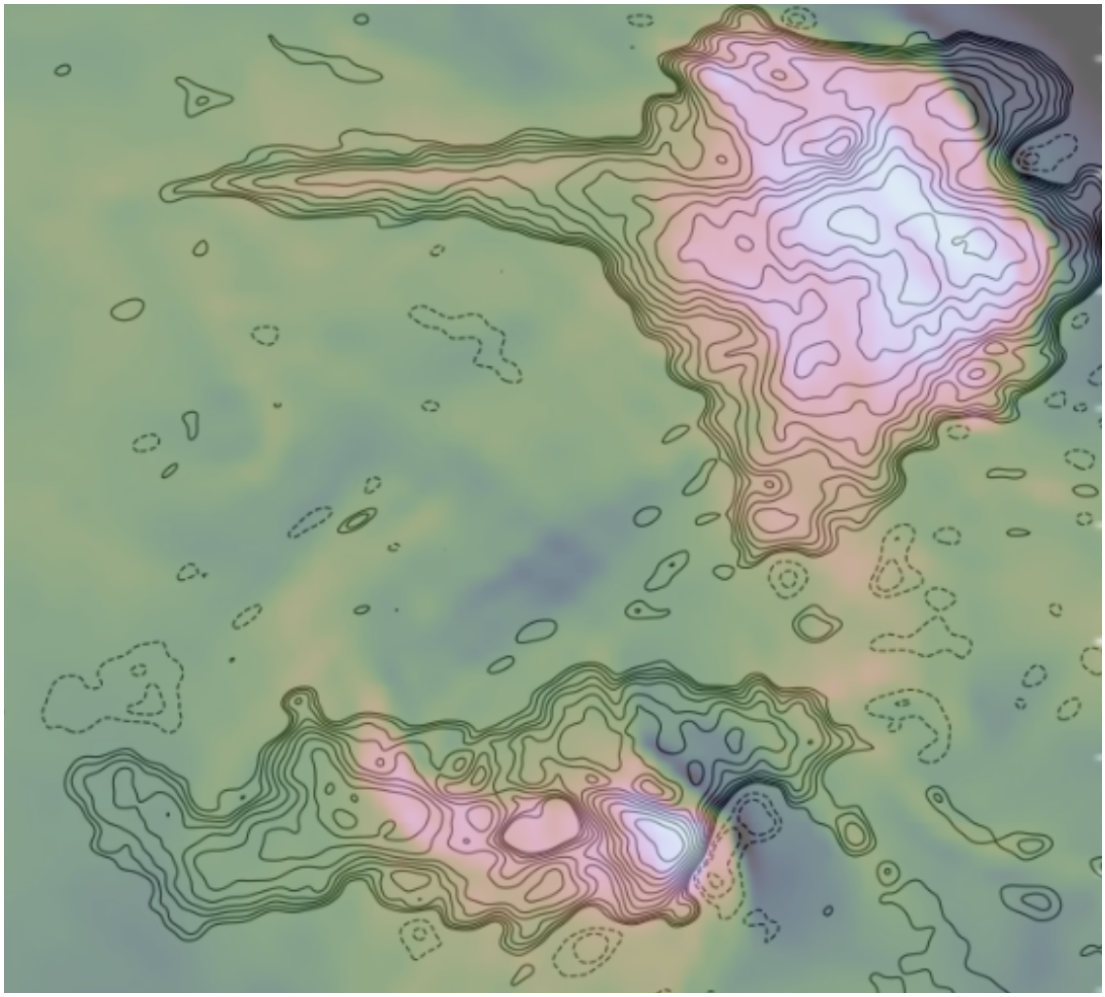

Figure 6.5: The total intensity distribution (black contours) from the L-band e-MERLIN map was superimposed on a C-band coloured, high-resolution VLA map from Dabbech et al. (2018) The C-band VLA west hotspots image and the L-band e-MERLIN map are not precisely to scale but served as a tool to test the quality of the e-MERLIN maps. Contours are drawn at -4, -2, -1 (dotted), 1, 1.414, 2, 2.828, 4, 5.657, 8, 11.31, 16, 22.63, 32, 45.25, 64, 90.51, 128, 181, 256, 362, 512, 724, and 1024 times 8.4 mJy per clean beam area.

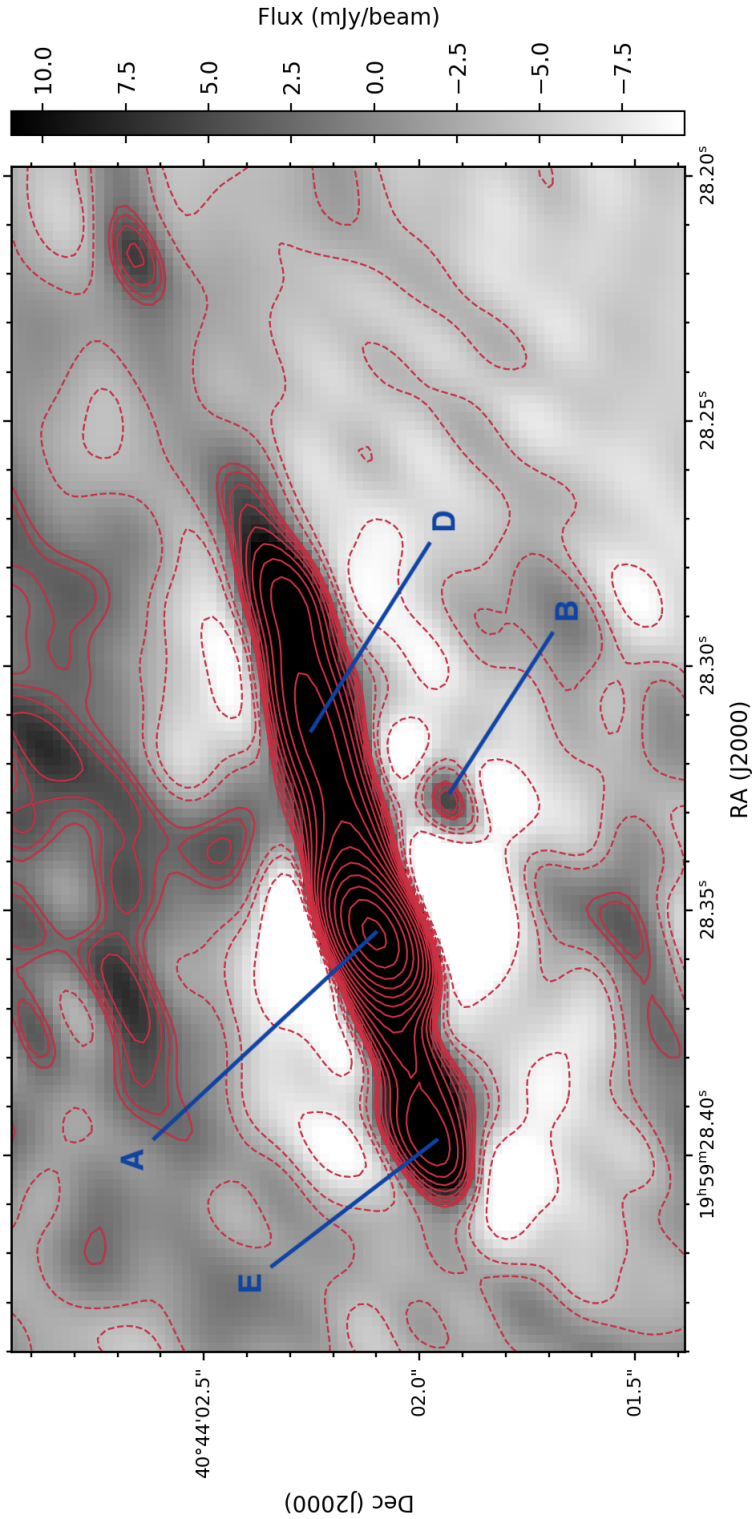

Figure 6.6: A map of the total intensity distribution of the nucleus of Cygnus A at 1.5 GHz. Contours are superimposed on a grey-scale representation of the total intensity. Contour levels are drawn at -4, -2, -1 (dotted), 1, 1.414, 2, 2.828, 4, 5.657, 8, 11.31, 16, 22.63, 32, 45.25, 64, 90.51, 128, 181, 256, 362, 512, 724, and 1024 times 2.0 mJy per clean beam area.

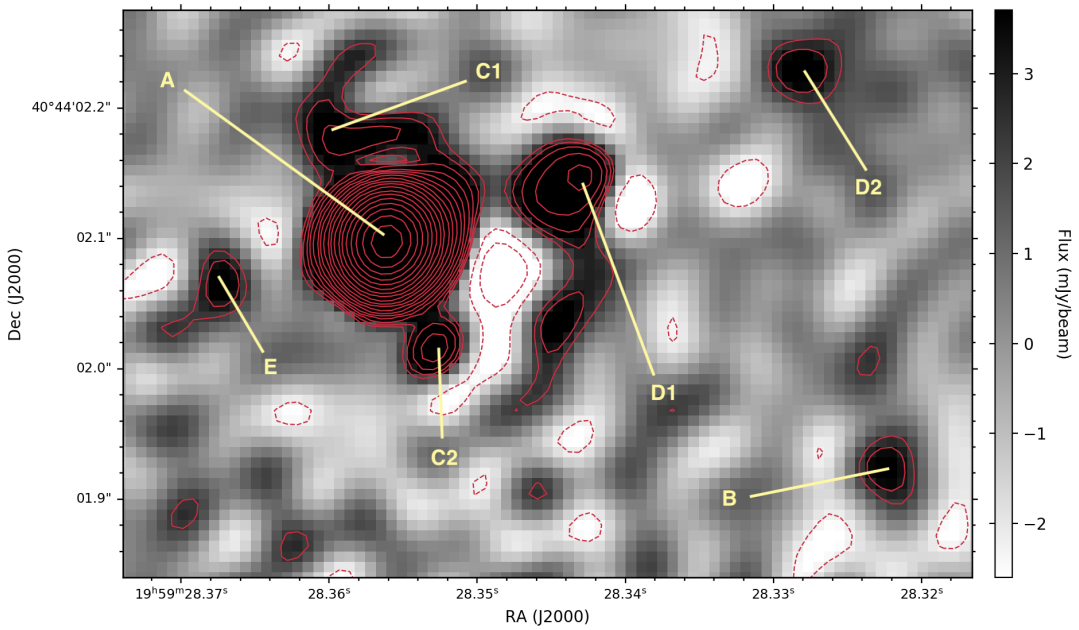

Figure 6.7: A map of the total intensity distribution of the nucleus of Cygnus A at 5 GHz. Contour levels are drawn at -4, -2, -1 (dotted), 1, 1.414, 2, 2.828, 4, 5.657, 8, 11.31, 16, 22.63, 32, 45.25, 64, 90.51, 128, 181, 256, 362, 512, 724, and 1024 times 2.4 mJy per clean beam area.

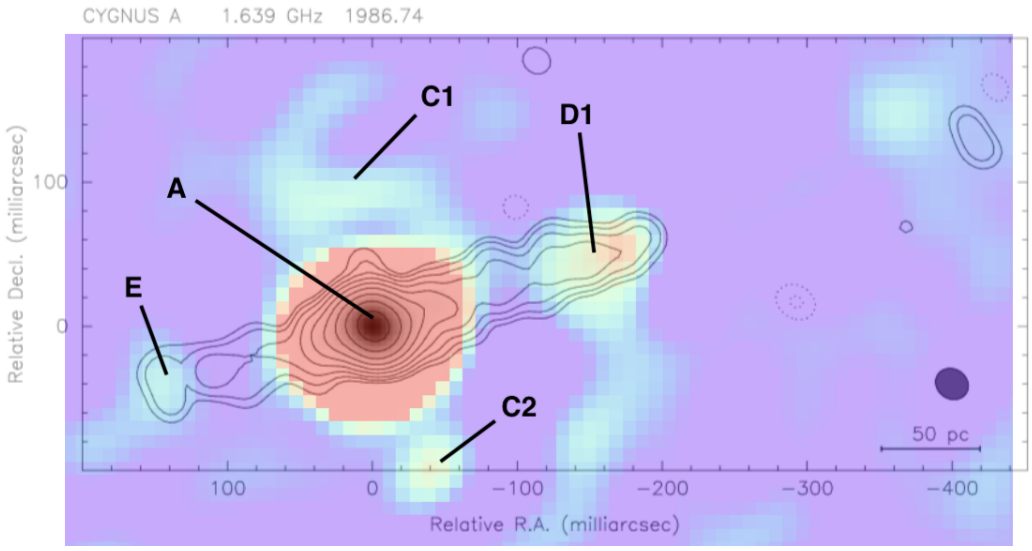

Figure 6.8: The e-MERLIN map of the total intensity distribution (rainbow coloured map) of the nucleus of Cygnus A at 5 GHz compared to a 1.6 GHz EVN-VLBI map by Krichbaum et al. (1998) (black contours).

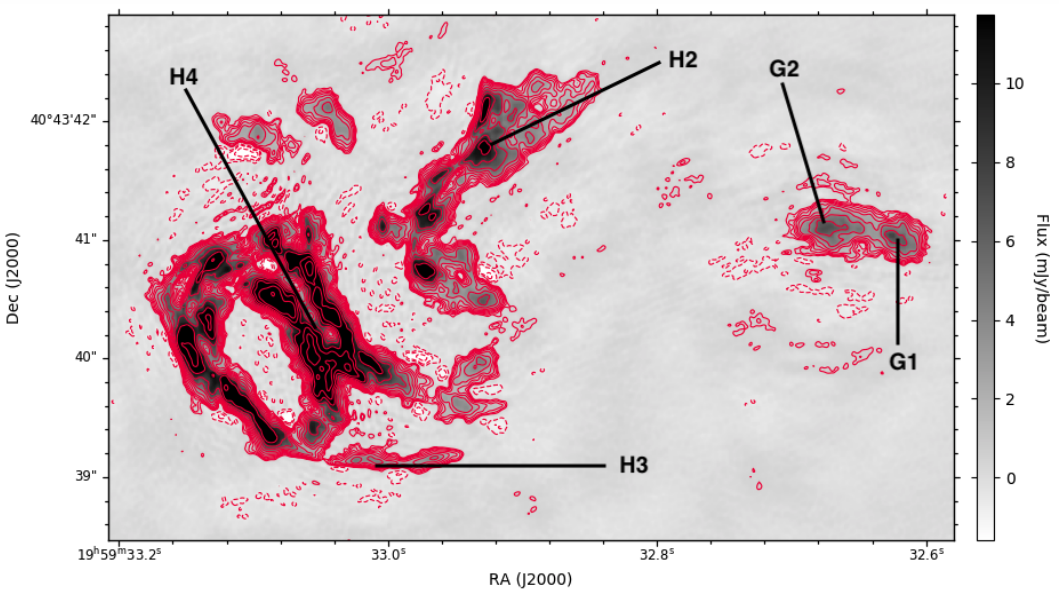

Figure 6.9: An e-MERLIN map of the total intensity distribution of the east hotspots in Cygnus A at 5 GHz. Contours are superimposed on a grey-scale representation of the total intensity. Contour levels are drawn at -4, -2, -1 (dotted), 1, 1.414, 2, 2.828, 4, 5.657, 8, 11.31, 16, 22.63, 32, 45.25, 64, 90.51, 128, 181, 256, 362, 512, 724, and 1024 times 0.51 mJy per clean beam area.

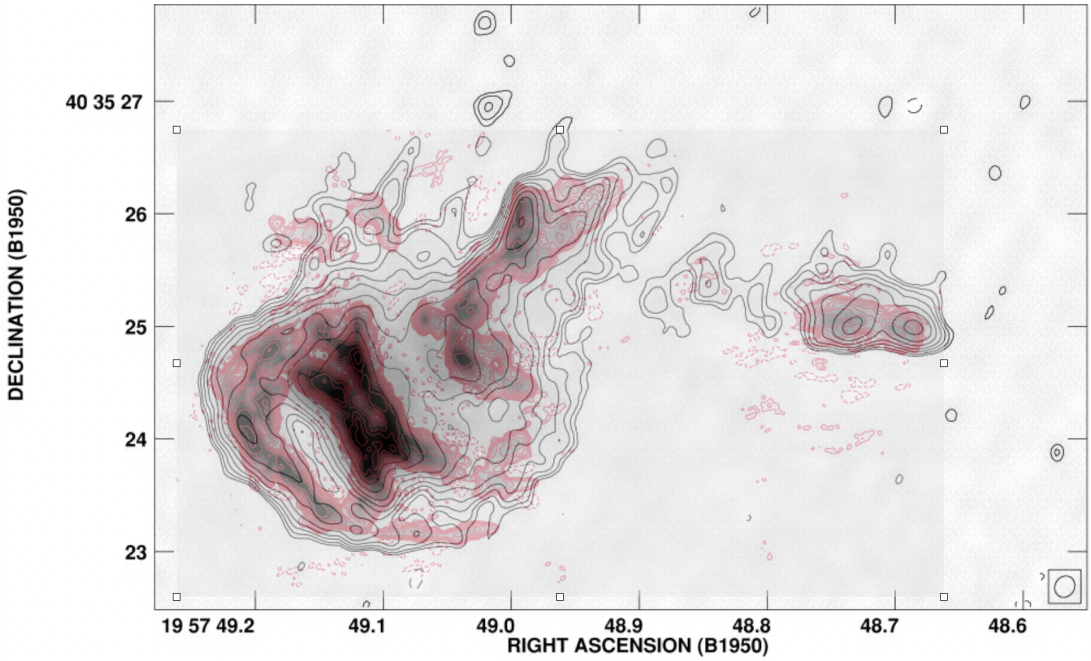

Figure 6.10: The e-MERLIN 5 GHz map of the east hotspots (red contours) superimposed on a VLA 43 GHz map (black contours and grey-scale representation) by Carilli et al. (1999). The e-MERLIN contour levels are drawn at -4, -2, -1 (dotted), 1, 1.414, 2, 2.828, 4, 5.657, 8, 11.31, 16, 22.63, 32, 45.25, 64, 90.51, 128, 181, 256, 362, 512, 724, and 1024 times 0.51 mJy per clean beam area.

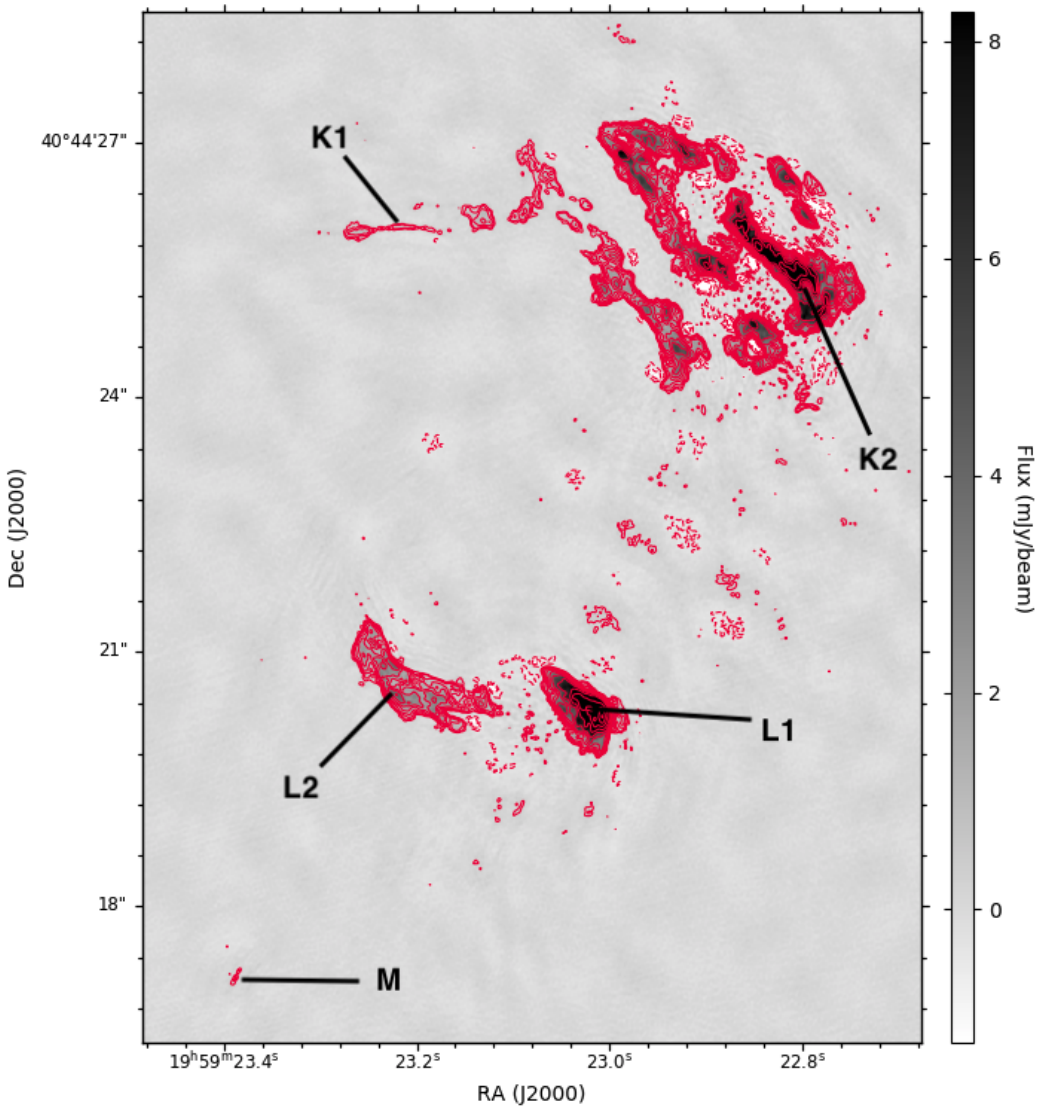

Figure 6.11: The e-MERLIN map of the total intensity distribution of the west hotspot of Cygnus A at 5 GHz. Contours are superimposed on a grey-scale representation. Contour levels are drawn at -4, -2, -1 (dotted), 1, 1.414, 2, 2.828, 4, 5.657, 8, 11.31, 16, 22.63, 32, 45.25, 64, 90.51, 128, 181, 256, 362, 512, 724, and 1024 times 0.39 mJy per clean beam area.

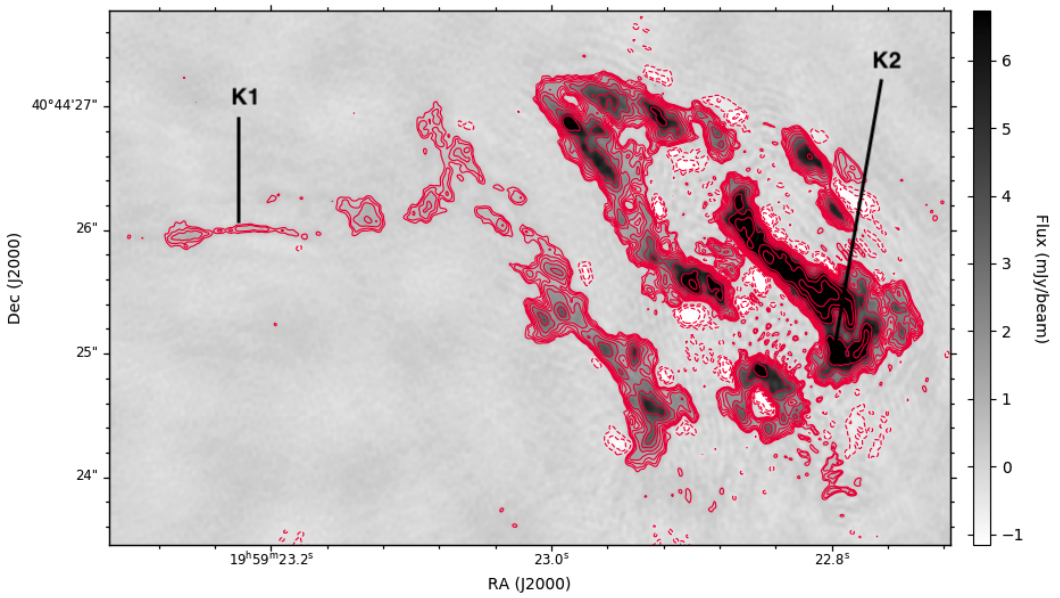

(a)

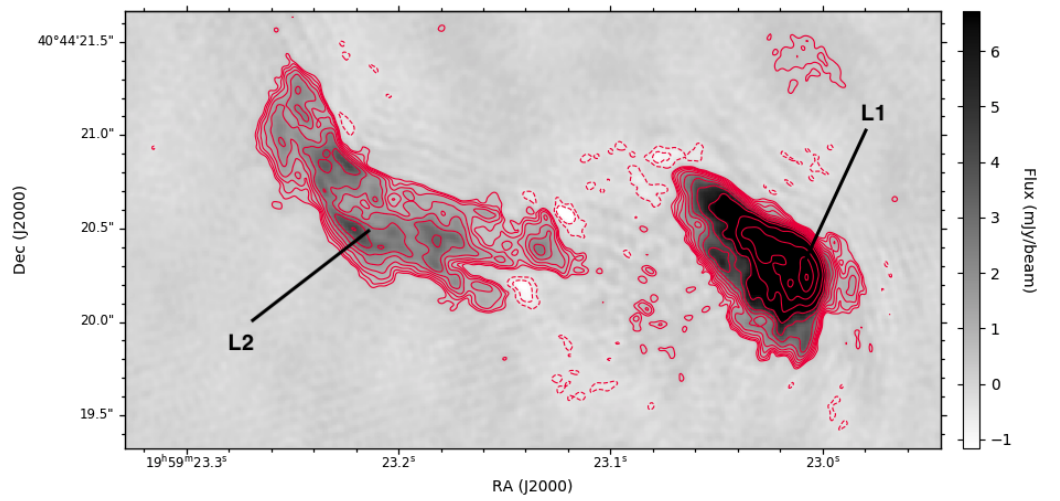

(b)

Figure 6.12: (a) The e-MERLIN map of the total intensity distribution of the northern component of the west hotspot of Cygnus A at 5 GHz. Contours are superimposed on a grey-scale representation. Contour levels are drawn at -4, -2, -1 (dotted), 1, 1.414, 2, 2.828, 4, 5.657, 8, 11.31, 16, 22.63, 32, 45.25, 64, 90.51, 128, 181, 256, 362, 512, 724, and 1024 times 0.39 mJy per clean beam area. (b) The e-MERLIN map of the total intensity distribution of the southern component of the west hotspot of Cygnus A.

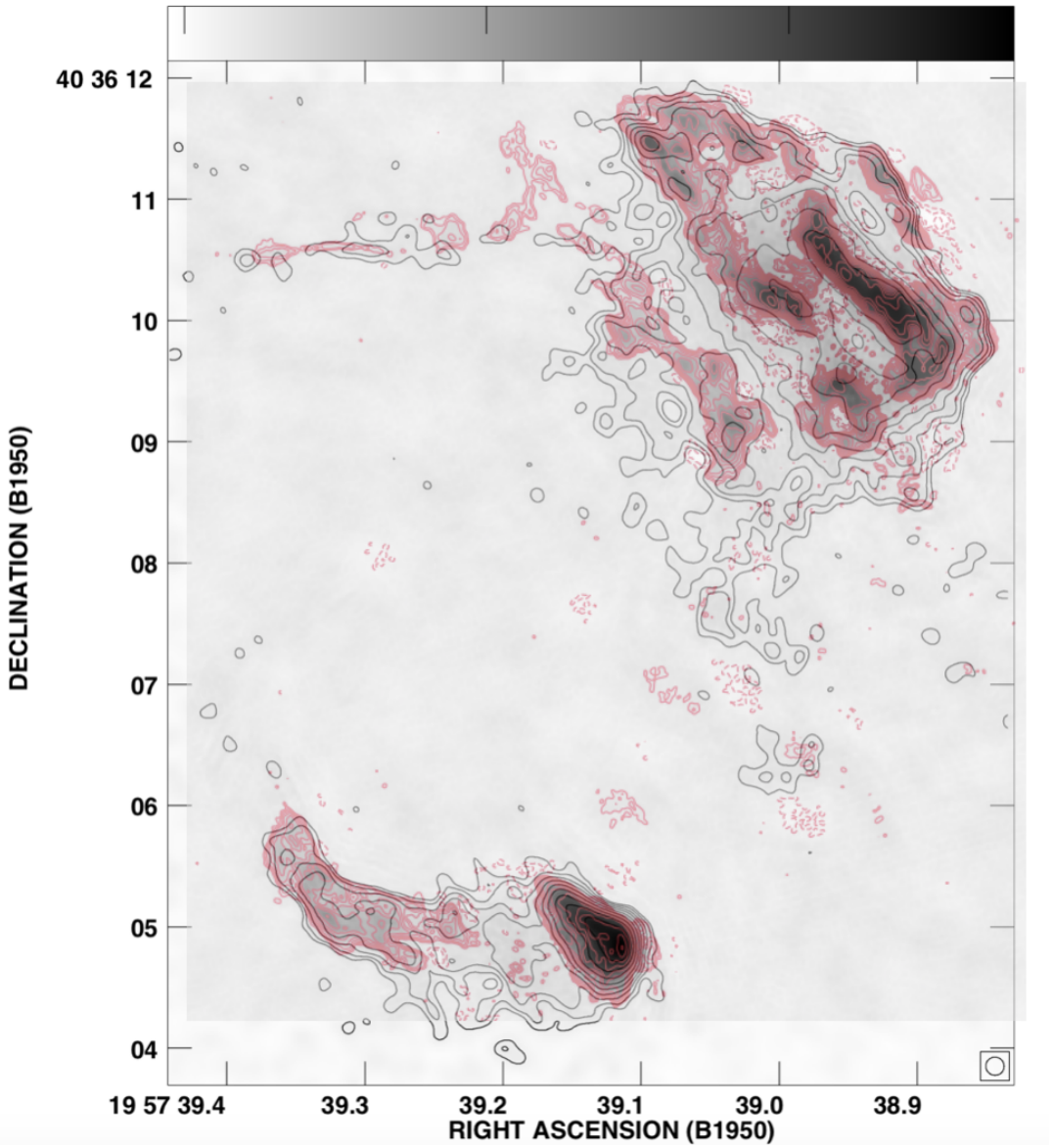

Figure 6.13: The e-MERLIN 5 GHz map of the west hotspots (red contours) superimposed on a VLA 43 GHz map (black contours and grey-scale representation) by Carilli et al. (1999). The e-MERLIN contour levels are drawn at -4, -2, -1 (dotted), 1, 1.414, 2, 2.828, 4, 5.657, 8, 11.31, 16, 22.63, 32, 45.25, 64, 90.51, 128, 181, 256, 362, 512, 724, and 1024 times 0.39 mJy per clean beam area.

6.2 The Spectral Index Maps

The e-MERLIN C-band maps were convolved with a $0\farcs19\times0\farcs12$ beam (PA -57°) to match the resolution of the L-band e-MERLIN maps. Larger errors were expected given the uncertainty in the quality of the L-band system temperature calibration and the sparse *uv* coverage at 5 GHz. The spectral index map of the brightest components in the east hotspots and the spectral index error map are presented in Figs. 6.14a and 6.14b. The compact features G1 and G2 in the primary hotspot have spectral indices $\sim 0.5 \pm 0.1$. In the secondary hotspot H, spectral indices are taken from the centre of the features. Feature H1 is not obviously visible in the spectral index map. Part of the feature is evident (with large errors) but most of the feature has been clipped from the map. The visible portion indicates a spectral index of -1.2 ± 0.73. At H2, the linear feature extending towards J, the spectral index is $\sim -0.5 \pm 0.04$. The hook-like feature H3 through the more central part H4 has an spectral index close to $\sim -1.2 \pm 0.5$.

A spectral index map of the west hotspots and the corresponding error map is provided in Figs. 6.15 and 6.16. At L2 the spectral index is close to $\sim -1.2 \pm 0.1$ but increases to $\sim -0.6 \pm 0.1$ in the primary hotspot L1. The main fragment of K1 reveals a spectral index similar to much of K2 ($\sim -1.2 \pm 0.2$). However, the most northern part of K2 shows a flatter spectral index ($\sim -0.8 \pm 0.1$).

A spectral index map of the inner jet and nuclear region are given in Figs. 6.17a and 6.17b. Near the brightest nuclear component the spectral index is $\sim 0.7 \pm 0.1$. The extended counterjet from the central component mostly has spectral indices near $\sim -0.8 \pm 0.1$

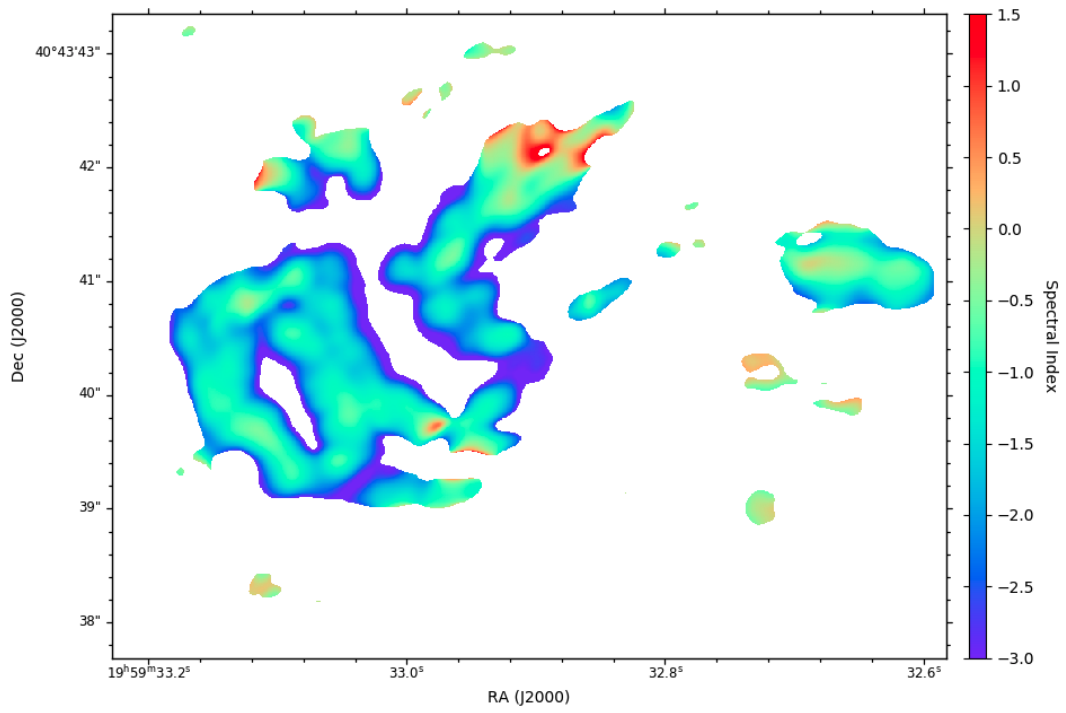

(a)

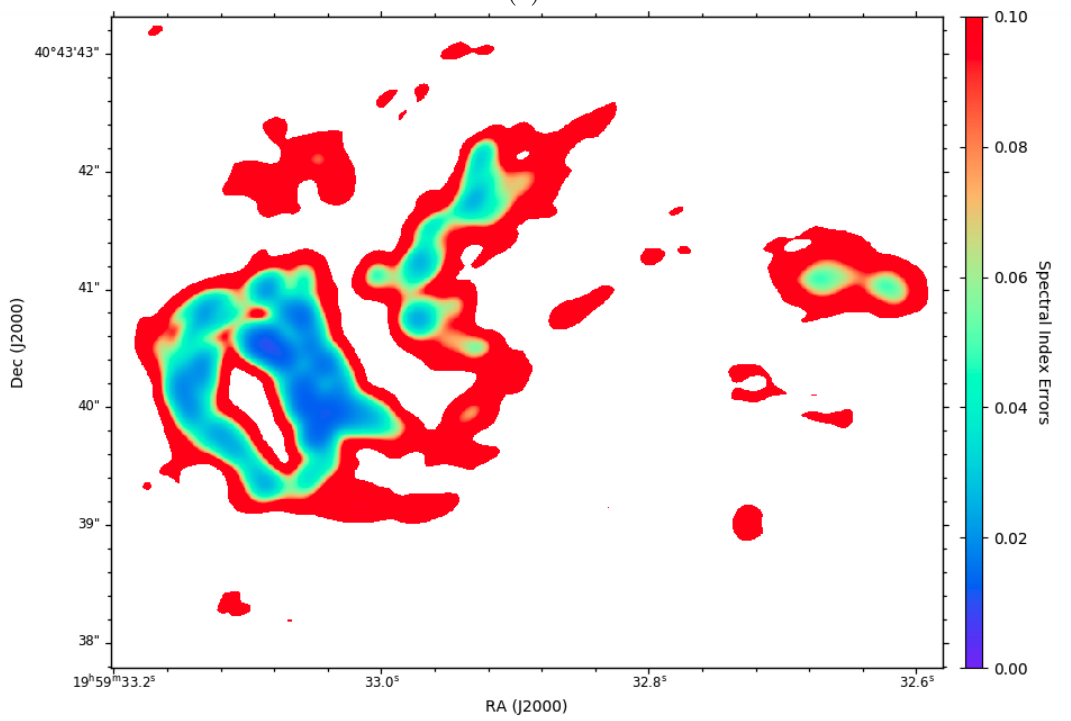

(b)

Figure 6.14: (a) A spectral index map of the east hotspots in Cygnus A. The spectral index map was produced using 1.5 GHz and 5 GHz e-MERLIN maps at resolution 0.″19×0.″12 (PA -57°). Both maps were clipped at 0.2 mJy. (b) The spectral index error map for the east hotspots.

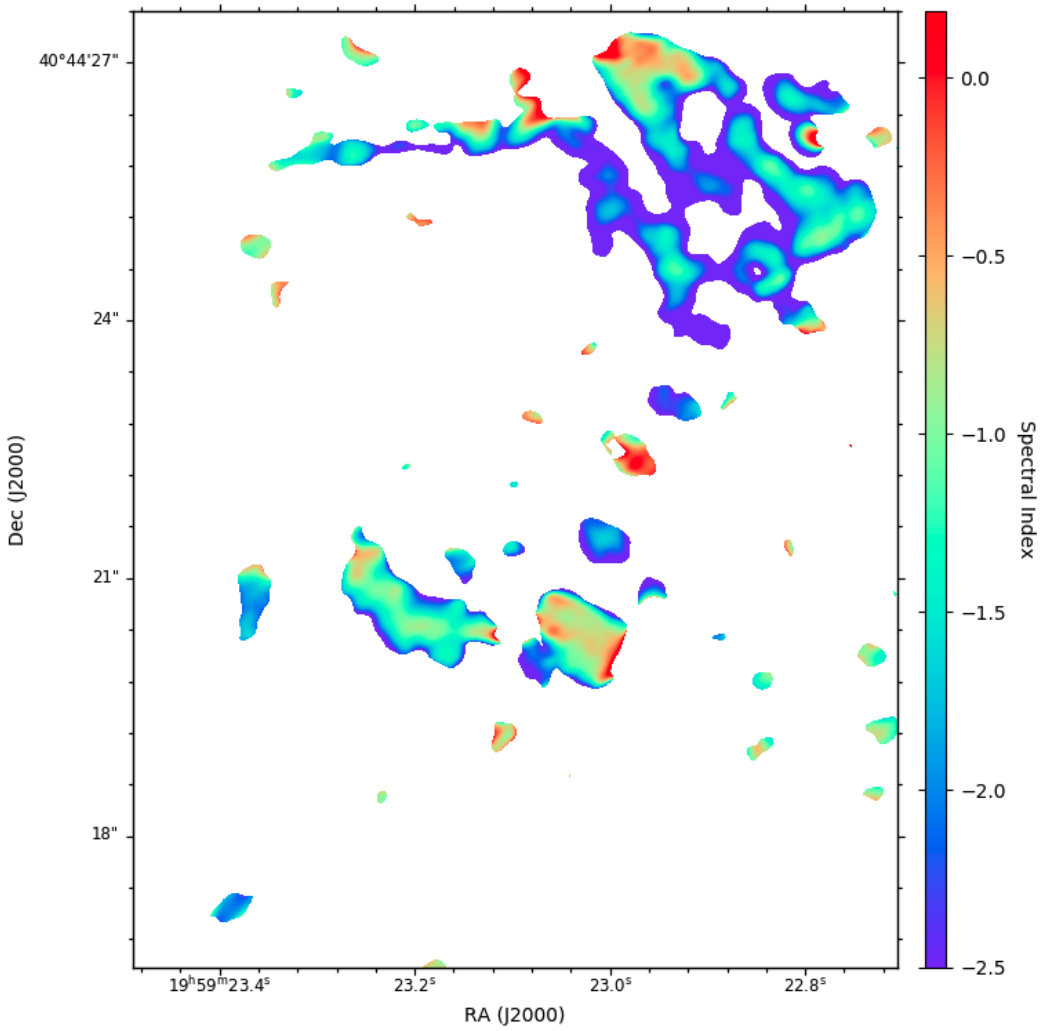

Figure 6.15: A spectral index map of the west hotspots in Cygnus A. The spectral index map was produced using 1.5 GHz and 5 GHz e-MERLIN maps at resolution 0.″19×0.″12 (PA -57°). Both maps were clipped at 0.2 mJy beam^{-1}. (b) The spectral index error map for the east hotspots.

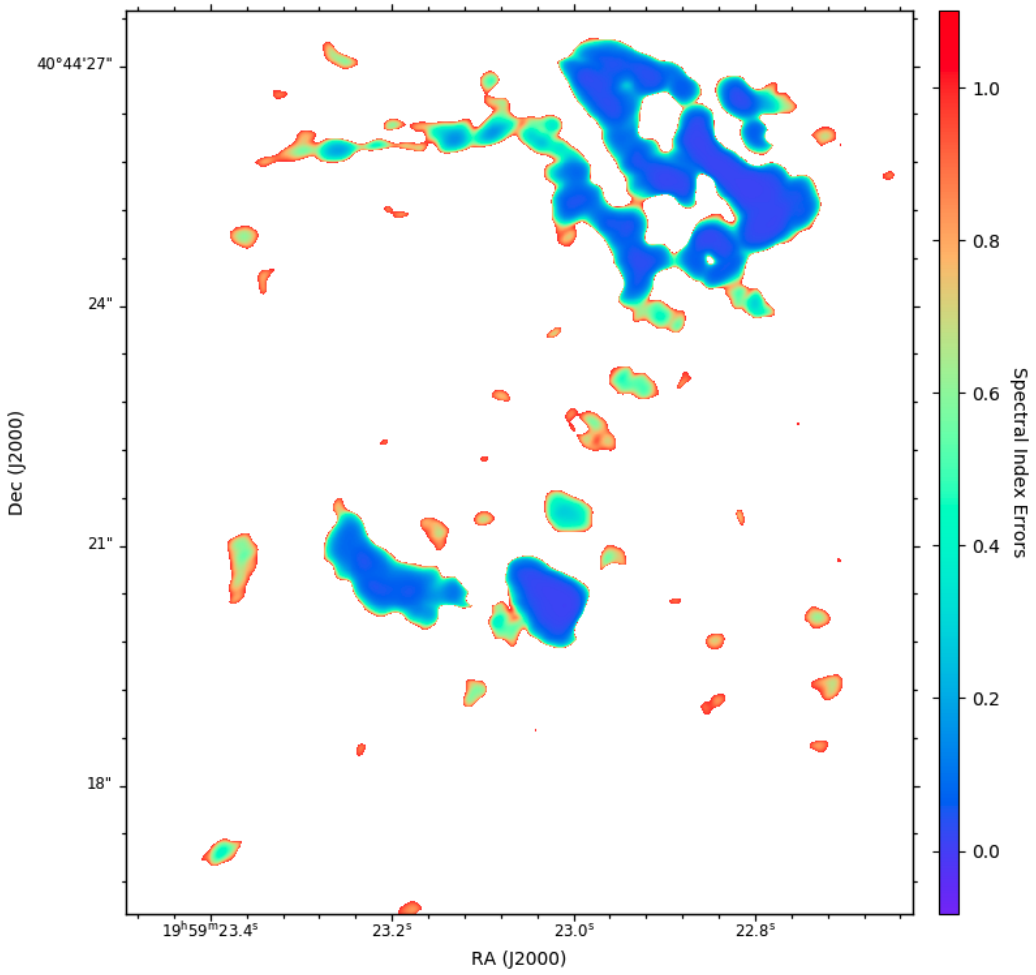

Figure 6.16: A spectral index error map of the west hotspots in Cygnus A. The spectral index error map was produced using 1.5 GHz and 5 GHz e-MERLIN maps at resolution 0.″9×0.″12 (PA -57°).

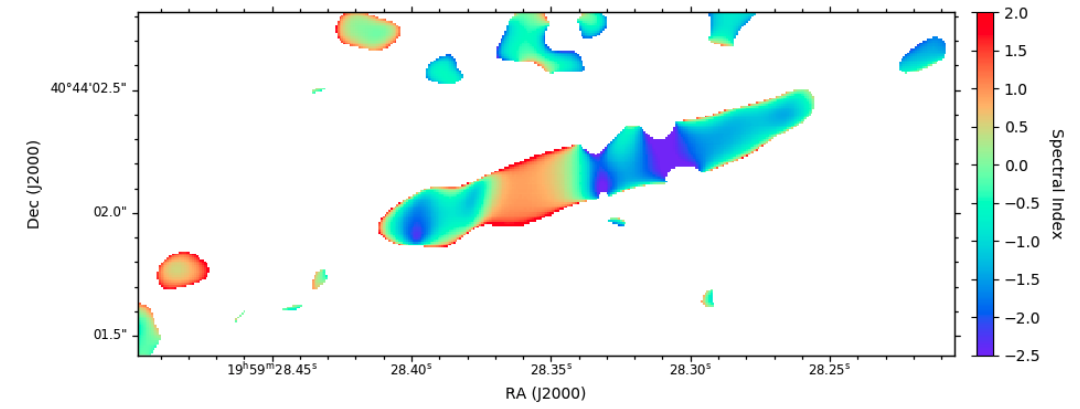

(a)

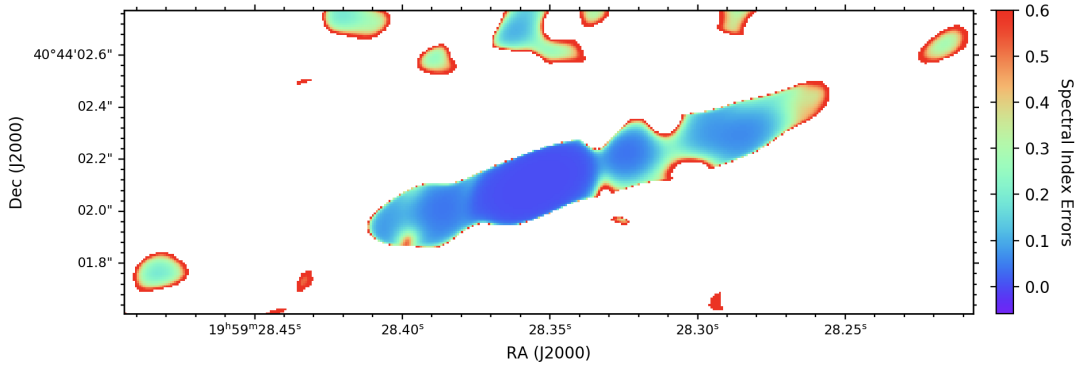

(b)

Figure 6.17: (a) A spectral index map of the nuclear region in Cygnus A. The spectral index map was produced using 1.5 GHz and 5 GHz e-MERLIN maps at resolution 0.″19×0.″12 (PA -57°). Both maps were clipped at 0.8 mJy beam^{-1}. (b) The spectral index error map for the east hotspots.

6.3 Discussion

6.3.1 Detection of the Off-nucleus Transient

Recent work with the JVLA led to the discovery of two new features near the nucleus of Cygnus A. One of the new discoveries, and the focus of this section, is a new compact radio source that was observed by Perley et al. (2017) with the JVLA. Early radio observations of Cygnus A's nucleus revealed components of a jet and counterjet extending out from the central feature. Absent from these maps was a compact feature close to the nucleus (see Fig. 6.1a). In 2016 new observations of Cygnus A revealed the new radio source with a flux density close to 4 mJy (Perley et al., 2017). This feature was coincident with NIR/adaptive optics observations of a bright secondary component in Cygnus A by Canalizo et al. (2003). Because the transient is located $\sim 0\farcs42$ from the centre of the nucleus, low-resolution observatories cannot detect the feature under the PSF of the nucleus. Very few non-radio observatories achieve resolutions $< 0\farcs4$. Radio observations are crucial to understanding the nature of feature B due to their ability to reach the resolutions required to spatially separate the nucleus from the transient. The e-MERLIN array is particularly special in that it has intermediate baseline lengths between the VLA and VLBI. Its long baselines allow the two components to be clearly resolved, even at 1.5 GHz. The VLA can only resolve the transient down to 8 GHz.

A faint, compact feature southwest of the core is detected in the 1.5 GHz and 5 GHz images. In the e-MERLIN maps the offset of the transient from the nucleus is $\sim 0\farcs416$, or 468 pc. The high rms noise surrounding the nucleus increases the flux and position uncertainty. A comparison of the positions of the transient and the nucleus between the e-MERLIN observations and JVLA observations is provided in Table 6.3. The off-nucleus peak is offset from the nucleus by -0.3795 arcsec in RA and -0.1696 arcsec in Dec at 5 GHz, and by -0.362582 arcsec in RA and -0.178 arcsec at 1.5 GHz. In the VLA observations this offset is measured to be -0.3754 arcsec in RA and -0.183 arcsec in Dec. The VLA offsets were calculated using the position of the nucleus that was determined by Gordon et al. (2016).

A plot of the spectral energy distribution of the core is provided in Fig. 6.18. The flux density of the core at 1.5 GHz is $S_\nu = 450 \pm 90$ mJy. The flux density of the core at 1.5 GHz in the 1987 VLA data $S_\nu \sim 635 \pm 64$ mJy. The difference in flux densities measured between the VLA and the e-MERLIN arrays can be

attributed to the difference in types of emission included in the measurement. The VLA measurement includes part of the jet emission, as it is difficult to exclude at lower resolution. The AGN core is also expected to be variable (e.g., Mushotzky et al., 1993), which could also lead to a difference in the measured flux between the two arrays at different epochs. In the e-MERLIN L-band image, the system temperature calibration was done by using estimated antenna temperatures. This added additional uncertainty in the flux scaling during calibration. The error on the flux calibration at 1.5 GHz is estimated to be $\leq 20\%$. Both 2016 JVLA data in Perley et al. (2017) show a rising spectrum from 8.5 GHz to 21.2 GHz before gradually decreasing. If the trend is extrapolated to the 1.5 GHz VLA data, the e-MERLIN fluxes at 1.5 GHz and 5 GHz are consistent with the expected core flux. Perley et al. (2017) suggest that the flux is decreasing at lower frequencies. More observations with e-MERLIN at 1.5 GHz and 5 GHz would detect temporal changes in flux on longer timescales to verify this claim.

A plot of the SED of the off-nucleus transient using VLA, JVLA, and e-MERLIN data is provided in Fig. 6.19. The flux density of the off-nuclear source at 1.5 GHz in the e-MERLIN map is $5.2\pm1.95\pm1.04$ mJy, where the first error is noise (dominated by sidelobes from the core) and the second error is the uncertainty in the gain calibration. In the 5 GHz e-MERLIN map the flux density is 4.02 ± 0.5 mJy. The flux densities at 1.5 GHz and 5 GHz are consistent with the trends set by the JVLA data. Since the positions of the source in the e-MERLIN map aligns with the position in the JVLA maps (see Table 6.3), a detection of the transient by e-MERLIN at 1.5 GHz and 5 GHz is confirmed.

6.3.2 Identifying the Transient Source

Although size estimates are still being improved, VLBA images indicate that the source is confined to a region < 4 pc (Perley et al., 2017). Perley et al. (2017) first considered the possibility that feature B is an unassociated source in the foreground or background of the radio galaxy, such as an active M-dwarf or a coincidental quasar (e.g., Robrade and Schmitt, 2005; Perley et al., 2017). Given that Cygnus A is positioned at low Galactic latitudes ($b = 5.76°$), it seems perfectly reasonable to assume a radio source in the Milky Way Galaxy could be responsible for the new signal (Canalizo et al., 2003). Stellar-sized radio sources within the Milky Way Galaxy were eliminated based on the difference in colours between Galactic stars and the emission within this region of Cygnus A (Canalizo

et al., 2003). There is also the problem that finding a Galactic radio source that aligns with the source to within $\sim 0\farcs42$ is quite low ($< 10^{-4}$) (Perley et al., 2017). Background sources such as quasars are even less likely to be detected in the inner region of Cygnus A due to the high extinction of signals (Ogle et al., 1997; Canalizo et al., 2003). Observations with the Keck II telescope revealed circular polarization vectors that corresponded to a quasar obscured by a large, dusty narrow-line region (Ogle et al., 1997). Even if the environment surrounding the quasar is clumpy, allowing some light through, the probability of a chance alignment within 1 arcsecond between a background quasar and the nucleus of Cyg A is even lower than that of a Galactic source (Canalizo et al., 2003; Perley et al., 2017). Based on these arguments it seems more likely that feature B is located within Cygnus A.

Any source within the host galaxy of Cygnus A must be capable of producing a signal that is bright at radio frequencies (see Fig. 6.19) and compact (< 4 pc) within $< 0\farcs5$ of the nucleus. At any given frequency the SED of B (including the e-MERLIN 5 GHz data) follows that of non-thermal emission. The integrated flux at 8.5 GHz ($\sim$2.83 mJy) and the flux density at 5 GHz have a spectral index of ~ -0.66. The $\leq 20\%$ increase in the flux calibration error at 1.5 GHz e-MERLIN limited the certainty of non-thermal emission at this frequency. Non-thermal emission (see §1.6) requires relativistically moving electrons in a magnetic field (i.e. synchrotron emission) and accelerated shocks to produce radio emission like this. The observed characteristics of the transient, along with the high luminosity measurements found by Perley et al. (2017) ($L_\nu \approx 3 \times 10^{29}$ erg s^{-1} Hz^{-1}) significantly narrow down the possibilities to two options: (1) supernovae (SNe) and (2) AGNs. This does not include all supernovae though since the luminosity is high even for most supernovae and radio signals are not produced in Type Ia (e.g., Perez-Torres et al., 2015; Perley et al., 2017).

For supernovae with luminosities exceeding the required luminosity through relativisitic jets or the interaction with the environment (i.e. relativistic SNe and strongly interacting SNe), there are still many problems remaining (Perley et al., 2017). First, there is the issue of supernovae in the dense inner region. Supernovae have previously been observed in dense, gas-rich nuclear regions of other AGN, such as SN 2006gy around the AGN Markarian 297A (e.g., Yin, 1994). Yet, in the case of of SN 2006gy the VLA was unable to detect radio signals. This is hardly unusual considering only some supernovae produce radio signals. The problem

lies in the probability of catching these radio-producing supernovae during an observation. Perley et al. (2017) argue that chance of catching a radio-producing supernovae during a random observation of the radio galaxy to be extremely low ($< 5 \times 10^{-3}$). Detection of the the transient in the infrared and optical bands from HST images (mid-1990s) and Keck images (2002) further complicates the supernovae model (Perley et al., 2017). The optical detection over many years suggests it would need to be a supernovae from a very massive star positioned within a dense star cluster (Perley et al., 2017). Again, this is not unusual given the environment is suitable for forming such regions. If the transient is located within a star cluster emission lines should be detected. Spectroscopic NIR/optical studies (e.g., Jackson et al., 1998; Canalizo et al., 2003) have so far been unsuccessful in detecting any.

It hardly seems surprising that massive black holes are the alternative option for being responsible for the radio emission given their ability to generate large energy outputs (see §1.4). The NIR/adaptive optics observations by Canalizo et al. (2003) suggest that the transient may be a tidally stripped core from a smaller galaxy that has not yet merged with the larger galaxy's central black hole. If Cyg A is merging with a much lower mass galaxy this could explain the bright nuclear region, the large radio jets and lobes, and the giant dust lane through the centre of the galaxy (Canalizo et al., 2003). Although most of the properties described for B directly supports AGN, there is one peculiar feature not typically observed in AGN. Radio observations of Cygnus A before the 1990s showed no detection of the source. Less than a decade later the source was bright enough to be easily detected. Cores are known to be variable, but are typically still observable. If the AGN has gone from an inactive stage to an active stage, there is usually some evidence that an AGN was previously active after it has turned off (Perley et al., 2017). In theory this can easily be explained by improvements in instrumentation, allowing fainter objects to be probed. Alternatively, a steadily accreting black hole or a tidal disruption event (TDE) could also trigger an increase in luminosity.

For now only black hole theories will be considered since both Keck II and VLA observations show significantly more evidence in support of this. Chandra observations (2015-2017) of the transient detected no strong X-ray emission ($<$ 5%) from B (De Vries et al., 2019); steadily accreting black holes are typically expected to have X-ray emission $>$ 5%. The fundamental plane relation (Plotkin

et al., 2012) can be applied to black holes radiating below the Eddington limit. It is defined as

$$\log L_{\rm X} = (1.45 \pm 0.04) \log L_{\rm R} - (0.88 \pm 0.06) \log M_{\rm BH} - 6.07 \pm 1.10, \qquad (6.1)$$

where where $L_{\rm X}$ is the X-ray luminosity, $L_{\rm R}$ is the radio luminosity at 5 GHz, and $M_{\rm BH}$ is the mass of the black hole in solar masses. From this we obtain the relationship between the luminosities and the mass of the black hole,

$$M_{\rm BH} \propto L_{\rm X}^{-1.14} L_{\rm R}^{1.65}. \qquad (6.2)$$

De Vries et al. (2019) extrapolated the VLA data to 5 GHz to obtain an integrated flux of ~ 3.5 mJy. Using the estimated flux with the X-ray luminosity from 0.5 to 10 keV (1.2×10^{43} ergs s^{-1}) in Eqn. 6.2 (e.g., Plotkin et al., 2012; De Vries et al., 2019), the lower limit on the black hole mass was determined to be 4×10^8 M$_\odot$ (De Vries et al., 2019). The integrated flux of the transient in the e-MERLIN 5 GHz map ($\sim 4.02 \pm 0.5$ mJy) gives a $\sim 15\%$ increase in the flux density. This suggests that if the fundamental plane equation can be applied to the transient, then the e-MERLIN flux gives a lower limit still on the order of $\sim 10^8$ M$_\odot$.

Table 6.3: The position and flux of the off-nuclear transient and nucleus of Cygnus A as observed by different arrays and frequencies. Given frequencies represent the centre frequencies. All of the JVLA/VLA transient data were taken from Perley et al. (2017). The Very Large Baseline Array (VLBA) data were taken from Gordon et al. (2016). The e-MERLIN data were derived from the work done for this thesis. The given RA and Dec positions belong to the position of the transient at each frequency and epoch. The flux of the transient and nucleus is given by S_{tran} and S_{nuc}.

Array	Observation Date	ν_c (GHz)	α_{tran}	δ_{tran}	S_{trans} (mJy)
VLA	1989/01	8.34	–	–	< 0.69
VLA	1992	22	–	–	< 0.5
VLA	1994	22	–	–	< 0.8
VLA	1996	22	–	–	< 1.32
VLA	1997	45	–	–	< 0.78
JVLA	2015/07	7.1-17.0	19:59:28.32345	$+40°44'01\overset{''}{.}9133$	4.0−4.86
JVLA	2015/08	21.2−47.0	19:59:28.32345	$+40°44'01\overset{''}{.}9133$	2.88−4.37
JVLA	2016/10	8.5−47.0	19:59:28.32345	$+40°44'01\overset{''}{.}9133$	2.83−4.49
e-MERLIN	2019/01	1.5	19:59:28.328	$+40°44'01\overset{''}{.}913$	5.2±2.2
e-MERLIN	2017/07	5	19:59:28.3227	$+40°44'01\overset{''}{.}9280$	4.02±0.5
Array	Observation Date	ν_C (GHz)	α_{nuc}	δ_{nuc}	S_{nuc} (Jy)
VLBA			19:59:28.35648	$+40°44'02\overset{''}{.}0963$	
e-MERLIN	2019/01	1.5	19:59:28.3546	$+40°44'02\overset{''}{.}106$	0.421±0.042
e-MERLIN	2017/07	5	19:59:28.35609	$+40°44'02\overset{''}{.}0976$	1.08±0.11

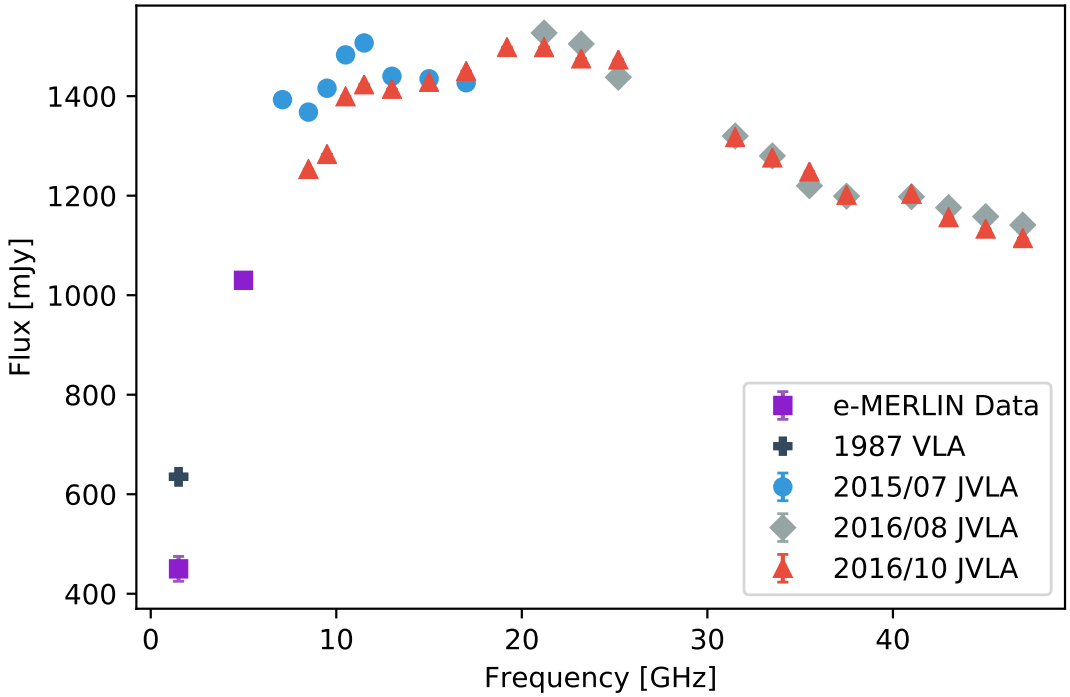

Figure 6.18: The spectral energy distribution of the core in Cygnus A. Image is reproduced with integrated fluxes given at three recent JVLA epochs (blue circles, grey diamonds, and orange triangles) by Perley et al. (2017). The 1987 VLA data (black cross) were obtained from a 1.5 GHz calibrated VLA map provided by Dr. Rick Perley (private communication) for this thesis. The integrated fluxes derived at 1.5 GHz and 5 GHz with the e-MERLIN array (purple squares) are included at one epoch each.

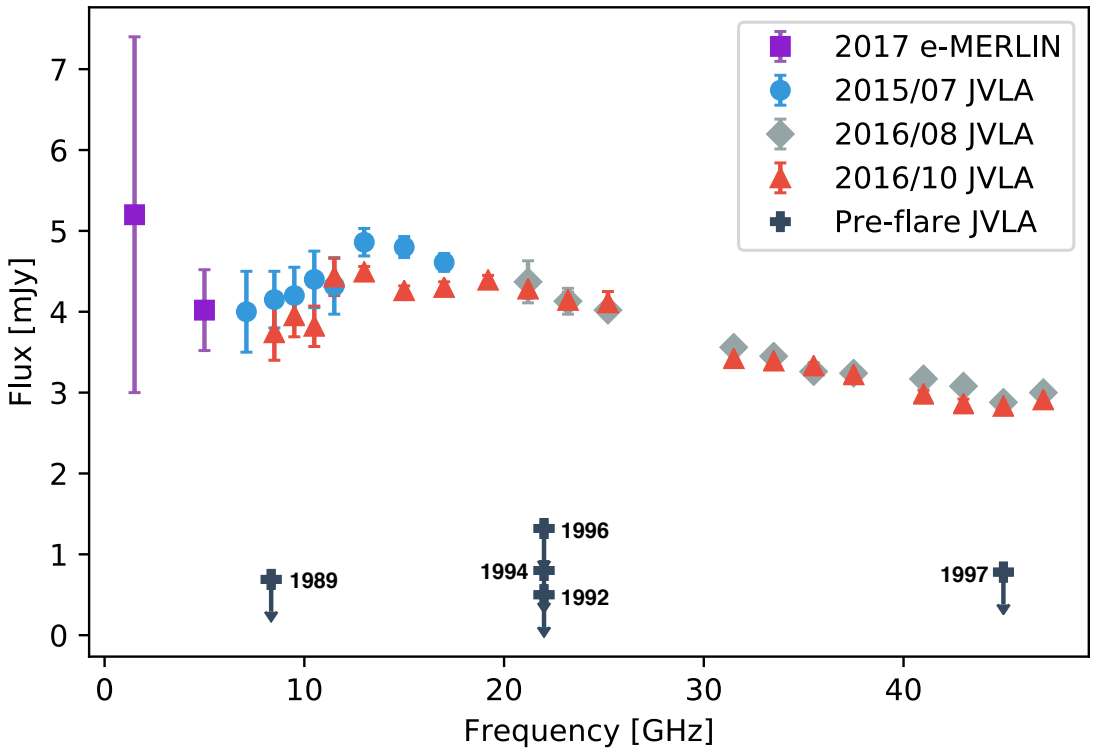

Figure 6.19: The spectral energy distribution of the Cygnus A transient (B). Image is reproduced with the integrated fluxes given at three recent JVLA epochs (blue circles, grey diamonds, and orange triangles) and five pre-flaring VLA epochs (black crosses) by Perley et al. (2017). Pre-flaring fluxes shown are upper limits. The integrated fluxes derived at 1.5 GHz and 5 GHz with the e-MERLIN array (purple squares) are included at two epochs.

6.3.3 Imaging the Torus

AGN models predict a detailed inner structure that can account for the various observed properties such as the detection of narrow and sometimes broad emission lines. At the centre lies a supermassive black hole (SMBH) surrounded by a hot accretion disk at a radius < 1 pc away from the SMBH. Beyond the accretion disk highly ionised gas lies, producing the broad emission lines (> 1000 km s^{-1}). Between the accretion disk and < 100 pc from the SMBH, conservation of angular momentum results in the formation of a torus composed of gas in the host galaxy (Carilli et al., 2019). The torus in AGN with jets is positioned perpendicular to the orientation of the jets. The presence and position of a torus is crucial in understanding differences between Type 1 and Type II AGN. A full description of the unified model is presented in §1.3. Detecting a torus in Cygnus A has been challenging; previous observations were limited by sensitivity and resolution. Carilli et al. (2019) presented what may be the first direct image of a torus around the AGN in Cygnus A using recent observations with the JVLA. The radio image revealing the torus structure at 22 GHz is shown in Fig. 6.1b.

Features C1 and C2 in the 5 GHz map shown in Fig. 6.7 point to a possible extended structure nearly perpendicular to the direction of the jet. These features are aligned with the position of the suspected torus at higher frequencies in the JVLA maps and extends $\sim 0\farcs10$ from the centre of the core. A comparison of the 5 GHz e-MERLIN map with the 22 GHz JVLA map is provided in Fig. 6.20. The nucleus in the e-MERLIN L-band map was severely affected by negative bowls in the position where the torus would be. In the 5 GHz e-MERLIN map the rms noise around the nuclear region is quite high, thus reducing the signal to noise near the torus (see Table 3.6 in §3.8). Also lowering confidence in the detection is the appearance of a large negative bowl of the same order as the structure west of C2. Carilli et al. (2019) modeled the spectral index of the torus using JVLA observations from $20 - 40$ GHz. The spectral index was determined to be 0.1, which is consistent with optically thin free-free emission (Carilli et al., 2019). The integrated flux density of the torus region after the core was subtracted from the 5 GHz e-MERLIN map was $< 8 \pm 0.85$ mJy (see Fig. 6.21). Using this integrated flux density with the 21 mJy measurement of the torus region at 34 GHz (Perley et al., 2017), the spectral index was determined to be ~ 0.5. This is slightly larger than the models predicted but expected due to the sidelobes surrounding the core.

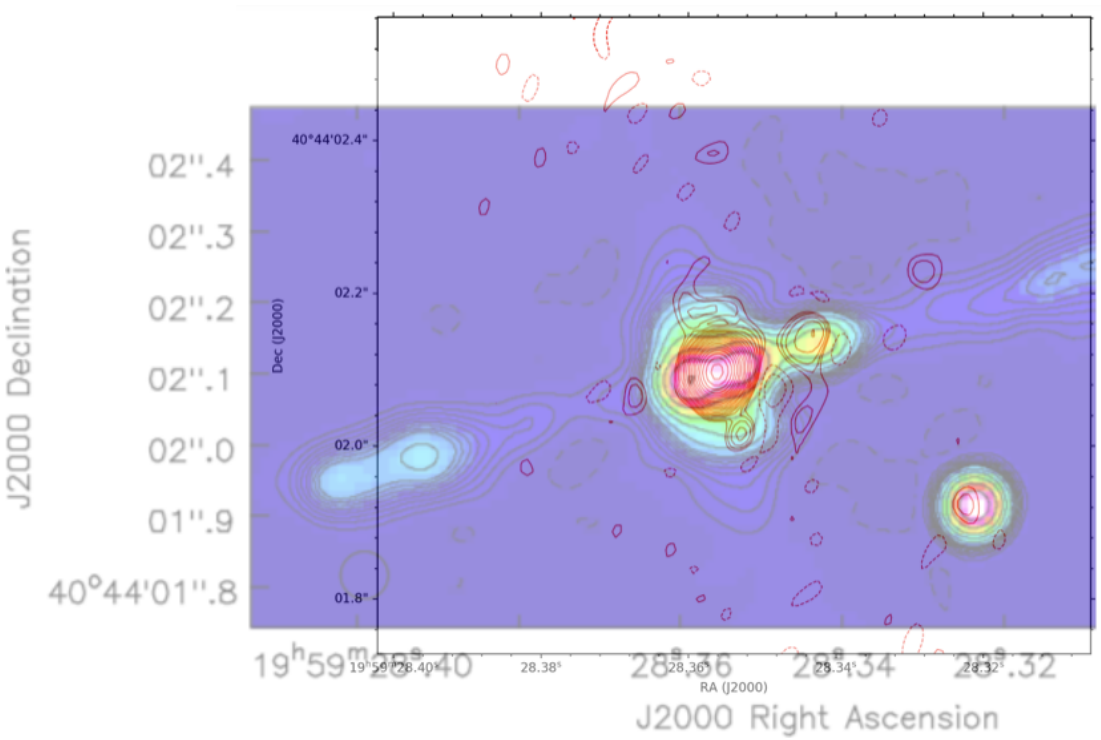

Figure 6.20: Red contours from the 5 GHz e-MERLIN images are superimposed on the 22 GHz JVLA map by Carilli et al. (2019). The position of the torus and transient in the 22 GHz JVLA map aligns with emission detected in the 5 GHz e-MERLIN map.

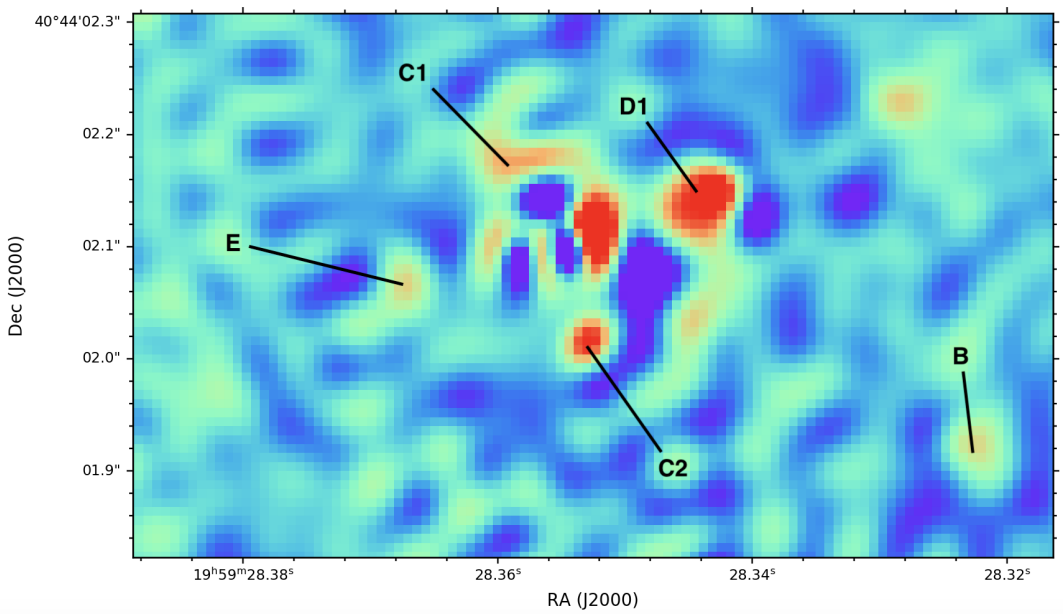

Figure 6.21: The Cyg A core was subtracted from the 5 GHz e-MERLIN map to highlight the structure that extends 0.″10 from the core (C1 and C2). The structure aligns with the position of the recently discovered torus in Cygnus A (Carilli et al., 2019).

6.3.4 Hotspots in Cygnus A

Relativistic jets in DRAGNs have been proposed to explain countless features including (i) the bright cores of quasars (e.g., Jackson and Browne, 2013), (ii) the apparent superluminal motion (e.g., Whitney et al., 1971; Cohen et al., 1971; Wehrle et al., 2001), and (iii) the apparent sidedness of jets in some sources. Various studies have attempted to calculate the speed of the jet through observations or numerical simulations (e.g., Carilli et al., 1996; Martí, 2019). Observations at VLBI resolution of blobs of emission in the inner region of the core have been pivotal in calculating apparent jet speeds at parsec-scales (see §1.5.4). It is still unclear how jets at kiloparsec distances differ, largely due to the low luminosity and uncertainty in their transverse jet profiles, although there is evidence that suggests relativistic speeds are maintained in powerful sources (e.g., Hardcastle et al., 1999). Hotspots may offer important clues to the nature of jets. It is generally accepted that hotspots are the product of a supersonic downstream flow interacting with the slow moving intergalactic medium (Blandford and Rees, 1974). When these fast moving flows are abruptly impeded by a slow moving material strong shocks can form, which power the hotspots. Most of the kinetic

energy of the jet dissipates in the hotspot, the remaining is dispersed behind the hotspot as a back flow of material (e.g., Longair, 2011). Studying the hotspots can reveal more about the jet that is driving it into the interstellar medium (Carilli et al., 1999). Double-lobed FRII type radio galaxies are excellent sources for probing the properties of DRAGNs due to their bright hotspots, extensive lobes, and detection of both the jet and counterjet (typically). Cygnus A is especially important because of its close proximity and its very bright hotspots have been extensively studied over the years in various bands and resolutions.

If we assume that (1) the jets are intrinsically symmetric, thus the hotspots are symmetric, and (2) the hotspots are coherent blobs of plasma moving outwards, we can place a limit on the advance speed of the jet-head (v_a). The brightness ratio S_a/S_r is related to v_a by

$$\frac{S_a}{S_r} = \left(\frac{1+\beta\cos(\theta_a)}{1-\beta\cos(\theta_a)}\right)^{3+\alpha}, \tag{6.3}$$

where $\beta = v_a/\mathrm{c}$, α is the spectral index of the hotspots, and θ_a is the angle between the observer's line of sight and the velocity of the approaching hotspot (e.g., Wilson and Scheuer, 1983; Komissarov and Falle, 1996; Miller-Jones et al., 2004). The flux ratio of the primary hotspots (L1 and G1) at 5 GHz was calculated to be $S_a/S_r = 2.3 \pm 0.3$. From Figs. 6.14a and 6.15 the spectral index of the hotspots was determined to be ~ -0.7. Given that β cannot be > 1, substituting the maximum value $\beta = 1$ into Eqn. 6.3 gives a maximum angle of $\sim 80°$. This orientation angle is consistent with previous work (e.g., Bartel et al., 1995) in which it was determined that Cygnus A is oriented at an angle between $55° - 85°$ from the line of sight.

Instead of coherent blobs, the hotspots can be considered as shocks with material flowing through them (see §1.2.3). In this case Eqn. 6.3 becomes

$$\frac{S_a}{S_r} = \left(\frac{1+\beta\cos(\theta_a)}{1-\beta\cos(\theta_a)}\right)^{2+\alpha},$$

where $\beta = v_f/c$ and v_f is the flow speed of the jet plasma through the shock. Using the same flux ratio and spectral index as in the other case, and remembering that β cannot be larger than 1, the angle to the line of sight is $\theta \leq 72°$. Since the e-MERLIN maps suffer from extensive sidelobes, the flux measurements of the primary hotspots most certainly include some flux contribution from the

sidelobes. Also considering the additional $\leq 20\%$ increase in error on the flux scaling in the L-band e-MERLIN maps (see §6.3.1), this would affect the spectral index values used in the calculation. Precession models by Steenbrugge and Blundell (2008) show that a $\sim 60^\circ$ angle to the line of sight best fits the curvature of Cygnus A's jets. The distance between corresponding pairs of knots on the jet and counterjet side at this angle give a jet speed $\lesssim 0.5c$ (Steenbrugge and Blundell, 2008). While a value of $\beta = 1$ is close to the value derived from the most extreme pairing of knots in Steenbrugge and Blundell (2008) ($v = 0.98c$), it is at least twice the stated value for most measurement points and larger than the quoted speeds ($0.27c < v < 0.82c$ derived at larger angles, $> 80^\circ$) in Krichbaum et al. (1998). Substituting θ_a with the best fit angle (60°) yields $v_f \sim 0.6c$, a number that is $\sim 20\%$ higher than the value obtained by Steenbrugge and Blundell (2008). Given that there is a small difference between the two values, a derived angle $\leq 72^\circ$ from the e-MERLIN data is consistent with the other work.

Decades of Cyg A observations have provided a unique opportunity to observe changes in hotspots over time. High-resolution maps are especially important for observing changes (e.g., superluminal motion) and are needed over a long period to determine pattern speeds of hotspots. Many years (or rather many decades) between observations are needed to notice changes in the structure of Cyg A's hotspots, even if the detailed structure changes at close to c. The FWHM of the beam in the 5 GHz e-MERLIN map, which is $0\farcs042$, is 147 light years in width. If observations over 20 years could measure a change of 0.1 beam width, a speed of $1c$ could just be seen in the source. The speed at which the hotspot advances in Cygnus A is still unknown. Some studies place the value at either $0.02c$ or $0.005c$ (e.g., Muxlow et al., 1988; Alexander and Pooley, 1996). Therefore, observations over more than 20 years could show bigger changes in the position of the hotspots. The shape of the hotspot is expected to fluctuate much faster than the overall speed of its outward motion though. With high fidelity maps these hotspot fluctuations could be noticeable between 20 years of observations.

The earliest high fidelity Cygnus A maps with resolutions comparable to e-MERLIN's resolution were taken by the VLA at 43 GHz during the 1990s (Carilli et al., 1999). Attempts were made to obtain the original combined map presented in Carilli et al. (1999) but it was determined by Dr. Chris Carilli that the maps are no longer readable (private communication). From the VLA archive the individual images from the observations in the study were retrieved. The images

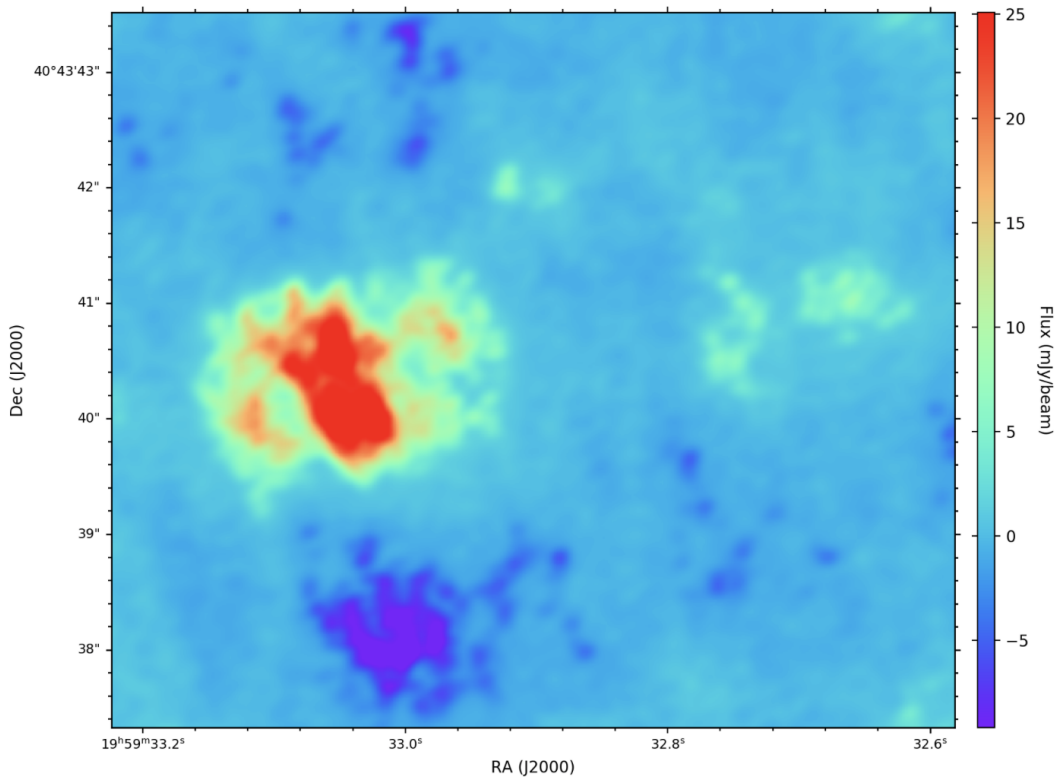

Figure 6.22: The east hotspot of Cygnus A as observed by the VLA at 43 GHz. Image is reproduced from Carilli et al. (1999).

were averaged together in an attempt to match the fidelity of the original study's map. The large difference in resolution between the maps in the study meant much of the fine detail was smoothed out when averaged. It was ultimately decided that only the best quality map, taken on 29 March 1997 at 0.″150 by 0.″121 resolution, should be used (see Figs. 6.22 and 6.23). The cores in the VLA map and the e-MERLIN map were aligned by the position of the peak pixel. The 43 GHz map was then subtracted from the 5 GHz map. The results of the map subtractions in the hotspots are provided in Figs. 6.24 and 6.25. The emission present in the subtracted maps presents an upper limit to the shape changes in the hotspots over 20 years. The residual maps are limited by the fidelity of the e-MERLIN map (e.g., large sidelobes) and spectral index effects (e.g., shifts in hotspot peaks across frequencies (e.g., Pyrzas et al., 2015). Despite this, changes can be seen in the hotspots, especially in the bright primary hotspot L1.

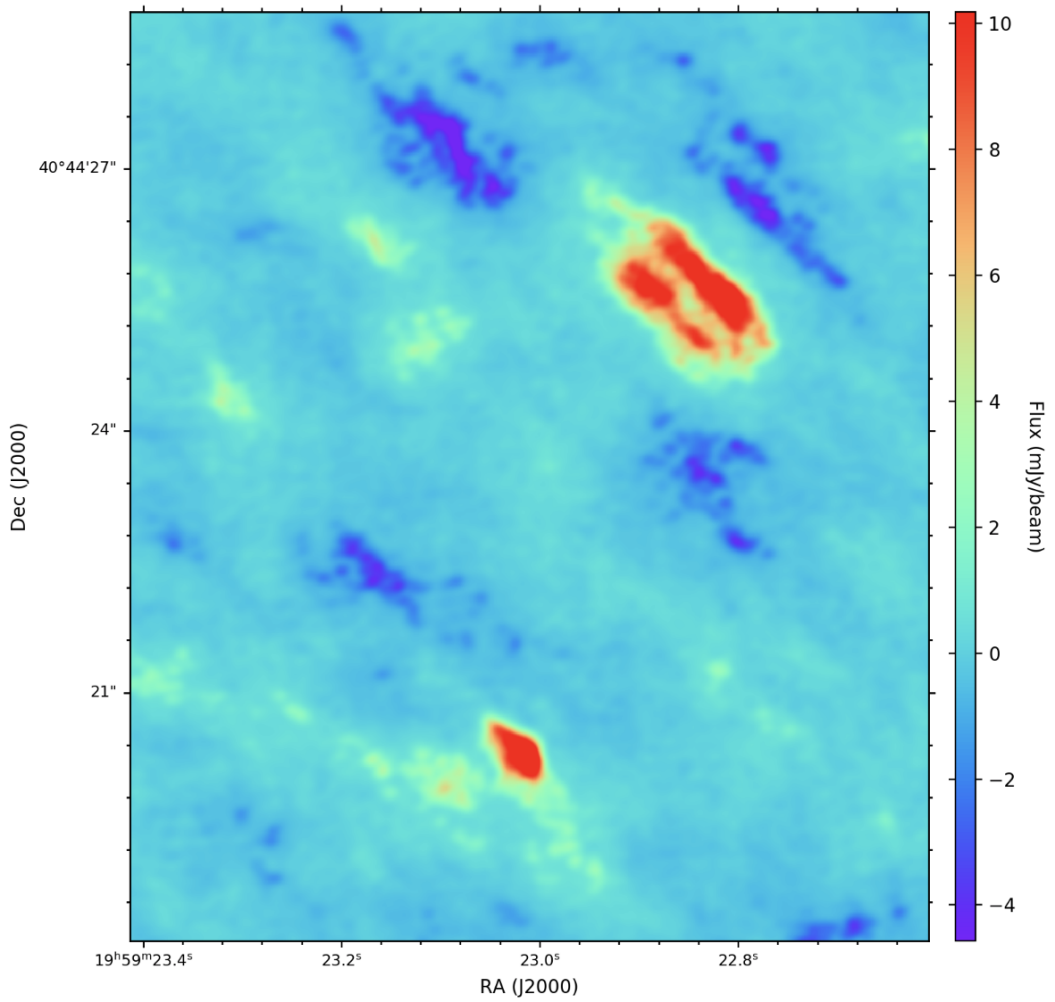

Figure 6.23: The west hotspot of Cygnus A as observed by the VLA at 43 GHz. Image is reproduced from Carilli et al. (1999).

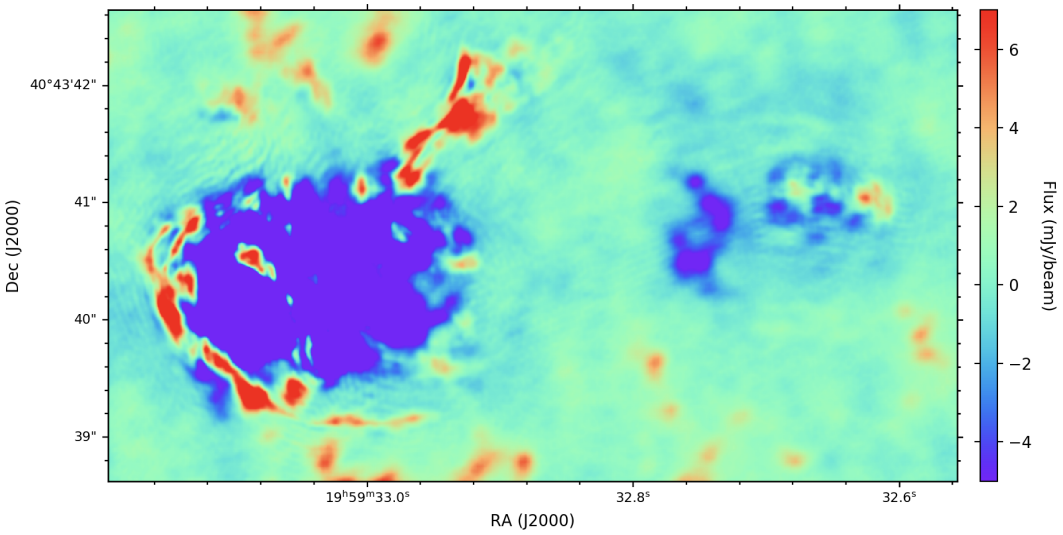

Figure 6.24: The 43 GHz VLA map of Cygnus A's east hotspot was subtracted from the 5 GHz e-MERLIN map to show changes in the hotspot over 20 years. This residual map shows an upper limit to the hotspot shape changes in the east hotspots.

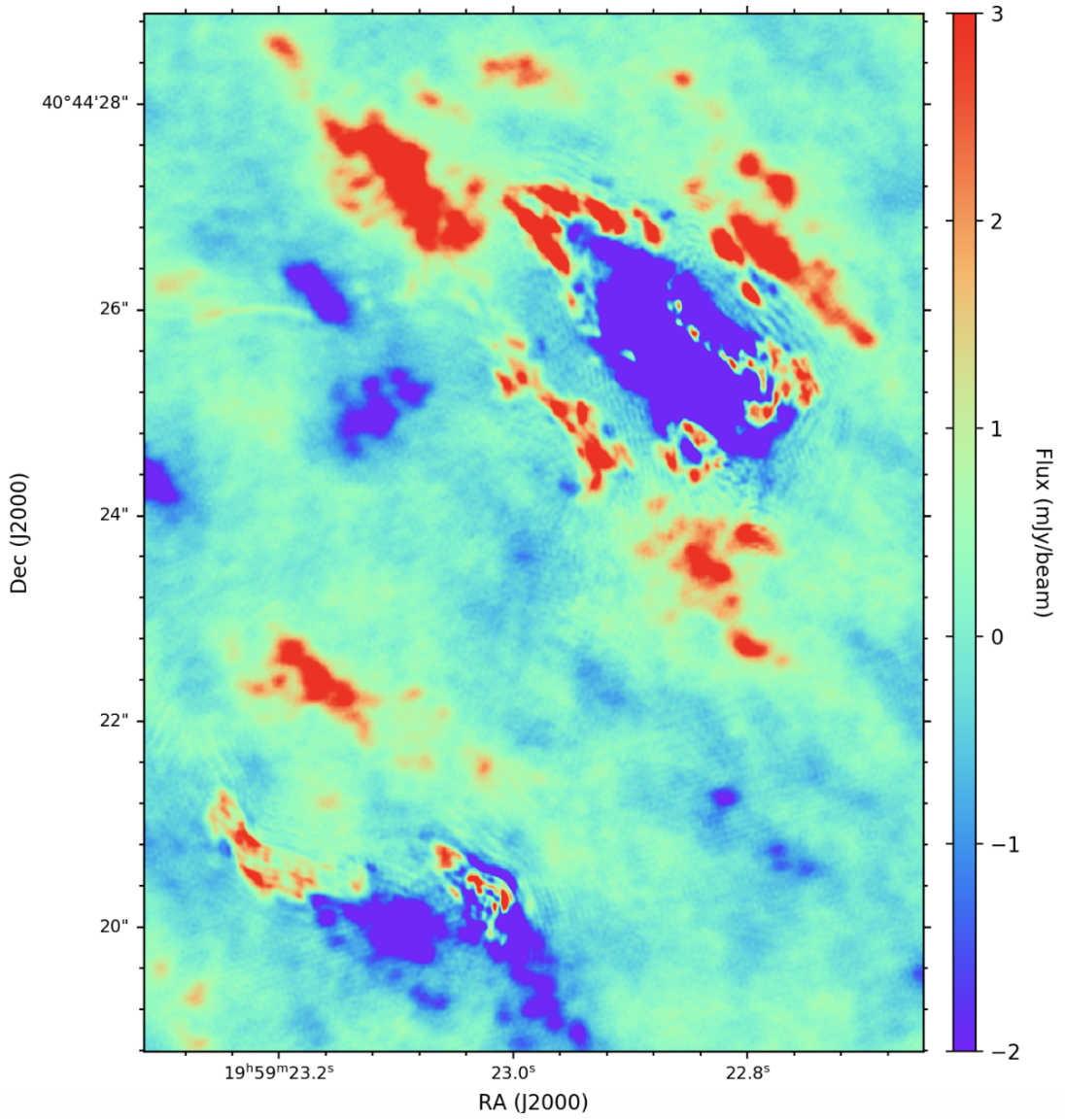

Figure 6.25: The 43 GHz VLA map of Cygnus A's west hotspot was subtracted from the 5 GHz e-MERLIN map to produce this residual map. The result gives an upper limit to the shape changes in the west hotspots after 20 years.

6.4 Summary

Observing Cygnus A with the e-MERLIN array provided a unique challenge for the dishes due to the bright, large, extended structure. The 1.5 GHz map and 5 GHz map from the e-MERLIN observations have shown:

(i) The hotspots can be resolved into complex sub-structures at e-MERLIN resolution. At L-band the hotspots are severely affected by sidelobes and flux calibration errors limit the image fidelity. Similarly, at C-band the sparse uv coverage introduced many sidelobes. Even with sidelobes the e-MERLIN maps are consistent with high fidelity maps produced by Dabbech et al. (2018) and Carilli et al. (1999).

(ii) The e-MERLIN array has detected the off-nuclear transient at 1.5 and 5 GHz. The flux density of the transient at 1.5 GHz is 5.2 ± 2.2 mJy and 4.02 ± 0.5 mJy, which is consistent with the SED of the transient. The transient is estimated to be 468 pc from the core in the e-MERLIN maps.

(iii) The jet and lobes in Cygnus A are mostly resolved out at e-MERLIN resolutions. At 1.5 GHz a small, elongated feature corresponding to the jet and counterjet can be seen. At 5 GHz only a few small knots of emission close to the nucleus is detected. In both maps feature M may be a knot in the jet.

(iv) Imaging the torus of Cygnus A at C-band with the e-MERLIN may be possible. The research presented in this thesis could not verify the detection of features C1 and C2. The spectral index at C1 and C2 was determined to be ~ 0.5 and an upper limit on the flux was determined to be $< 8 \pm 0.85$ mJy. Additional polarization calibration could help by revealing whether the emission is polarized or unpolarized, thus determining the typie of emission it is.

(v) Assuming that $v_f = 1c$, the maximum angle to the line of sight of the jet axis is shown to be $\leq 72°$.

(vi) An upper limit to the hotspot shape changes over 20 years is presented in this chapter. The maps were produced by subtracting the 43 GHz VLA map from the 5 GHz e-MERLIN map.

Chapter 7

Conclusions

7.1 Reflection

In this thesis I presented high resolution radio maps of three powerful FRII DRAGNs. The sample included two quasars (3C 334 and 3C 263) and one radio galaxy (Cygnus A).

In Chapter 2 I discussed the theory of radio astronomy and introduced the procedures used to create reliable radio maps from interferometry. By using many baselines radio interferometers can simulate a single dish with a diameter equivalent to the maximum baseline of the array. Imaging bright, extended structures from sparse *uv* data typically requires multiple iterations of self-calibration and a combination of various deconvolution and advanced imaging strategies.

In Chapter 3 I presented e-MERLIN+JVLA observations of 3C 334, 3C 263, and Cygnus A at L- and C-band. The calibration and imaging theory presented in Chapter 2 was utilised to calibrate and image the three DRAGNs as part of the e-MERLIN Extragalactic Jets Legacy Project. The strategy used to correct Cygnus A's contribution to the system temperature in the e-MERLIN array in CASA was described. Final calibrated images of each of the sources are presented.

In Chapter 4 I presented an analysis of the quasar 3C 334 based off of the final calibrated images provided in Chapter 3. The radio images of 3C 334 at e-MERLIN resolution are the best resolution maps to date. Many of the knots (H,I,J,M,N) in the Bridle et al. (1994a) are resolved into two structures in the e-MERLIN+JVLA map. In the counterjet side lobe, feature B is resolved into two peaks and is shown to be a secondary hotspot in the head. The spectral index and polarization maps suggest B is still being energised by a 'splatter' from the

primary hotspot C. Based on the alignment of many features there is evidence in support of jet precession in 3C 334.

Close to feature F the jet has an initial apparent opening angle close to 9° that decreases until widening again ∼3″ from the core. The α_{app} remains below 5° from ∼ 4″ from the core. The jet is recollimating throughout the straight jet. Emission between N2 and O and N2 and P1 dims before brightening again, with N2 pointed in the direction of P1. From this, the maps indicate that the shock at the end of the jet (hotspot O) does not cross the whole of the jet.

In Chapter 5 I presented e-MERLIN+JVLA maps of the total intensity distribution in the quasar 3C 263. Although the radio maps were severely affected by sidelobes from the east hotspot (at least on the east side of the source), the maps revealed a strikingly narrow and straight jet. Some of the knots close to the hotspot were well below the noise. Sub-features were observed in the knots closer to the core, even though the jet was not fully resolved at e-MERLIN resolution. The first knot from the core, previously missing from the VLA map, is identified in the e-MERLIN+JVLA map. The deflected jet entering the hotspot is well-defined despite the presence of sidelobes. X-ray maps show evidence of hot, dense gas asymmetrically located around 3C 263. The east lobe is embedded in more hot gas than the west lobe. This has caused the jet to be much shorter than the counterjet and hotspot K to be exceptionally compact and bright (compared to hotspot B).

The counterjet side lobe is less affected by the sidelobes from the east hotspot. In the west lobe the hotspot is positioned within the lobe, close to the centre, and slightly back from the leading edge. The hotspot is complex with multiple steep gradients beyond the central component. Feature A in the (Bridle et al., 1994a) is resolved into many sub-features spread out near the western edge of the lobe.

In Chapter 6 I presented the results of the 1.5 GHz and 5 GHz radio maps of Cygnus A as observed by the e-MERLIN array. An error of $\leq 20\%$ in the system temperature calibration at 1.5 GHz led to an increase in flux measurements. The ridge (I1,I2) and J at 1.5 GHz are features observed in lower-resolution VLA maps. Maps of the hotspots are consistent with high fidelity VLA maps by Dabbech et al. (2018) and Carilli et al. (1999).

The nucleus of Cygnus A reveals components of a jet, the core, and evidence of an off-nucleus transient (B). The centre position of the radio source was found to be at $\alpha = 19{:}59{:}28.328$, $\delta = +40°44'01913$ at 1.5 GHz, and $\alpha = 19{:}59{:}28.3227$,

$\delta = +40°44'019280$ at 5 GHz. The positions at both frequencies coincide with the position described by Perley et al. (2017) ($\alpha = 19{:}59{:}28.32345$, $\delta = +40°44'019133$). The SED of the transient indicates that a flux between 3 and 4 mJy would be appropriate at 1.5 GHz and 5 GHz. At 5 GHz $S = 4.02 \pm 0.5$ mJy. At 1.5 GHz $S = 5.2 \pm 2.2$ mJy. Both values are within the estimated range for the source's flux. Therefore, e-MERLIN has detected the transient.

At 5 GHz an extended structure perpendicular to the jet that was suggested to be a torus was imaged by Carilli et al. (2019). The 5 GHz e-MERLIN map resolved a similar structure coinciding with the identified torus. While the position and extent of the source ($\sim 10''$) matched that in the higher frequency JVLA maps, it was not clear whether the features were real or not. A large negative bowl resided next to the southern part of the structure (C2) which lowered confidence in a detection. At this point detection of the torus by e-MERLIN was inconclusive.

7.2 Future Work

The radio maps presented here give a first look at FRII DRAGNs observed for the e-MERLIN Extragalactic Jets Legacy Project. The e-MERLIN array has proven its ability to image bright, extended sources with high sensitivity and resolution. The project can improve and advance in several areas:

- Imaging the other FRII DRAGNs in the project could assist with our understanding of steady flows and how common (or uncommon) unsteady flows are in jet producing DRAGNs. All sources in the sample have been observed but require calibration and imaging.

- By comparing the FRII DRAGNs with the FRI sources in the project we may begin to understand more about their differences. Some of the FRI sources have been calibrated and imaged by other members of the project.

- The self-calibration of 3C 263 should be improved. Advanced imaging techniques, such as peeling, should be used to improve the fidelity of the map. This can lead to a better detection of the jet and an improved spectral index map.

- The project should seek to improve the sensitivity of the 3C 334 map. Although the map of 3C 334 had a decent peak to noise ratio, the removal of all

Lovell baselines reduced the sensitivity. It could very well not change much in regards to the features visible in the map, but improving the sensitivity will lead to a better transverse profile.

- The e-MERLIN observations of Cygnus A should be supplemented with the VLA observations to reduce the prevalence of negative bowls and bright sidelobes. Advanced self-calibration techniques should be used. A more accurate system temperature calibration could provide additional insight into the transient at 1.5 GHz.

- Additional polarization calibration should be done on 3C 334 and 3C 263 to compare with the results from Bridle et al. (1994a).

Bibliography

Alexander, P. and Leahy, J. P.: 1987, *MNRAS* **225**, 1

Alexander, P. and Pooley, G. G.: 1996, *The large-scale structure, dynamics and thermodynamics of Cygnus A*, p. 149

Anderson, K. S.: 1974, *ApJ* **189**, 195

Antonucci, R.: 1993, *ARA&A* **31**, 473

Antonucci, R., Hurt, T., and Kinney, A.: 1994, *Nature* **371(6495)**, 313

Argo, M.: 2015, *Journal of Open Research Software* **3**, e2

Baade, W. and Minkowski, R.: 1954, *ApJ* **119**, 206

Bally, J.: 2016, *Annual Review of Astronomy and Astrophysics* **54(1)**, 491

Bartel, N., Sorathia, B., Bietenholz, M. F., Carilli, C. L., and Diamond, P.: 1995, *Proceedings of the National Academy of Science* **92(25)**, 11371

Barthel, P.: 1989a, *Scientific American* **260**, 20

Barthel, P. D.: 1989b, *ApJ* **336**, 606

Beckmann, V. and Shrader, C. R.: 2012, *Active Galactic Nuclei*, Wiley, New York

Bennett, A. S.: 1962, *MmRAS* **68**, 163

Bicknell, G. V.: 1994, *Australian Journal of Physics* **47**, 669

Bicknell, G. V.: 1995, *The Astrophysical Journal Supplement Series* **101**, 29

Blandford, R. and Eichler, D.: 1987, *Physics Reports* **154(1)**, 1

Blandford, R., Meier, D., and Readhead, A.: 2018, *arXiv e-prints*

Blandford, R. D. and Payne, D. G.: 1982, *MNRAS* **199**, 883

Blandford, R. D. and Rees, M. J.: 1974, *MNRAS* **169**, 395

Blandford, R. D. and Znajek, R. L.: 1977, *MNRAS* **179**, 433

Boettcher, M., Harris, D. E., and Krawczynski, H.: 2012, *Relativistic Jets from Active Galactic Nuclei*, Wiley, New York

Bogers, W. J., Hes, R., Barthel, P. D., and Zensus, J. A.: 1994, **105**, 91

Bolton, J. G., Stanley, G. J., and Slee, O. B.: 1949, *Nature* **164**, 101

Bonafede, A.: 2010, *Ph.D. thesis*, Universita degli Studi di Bologna

Böttcher, M., Baring, M. G., Liang, E. P., Summerlin, E. J., Fu, W., Smith, I. A., and Roustazadeh, P.: 2015, in F. Massaro, C. C. Cheung, E. Lopez, and A. Siemiginowska (eds.), *Extragalactic Jets from Every Angle*, Vol. 313 of *IAU Symposium*, pp 153–158

Bowman, M., Leahy, J. P., and Komissarov, S. S.: 1996, *MNRAS* **279**, 899

Bremer, M. N.: 1997, **284(1)**, 126

Bridle, A. H.: 1982, *Physics in Canada* **38**, 59

Bridle, A. H.: 1984, *The Astronomical Journal* **89**, 979

Bridle, A. H.: 1986, *Canadian Journal of Physics* **64**, 353

Bridle, A. H., Hough, D. H., Lonsdale, C. J., Burns, J. O., and Laing, R. A.: 1994a, *AJ* **108**, 766

Bridle, A. H., Laing, R. A., Scheuer, P. A. G., and Turner, S.: 1994b, in G. V. Bicknell, M. A. Dopita, and P. J. Quinn (eds.), *The Physics of Active Galaxies*, Vol. 54 of *Astronomical Society of the Pacific Conference Series*, p. 187

Bridle, A. H. and Perley, R. A.: 1984, **22**, 319

Briggs, D. S., Schwab, F. R., and Sramek, R. A.: 1999, in G. B. Taylor, C. L. Carilli, and R. A. Perley (eds.), *Synthesis Imaging in Radio Astronomy II*, Vol. 180 of *Astronomical Society of the Pacific Conference Series*, p. 127

Brocksopp, C., Kaiser, C. R., Schoenmakers, A. P., and de Bruyn, A. G.: 2007, *MNRAS* **382(3)**, 1019

Brown, D. L. and Burns, J. O.: 1991, *AJ* **102**, 1917

Burke, B. F. and Graham-Smith, F.: 1997, *An introduction to radio astronomy*, Cambridge University Press, Cambridge

Canalizo, G., Max, C., Whysong, D., Antonucci, R., and Dahm, S. E.: 2003, **597(2)**, 823

Carilli, C. L., Dreher, J. W., and Perley, R. A.: 1989, *Cygnus a and the Williams Model*, Vol. 327, p. 51

Carilli, C. L., Kurk, J. D., van der Werf, P. P., Perley, R. A., and Miley, G. K.: 1999, **118(6)**, 2581

Carilli, C. L., Perley, R. A., Bartel, N., and Sorathia, B.: 1996, in P. E. Hardee, A. H. Bridle, and J. A. Zensus (eds.), *Energy Transport in Radio Galaxies and Quasars*, Vol. 100 of *Astronomical Society of the Pacific Conference Series*, p. 287

Carilli, C. L., Perley, R. A., Dhawan, V., and Perley, D. A.: 2019, *ApJ* **874(2)**, L32

Carilli, C. L., Perley, R. A., and Dreher, J. H.: 1988, *ApJl* **334**, L73

Cawthorne, T. V.: 1991, in *Beams and Jets in Astrophysics*, Vol. 19, p. 187, Cambridge University Press, Cambridge

Celotti, A. and Fabian, A. C.: 1993, *MNRAS* **264**, 228

Clarke, D. A. and Burns, J. O.: 1991, *ApJ* **369**, 308

Clausen-Brown, E., Lyutikov, M., and Kharb, P.: 2011, *Monthly Notices of the Royal Astronomical Society* **415(3)**, 2081

Cohen, M. H., Cannon, W., Purcell, G. H., Shaffer, D. B., Broderick, J. J., Kellermann, K. I., and Jauncey, D. L.: 1971, *ApJ* **170**, 207

Condon, J. J., Condon, M. A., Gisler, G., and Puschell, J. J.: 1982, *ApJ* **252**, 102

Contini, M., Viegas, S. M., and Prieto, M. A.: 2004, *Monthly Notices of the Royal Astronomical Society* **348(3)**, 1065

Cornwell, T. J.: 2008, *IEEE Journal of Selected Topics in Signal Processing* **2**, 793

Cornwell, T. J., Golap, K., and Bhatnagar, S.: 2008, *IEEE Journal of Selected Topics in Signal Processing* **2**, 647

Cotton, W. D., Wittels, J. J., Shapiro, I. I., Marcaide, J., Owen, F. N., Spangler, S. R., Rius, A., Angulo, C., Clark, T. A., and Knight, C. A.: 1980, *ApJl* **238**, L123

Cox, C. I., Gull, S. F., and Scheuer, P. A. G.: 1991, *MNRAS* **252**, 558

Crawford, C. S. and Fabian, A. C.: 2003, **339(4)**, 1163

Crawford, C. S., Fabian, A. C., George, I. M., and Naylor, T.: 1991, **248**, 139

Croston, J. H., Ineson, J., and Hardcastle, M. J.: 2018, *MNRAS* **476(2)**, 1614

Curtis, H. D.: 1918, *Publications of Lick Observatory* **13**, 9

Dabbech, A., Onose, A., Abdulaziz, A., Perley, R. A., Smirnov, O. M., and Wiaux, Y.: 2018, **476(3)**, 2853

Davidson, K. and Netzer, H.: 1979, *Reviews of Modern Physics* **51**, 715

De Vries, M., Wise, M., Nulsen, P. E. J., Siemiginowska, A., Rowlinson, A., and Reynolds, C.: 2019, in *AAS/High Energy Astrophysics Division*, AAS/High Energy Astrophysics Division, p. 106.62

Dennett-Thorpe, J., Bridle, A. H., Scheuer, P. A. G., Laing, R. A., and Leahy, J. P.: 1997, *MNRAS* **289(4)**, 753

Diamond, P. J., Garrington, S. T., Gunn, A. G., Leahy, J. P., McDonald, A., Muxlow, T. W. B., Richards, A. M. S., and Thomasson, P.: 2003, *MERLIN User Guide*

Dibai, E. A., Postnov, K. A., and Charugin, V. M.: 1983, *Soviet Astronomy* **27(3)**, 257

Donohoe, J. and Smith, M. D.: 2016, *MNRAS* **458**, 558

Edge, D. O., Shakeshaft, J. R., McAdam, W. B., Baldwin, J. E., and Archer, S.: 1959, *MmRAS* **68**, 37

Eilek, J. A. and Shore, S. N.: 1989, **342**, 187

Ekers, R. D., Fanti, R., Lari, C., and Parma, P.: 1978, **276**, 588

Elvis, M., Wilkes, B. J., McDowell, J. C., Green, R. F., Bechtold, J., Willner, S. P., Oey, M. S., Polomski, E., and Cutri, R.: 1994, *ApJs* **95**, 1

English, W., Hardcastle, M. J., and Krause, M. G. H.: 2016, *MNRAS* **461**, 2025

Fabian, A. C., Naylor, T., and Sciama, D. W.: 1991, *Monthly Notices of the Royal Astronomical Society* **249(1)**, 21P

Fanaroff, B. L. and Riley, J. M.: 1974, *MNRAS* **167**, 31P

Fath, E. A.: 1909, *Popular Astronomy* **17**, 504

Fernini, I.: 2001, *The Astronomical Journal* **122(1)**, 83

Fernini, I.: 2019, **364(10)**, 167

Garrington, S. T., Conway, R. G., and Leahy, J. P.: 1991, *MNRAS* **250**, 171

Garrington, S. T., Leahy, J. P., Conway, R. G., and Laing, R. A.: 1988, *Nature* **331(6152)**, 147

Gilbert, G. M., Riley, J. M., Hardcastle, M. J., Croston, J. H., Pooley, G. G., and Alexander, P.: 2004, *MNRAS* **351**, 845

Giroletti, M., Giovannini, G., Feretti, L., Cotton, W. D., Edwards, P. G., Lara, L., Marscher, A. P., Mattox, J. R., Piner, B. G., and Venturi, T.: 2004, *ApJ* **600(1)**, 127

Gomez, J. L., Alberdi, A., and Marcaide, J. M.: 1993, *Astronomy and Astrophysics* **274**, 55

Gomez, J. L., Alberdi, A., and Marcaide, J. M.: 1994, *Astronomy and Astrophysics* **284**, 51

Gopal-Krishna and Wiita, P. J.: 1991, **373**, 325

Gordon, D., Jacobs, C., Beasley, A., Peck, A., Gaume, R., Charlot, P., Fey, A., Ma, C., Titov, O., and Boboltz, D.: 2016, *VizieR Online Data Catalog* p. J/AJ/151/154

Gourgouliatos, K. N. and Komissarov, S. S.: 2018, *Nature Astronomy* **2**, 167

Graham, I.: 1970, *MNRAS* **149**, 319

Greisen, E. W.: 2003, in A. Heck (ed.), *Information Handling in Astronomy - Historical Vistas*, Vol. 285 of *Astrophysics and Space Science Library*, p. 109

Haardt, F. and Maraschi, L.: 1991, *ApJ* **380**, L51

Hall, P. B., Ellingson, E., Green, R. F., and Yee, H. K. C.: 1995, **110**, 513

Halliday, I.: 1969, *JRASC* **63**, 91

Hardcastle, M.: 2015, in I. Contopoulos, D. Gabuzda, and N. Kylafis (eds.), *The Formation and Disruption of Black Hole Jets*, Vol. 414 of *Astrophysics and Space Science Library*, p. 83

Hardcastle, M. J.: 2001, *Extended X-Ray Emission Around Radio-Loud Quasars*, pp 127–132, Springer US, Boston, MA

Hardcastle, M. J.: 2008, in T. A. Rector and D. S. De Young (eds.), *Extragalactic Jets: Theory and Observation from Radio to Gamma Ray*, Vol. 386 of *Astronomical Society of the Pacific Conference Series*, p. 46

Hardcastle, M. J., Alexander, P., Pooley, G. G., and Riley, J. M.: 1997, *MNRAS* **288(4)**, 859

Hardcastle, M. J., Alexander, P., Pooley, G. G., and Riley, J. M.: 1999, **304(1)**, 135

Hardcastle, M. J., Birkinshaw, M., Cameron, R. A., Harris, D. E., Looney, L. W., and Worrall, D. M.: 2002, **581(2)**, 948

Hardcastle, M. J., Croston, J. H., and Kraft, R. P.: 2007, **669(2)**, 893

Hardee, P. E. and Norman, M. L.: 1990, **365**, 134

Hargrave, P. J. and Ryle, M.: 1974, **166**, 305

Hazard, C., Mackey, M. B., and Shimmins, A. J.: 1963, *Nature* **197**, 1037

Heckman, T. M., Smith, E. P., Baum, S. A., van Breugel, W. J. M., Miley, G. K., Illingworth, G. D., Bothun, G. D., and Balick, B.: 1986, *ApJ* **311**, 526

Hewitt, A. and Burbidge, G.: 1987, *ApJs* **63**, 1

Hey, J. S., Phillips, J. W., and Parsons, S. J.: 1946, *Nature* **157**, 296

Hill, G. J. and Lilly, S. J.: 1991, *ApJ* **367**, 1

Ho, L. C., Filippenko, A. V., Sargent, W. L. W., and Peng, C. Y.: 1997, in *American Astronomical Society Meeting Abstracts #189*, Vol. 189 of *American Astronomical Society Meeting Abstracts*, p. 122.09

Hoffmeister, C.: 1929, *Astronomische Nachrichten* **236**, 233

Hughes, P. A. and Miller, L.: 1991, in *Beams and Jets in Astrophysics*, Vol. 19, p. 1, Cambridge University Press, Cambridge

Ishwara-Chandra, C. H., Saikia, D. J., Kapahi, V. K., and McCarthy, P. J.: 1998, **300(1)**, 269

Jackson, N. and Browne, I. W. A.: 2013, **429(2)**, 1781

Jackson, N., Tadhunter, C., and Sparks, W. B.: 1998, **301(1)**, 131

Jennison, R. C.: 1958, *MNRAS* **118**, 276

Jennison, R. C. and Das Gupta, M. K.: 1953, *Nature* **172**, 996

Kauffmann, G. and Haehnelt, M. G.: 2002, *Monthly Notices of the Royal Astronomical Society* **332(3)**, 529

Kellermann, K. I. and Pauliny-Toth, I. I. K.: 1981, *ARA&A* **19**, 373

Kellermann, K. I., Sramek, R., Schmidt, M., Shaffer, D. B., and Green, R.: 1989, *AJ* **98**, 1195

Kirk, J. G.: 1997, in M. Ostrowski, M. Sikora, G. Madejski, and M. Begelman (eds.), *Relativistic Jets in AGNs*, pp 145–152

Komissarov, S. S. and Falle, S. A. E. G.: 1996, in P. E. Hardee, A. H. Bridle, and J. A. Zensus (eds.), *Energy Transport in Radio Galaxies and Quasars*, Vol. 100 of *Astronomical Society of the Pacific Conference Series*, p. 327

Konigl, A.: 1981, *ApJ* **243**, 700

Krause, M. G. H., Shabala, S. S., Hardcastle, M. J., Bicknell, G. V., Böhringer, H., Chon, G., Nawaz, M. A., Sarzi, M., and Wagner, A. Y.: 2019, *MNRAS* **482**, 240

Krichbaum, T. P., Alef, W., Witzel, A., Zensus, J. A., Booth, R. S., Greve, A., and Rogers, A. E. E.: 1998, **329**, 873

Krolik, J. H.: 1999, *Active galactic nuclei : from the central black hole to the galactic environment*, Princeton University Press, Princeton

Kukula, M. J., Dunlop, J. S., Hughes, D. H., and Rawlings, S.: 1998, *MNRAS* **297**, 366

Lai, I.-L., Ip, W.-H., Su, C.-C., Wu, J.-S., Lee, J.-C., Lin, Z.-Y., Liao, Y., Thomas, N., Sierks, H., Barbieri, C., Lamy, P., Rodrigo, R., Koschny, D., Rickman, H., Keller, H. U., Agarwal, J., AHearn, M. F., Barucci, M. A., Bertaux, J.-L., Bertini, I., Boudreault, S., Cremonese, G., Da Deppo, V., Davidsson, B., Debei, S., De Cecco, M., Deller, J., Fornasier, S., Fulle, M., Groussin, O., Gutirrez, P. J., Gttler, C., Hofmann, M., Hviid, S. F., Jorda, L., Knollenberg, J., Kovacs, G., Kramm, J.-R., Khrt, E., Kppers, M., Lara, L. M., Lazzarin, M., Lopez Moreno, J. J., Marzari, F., Naletto, G., Oklay, N., Shi, X., Tubiana, C., and Vincent, J.-B.: 2017, *Monthly Notices of the Royal Astronomical Society* **462(Suppl$_1$)**, $S533$

Laing, R.: 1982, in D. S. Heeschen and C. M. Wade (eds.), *Extragalactic Radio Sources*, Vol. 97 of *IAU Symposium*, pp 161–162

Laing, R.: 1989, *Radio Observation of Hot Spots*, Vol. 327, p. 27, Springer, New York

Laing, R. A.: 1988, *Nature* **331(6152)**, 149

Laing, R. A.: 1993, in R. J. Davis and R. S. Booth (eds.), *Sub-arcsecond Radio Astronomy*, p. 346

Laing, R. A.: 1994, in G. V. Bicknell, M. A. Dopita, and P. J. Quinn (eds.), *The Physics of Active Galaxies*, Vol. 54 of *Astronomical Society of the Pacific Conference Series*, p. 227

Laing, R. A.: 1996, in P. E. Hardee, A. H. Bridle, and J. A. Zensus (eds.), *Energy Transport in Radio Galaxies and Quasars*, Vol. 100 of *Astronomical Society of the Pacific Conference Series*, p. 241

Laing, R. A. and Bridle, A. H.: 2002, *Monthly Notices of the Royal Astronomical Society* **336(1)**, 328

Laing, R. A. and Bridle, A. H.: 2008, in T. A. Rector and D. S. De Young (eds.), *Extragalactic Jets: Theory and Observation from Radio to Gamma Ray*, Vol. 386 of *Astronomical Society of the Pacific Conference Series*, p. 70

Laing, R. A., Parma, P., Murgia, M., Feretti, L., Giovannini, G., Bridle, A. H., and Perley, R. A.: 2001, in R. A. Laing and K. M. Blundell (eds.), *Particles and Fields in Radio Galaxies Conference*, Vol. 250 of *Astronomical Society of the Pacific Conference Series*, p. 437

Leahy, J., Black, A. R. S., Dennett-Thorpe, J., Hardcastle, M. J., Komissarov, S., Perley, R. A., Riley, J. M., and Scheuer, P. A. G.: 1997, *Monthly Notices of the Royal Astronomical Society* **291(1)**, 20

Leahy, J. P.: 1991, in *Beams and Jets in Astrophysics*, Vol. 19, p. 100, Cambridge University Press, Cambridge

Leahy, J. P.: 1993, in H.-J. Röser and K. Meisenheimer (eds.), *Jets in Extragalactic Radio Sources, Proceedings of a Workshop Held at Ringberg Castle, Tegernsee, FRG, September 22-28, 1991. Edited by H.-J. Röser and K. Meisenheimer. Springer-Verlag Berlin Heidelberg New York. Also Lecture Notes in Physics, volume 421, 1993, p.1*, Vol. 421, p. 1, Springer, New York

Leahy, J. P. and Perley, R. A.: 1991, *AJ* **102**, 537

Liu, R. and Pooley, G.: 1991, *MNRAS* **253**, 669

LOFAR Collaboration: 2013, *A&A* **556**, A2

Longair, M. S.: 2011, *High Energy Astrophysics*, Cambridge University Press, Cambridge

Lonsdale, C. J. and Barthel, P. D.: 1986, **92**, 12

Lonsdale, C. J. and Morison, I.: 1983, *MNRAS* **203**, 833

Looney, L. W. and Hardcastle, M. J.: 2000, **534(1)**, 172

Lynden-Bell, D.: 1969, *Nature* **223(5207)**, 690

MacDonald, G. H., Kenderdine, S., and Neville, A. C.: 1968, **138**, 259

Marecki, A.: 2012, *A&A* **545**, A132

Marscher, A. P.: 1977, *AJ* **82**, 781

Martí, J.-M.: 2019, *Galaxies* **7(1)**, 24

Massaro, E., Nesci, R., and Piranomonte, S.: 2012, *MNRAS* **422**, 2322

Matthews, T. A. and Sandage, A. R.: 1963, *ApJ* **138**, 30

Meliani, Z. and Keppens, R.: 2007, *A&A* **475(3)**, 785

Miller-Jones, J. C. A., Blundell, K. M., and Duffy, P.: 2004, **603(1)**, L21

Mizuno, Y., Hardee, P., and Nishikawa, K.-I.: 2007, *ApJ* **662(2)**, 835

Monceau-Baroux, R., Porth, O., Meliani, Z., and Keppens, R.: 2014, *A&A* **561**, A30

Mullin, L. M., Riley, J. M., and Hardcastle, M. J.: 2008, *MNRAS* **390(2)**, 595

Mushotzky, R. F., Done, C., and Pounds, K. A.: 1993, **31**, 717

Muxlow, T. W. B. and Garrington, S. T.: 1991, in *Beams and Jets in Astrophysics*, Vol. 19, p. 52, Cambridge University Press, Cambridge

Muxlow, T. W. B., Pelletier, G., and Roland, J.: 1988, **206**, 237

Nalewajko, K. and Sikora, M.: 2008, in F. A. Aharonian, W. Hofmann, and F. Rieger (eds.), *American Institute of Physics Conference Series*, Vol. 1085 of *American Institute of Physics Conference Series*, pp 483–485

Netzer, H.: 1987, *MNRAS* **225**, 55

Ogle, P. M., Cohen, M. H., Miller, J. S., Tran, H. D., Fosbury, R. A. E., and Goodrich, R. W.: 1997, **482(1)**, L37

Panessa, F., Baldi, R. D., Laor, A., Padovani, P., Behar, E., and McHardy, I.: 2019, *Nature Astronomy* **3**, 387

Pearson, T. J.: 1996, in P. E. Hardee, A. H. Bridle, and J. A. Zensus (eds.), *Energy Transport in Radio Galaxies and Quasars*, Vol. 100 of *Astronomical Society of the Pacific Conference Series*, p. 97

Peck, L. W. and Fenech, D. M.: 2013, *Astronomy and Computing* **2**, 54

Peckham, R. J.: 1973, *Nature Physical Science* **246**, 54

Pedelty, J. A., Rudnick, L., McCarthy, D., and Spinrad, H.: 1989, in *Bulletin of the American Astronomical Society*, Vol. 21 of , p. 1093

Perez-Torres, M., Alberdi, A., Beswick, R. J., Lundqvist, P., Herrero-Illana, R., Romero-Cañizales, C., Ryder, S., della Valle, M., Conway, J., Marcaide, J. M., Mattila, S., Murphy, T., and Ros, E.: 2015, in *Advancing Astrophysics with the Square Kilometre Array (AASKA14)*, p. 60

Perley, D. A., Perley, R. A., Dhawan, V., and Carilli, C. L.: 2017, *ApJ* **841(2)**, 117

Perley, R. A. and Butler, B. J.: 2013, *ApJs* **204**, 19

Perley, R. A. and Butler, B. J.: 2017, *The Astrophysical Journal Supplement Series* **230(1)**, 7

Perley, R. A., Chandler, C. J., Butler, B. J., and Wrobel, J. M.: 2011, *ApJl* **739(1)**, L1

Perley, R. A., Schwab, F. R., and Bridle, A. H.: 1989, in R. A. Perley, F. R. Schwab, and A. H. Bridle (eds.), *Synthesis Imaging in Radio Astronomy*, Vol. 6 of *Astronomical Society of the Pacific Conference Series*, Astronomical Society of the Pacific, San Francisco

Peterson, B. M.: 1997a, *An Introduction to Active Galactic Nuclei*, Cambridge University Press, Cambridge

Peterson, B. M.: 1997b, *An Introduction to Active Galactic Nuclei*, Cambridge University Press, Cambridge

Peterson, B. M., Foltz, C. B., Cranshaw, D. M., Meyers, K. A., and Byard, P. L.: 1984, *ApJ* **279**, 529

Peterson, B. M., Wanders, I., Bertram, R., Hunley, J. F., Pogge, R. W., and Wagner, R. M.: 1998, *ApJ* **501**, 82

Phinney, E. S.: 1985, in J. S. Miller (ed.), *Astrophysics of Active Galaxies and Quasi-Stellar Objects*, pp 453–496

Piner, B. G., Bhattarai, D., Edwards, P. G., and Jones, D. L.: 2004, in *American Astronomical Society Meeting Abstracts*, Vol. 36 of *Bulletin of the American Astronomical Society*, p. 1536

Planck Collaboration: 2018, *arXiv e-prints*

Plotkin, R. M., Markoff, S., Kelly, B. C., Körding, E., and Anderson, S. F.: 2012, **419(1)**, 267

Pudritz, R. E., Ouyed, R., Fendt, C., and Brandenburg, A.: 2007, in B. Reipurth, D. Jewitt, and K. Keil (eds.), *Protostars and Planets V*, p. 277

Pushkarev, A. B., Kovalev, Y. Y., Lister, M. L., and Savolainen, T.: 2011, *Mem. Societa Astronomica Italiana* **82**, 190

Pyrzas, S., Steenbrugge, K. C., and Blundell, K. M.: 2015, **574**, A30

Rau, U.: 2012, *Imaging and Deconvolution*

Rau, U. and Cornwell, T. J.: 2011, *A&A* **532**, A71

Rees, M. J.: 1966, *Nature* **211**, 468

Reynolds, C. S., Fabian, A. C., Celotti, A., and Rees, M. J.: 1996, *MNRAS* **283**, 873

Rich, J. W., de Blok, W. J. G., Cornwell, T. J., Brinks, E., Walter, F., Bagetakos, I., and Kennicutt, R. C., J.: 2008, *AJ* **136(6)**, 2897

Risaliti, G., Harrison, F. A., Madsen, K. K., Walton, D. J., Boggs, S. E., Christensen, F. E., Craig, W. W., Grefenstette, B. W., Hailey, C. J., Nardini, E., Stern, D., and Zhang, W. W.: 2013, *Nature* **494**, 449

Robrade, J. and Schmitt, J. H. M. M.: 2005, **435(3)**, 1073

Robson, I.: 1996, *Active galactic nuclei*, Praxis Publishing, New York

Rodriguez-Pascual, P. M., Mas-Hesse, J. M., and Santos-Lleo, M.: 1997, *A&A* **327**, 72

Romero, G. E., Boettcher, M., Markoff, S., and Tavecchio, F.: 2017, *Space Sci. Rev.* **207(1-4)**, 5

Roncarelli, M., Gaspari, M., Ettori, S., Biffi, V., Brighenti, F., Bulbul, E., Clerc, N., Cucchetti, E., Pointecouteau, E., and Rasia, E.: 2018, **618**, A39

Roy, A. L., Colbert, E. J. M., Wilson, A. S., and Ulvestad, J. S.: 1998, *ApJ* **504(1)**, 147

Ruszkowski, M. and Begelman, M. C.: 2002, *ApJ* **573**, 485

Rybicki, G. B. and Lightman, A. P.: 1979, *Radiative processes in astrophysics*, Wiley-Interscience Publication, New York

Ryle, M. and Hewish, A.: 1950, *Geophysical Journal* **6**, 138

Ryle, M. and Hewish, A.: 1960, *MNRAS* **120**, 220

Saripalli, L.: 2012, *AJ* **144**, 85

Sault, R. J. and Conway, J. E.: 1999, in G. B. Taylor, C. L. Carilli, and R. A. Perley (eds.), *Synthesis Imaging in Radio Astronomy II*, Vol. 180 of *Astronomical Society of the Pacific Conference Series*, p. 419

Sauty, C., Tsinganos, K., and Trussoni, E.: 2002, in A. W. Guthmann, M. Georganopoulos, A. Marcowith, and K. Manolakou (eds.), *Relativistic Flows in Astrophysics*, Vol. 589 of *Lecture Notes in Physics, Berlin Springer Verlag*, p. 41

Savage, B. D., Lu, L., Bahcall, J. N., Bergeron, J., Boksenberg, A., Hartig, G. F., Jannuzi, B. T., Kirhakos, S., Lockman, F. J., Sargent, W. L. W., Schneider, D. P., Turnshek, D., Weymann, R. J., and Wolfe, A. M.: 1993, *ApJ* **413**, 116

Scheuer, P. A. G.: 1982, in D. S. Heeschen and C. M. Wade (eds.), *Extragalactic Radio Sources*, Vol. 97 of *IAU Symposium*, pp 163–165

Schilizzi, R. T.: 1988, in L. Bianchi and R. Gilmozzi (eds.), *Mass Outflows from Stars and Galactic Nuclei*, pp 151–162, Springer Netherlands, Dordrecht

Seale, J. P. and Looney, L. W.: 2008, *The Astrophysical Journal* **675(1)**, 427

Seyfert, C. K.: 1943, *ApJ* **97**, 28

Shen, B. S. P.: 1970, *Nature* **228**, 1070

Shields, G. A.: 1999, *PASP* **111**, 661

Sikora, M. and Madejski, G.: 2000, *ApJ* **534(1)**, 109

Sikora, M., Stawarz, Ł., and Lasota, J.-P.: 2007, *ApJ* **658(2)**, 815

Slipher, V. M.: 1917, *Proceedings of the American Philosophical Society* **56**, 403

Smith, E. P. and Heckman, T. M.: 1989, *ApJ* **341**, 658

Smith, M. D.: 2012, *Astrophysical Jets and Beams*, Cambridge University Press, Cambridge

Sol, H., Pelletier, G., and Asseo, E.: 1989, *MNRAS* **237**, 411

Steenbrugge, K. C. and Blundell, K. M.: 2008, **388(4)**, 1457

Stein, W. A., Odell, S. L., and Strittmatter, P. A.: 1976, *ARA&A* **14**, 173

Sulentic, J. W., Marziani, P., Zwitter, T., Dultzin-Hacyan, D., and Calvani, M.: 2000, *ApJ* **545**, L15

Swarup, G., Sinha, R. P., and Hilldrup, K.: 1984, *MNRAS* **208**, 813

Thomasson, P., Saikia, D. J., and Muxlow, T. W. B.: 2006, **372(4)**, 1607

Thompson, A. R.: 1986, in R. A. Perley, F. R. Schwab, and A. H. Bridle (eds.), *Synthesis Imaging*, pp 9–30

Thompson, A. R., Moran, J. M., and Swenson, Jr., G. W.: 2017, *Interferometry and Synthesis in Radio Astronomy, 3rd Edition*, Springer Publishing, New York

Trammell, S. R. and Goodrich, R. W.: 2002, *The Astrophysical Journal* **579(2)**, 688

Urry, C. M. and Padovani, P.: 1995, *PASP* **107**, 803

van Diepen, G. and Farris, A.: 1994, in D. R. Crabtree, R. J. Hanisch, and J. Barnes (eds.), *Astronomical Data Analysis Software and Systems III*, Vol. 61 of *Astronomical Society of the Pacific Conference Series*, p. 417

Wagner, A. Y. and Bicknell, G. V.: 2011, *ApJ* **728**, 29

Walg, S., Achterberg, A., Markoff, S., Keppens, R., and Meliani, Z.: 2013, *Monthly Notices of the Royal Astronomical Society* **433(2)**, 1453

Wardle, J. F. C., Homan, D. C., Ojha, R., and Roberts, D. H.: 1998, *Nature* **395**, 457

Wardle, J. F. C. and Potash, R. I.: 1982, in D. S. Heeschen and C. M. Wade (eds.), *Extragalactic Radio Sources*, Vol. 97 of *IAU Symposium*, pp 129–131

Wehrle, A. E., Piner, B. G., Unwin, S. C., Zook, A. C., Xu, W., Marscher, A. P., Teräsranta, H., and Valtaoja, E.: 2001, *ApJs* **133**, 297

Whitney, A. R., Shapiro, I. I., Rogers, A. E. E., Robertson, D. S., Knight, C. A., Clark, T. A., Goldstein, R. M., Marandino, G. E., and Vandenberg, N. R.: 1971, *Science* **173**, 225

Wiita, P. J.: 2006, *arXiv Astrophysics e-prints*

Wilkes, B.: 1999, in G. Ferland and J. Baldwin (eds.), *Quasars and Cosmology*, Vol. 162 of *Astronomical Society of the Pacific Conference Series*, p. 15

Williams, A. G.: 1991, in *Beams and Jets in Astrophysics*, Vol. 19, p. 342, Cambridge University Press, Cambridge

Williams, A. G. and Gull, S. F.: 1984, *Nature* **310(5972)**, 33

Williams, A. G. and Gull, S. F.: 1985, **313(5997)**, 34

Wilson, A. S. and Colbert, E. J. M.: 1995, *ApJ* **438**, 62

Wilson, M. J.: 1989, in K. Meisenheimer and H.-J. Roeser (eds.), *Hot Spots in Extragalactic Radio Sources*, Vol. 327 of *Lecture Notes in Physics, Berlin Springer Verlag*, pp 215–218

Wilson, M. J. and Scheuer, P. A. G.: 1983, **205**, 449

Wright, E. L.: 2006, *Publications of the Astronomical Society of the Pacific* **118(850)**, 1711

Wrobel, J. M. and Walker, R. C.: 1999, in G. B. Taylor, C. L. Carilli, and R. A. Perley (eds.), *Synthesis Imaging in Radio Astronomy II*, Vol. 180 of *Astronomical Society of the Pacific Conference Series*, p. 171

Yee, H. K. C., Green, R. F., and Stockman, H. S.: 1986, **62**, 681

Yin, Q. F.: 1994, **420**, 152